Energy deposition in the lower auroral ionosphere through energetic particle precipitation

A Thesis

Submitted for the Degree of

Doctor of Philosophy

in the

Department of Communication Systems

Lancaster University

Lancaster, UK.

By

Andrew John Kavanagh M.Phys.

October 2002

For James and Barbara Kavanagh

Energy deposition in the lower auroral ionosphere through energetic particle precipitation

(Ground and Space Based Observations of the Ionosphere)

Submitted for the Degree of Doctor of Philosophy
October 2002
by
Andrew John Kavanagh M.Phys.

Abstract

Ground-based imaging and broad beam riometers are used in conjunction with ionospheric radars and satellite instruments to investigate high-energy precipitation in the auroral zone. There are two dominant precipitation regimes in the auroral zone which lead to enhanced high frequency radio absorption; high energy electrons (> keV) from closed field lines, and protons (> MeV) penetrating from the solar wind following solar flares. Much of the work in this thesis uses data from riometers in Fennoscandia to measure the extent and movement of energetic precipitation from both sources. A case study of dayside absorption combines data from the imaging riometer with radar and satellite observations leading to an estimation of the energy of precipitation based on the riometer data. Two separate precipitation mechanisms were identified in the case study through the use of satellite particle measurements and ground-based observations of geomagnetic pulsations. The riometer showed varying movements of the absorption patches through the case study and a determination of different dominating particle drift regimes was possible through comparison with coherent HF radar. A statistical analysis of absorption in the imaging riometer field of view is carried out. The absorption is linked to both K_P and solar wind velocity using linear and quadratic fits of the data. The daily variation and distribution of absorption is investigated along with seasonal effects which are shown to be reliant on geomagnetic activity. A study of the large number of solar proton events from 1995 to 2001 inclusive is carried out with particular reference to those that produce significant absorption in the northern hemisphere polar cap (polar cap absorption –PCA). The occurrence of the absorption events is investigated and a simple empirical relationship between the integral proton flux and the absorption observed during geomagnetically undisturbed PCA conditions is developed.

Contents

Chapter Three : Instrumentation

Chapter Five : Absorption in the dayside Ionosphere – case study

Chapter 6 : Statistics of the variation of Absorption observed with IRIS

List of Figures

Chapter 1

Chapter 2

Chapter 3

Chapter 4

Chapter 5

Chapter 6

Chapter 7

Chapter 8

Declaration

The research presented in this thesis is my own work and has not been submitted in substantially the same form for the award of a higher degree elsewhere.

Some of the results have led to the publication of the following scientific paper in a refereed journal:

Kavanagh, A.J., F. Honary, I.W. McCrea,. E. Donovan, E.E. Woodfield, J. Manninen, and P.C. Anderson, Substorm related changes in precipitation in the dayside auroral zone – a multi instrument case study, *Ann. Geophys*., **20**, 1321-1334, 2002.

Acknowledgements

There are many people and organisations that I would like to thank and without whom this thesis would never have been written: PPARC and the Rutherford Appleton Laboratory for funding my studies.
Professor Farideh Honary for giving me the opportunity to study in the Ionosphere and Radio Propagation Group and for supervision together with Dr. Ian McCrea.
Every member of the IRPG from 1999 to 2002. Steve for computing advice and enormous help. Mike for sharing his campaigns. Andrew for tolerating my music and all the programming questions. John Hargreaves for pointing out where I went wrong.
The EISCAT group at RAL for their help and particularly to Vikki for introducing me to the joys of the EISCAT campaign.
Bern Blake, Phil Anderson and others at Aerospace, many thanks for lots of stimulating conversation, advice, references, SAMPEX and DMSP data and the invitation; I hope to continue to work with you.
The Leicester RSPPG (1999-2002) for the many hours of beer swilling, and in particular Adrian.
Agneta Svensson for being an excellent undergraduate tutor and supporting me all the way; and Tony Knight for starting me on the physics path. I hope that he isn't too disappointed that I'm not an engineer.
The most important people: my family. Too many to name but thank you for the support.
Special thanks go to my Mum and Dad without whose support (both emotional and financial) I could not have got this far; and a special dedication to Emma for keeping me happy and organised and for making sure that I got through this in one piece.

The Imaging Riometer for Ionospheric Studies (IRIS) is operated by the Department of Communications Systems at Lancaster University (UK), funded as a UK National Facility by the Particle Physics and Astronomy Research Council (PPARC) in collaboration with the Sodankylä Geophysical Observatory.
EISCAT is an international facility funded collaboratively by the research councils of Finland (SA), France (CNRS), Germany (MPG), Japan (NIPR), Norway (NAVF), Sweden (NFR) and the UK (PPARC). EISCAT data have been supplied through the UK EISCAT group at RAL.
The CUTLASS HF radars are deployed and operated by the University of Leicester and are jointly funded by the UK Particle Physics and Astronomy Research Council (PPARC), the Swedish Institute for Space Physics, Uppsala and the Finnish Meteorological Institute, Helsinki.
CANOPUS operations are funded by the Canadian Space Agency. The CANOPUS riometer data has been baselined by E. Spanswick and supplied by Eric Donovan.
Data from the Finnish chain of riometers was provided by Jyrkki Manninen at Sodankylä Geophysical University, an independent national institute of the University of Oulu.
Thanks to Dr. Tilmann Bösinger of the Space Research Group of the University of Oulu, who kindly provided the pulsation magnetometer data.
GEOTAIL magnetic field and plasma data were provided by S. Kokubun and T. Mukai through DARTS at the Institute of Space and Astronautical Science (ISAS) in Japan.

Chapter 1

The Solar Terrestrial Environment

1.1 Introduction

The Sun and Earth environments are coupled through radiative, dynamic and magnetic processes. The aim of this chapter is to summarise the regions of the solar-terrestrial environment, dwelling particularly on the high latitude, lower altitude ionosphere and the magnetosphere. This chapter also includes a brief summary of the techniques used to probe regions of the solar terrestrial environment. There then follows an outline of the research presented in this thesis.

1.2 The Sun

The sun emits radiation across a broad spectrum. X-rays and ultraviolet (UV) radiation are of particular importance in the interaction of the sun with the Earth's atmosphere. The radiation at these wavelengths follows an average eleven-year periodicity (the solar cycle) producing variations in the flux of orders of magnitude (Figure 1.1). Variability is largest at the shorter wavelengths (e.g. X-rays) and is related to the occurrence of solar flares (Rees, 1989).

1.3 Interplanetary Space

Between the Sun and the Earth is the region defined as interplanetary space. Contrary to popular belief this space is not a vacuum, but is instead populated by a low density,

variable medium. This medium and the manner through which the sun controls it are described in the following section.

1.3.1 The Solar Wind

Interplanetary space is filled by flowing plasma that has been identified as the outer solar atmosphere expanding, radially through the solar system. This plasma (the solar wind) is predominantly comprised of protons and electrons that are energetic enough to escape the solar gravity. At one astronomical unit (AU) the particles have velocities in the range of 300 to 700 km/s, though during periods of high solar activity, the solar wind can reach as high as 1000 km/s (e.g. Kivelson and Russell, 1995). Typical particle densities as measured at the Sun-Earth distance show protons at 6.6 cm^{-3} and electrons at 7.1 cm^{-3}, although the solar wind is extremely dynamic with large variations in both flow speed and density. Phenomena occurring at the Sun can dramatically affect the solar wind parameters. For example coronal holes are regions where solar plasma flows out into interplanetary space at high velocities creating regions in the solar wind known as high speed streams. Measurements downstream often show a sharp increase in solar wind speed as the stream rotates with the Sun. Another manifestation of the sun's influence on interplanetary space are solar flares. These are 'explosions' from the sun that occur when magnetic energy is suddenly released resulting in large amounts of electromagnetic radiation (across the entire spectrum) and the expulsion of very energetic charged particles (Figure 1.2). These will be described in more detail in later chapters. Flares occasionally occur with Coronal Mass Ejections (CME). These are huge clouds of plasma (~10^{13} kg) that

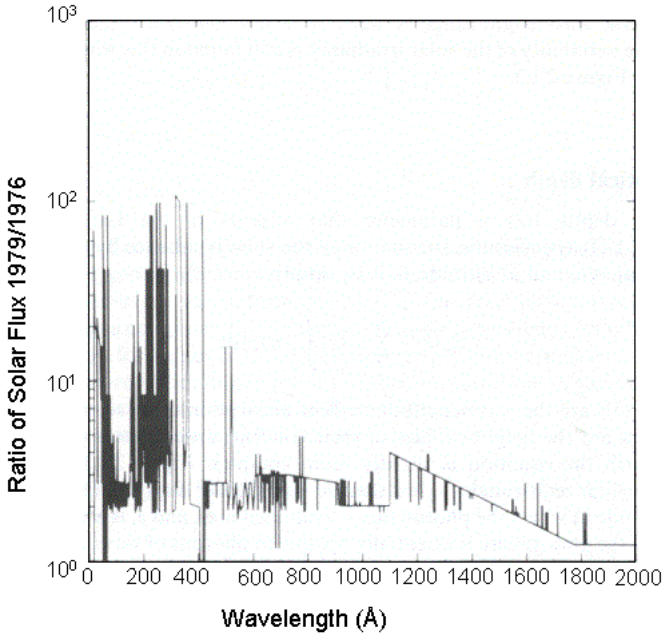

Figure 1.1. **Ratio of solar UV intensities on 19 February 1979 to observations obtained during periods of zero sunspots (Roble and Emery, 1983).**

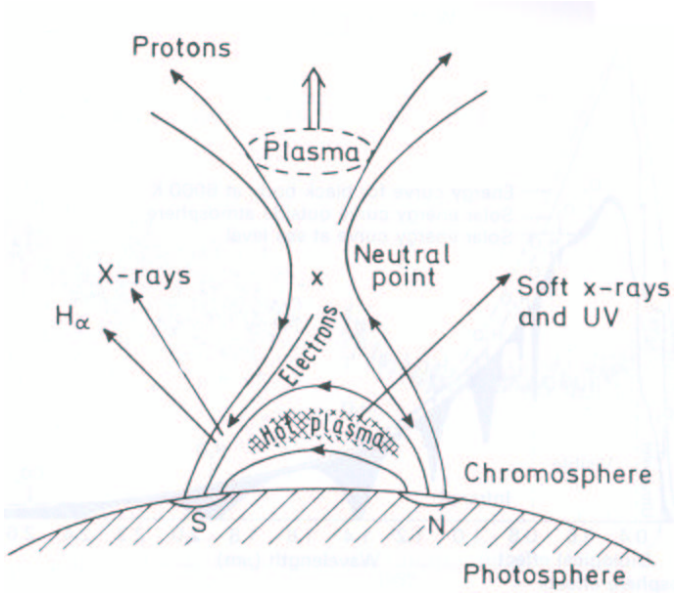

Figure 1.2. **A model of a solar flare showing possible sources for different radiation types (After Piddington, 1969).**

break away from the sun and expand at speeds as high as 2000 km/s. When CME collide with the Earth, they often excite geomagnetic storms.

1.3.2 The Interplanetary Magnetic Field

The Interplanetary Magnetic Field (IMF) is an extension of the solar magnetic field that is carried 'frozen in' to the solar wind. When the electrical conductivity of a plasma is large relative motion between the plasma and magnetic field becomes impossible (Alfvén and Falthammar, 1963). In the solar wind the energy density of the plasma is larger than that of the magnetic field and so the plasma determines the overall motion. Since the IMF is embedded in the solar wind plasma, a parcel of plasma will drag the field line radially away from the sun. The source region of the field line will be rotating with the Sun resulting in a spiral effect in the IMF known as the Parker Spiral. The Parker Spiral is an idealized case and in reality the magnetic field of the sun is extremely complex, although it does serve as a good approximation (Figure 1.3). The magnetic field of the sun, and hence the IMF, vary greatly over the course of a solar cycle. At sunspot minimum the field is ordered with a disc like current sheet separating the inward and outward orientated magnetic field lines (Figure 1.4). Towards solar maximum the current sheet becomes wavy with a disordered magnetic field, leading to a gusty solar wind. On average this occurs every 11 years, however a true solar cycle lasts for 22 years due to the changing orientation of the solar magnetic field over each 11 year cycle.

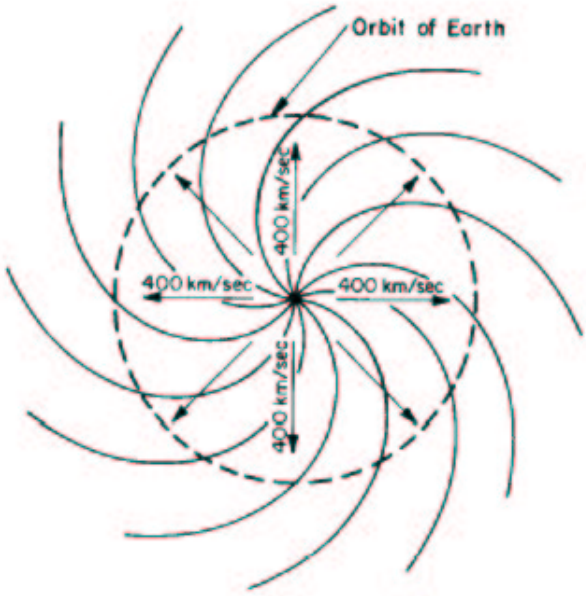

Figure 1.3 **Parker Spiral configuration of the interplanetary magnetic field. The IMF is pulled away from the Sun by the solar wind (Kivelson and Russell, 1995)**

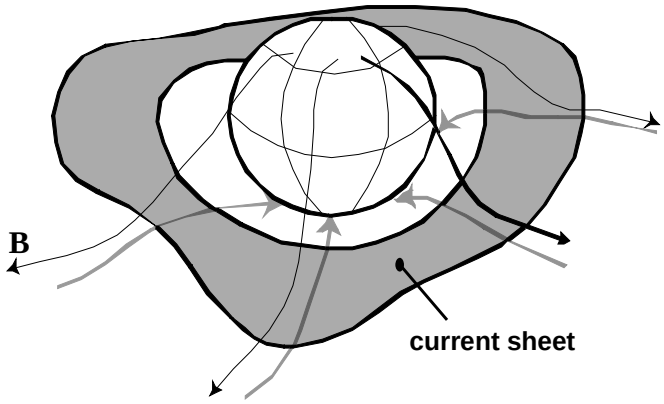

Figure 1.4 **Ordered IMF with current sheet separating the oppositely orientated magnetic field (Ballerina Skirt model).**

1.4 The Earth's Magnetosphere

The term magnetosphere describes near-Earth space that is confined within the magnetic field of the Earth. This section describes the general topology of the field including descriptions of some of the distinct regions that make up the magnetosphere. The populations of energetic particles are also discussed, particularly those that map along magnetic field lines into the auroral zones in the ionosphere.

1.4.1 Magnetic Topology

The Earth's magnetic field forms a barrier to the solar wind resulting in a magnetic cavity in the IMF known as the magnetosphere. The solar wind flows along the boundary of the magnetosphere forming a current sheet known as the magnetopause. The separation between solar wind and magnetosphere occurs at ~10 R_e, at the sub-solar point. Since the solar wind is supersonic and super Alfvénic in nature a bowshock forms upstream (~12 R_E) of the magnetosphere where the solar wind flow is slowed, compressed and heated. The region containing this hot plasma is called the magnetosheath. The dayside magnetosphere is compressed due to the pressure balance between the solar wind dynamic pressure and the magnetic pressure of the geomagnetic field. On the nightside the geomagnetic field is extended downstream into a long tail configuration that has been observed out to distances of ~1000 R_E (Villante, 1975). It has the form of a cylinder 40 R_e in diameter with two distinct lobes of oppositely directed magnetic fields that map to the polar caps. The two lobes are separated by the plasma sheet which extends around the Earth to the dayside magnetopause. The magnetosphere also contains regions of trapped energetic particles known as the Van Allen or Radiation belts. The belts extend from a few

hundred km above the Earth to about 7 R_E. Figure 1.5 shows a two dimensional schematic representation of the magnetosphere with the positions of each of the aforementioned regions clearly marked.

Although the magnetosphere and solar wind have been described as two distinct systems so far, this is not actually the case. Dungey (1961) proposed that the IMF and magnetosphere could merge under certain conditions (typically with a strong southward IMF component) leading to an 'open' magnetosphere. Dungey's theory of magnetic reconnection describes the process by which magnetic field lines diffuse across a current sheet and merge with an oppositely aligned field. This coupled system involves transfer of particles and energy between the solar wind and the magnetosphere. Reconnection on the dayside leads to increased magnetic flux in the polar cap with the resulting field lines trailing back into space and ultimately connecting to the IMF. Nightside reconnection removes open flux from the polar cap. In reality the magnetosphere is thought to be open most (if not all) of the time. Observations suggest that reconnection can occur in a steady-state form as predicted by Dungey, but also in a pulsed manner. Newly opened field lines convect across the polar cap adding to the flux of open field lines. Eventually these open field lines once again merge with the closed field in the tail. Figure 1.6 displays the two examples of the magnetosphere: open (a) and closed (b). Both have been produced using the Tsyganenko 2001 field model calculated for near equinox to give little tilt of the Earths magnetic axis. Quiet conditions were used as inputs (dynamic pressure of 2 nPa, D_{st} = -10 nT, B_y = 0, and B_z = ± 2) for each of the figures.

Magnetic field lines contained within the magnetosphere are described using the McIlwain (1961) parameter of L shell. For a closed field line, the form of the field is

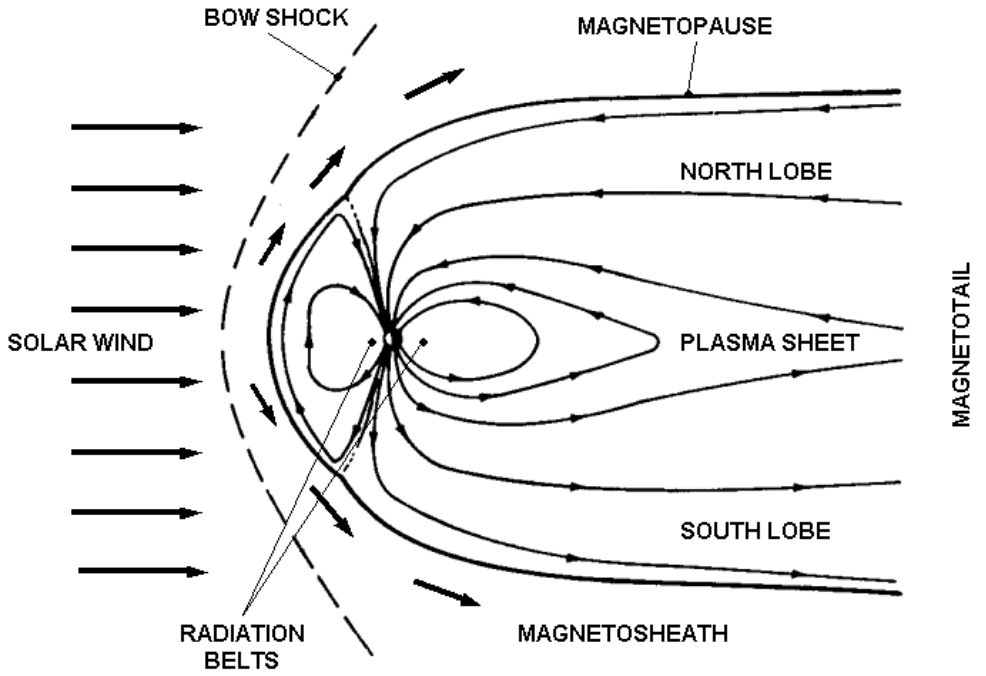

Figure 1.5. Schematic representation of the Earth's magnetosphere in two dimensions. The locations of some of the principle magnetospheric regions are indicated together with the solar wind and bow shock (After Vasyliunas, 1983).

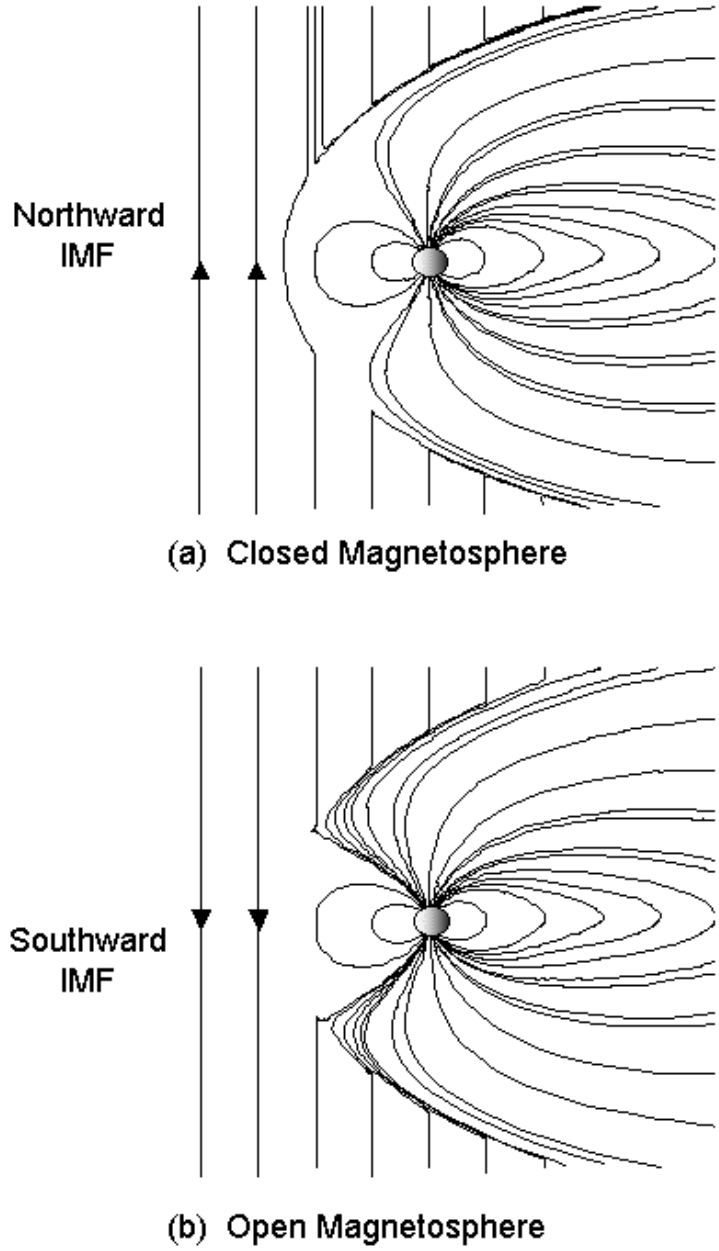

Figure 1.6. Examples of the closed (a) and open (b) magnetosphere. These have been derived using the Tsyganenko 2001 field model based on a period close to equinox giving little axial tilt (P_{dyn} = 2nPa, D_{st} = -10 nT, B_y = 0, B_z = ±2 nT) (Courtesy of A. Senior, private communication).

roughly dipolar and connects the northern and southern hemispheres. The point of greatest distance from the Earth occurs in the equatorial plane and is used to characterise the field line. Thus a field line at 6 Earth radii from the centre of the Earth will be at L=6. L is connected to the invariant magnetic latitude by the relationship:

$$\lambda = \cos^{-1}\left(\frac{1}{L}\right)^{\frac{1}{2}} \qquad (1.1)$$

Since the magnetosphere is not truly dipolar the L shell becomes nonsensical for higher latitudes where the field lines extend into the tail, however it is still a useful indicator of field line position.

1.4.2 Particles in the Magnetosphere

Within the magnetosphere there are several distinct populations of charged particles. The cusps and polar caps are regions of direct entry of solar wind plasma to the open magnetosphere. Particles are accelerated in the cusps leading to energies of 10s of keV. High energies are observed at the equatorward cusp with progressively lower energies at higher latitudes as particles are accelerated due to the higher magnetic tension in the cusp which decreases towards the pole.

As described above the tail lobes of the magnetosphere connect to the polar caps and these contain low-density plasma (<0.1 cm^{-3}) of low energy (~eV). The open field lines in the tail are dominated by plasma of solar wind origin plus a few cold ions that have escaped from the Earth's atmosphere. Plasma sheet particles that separate the tail lobes tend to be hotter (keV) and the plasma is denser (~1 cm^{-3}). At the edges

of the plasma sheet is a boundary layer where the cold tail lobe plasma meets the hot plasma sheet. The particles in this plasma sheet boundary are of similar energies to the plasma sheet but of lower density (~ 0.1 cm^{-3}). Most of the particle energy in the boundary layer is field aligned rather than thermal and beams of particles are accelerated along the magnetic field lines as a result of reconnection in the tail.

The inner magnetosphere is fairly described as dipolar and consists of two important regions, the plasmasphere and the radiation belts. These are sometimes co-located and describe two different energy regimes; the plasmasphere is cold whereas the radiation (or Van Allen) belts are composed of the most energetic particles found in the magnetosphere.

The plasmasphere is a very dense, cold region (~10^3 cm^{-3}, ~ 1 keV) that is bounded by a sharp change in density known as the plasmapause. This is typically located at L=4, but is dependent on the level of geomagnetic activity, occasionally extending to L=6 for very quiet periods. Plasmasphere particles are generally ionospheric in origin. In 1958 Van Allen discovered very intense radiation deep in the magnetosphere using a Geiger counter on board the Explorer 1 satellite. Eventually two zones (inner and outer) of high-energy particles were identified as being trapped within the magnetosphere. It is the inner zone that is usually located with the plasmasphere. The total picture of the radiation belts is more complicated than this but some spatial distributions of trapped protons and electrons are presented in Figure 1.7 As can be seen the higher the particle energy the closer to the Earth the particles are trapped. Thus protons with energies > 30 MeV are confined to the belts within L=2 and dense electrons of energy > 40 keV extend from L=2 to L=8.5. These outer

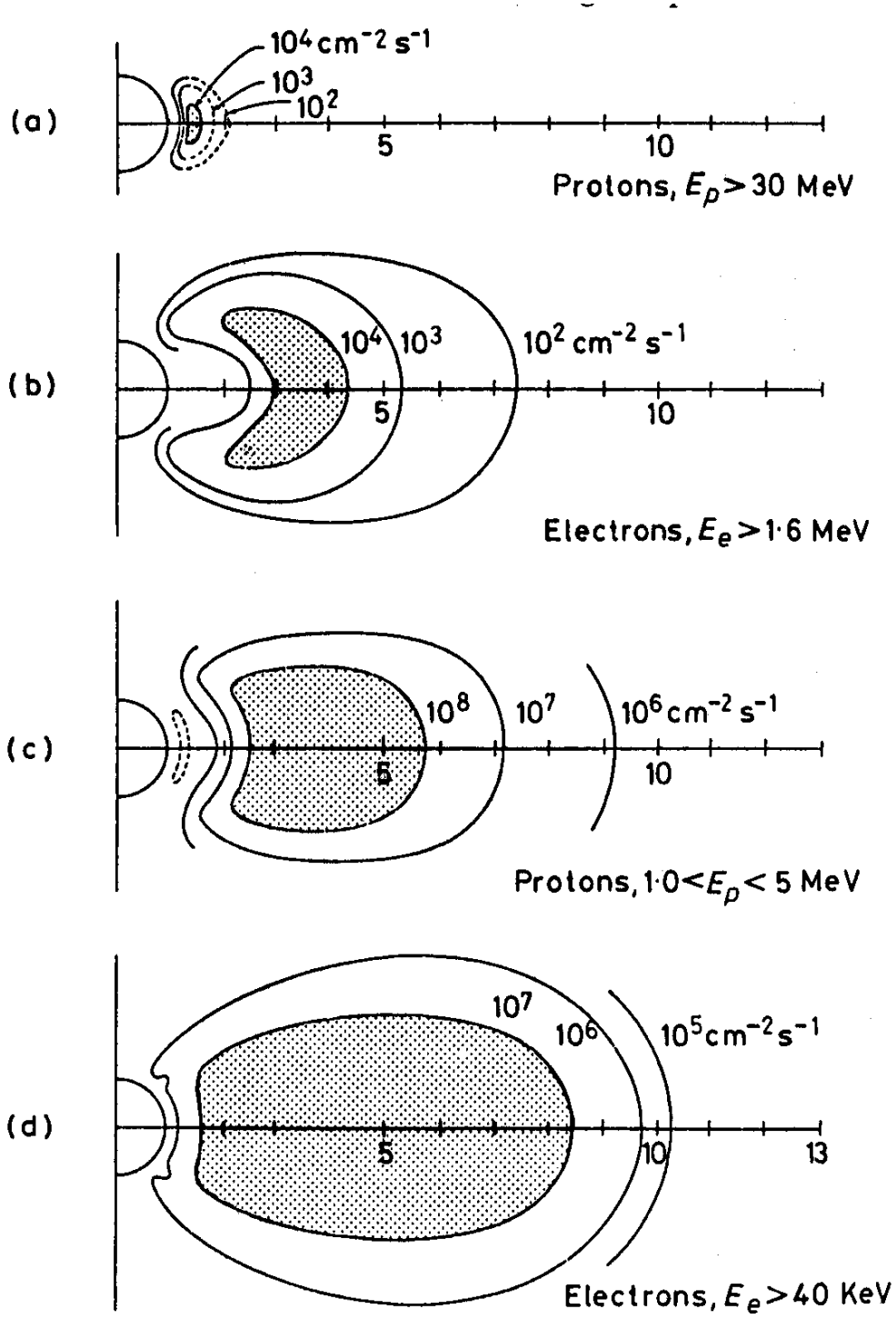

Figure 1.7. The Van Allen radiation belts Spatial distributions of trapped protons and electrons (After Hess, Radiation Belt and Magnetosphere, Blaisdell, 1968).

zone field lines map to the auroral zone and during disturbed conditions some particles are caused to precipitate and be lost to the dense atmosphere, helping to form the auroral ionosphere. The basic principles of particle trapping and motion within the radiation belts will be discussed in Chapter 2. Amongst others, Hargreaves (1995) gives a comprehensive introduction to the solar terrestrial environment and Kivelson and Russell (1995) provides a good overview of magnetospheric processes.

1.5 The Ionosphere

The ionosphere is that part of the atmosphere that stretches upwards from about 60 km to 1000 km altitude. It is comprised of weakly ionised plasma that co-exists with the neutral atmosphere. Most of the ionisation is produced by sunlight at very short wavelengths (UV and X-rays). This section details the vertical structure of the ionosphere and also highlights the auroral ionosphere as being very different from the low to mid latitude ionosphere.

1.5.1 Structure of the ionosphere

The structure and density of the ionosphere varies with both time and location, maximising during the day and at sunspot maximum, and minimising at night and solar minimum as shown in Figure 1.8. Due to the changing composition as height increases in the atmosphere, the production of ions changes also. Balancing the ionisation rate with the recombination rate leads to the formation of layers in the ionosphere and in practical terms these are local maxima defined by peaks in the electron density. These layers or regions are called the D, E and F layers (with ascending altitude) with the topside occurring above the F layer. The variation of

electron density in a given ionospheric layer is governed by the balance of production, loss and transport processes which satisfies the continuity equation:

$$\frac{\partial n_e}{\partial t} = Q - L - \nabla.(n_e v) \qquad (1.2)$$

where n_e is the electron density, Q is the production rate, L is the loss rate and v is a plasma velocity. The loss and transport terms gain different levels of importance in the different layers of the ionosphere. The loss term is highly dependent on the altitude and is determined by whether an ionospheric layer is described in terms of attachment or recombination. First we assume that electrons recombine directly with positive ions:

$$A^+ + e \rightarrow A \qquad (1.3)$$

Then the loss rate of electrons is:

$$L = \alpha [A^+] N = \alpha N^2 \qquad (1.4)$$

Where N is the electron density (equal to the ion density, $[A^+]$) and α is the recombination coefficient. This process describes a Chapman alpha layer.

At higher altitudes the attachment of electrons to neutrals to form negative ions becomes the dominant loss mechanism:

$$A + e \rightarrow A^- \qquad (1.5)$$

Since the neutral species is considered to be considerably more numerous the loss relationship becomes linear, depending only on the electron concentration.

$$L = \beta N \qquad (1.6)$$

This is a Chapman Beta layer.

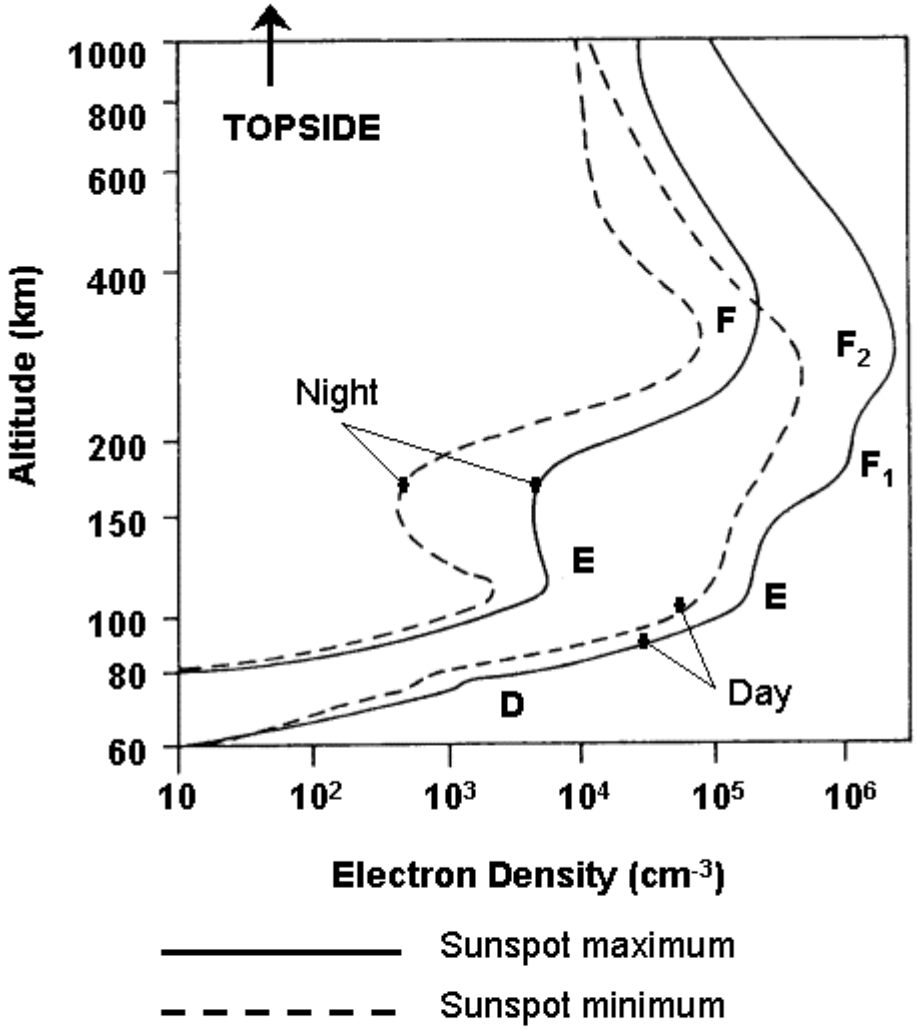

Figure 1.8. **Ionospheric layers during the day and night for Sunspot maximum and minimum (After Hargreaves, 1995)**

The D layer of the ionosphere is of particular relevance to the present thesis. This layer covers altitudes between about 60 and 90 km. Hard X–rays produce most of the ionisation below 70 km and EUV (extreme ultra-violet) becomes increasingly important above this altitude. Free electrons exist for a short period in the upper D layer before being captured by positive ions. Descending in altitude and the attachment of electrons to neutral species to form negative ions becomes more dominant over recombination. Balance is now between electrons, negative ions and positive ions and so at equilibrium:

$$Q = L = \alpha_e N_e N_+ + \alpha_i N_- N_+ \qquad (1.7)$$

α_e and α_i are the recombination coefficients for electrons and negative ions with positive ions respectively. To simplify this a ratio of negative ions to electron density (λ) is introduced. Now $N_- = \lambda N_e$ and $N_+ = (1+\lambda)N$ and so:

$$Q = (1+\lambda)(\alpha_e + \lambda\alpha_i)N_e^2 \qquad (1.8)$$

The coefficient of N_e^2 is called the effective recombination coefficient. This process is much reduced in the presence of ultraviolet radiation so during the night it is an important factor when considering electron loss mechanisms. The D layer disappears in the un-illuminated ionosphere.

Above the D layer are the E and F layers. Stretching to160 km altitude is the E layer, formed mainly by EUV radiation with some contribution from soft X-rays. The F layer can be split into two separate height regimes during the day. The F_1 layer maximises at 180 km and a second peak, the F_2 layer, occurs at ~300 km. During the

night the F_1 layer disappears as solar illumination wanes. The loss of electrons in the F region occurs through a two-step process known as dissociative recombination:

$$A^+ + M_2 \rightarrow MA^+ + M \quad (1.9)$$

$$MA^+ + e \rightarrow M + A \quad (1.10)$$

M_2 is a common molecular species. The rate of equation 1.9 is $\beta[A^+]$ and the rate of 1.10 is $\alpha[MA^+]N$. β is large at low altitudes leading to a rapid rate and causing the α term to dominate. At high altitudes β is small and so dominates the reaction. The change of alpha to beta Chapman layers occurs at a height h_t, where

$$\beta(h_t) = \alpha N \quad (1.11)$$

Figure 1.9 illustrates some typical values for height profiles of ions in the ionosphere. This includes the principal ionisation species for each layer. Direct photo-ionisation produce the ion species N_2^+, N^+, O_2^+, O^+, He^+ and H^+, but the chemical composition of the ionosphere is dictated by a variety of subsequent chemical reactions along with transport mechanisms such as diffusion. The chemical and physical processes that control ionospheric ion composition are discussed by Rees (1989). Observations and theory behind the dynamics of the Earth's ionosphere are presented in some detail by authors such as Hargreaves (1992). The geomagnetic orientation at low and high latitudes is responsible for deviations from the normal ionospheric behaviour. At equatorial latitudes, the geomagnetic field lines are virtually horizontal leading to depletion in electron density. West to east electric fields generated in the E region result in a vertical drift of the F region plasma (electrodynamic lifting). The plasma diffuses under gravity down field lines to higher latitudes in a process described as the Fountain effect (Hanson and Moffett, 1966).

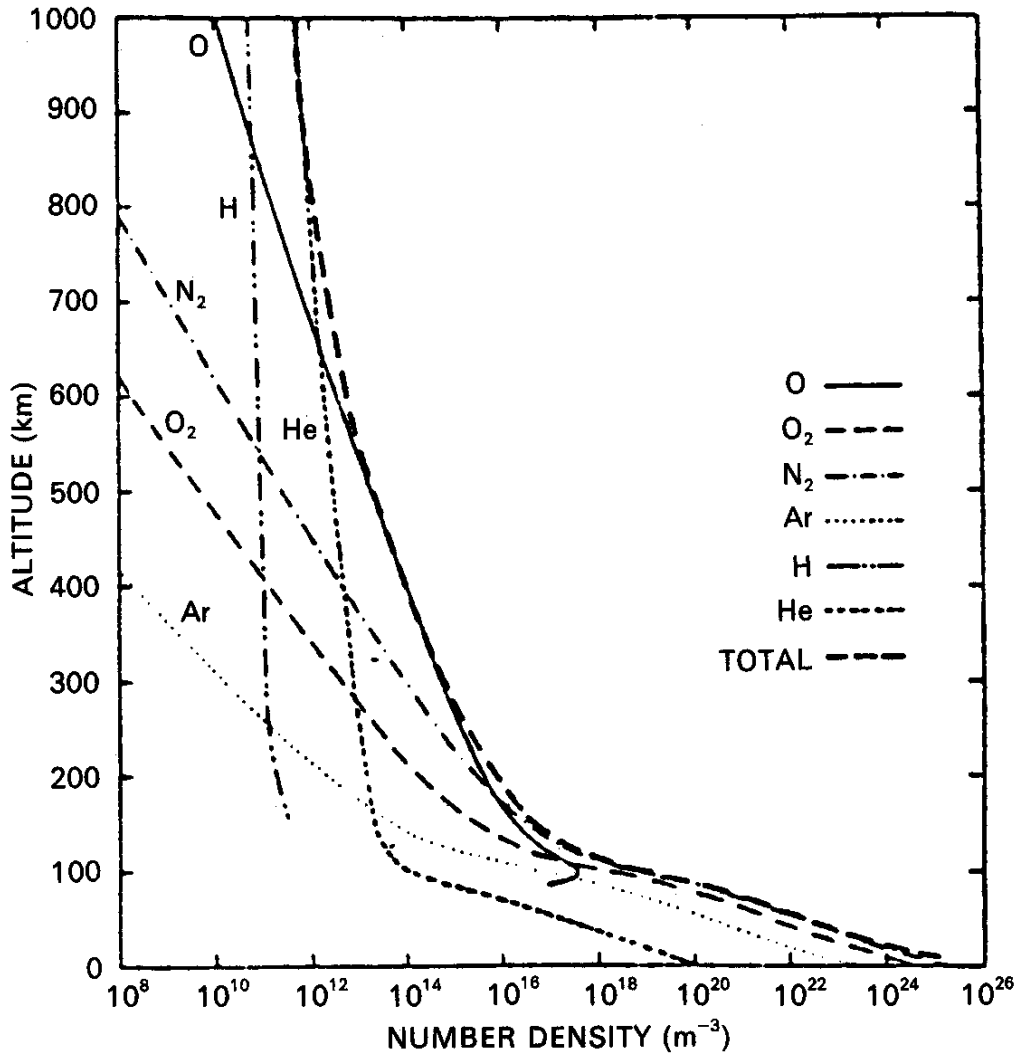

Figure 1.9. **The typical chemical composition of the ionosphere (After A.D. Richmond, in Solar-Terrestrial Physics, Reidel, 1983).**

This produces two maxima around ±10° magnetic latitude where the plasma diffusion and gravity balance. At high latitudes there are some distinct differences in the structure and dynamics of the ionosphere. Its behaviour is described in the following section.

1.5.2 The High latitude Ionosphere

Due to the solar wind interaction with the geomagnetic cavity, the magnetic field lines at high latitudes extend deep into the magnetosphere or open into interplanetary space in the polar cap. Magnetospheric processes therefore have an important effect on the high latitude ionosphere. Figure 1.10 illustrates some of the regions of the high latitude ionosphere that are related to magnetospheric regions.

Since field lines open to the IMF thread the polar cap, direct entry of solar wind particles is possible as mentioned in section 1.4.2. This produces a drizzle of low energy particles termed the polar rain. Conversely light ions of ionospheric origin (mostly H^+ and He^+) are also lost from the high altitude polar cap. The energies of these ions is sufficient to escape the gravitational potential well and so they travel along the open flux tubes in the polar cap. This is referred to as the polar wind.

High-energy particles (> keV) precipitate from the magnetospheric plasma sheet at high latitudes. The mechanisms for describing how these particles are accelerated to these high energies are not yet fully understood, but upon entering the atmosphere they excite neutral species, emitting photons and producing the optical aurora. This auroral precipitation is confined to a zone (the auroral oval) centred on the magnetic pole. The boundary of the oval extends to lower latitudes on the nightside than on the dayside. Optical aurora broadly fits into two categories, diffuse and discrete. The

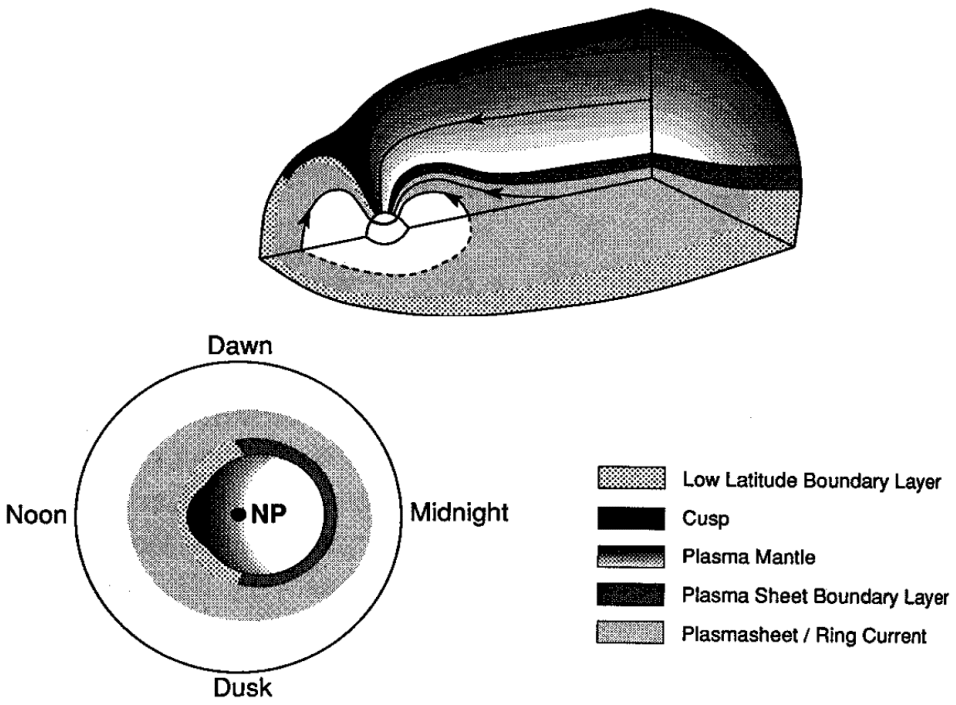

Figure 1.10. **The mapping of magnetospheric regions into the ionosphere. NP indicates the position of the north magnetic pole. (Kivelson and Russell, 1995).**

discrete aurora is structured and intense whereas the diffuse aurora appears as a glow in the sky. Both have similar overall intensities but the discrete form is easier to observe due to the low intensity per unit area of the diffuse form. The discrete aurora maps to the plasma sheet boundary layer and appears poleward of the diffuse aurora, which is linked to the central plasma sheet. Particle precipitation plays an important role in the coupling between the ionosphere and the magnetosphere.

Associated with the aurora is auroral radio absorption. This is produced by the more energetic particles (usually electrons) that penetrate to the lower layers of the ionosphere. The precipitation of these energetic particles enhances the electron density allowing the formation of a D layer at night when photo-ionisation has ceased. The enhanced electron concentration leads to absorption of high frequency radio waves in the ionosphere. This band of precipitation tends to maximise equatorward of the auroral oval and is more circular in nature. It is mostly associated with the diffuse aurora but often occurs colocated or close to auroral arcs. The particular dynamics and occurrence of auroral absorption are discussed in Chapter 4 and the physical mechanisms that lead to HF radio wave absorption are detailed in Chapter 2.

1.6 Observations of the Ionosphere

There are two basic techniques used to investigate the ionosphere. The first makes use of in-situ observations with equipment such as magnetometers or particle detectors, flown on balloons, rockets or satellites. The second technique consists of remote sensing of the ionosphere mostly with ground-based instrumentation, for example using radars and optical equipment. Optical and radiation sensors are an increasing component of satellite payloads. These instruments are capable of

producing large-scale images of the auroral region that complement the observations of ground based imagers and radars.

When studying the ionosphere on small scales, ground based auroral imagers are important tools. Instruments such as imaging riometers measure the extent and variation of energetic particle precipitation in the auroral regions. The large coverage combined with high spatial resolution allows detailed observations of the structure of HF radio absorption, which acts as a proxy for detecting particle precipitation. There are currently 20 imaging riometers operating in the world, 8 of these are based in the northern hemisphere with a further 4 planned for the next few years. The principal experimental facility utilised in the present investigation is the Imaging Riometer for Ionospheric Studies (IRIS) based at Kilpisjärvi in northern Finland (Browne *et al*., 1995). This facility has a 240 × 240 km field of view in the D region (90 km altitude) and provides maps of energetic particle precipitation well within the auroral zone. The theory of ionospheric HF radio absorption and the operational characteristics of IRIS are discussed in detail in Chapters 2 and 3.

A bonus to the observations of IRIS is the wealth of instrumentation available in northern Fennoscandia. The field of view of IRIS intersects with those from all-sky cameras and coherent radars, and covers several magnetometer sites. Most importantly beams from IRIS intersect the beam from the EISCAT (European Incoherent Scatter) radar. Incoherent scatter is a powerful tool for probing the ionosphere over a large range of altitudes. When used in conjunction with IRIS a four-dimensional picture of ionospheric processes can be developed (Collis and Hargreaves, 1996).

1.7 Aims of the Present Study

This thesis documents an investigation into various aspects of energetic particle precipitation in the auroral zone. This can be broadly split into two categories: precipitation from closed field lines and from open field lines. These are controlled by geomagnetic and solar activity respectively.

Chapter 5 presents a case study of morning sector precipitation that is linked to night side substorm activity. The changes in precipitation spectrum are investigated using EISCAT measurements and DMSP satellite data. Observations of the movement of absorption patches are compared with ionospheric flows obtained from coherent scatter radars.

Chapter 6 expands this case study by investigating the statistical daily variation in absorption and its dependence on geomagnetic activity. The general structure and occurrence is described and quantified and empirical relationships between absorption and solar wind speed are estimated. Chapter 7 documents a study of the variation of absorption events with solar activity, specifically, the dependence of polar cap absorption on solar proton events that originate from X-ray solar flares.

The conclusions of Chapter 5 to 7 are summarised in Chapter 8 together with some suggestions for further study that expands the work presented here.

Chapter 2

Charged Particle Motion and Radio Absorption in the ionosphere and magnetosphere

2.1 Introduction

Particle precipitation is a major contributor to the energy input of the ionosphere. In this chapter the motion of particles in the geomagnetic field is reviewed and also the manner in which energetic charged particles are deposited into the ionosphere from the magnetosphere is discussed. Following this discussion is a section detailing the propagation of high frequency (HF) radio waves in the ionosphere. This includes a description of the absorption of these radio waves and how this is dependent on the electron density in the lower ionosphere and is thus affected by the precipitation of high-energy particles.

2.2 Charged Particle Motion in the Magnetosphere

Chapter 1 described the various particle populations that are contained within magnetosphere. So far no mention has been made of the movement of the particles within these regions and particularly the deposition of particles into the ionosphere. This section addresses the motion of the particles by briefly describing two main components that are relevant to this thesis; bounce motion and gradient curvature drift. Parks (1991) provides an introduction to the motion of charged particles in the

magnetosphere; in-depth treatments are available by Roederer (1970) and Schulz and Lanzerotti (1974).

2.2.1 Bounce Motion and the Loss cone

In a magnetic field a charged particle will follow a curved path due to the Lorentz force. Associated with this motion is a frequency that is dependent on the particle charge, mass and the magnetic field. The radius of motion is also dependent on the tangential velocity of the particle. Thus charged particles can be 'trapped' onto magnetic field lines. If a particle (electron or proton) in the magnetosphere has a velocity $v_{\perp}$ normal to the magnetic field and $v_{\parallel}$ along it, the trajectory is a spiral (Figure 2.1). With no work done on the particle, the magnetic flux through the orbit is constant (i.e. no electric field can be present):

$$\Phi = B \cdot r_G^2 \pi = \frac{2mE_{\perp}\pi}{e^2 B} = \text{constant} \qquad (2.1)$$

where m and r_G are the particle mass and gyroradius respectively, e is the charge of an electron, B is the magnetic field strength and $E_{\perp}$ is the kinetic energy associated with the field-normal velocity component. Hence $E_{\perp}/B$ is constant and represents the magnetic moment of the current loop represented by the gyrating particle. This leads to the first adiabatic invariant of charged particle motion in a magnetic field: *The magnetic moment is constant*. This condition holds so long as the magnetic field does not change significantly during one gyration period.

The perpendicular velocity of the particle can then be expressed as a function of the angle between the velocity vector and the magnetic field direction: the pitch angle, α.

$$v_{\perp} = v \sin \alpha \tag{2.2}$$

Which can be converted into terms of energy:

$$\frac{m v_{\perp}^2}{2\mathbf{B}} = \frac{E_{\perp}}{\mathbf{B}} = \frac{E \sin^2 \alpha}{\mathbf{B}} = \text{constant} \tag{2.3}$$

Which shows that:

$$\sin^2 \alpha \propto \mathbf{B} \tag{2.4}$$

If a charged particle moves from the equator to higher latitudes in a dipole field it will encounter an increasing B and therefore the pitch angle will increase. When α = 90˚ all forward motion stops and the particle will be reflected back along the field line towards the equator. This point of reflection is called the mirror point and occurs when B = B_M. In this simple case, no acceleration of the particle occurs and so the total energy remains constant ($E = E_{\perp} + E_{\parallel}$). The parallel energy falls to zero at the mirror point and the parallel velocity can be represented as:

$$v_{\parallel}^2 = v^2 - v_{\perp}^2 = v^2 \cos^2 \alpha \tag{2.5}$$

For a given particle the position of the mirror point is determined by the pitch angle as the particle crosses the equator (i.e. where the field is weakest, B_{eq}):

$$\frac{B_{eq}}{B_M} = \sin^2 \alpha_{eq} \tag{2.6}$$

This is the principle of particle bounce in the magnetosphere. The position of the mirror point determines the length of field line traversed in a single bounce and

since the magnetic field can be derived as a function of latitude for a dipole field, equation 2.5 can be represented in terms of the latitude of the mirror point (λ_M):

$$\frac{\cos^6 \lambda_M}{\left[4-3\cos^2 \lambda_M\right]^{\frac{1}{2}}} = \sin^2 \alpha_{eq} \qquad (2.7)$$

Thus for a given pitch angle, the mirror point latitude is independent of the field line. All particles of given equatorial pitch angle, α_{eq}, mirror at the same latitude in a dipole field, irrespective of their L shell.

It is immediately apparent that for the case of the Earth's dipole field there must be an upper limit for the mirror latitude for a given field line: the mirror point must always lie above the surface of the Earth and in fact, above the denser atmosphere. If the mirror point is situated within the dense atmosphere (e.g. <100 km altitude) then a particle is more likely to collide and be lost to the magnetosphere. The proportion of particles that are no longer 'trapped' on closed field lines can be described as being within a 'Loss cone' (Figure 2.1). By considering equations 1.1 and 2.7, the half aperture of the equatorial loss cone (α_L) can be defined as:

$$\sin^2 \alpha_L = \frac{1}{L^3\left[4-\frac{3}{L}\right]^{\frac{1}{2}}} \qquad (2.8).$$

where L is measured in Earth radii. The equatorial pitch angle must satisfy the following inequality in order for a particle to mirror successfully:

$$\sin^2 \alpha_{eq} > \sin^2 \alpha_L \qquad (2.9).$$

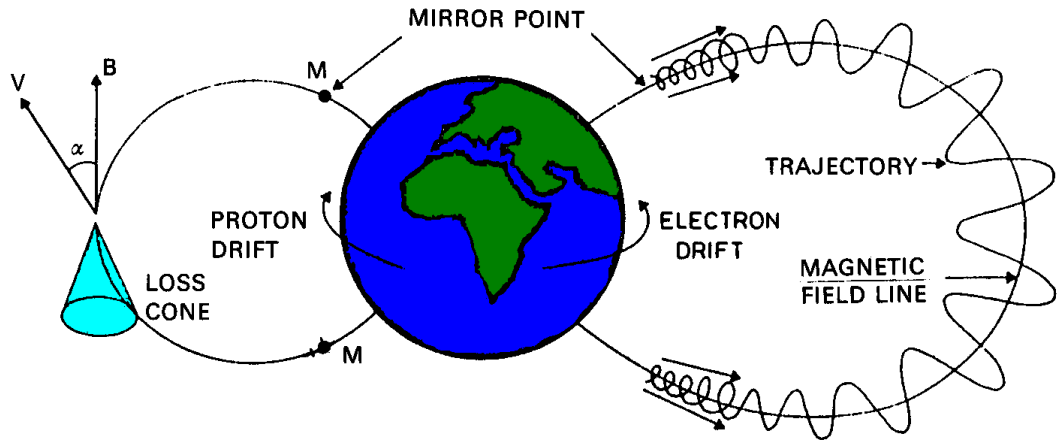

Figure 2.1. Typical motions of particles trapped on closed field lines including the equatorial loss cone and the mirror points of bouncing particles (After J. Lemaire, 1982)

As the pitch angle increases when a particle approaches the mirror point, so too the loss cone widens. The manner in which pitch angle scattering of particles into the loss cone occurs is discussed in section 2.2.3.

2.2.2 Gradient Curvature Drift

So far particle motion in the presence of a magnetic field has been discussed. If an electric field (**E**) exists perpendicular to **B** then the particles will also drift in an orthogonal direction (**E**×**B** drift). In the particle frame of reference **E**=0, and so the particle motion is circular. The general motion is a sum of the gyration and a drift in the **E**×**B** direction at a speed **E**/**B**. This is independent of energy, charge or mass. Particles gyrating about a field line will also drift transverse to B but their guiding centres will all remain on the same field line. The particles drift and drag the magnetic field with them, similar to the flow of solar wind plasma with the IMF 'frozen' into it. This is Alfvén's theorem of frozen in flow (see Chapter 1). If other drifts occur, this frozen in approximation breaks down. One such example is due to the variation of the magnetic field strength across the field.

A gradient in the magnetic field strength alters the gyroradius of a particle. The gyroradius varies inversely with B, leading to the drift shown in Figure 2.2. The velocity of this drift can be derived by considering the continuous gyro motion in two differing field strengths and using the limiting case of small variations of **B**. The final velocity is termed the Gradient drift velocity and has the form:

$$\mathrm{V}_{\nabla \mathrm{B}} = \frac{m v_{\perp}}{2qB^{3}} . \mathrm{B} \times \nabla \mathrm{B} \qquad (2.10)$$

Similarly, the curvature of the geomagnetic field lines produces a second drift of particles (Figure 2.3). A bouncing particle experiences a centrifugal force that combines with the motion of gyration to produce a lateral movement. The motion is in the same direction as the gradient drift but relies instead on the parallel velocity of the particle rather than the velocity perpendicular to the magnetic field:

$$\mathrm{V}_C = \frac{mv_{\parallel}}{qB^3}.\mathrm{B}\times\left[\left(\frac{\mathrm{B}}{B}.\nabla\right)\mathrm{B}\right] \qquad (2.11).$$

The two equations can be combined into a single expression for gradient curvature drift by simplifying and considering a local field line radius (r_c):

$$V_{GC} = \frac{mv^2}{eB^2}.\frac{\partial B}{\partial R}.(\tfrac{1}{2}v_{\perp}^2 + v_{=}^2) \qquad (2.12)$$

$$V_{GC} = \frac{mv^2}{2eBr_c}.(1+\cos^2\alpha) = \frac{E}{2eBr_c}.(1+\cos^2\alpha) \qquad (2.13)$$

Gradient-curvature drift causes electrons to drift to the east and protons to the west due to the opposite gyromotions. Since the drift is energy dependent particles are dispersed in energy as they travel through the field. In a dipole field this serves to distribute particles to all longitudes. In the non-dipolar field of the inner magnetosphere the drift path is more complicated but can be derived from the second adiabatic invariant (the integral invariant): *the integral of the parallel momentum over one bounce between mirror points is constant*. Just as the first invariant, this holds provided the field does not change appreciably in a short time scale (e.g. one bounce period). At this point it is worth mentioning the third adiabatic invariant involved in the motion of trapped particles. The flux invariant: *the total geomagnetic flux enclosed*

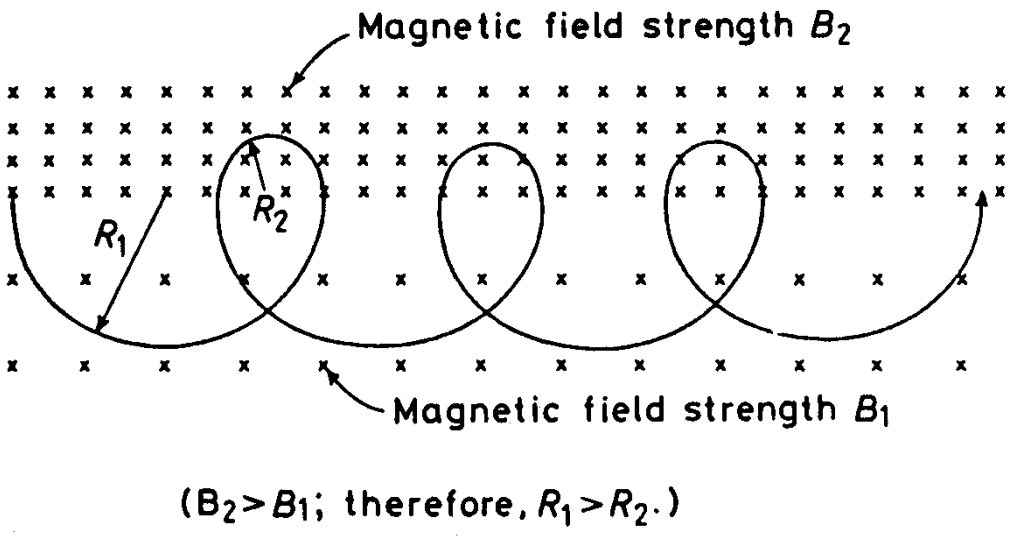

Figure 2.2. **Longitude drift caused by a gradient in the geomagnetic field intensity. Note that the magnetic field gradient is perpendicular to the effective direction of drift motion. (After Hess, Radiation Belt and Magnetosphere, 1968).**

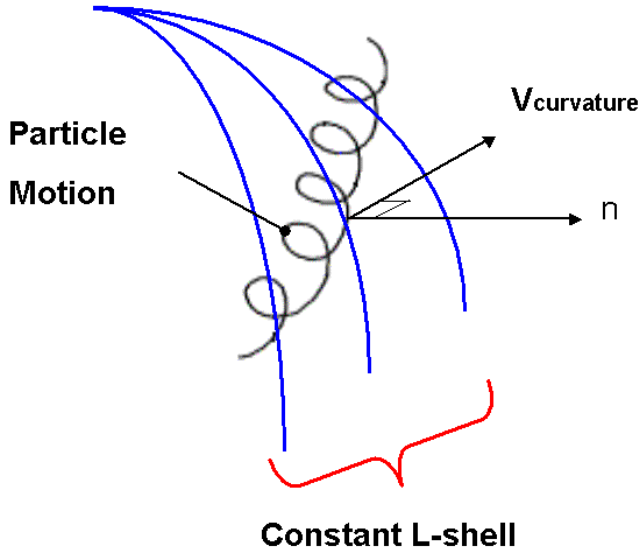

Figure 2.3. **Curvature drift caused by the combination of centrifugal force with the gyromotion. n is the unit normal vector to the magnetic field line.**

by the drift orbit is constant. This invariant is violated if changes occur in a time scale less than the drift period around the Earth. Changes on this time scale are relatively common, especially during geomagnetic storms.

A particle drifting in the asymmetrical field of the magnetosphere will attempt to remain at constant field intensity. At the equator the geomagnetic field is squashed by the solar wind increasing the field strength . Particles of flat pitch angle ($\alpha_{eq} = 90^{o}$) will move outwards on the day side with some leaving the magnetosphere. Thus the pitch angle distribution at midnight may include a drift loss cone (Figure 2.4). Some small pitch angle particles at noon will be subsequently lost in the night sector as they drift, so including a drift loss cone surrounding the bounce loss cone. The movement of particles to different L values in order to remain at the same field intensity is known as shell splitting and together with the drift loss cone this gives rise to parts of the magnetosphere known as the pseudo-trapping regions (Hargreaves, 1995; Roederer, 1970). A particle in a pseudo trapping region will not be able to complete a circuit of the Earth being lost either in the magnetotail or at the magnetopause.

2.2.3 Particle Precipitation

The principles of how and why particles precipitate into the atmosphere is a wide and still highly debated topic that is beyond the scope of this work. Generally speaking for a particle to precipitate its pitch angle must change enough to place the particle within the loss cone such that on the next bounce, the particle will not mirror but instead will be lost to the atmosphere. For the pitch angle to change the ratio of the parallel and perpendicular velocities of the particle must alter since

$$\alpha = \tan^{-1}\left(v_{\perp}/v_{=}\right) \qquad (2.14)$$

A generally accepted mechanism for altering pitch angles is through the doppler shifted cyclotron resonance with very low frequency (VLF) waves. A gyrating electron may feed energy into a VLF wave by transverse resonance so reducing its velocity perpendicular to the magnetic field line; the electron and wave must be anti-parallel (Figure 2.5). A spectrum of VLF signatures alters the pitch angle distribution of trapped particles causing some to be lost at the next bounce. A non-isotropic pitch angle distribution is unstable; the particles produce waves which then alter the pitch angles such that the distribution becomes more isotropic. The point of interaction is usually taken to be in the equatorial region (Figure 2.6) Similarly to the electron-whistler interaction, ion cyclotron waves (ULF) couple to gyrating ions and lead to precipitation. A number of authors have dealt with the loss of charged particles to the atmosphere due to pitch angle diffusion driven by VLF/ULF waves (e.g. Brice, 1964; Kennel and Petschek, 1966; Cornwall, 1966; Kennel, 1969).

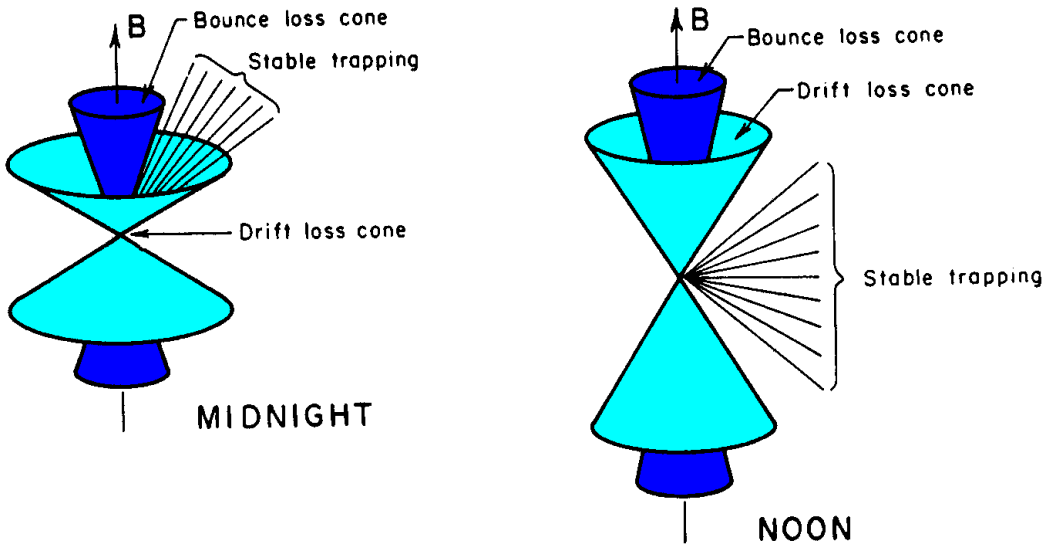

Figure 2.4. **Drift loss cones for the midnight and noon meridians. Note that the bounce loss cone is always present (after Roederer, 1970).**

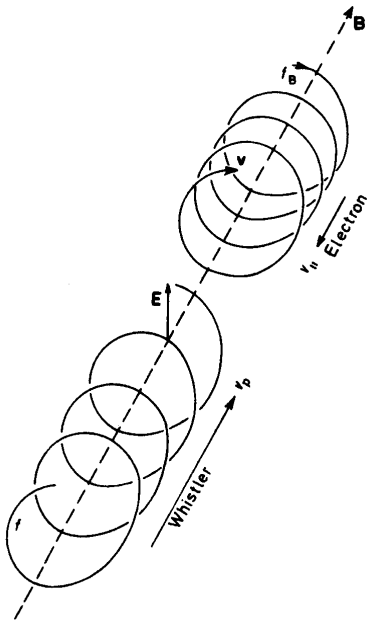

Figure 2.5. **Spiral motions of electrons and whistler waves about the geomagnetic field. For cyclotron interaction the electric field vector of the wave must be parallel to the velocity of the electron (Hargreaves, 1995).**

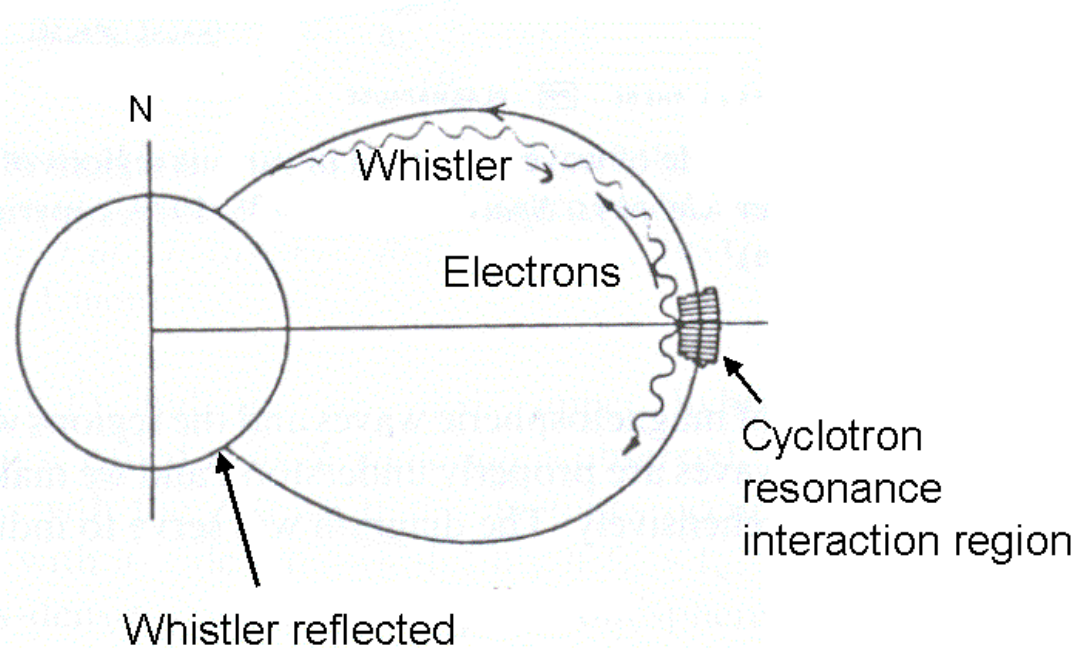

Figure 2.6.. A possible explanation of VLF-electron interaction that leads to precipitation. Lightning can produce whistlers that resonate with the electrons in the equatorial region (After M.J. Rycroft, 1973)

2.3 High Frequency Radio Propagation and Absorption

The precipitation of charged particles into the atmosphere results in large effects on the propagation of radio waves. An increase in ionospheric density will lead to changes in the refractive index causing the deviation of waves from their original paths. It can also lead to significant drops in signal strength due to attenuation in the lower ionosphere. The work presented in this thesis is dependent on observations that rely on the measurement of this radio wave absorption. Thus it is necessary to describe how the waves interact with the ionospheric plasma.

2.3.1 The Altar-Appleton-Hartree Equation

Usually a wave in the ionosphere is considered to have a complex wave propagation number, k, implying that the medium is dissipative. The relationship between the wave propagation number and the refractive index for an exponentially decaying plane wave of the form $e^{i(\omega t - kx)}$ is defined as

$$n = (\mu - i\chi) = \frac{ck}{\omega} \qquad (2.15)$$

The refractive index of a magnetoplasma is determined by the Altar-Appleton-Hartree equation and is also complex in nature. Davies (1969) gives a full derivation of the equation. Altar-Appleton-Hartree dispersion relation:

$$n^2 = (\mu - i\chi)^2 = 1 - \frac{X}{1 - iZ - \frac{Y^2 \sin^2\theta}{2(1 - X - iZ)} \pm \left[\frac{Y^4 \sin^4\theta}{4(1 - X - iZ)^2} + Y^2 \cos^2\theta \right]^{\frac{1}{2}}} \qquad (2.16)$$

Where,

$$X = \frac{\omega_p^2}{\omega^2} = \frac{N_e e^2}{\varepsilon_0 m_e \omega^2} \tag{2.17}$$

$$Y = \frac{\omega_H}{\omega} = \frac{eB}{m_e \omega} \tag{2.18}$$

$$Z = \frac{\nu}{\omega} \tag{2.19}$$

ω_H is the electron angular gyrofrequency, ω_p is the plasma angular frequency, ω is the wave angular frequency, e is the electric charge on an electron, m_e is the mass of an electron, ε_0 is the permittivity of free space, N_e is the plasma electron density, B is the external magnetic field magnitude, ν is the collision frequency between electrons and all other particles, θ is the angle between the direction of wave phase propagation and the external magnetic field.

The dispersion relationship is complicated but can be simplified by making a number of assumptions. When the magnetic field and collision frequency are neglected the equation simplifies to

$$n^2 = 1 - X = 1 - \frac{\omega_P^2}{\omega^2} \tag{2.20}$$

In this case the imaginary part of the refractive index is zero. A wave with an angular frequency that equals the plasma frequency will reflect. Thus a wave with a frequency that exceeds the plasma frequency will pass straight through the ionosphere.

There are two distinct cases of ionospheric absorption of HF radio waves: Deviative and non-deviative absorption.

2.3.2 Deviative Absorption

Deviative absorption applies in the F region of the ionosphere where the collision frequency is small. In this case equation (2.15) becomes relevant with $n^2 = \mu^2 = 1\text{-}X$. This leads to

$$\kappa = \frac{\nu}{2c}\left(\frac{1}{\mu} - \mu\right) \tag{2.21}$$

where c is the speed of light in vaccuo and ν is the effective collision frequency. From this equation it is clear that the absorption will be enhanced as the ray approaches the reflection level where $\mu \rightarrow 0$ and the wave group velocity approaches zero. This case is less relevant to the work presented in this study than the case of non-deviative absorption.

2.3.3 Non-Deviative Absorption

Radio waves passing through an ionised medium cause the electrons to vibrate. If the electrons collide with heavy particles energy is transferred from the wave to the medium in the form of plasma thermal energy. The number of collisions per oscillation determines the rate of wave attenuation. When considering the case of ionospheric radio wave absorption it is important to include the effects of collisions. If a radio wave propagates close to the direction of the magnetic field the dispersion relationship can be simplified again. In this case as θ tends towards zero, $\sin\theta \rightarrow 0$ and $\cos\theta \rightarrow 1$ the AAH equation (2.16) reduces to

$$n^2 = 1 - \frac{X}{1 - iZ \pm Y\cos\theta} = 1 - \frac{\omega_P^2/\omega^2}{1 - i\nu/\omega \pm \omega_H \cos\theta/\omega} = (\mu - i\chi)^2 \tag{2.22}$$

Returning to the wave solution suggested earlier ($e^{i(\omega t-kx)}$) and considering that the wave number is complex, the wave can be defined in terms of the refractive index (μ-$i\chi$) from equation (2.13):

$$k = \frac{n\omega}{c} = (\mu - i\chi)\frac{\omega}{c} \qquad (2.23)$$

so by substitution we get the wave solution:

$$\exp\left[-\left(\frac{\omega\chi}{c}.x\right)\right]\exp\left[i\left(\omega t - \frac{\omega\mu}{c}.x\right)\right] \quad (2.24)$$

Here, the first term represents an attenuation rate (κ) of (ω/c).χ Nepers per metre. From Equation (2.22) it is possible to define values for χ by separating into real and imaginary parts:

$$\mu^2 - \chi^2 = 1 - \frac{X.(1 \pm Y.\cos\theta)}{(1 \pm Y.\cos\theta)^2 + Z^2} \qquad (2.25a)$$

$$2.\mu.\chi = \frac{Z.X}{(1 \pm Y.\cos\theta)^2 + Z^2} \qquad (2.25b)$$

Hence by substituting the values of X, Y and Z (Equations 2.17 to 2.19) a value for the coefficient of attenuation (κ) can be found:

$$\kappa = \frac{\omega\chi}{c} = \frac{\omega}{c}.\frac{1}{2\mu}.\frac{\omega_p^2}{\omega}.\frac{\nu}{\left[\nu^2 + (\omega \pm \omega_H\cos\theta)^2\right]} \qquad (2.26a)$$

$$\kappa = \frac{e^2}{2m_e c\varepsilon_0}.\frac{1}{\mu}.\frac{N_e\nu}{\nu^2 + (\omega \pm \omega_H\cos\theta)^2} \qquad \text{Np/m} \qquad (2.26b)$$

Absorption is usually defined in terms of a logarithmic unit, commonly the Neper or the decibel. Two signals amplitudes S_1 and S_2 are said to differ by n Nepers when $n=\ln(S_1/S_2)$. Rather than signal voltages, the bel is based on ratios of signal power. The powers P_1 and P_2 differ by A bels when $A = \log_{10}(P_1/P_2) = 2\log_{10}(S_1/S_2)$.

Thus 1 Neper = 8.68 decibels. Therefore the total absorption over a path can be described as

$$A = 4.6\times10^{-5}\int \frac{N_e \nu .dl}{\nu^2 + (\omega \pm \omega_H \cos\theta)^2} \qquad \text{dB.} \qquad (2.27)$$

The absorption is greater for the X wave than for the O wave, the negative and positive signs in the AAH equation (2.14) applying respectively. In the D and lower E region, HF radio waves undergo very little refraction and $\mu \approx 1$. The velocity of the wave is not altered and so there is no bending. This case is known as non-deviative absorption.

With a small collision frequency (ν) relative to the angular wave frequency (ω), the absorption coefficient is proportional to the product of the electron density and the collision frequency and is inversely related to the square of the wave frequency (Figure 2.7).

2.3.4 Collision Frequencies in the Ionosphere

A relationship between ionospheric electron density and radio absorption has been defined and this can be seen to depend on the effective collision frequency between electrons and all other species. The velocity dependent monoenergetic collision frequency of electrons is defined as

$$\nu_m = nvQ_m(v) \qquad (2.28)$$

where n is the gas number density, v is the relative speed of the colliding momentum and $Q_m(v)$ is the velocity dependent momentum transfer cross section (Aggarwal et al , 1979). It has been shown that the distribution of electron velocities is best represented as a Maxwellian.

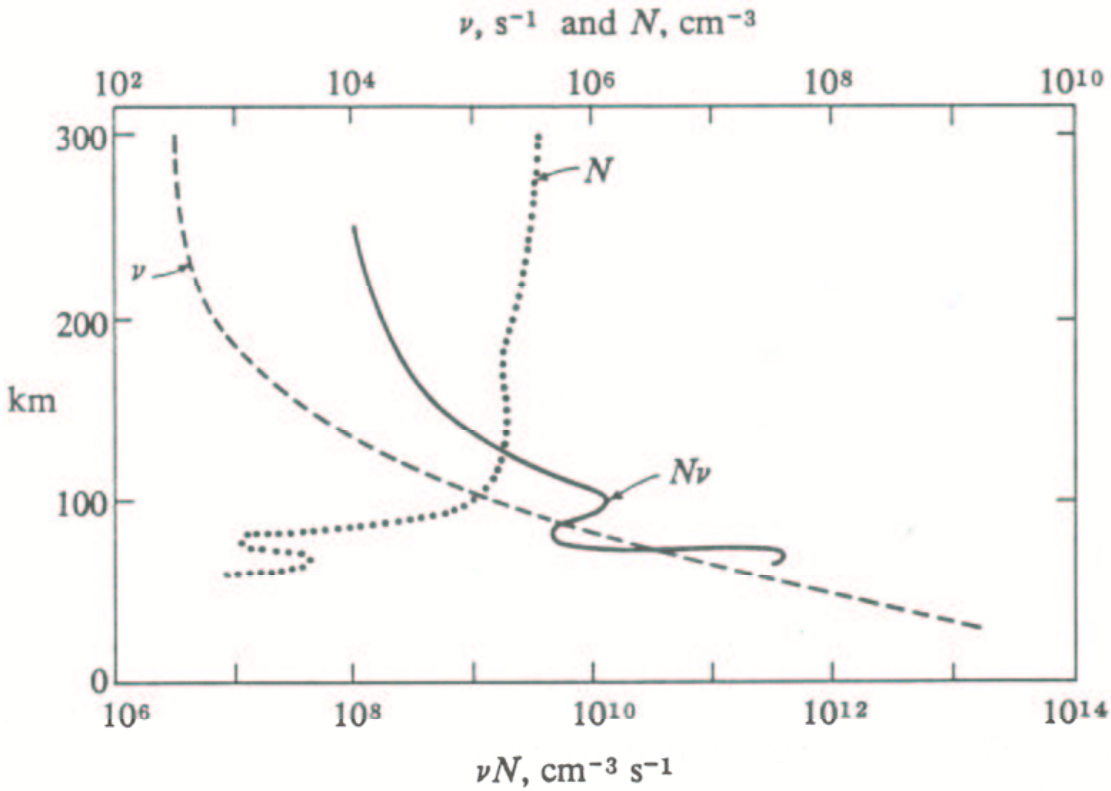

Figure 2.7. **An example of the height variation of the electron collision frequency, electron density and the product (Nυ) that is a measure of the radio absorption. Note that although the electron density is higher at >100 km altitude, the absorption peaks close to 90 km due to the dominance of the collision frequency (After Davies, 1990).**

Thus an average of ν_m is taken over the entire distribution to obtain the effective collision frequency. The total effective electron collision frequency is given by the sum of the electron-ion and electron neutral collision rates.

$$\nu_{eff} = \langle \nu_{en} \rangle + \langle \nu_{ei} \rangle \tag{2.29}$$

For the case of elastic scattering of electrons in a pure coulomb field of ions, the electron-ion collision frequency is given by

$$\langle \nu_{ei} \rangle = \frac{8\pi}{3} . \frac{Z^2 e^4 N_i}{(2m_e \pi)^{1/2} (kT_e)^{3/2}} . \ln \left[\frac{k^{3/2}}{1.78 Z e^3} . \left(\frac{T_e^3}{N_e \pi} \right)^{1/2} . \left(\frac{T_i}{Z T_e + T_i} \right)^{1/2} \right] \tag{2.30}$$

m_e, N_e and T_e are the mass, number density and temperature of the electrons; Z, N_i and T_i are the atomic charge number, number density and temperature of ions; k is the Boltzmann constant. The electron-neutral collision frequency is derived from the sum of the collisional rates between electrons and the neutral species that constitute the upper atmosphere. The Maxwellian-averaged electron-neutral collision frequencies have been determined from laboratory data and theoretical derivations by Schunk and Nagy (1987).

$$\langle \nu_{eN_2} \rangle = 2.33 \times 10^{-11} . N(N_2) . \left[1 + 1.21 \times 10^{-4} T_e \right] T_e \tag{2.31}$$

$$\langle \nu_{eO_2} \rangle = 1.82 \times 10^{-10} N(O_2) \left[1 + 3.6 \times 10^{-2} T_e^{1/2} \right] T_e^{1/2} \tag{2.32}$$

$$\langle \nu_{eO} \rangle = 8.9 \times 10^{-11} N(O) \left[1 + 5.7 \times 10^{-4} T_e \right] T_e^{1/2} \tag{2.33}$$

$$\langle \nu_{eHe} \rangle = 4.6 \times 10^{-10} N(He) . T_e^{1/2} \tag{2.34}$$

$$\langle \nu_{eH} \rangle = 4.5\times10^{-9} N(H)\left[1-1.35\times10^{-4} T_e\right] T_e^{1/2} \qquad (2.35)$$

It is clear that radio absorption in the ionosphere does not simply rely on electron density or the density of the neutral species. The inclusion of the effective collision frequency introduces a dependence on the ionospheric temperature parameters. When studying the effects of HF radio absorption it is important to determine the role played by these changing parameters during active periods. In the D and lower E layers it is the electron-neutral collision frequency that dominates leading to electron temperature as an important factor in determining the amount of radio absorption; increases in electron temperature result in increased absorption at lower altitudes. At higher altitudes the electron-ion collision frequency increases resulting in a more prominent role for ion temperature, though the temperature of the electrons is still most significant. In the F layer an increase in temperature will produce a decrease in absorption.

2.4 Summary

This chapter has introduced basic concepts of how particles move in the magnetosphere and the process by which they deposit their energy into the ionosphere. The drift and bounce motions of charged magnetospheric particles are important topics that relate significantly to the research presented in this thesis. Bounce motion due to the changing magnetic field and particle pitch angle along a field line leads to the formation of mirror points and the trapping of charged particles in the magnetosphere. Precipitation of charged particles is dependent on the pitch angle of the particle and the position of the mirror point in the atmosphere. This leads

to the concept of the Loss cone; particles with pitch angles within the loss cone will fail to mirror at their next bounce and will instead collide in the atmosphere producing ionisation. The orientation and morphology of the geomagnetic field leads the trapped particles to drift around the Earth; electrons eastward and protons westward.

HF radio wave propagation has been discussed and the Altar-Appleton-Hartree equation presented. This describes the dispersion relationship of radio waves in plasma and in this case the ionosphere. From the AAH equation the coefficient of attenuation of a radio wave is calculated and it has been shown that changes in ionospheric parameters (significantly electron density but also temperature) can lead to an increase in the non-deviative absorption of radio waves. The majority of this absorption occurs in the lower portion of the ionosphere (D layer).

Chapter 3

Instrumentation

3.1 Introduction

The drive of this thesis is the study of high-energy particle precipitation and its effects in the auroral ionosphere. The principle instrument used to monitor the precipitation in this study has been the Imaging Riometer for Ionospheric Studies (IRIS), which is located at Kilpisjärvi, Finland. Section 3.2 describes how this riometry works and also describes the chain of broad beam riometers located in Fennoscandia. Complementing the riometer observations are measurements from the EISCAT (European Incoherent Scatter) radar located at Tromsø, Norway. Various other instruments such as magnetometers and coherent radars have been used in support; most notably satellite data has been exploited to place the ground-based observations in a magnetospheric context. Particle detectors on board the DMSP (Defence Meteorological Satellite Program) and SAMPEX (Solar, Anomalous, Magnetospheric, Particle Explorer) spacecraft provide in-situ measurements of energetic particles that produce the absorption signature in the ionosphere.

3.2 Imaging Riometer for Ionospheric Studies (IRIS)

3.2.1 Riometry

The RIOMETER (Relative Ionospheric Opacity Meter using Extra Terrestrial Electromagnetic Radiation) is a simple instrument developed in the 1950s (e.g. Little

and Leinbach, 1959). It operates passively by constantly monitoring the background cosmic radio noise from the sky. These measurements are usually made in the range of 20 to 50 MHz, which by necessity are comfortably above f_0F2. By comparing the received signal with that for an undisturbed day it is possible to determine the variation of ionospheric absorption. The riometer is based on developments in radio astronomical techniques (Machin *et al*., 1952) and achieves high gain stability by switching rapidly between the antenna and a local noise source. The local noise source is continuously adjusted so that its power output equals that received by the antenna. Thus gain variations are unimportant as the receiver acts as a sensitive null indicator. The current through the noise source is recorded and this is monotonically related to the power output. By using the received power from an inactive period the general background absorption can be removed and only the variation above this level will be considered. In the auroral zone this variation is predominantly due to the precipitation of high-energy charged particles that produce enhanced electron density in the D and E layers of the ionosphere. The principle of ionospheric radio absorption has been explained in Chapter 2 and the following section (3.3.2) examines the principal instrument used in this study that uses the riometry technique.

3.3.2 The IRIS at Kilpisjärvi

The most common form of riometer uses a broad or wide beam antenna with beamwidths of the order of 60 degrees. Small spatial scale details of the absorption variation are lost since this method integrates over a large portion of the sky (~8500 km^2 at 90 km altitude). Narrow beams (10 to 20 degrees) can probe these small-scale features, however the area of the ionosphere that is monitored is much reduced. A

recent development is the imaging riometer (Detrick and Rosenberg, 1990), first deployed at the South Pole by the University of Maryland, USA. This system operates as a fast-scan multiple beam instrument to examine the entire ionospheric sky to 45 degrees from the zenith. Several of these systems have now been deployed including one operated by Lancaster University as a UK National Facility.

The Imaging Riometer for Ionospheric Studies (IRIS) (Browne *et al.*, 1995) is located at Kilpisjärvi in northern Finland, (69.05° N, 20.79° E). It began operations in September 1994 and is run by the Ionosphere and Radio Propagation Group of Lancaster University in collaboration with the Sodankylä Geophysical Observatory, Finland. IRIS samples the cosmic radio noise at 38.2 MHz (a protected frequency for Astronomy) and consists of an imaging array and a single, wide beam riometer. The system uses 64 circularly polarised cross dipole antennas grouped in a square array and separated by half a wavelength (Figure 3.1). The signals from each row of eight antennas are phased by Butler matrices and produce 49 narrow beams of width between 13° and 16° (Figure 3.2). The outputs are fed into 7 riometers through the use of time division switching. The whole array is sampled every second and switching is arranged so that each second is divided into 8 time slots. The eighth time slot is used to record the output from the co-located wide beam antenna.

Once the raw power has been sampled it is necessary to compare it with a base line that will provide an indication of how the absorption varies in time. This base line is known as a Quiet Day Curve (QDC) since it represents the received cosmic radio noise on a day when there are no absorption contributions from particle precipitation or from enhanced X-ray fluxes (Figure 3.3). There are a number of methods for determining a QDC and all make use of observations of the radio sky. In particular

Figure 3.1 **The top photograph shows the IRIS phased array during summer and the bottom panel displays a typical winter scene when snow increases the height of the ground plane (Photographs courtesy of S.Browne).**

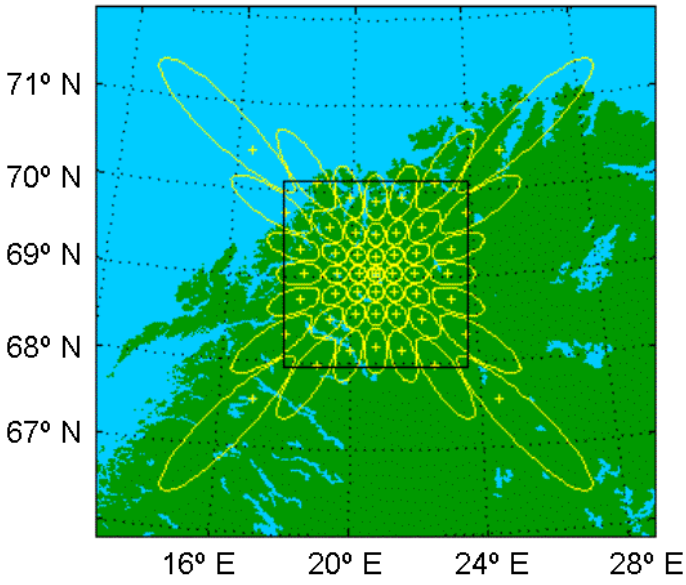

Figure 3.2

Beam projection of IRIS at 90 km altitude. The contours define the –3 dB points and the black square shows the calculated field of view used in the IRIS images.

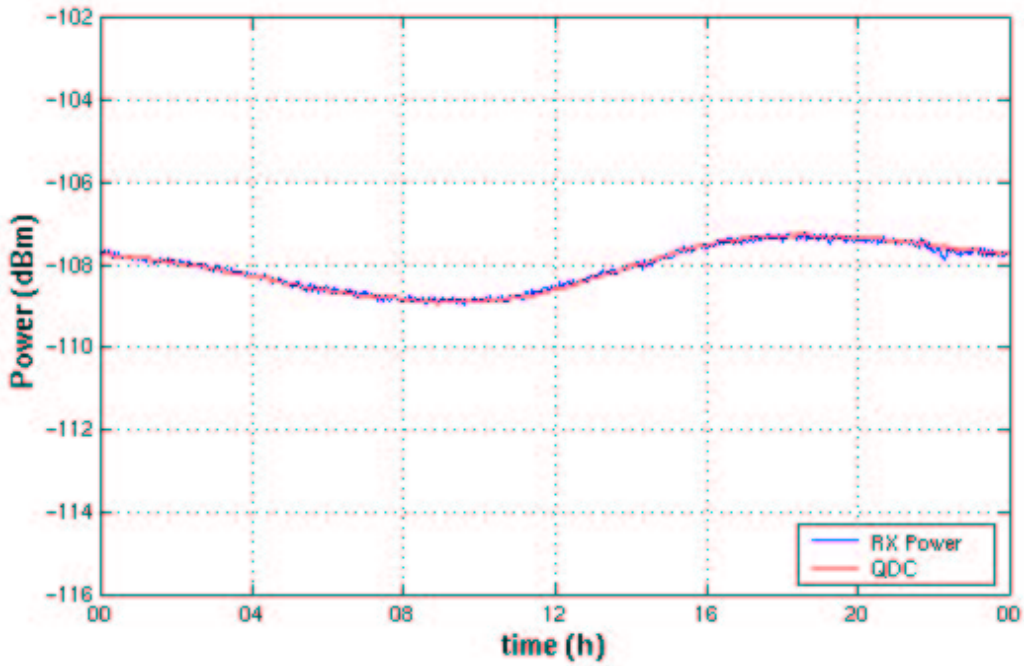

Figure 3.3. A typical quiet day. The blue line shows the received power and the red line is the QDC for the 14 day period during which the day occurs.

there are two principle techniques; the first makes use of a sky map of the comic radio noise temperature at the receiving frequency to determine the expected signal at every local time (e.g. Cane, 1978; Milogradov-Turin and Smith, 1973). This method leads to a base line above which absorption from both solar ionisation and particle precipitation could be measured and uses long term observations to determine the sky map. Empirical processes such as the Inflection Point method, which places the QDC above the mean of the cosmic radio noise power (e.g. Krishnaswamy *et al*, 1985), use the measured power to generate a base line on much shorter time scales and so the solar component of the absorption is lost.

For IRIS, each of the 49 beams requires a quiet day curve and the method for generating them is numerical. Rather than adopt the inflection point method, a percentile method is used; described by Browne *et al*. (1995) this process has since been refined (S.R. Marple, private communication) to compute the QDC at the same resolution as the data are recorded. Due to possible seasonal variations (e.g. snow melt in spring) the QDC are computed for a relatively short period but not so short that no quiet days occur. For IRIS a minimum of 14 days is used, more during active periods, and the data are filtered for solar radio emission and other interference; this process is described in Marple and Honary (in preparation, 2002). The data is smoothed and outlying points removed using a sliding median with a window size of 599 seconds after which the data are binned according to sidereal time resulting in 14 or 15 samples in each bin. Sidereal time is used since the region of the sky at which the riometer beam is directed determines the received power; thus the power varies with the apparent rotation of the stars. The mean of the second and third highest values for each time interval is calculated and this gives a good estimate of the quiet

time value; the largest value is discarded since it may be corrupted by interference (solar radiation) or scintillation. A sliding mean filter (299 seconds) is then applied to smooth the data. The absorption is calculated using the following formula:

$$\text{Abs} = \frac{\text{QDC} - \text{Received Power}}{\text{Obliquity factor}} \qquad (3.1)$$

The obliquity factor is introduced due to the tilted nature of the beams. To produce an image of the absorption variations the beams must be mapped to an assumed height (usually 90 km). This means that any beam off zenith will travel through a greater portion of the ionosphere. The obliquity factor represents the additional path length (as a factor) through a thin ionospheric layer of an oblique ray, compared to a zenithal ray. For the zenithal beam the obliquity factor = 1.

3.2.3 The SGO chain

Sodankylä Geophysical Observatory operates a chain of eight broad-beam riometers that stretch from the southernmost tip of Svalbard (Hornsund 77.0° N, 15.6° E) to the centre of Finland (Jyväskylä, 62.42° N, 25.28° E). The locations and current operating frequencies of these instruments are presented in Table 3.1. This table also includes the coordinates of IRIS, together with the L value calculated for 90 km altitude. Rather than using an empirical method to derive the quiet day curves, SGO bases them on a theoretical model of the sky temperature at the appropriate frequency.

Figure 3.4 presents a map of northern Europe with the positions of the ground-based instruments marked on them. This includes the IRIS and SGO riometer chain beam patterns and the locations of the radars that will be discussed in the next sections.

Station	**Geographic Latitude (AACGM)**	**Geographic Longitude (AACGM)**	**Operating Frequency (MHz)**	**L-shell**
Hornsund	77.0° (74.13°)	15.60° (109.82°)	30.0	13.56
Kilpisjarvi	69.05° (65.9°)	20.79° (104°)	38.2	6.08
Absiko	68.40° (65.24°)	18.90° (102.64°)	30.0	5.78
Ivalo	68.55° (65.07°)	27.28° (108.73°)	29.9	5.71
Sodankyla*	67.42° (64.16°)	26.39° (107.27°)	30.0 (51.4)	5.26
Rovaniemi	66.78° (63.33°)	25.94° (106.51°)	32.4	5.04
Oulu	65.05° (61.58°)	25.54° (105.19°)	30.0	4.48
Jyvaskyla	62.42° (58.87°)	25.28° (103.67°)	32.4	3.79

Table 3.1 Positions and operating frequencies for the SGO riometer chain and IRIS. The CGM coordinates and L shells are calculated from the IGRF model for 2001. *There are two riometers operating at Sodankylä

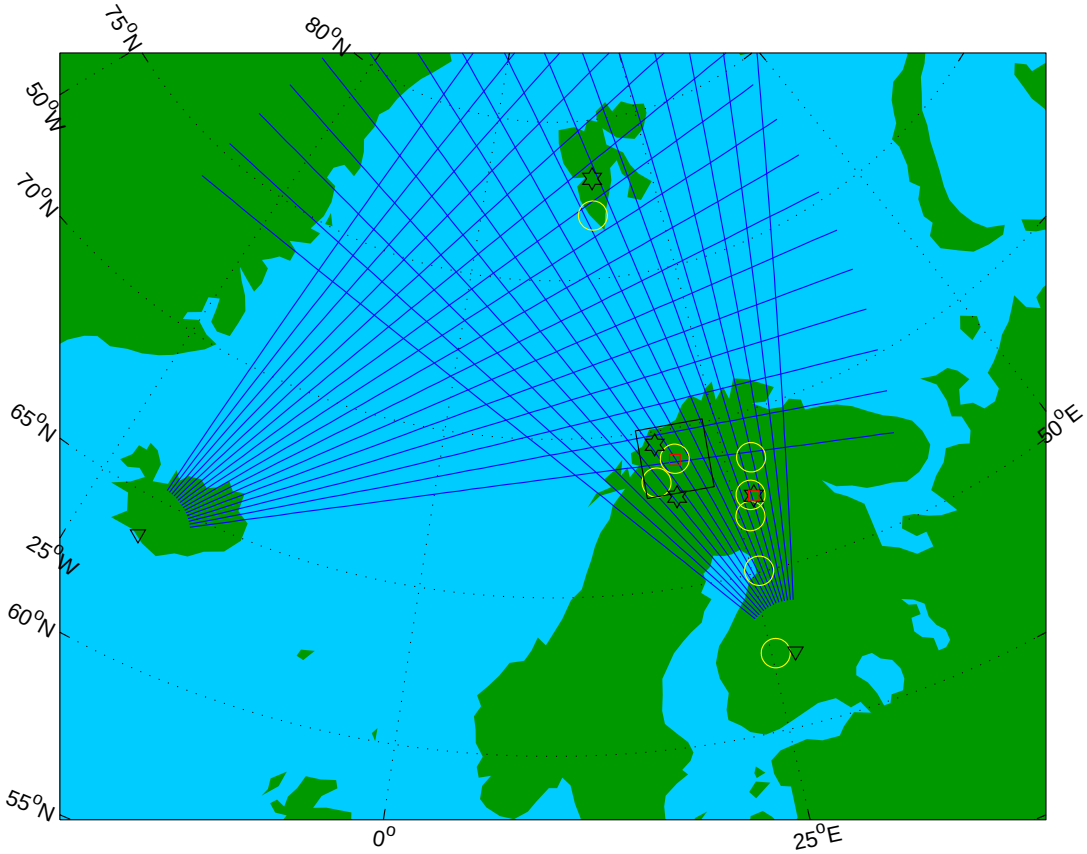

Figure 3.4. **Map showing the locations of some of the instruments used in the course of this study. The yellow circles display the 90 km altitude field of views of the wide beam riometers of the SGO chain and IRIS. The two red squares pinpoint the locations of pulsation magnetometers operated by Sodankylä Geophysical Observatory. Black triangles mark the positions of the CUTLASS radars and black hexagons mark the locations of the ESR and EISCAT mainland radars including the remote sites. The black box demonstrates the field of view of IRIS whereas the blue lines illustrate the individual beams of the CUTLASS radars.**

3.3 The EISCAT Radars

Six European research councils (UK, Germany, Norway, Sweden, France and Finland) founded the European Incoherent Scatter (EISCAT) Scientific Association in December 1975. This number has since grown to seven when Japan joined in 1995. The aim of EISCAT is to provide the opportunity to conduct ionospheric research at high latitudes. The following sections summarise the principles of incoherent scatter and discuss the operations of the EISCAT mainland radars and the experiments used in this thesis.

3.3.1 Theory of Incoherent Scatter

In 1906, J. J. Thomson demonstrated that a single free electron can scatter electromagnetic radiation with a cross section, σ, given by (Thomson, 1906):

$$\sigma = 4\pi\left(r_e \sin\gamma\right)^2 \qquad (3.\ 2)$$

where r_e is the classical radius of an electron and γ is the polarisation angle (the angle between the direction of the electric field in the incident radiation and the direction of the observer). For direct backscatter, this cross-section is of the order of $10^{-28}m^2$. It was Fabry (1928) who first suggested that incoherent scatter might be used to probe the ionosphere since a monochromatic radar beam scattered from free electrons of the ionosphere would form a single peak, centred on the radar frequency, with Doppler broadening due to the thermal velocities of the scattering electrons. The electrostatic forces in ionospheric plasma lead to a 'shielding' layer around any single charge so scattering does not originate from free electrons. The radius of the shielding layer is termed the Debye length, D;

$$D = \left(\frac{\varepsilon_0 k_B T_e}{e^2 N_e} \right)^{\frac{1}{2}} \approx 69 \left(\frac{T_e}{N_e} \right)^{\frac{1}{2}} \qquad (3.3)$$

in which ε_0 represents the permittivity of free space.

The dependence of the Debye length on electron temperature and density, results in a variation with altitude. D is therefore greater in the upper F-layer than in the E layer. Factors such as season, solar cycle and geographic location also affect D. For ionospheric conditions, Debye lengths vary between ~0.3 and 6.0 cm. Organised motion cannot be sustained in the plasma on scales shorter than the Debye length so the electrons may be considered as free and the backscatter spectrum has the form predicted by Fabry. At larger scales, random thermal motions of the electrons generate wave-like irregularities due to electrostatic coupling. These are known as ion-acoustic and electron-acoustic waves. Acoustic modes in plasma propagate isotropically and over a wide and continuous range of frequencies, and have been studied theoretically by, amongst others, Fejer (1960), Dougherty and Farley (1960) and Hagfors (1961).

Transmitted wavelengths that greatly exceed the Debye length undergo strong quasi-coherent scatter from those ion- and electron-acoustic waves that satisfy the Bragg criterion for the radar wavelength. The resulting frequency spectrum consists of four components corresponding to the ion- and electron-acoustic waves propagating towards and away from the radar. The Doppler shifts arising from these wave modes are given by:

$$F_i(\lambda) = \pm \frac{2}{\lambda} \left[\left(\frac{k_B T_i}{m_i} \right) \left(1 + \frac{T_e}{T_i} \right) \right]^{\frac{1}{2}} \qquad (3.4a)$$

$$F_e(\lambda) = \pm f_p \left(1 + \frac{12\pi^2 D^2}{\lambda^2}\right)^{\frac{1}{2}} \qquad (3.4b)$$

in which f_p, the plasma frequency, is given by

$$f_p = \left(\frac{e^2 N_e}{4\pi^2 \varepsilon_0 m_e}\right)^{\frac{1}{2}} \qquad (3.5)$$

The transmitted radio wave will scatter from acoustic waves with phase fronts normal to the direction that is along the bisector of the angle between the transmitter and receiver beams. Thus for a monostatic system, a system in which the transmitter and receiver are co-located, the radar is sensitive to acoustic waves with phase fronts normal to the wave vector, i.e. along the direction of the beam.

A charged particle in plasma can be accelerated due to the transfer of energy from an electrostatic wave moving in the same direction but with a slightly higher speed. This results in attenuation of the wave, termed Landau damping. Conversely, particles moving slightly faster will result in an enhancement of the wave. More ions travel slightly slower than the ion-acoustic wave than travel slightly faster leading to substantial broadening of the ion-acoustic lines of the backscattered spectrum. The ion lines broaden to such an extent that they merge (Figure 3.5). The total width of the backscattered ion line spectrum from the ionospheric plasma varies between 10 kHz (E-region) and 50 kHz (F-region). Electron acoustic waves travel at far greater velocities than the majority of thermal electrons, thus the electron-acoustic lines (or plasma) lines will remain sharp.

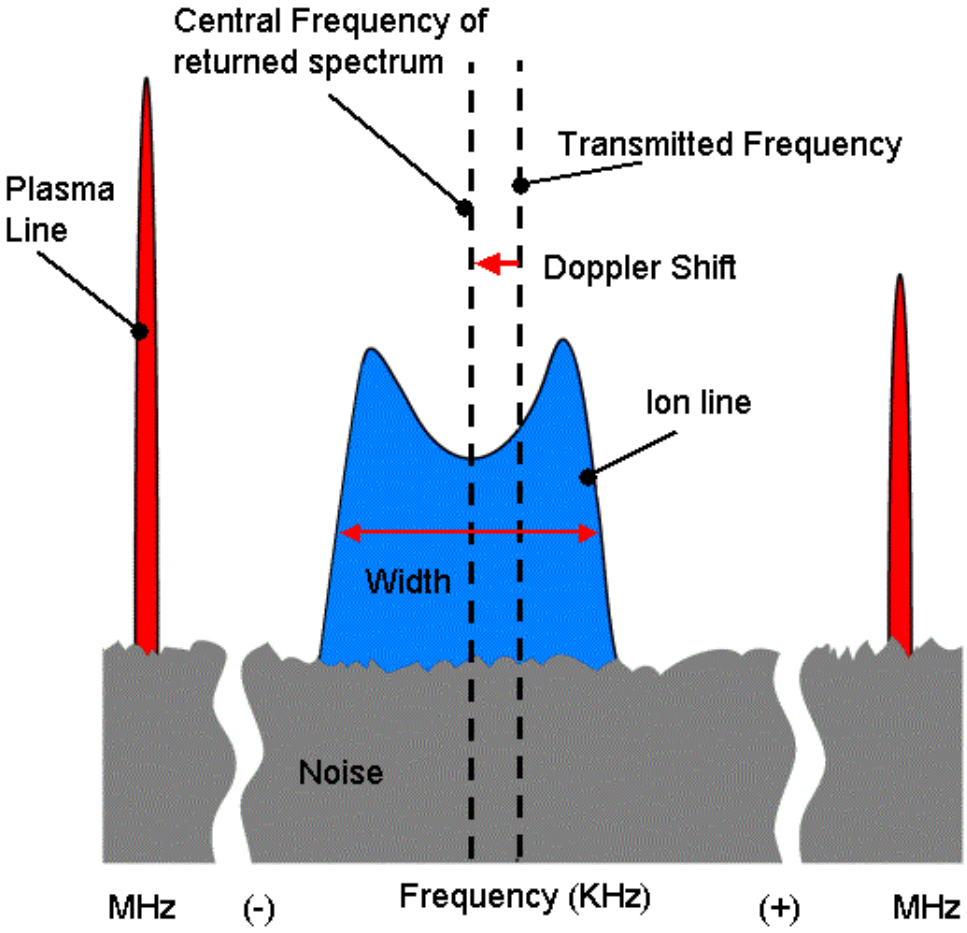

Figure 3.5. A typical F region spectrum of the returned power.

For transmission of a radio wave with a wavelength significantly longer than the Debye length, scatter is quasi-coherent rather than truly incoherent. Nevertheless, in the absence of more appropriate nomenclature, this process is still universally referred to as incoherent scatter.

3.3.2 Ionospheric parameters

Incoherent Scatter is considered to be the most powerful ground based tools available for probing the ionosphere. A number of physical parameters can be derived from the returned spectrum of a transmitted radio wave:

Electron Number Density. The ionospheric electron number density profile can be determined to a first order from the total power of the returned signal:

$$N_e(h) = \frac{K\sigma_e P_s(h)}{[1 + (T_e/T_i)]h^2} \qquad (3.6)$$

in which K is a system constant proportional to both the effective collecting area of the receiver and the transmitted power. The system constant can be established by calibration of the measured density with an independent diagnostic. The correction for the effect of the ratio of the electron and ion temperatures is derived from the shape of the incoherent scatter spectrum. The majority of power scattered by acoustic modes in a plasma is contained within the ion line spectrum. For observations of the lower ionosphere (e.g. D and lower E layer) it can often be assumed that $T_e \approx T_i$ and thus equation (3.6) is simplified. This is the only ionospheric parameter that can be measured with a degree of certainty in the D layer of the ionosphere due to the single

peaked nature of the returned spectrum (Figure 3.6); a product of the inability of ion-acoustic waves to propagate in a region of high collision frequency. The electron number density is also known as the electron concentration, however it has become common to refer to this parameter as simply the electron density. Although this term is technically incorrect it is generally accepted and understood by the community and so for ease will be used throughout this thesis.

Plasma temperature and Ion Mass. Landau damping, the degree of which depends on the ratio of the electron and ion temperatures, broadens the ion lines of an incoherent scatter spectrum. The ratio of the depth of the spectrum trough to the height of the ion line is a sensitive function of the temperature ratio. The temperature ratio is thus a controlling factor in determining the sharpness of the ion lines, and can be obtained from the ratio of the peak spectral power density of the ion line spectrum to that at its central minimum. By measuring the separation of the two peaks of the ion line spectrum, the ratio of the ion temperature to the mass of the ions can be obtained. This is because the separation is approximately equivalent to twice the ion-acoustic frequency.

$$2F_i(\lambda) = \frac{4}{\lambda}\left[\left(\frac{k_B T_i}{m_i}\right)\left(1+\frac{T_e}{T_i}\right)\right]^{\frac{1}{2}} \qquad (3.7)$$

By assuming the mass of the ion species (and hence the composition) the absolute values of the ion and electron temperature can be calculated.

Plasma velocities. A Doppler shift in the frequency of the ion line spectrum is produced through the bulk motion of a plasma. This corresponds to the component of the velocity along the line-of-sight of the radar or the mirror direction of the radar.

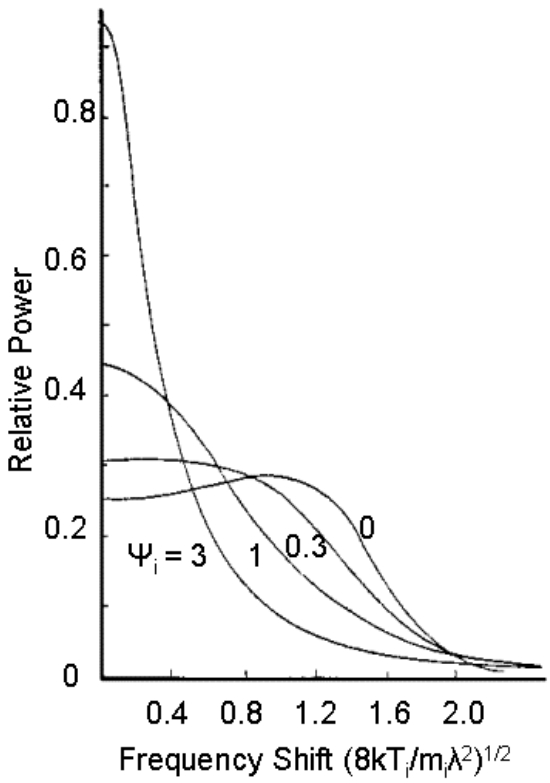

Figure 3.6. **Effect on the ion line of increasing the ion-neutral collision frequency. The quantity ψ_i is equal to $\lambda/4\pi l_i$ where λ is the radar wavelength and l_i the mean free path of the ions (Evans, 1969).**

The mirror direction is that along the radar beam for monostatic radar and along the bisector between the transmitter and receiver beams for a bistatic system. The Doppler shift, Δf_d, due to an ion velocity $\mathbf{v}_m$ along the mirror direction is given by:

$$\Delta f_d = \frac{2\mathbf{v}_m}{\lambda}\cos\left(\frac{\gamma}{2}\right) \qquad (3.8)$$

This shift is small compared to the spectral width, but can be gained from accurate measurement. As long as the electrons and the ions of the plasma move together the plasma drift does not affect the spectral shape.

Other parameters. All of the parameters that can either be measured directly or derived by incoherent scatter are listed in Table 3.2. Parameters in Table 3.1 that are marked with an asterisk are only the line of sight values. Radars with multiple receivers are able to fully resolve these values.

3.3.3 The EISCAT system

EISCAT operate three incoherent scatter radar systems. Two of the radars are located in northern Norway near to Tromsø (Rishbeth and Williams, 1985) and the third operates on the island of Spitzbergen, part of the Svalbard archipelago. This ESR (EISCAT Svalbard Radar) actually consists of two dishes that alternate transmission and data dumping. One dish is permanently field aligned; however the second dish is steerable. The mainland facility consists of a tristatic UHF (931 MHz) radar system and a single VHF transmitter/receiver (223 MHz) (Figure 3.7).

Directly Measured	**Derived indirectly**
Electron density, $\mathbf{N_e}$	Electric field
Electron Temperature, $\mathbf{T_e}$	Hall conductivity
Ion Temperature, $\mathbf{T_i}$*	Pedersen conductivity,
Ion velocity, $\mathbf{v_i}$*	Exospheric heat flux,
Electron velocity, $\mathbf{v_e}$*	Neutral density
Ion-neutral collision frequency, ν_{in}	Neutral temperature
Ion composition, $\mathbf{m_i}$	Neutral velocity/wind
Photoelectron flux	
Electric current density, **J***	

Table 3.2. Parameters measured and derived from incoherent scatter, those marked with an asterisk are line of sight values only. The incoherent scatter technique relies on assuming at least one parameter out of the T_e, T_i, N_e and m_i since the number of unknowns and equations makes it an underdetermined system.

Figure 3.7. The EISCAT mainland radars, located in Ramfjord, near Tromsø. To the left is the UHF transmitter/receiver dish (32 metres). Below is the VHF radar which consist of four segments (128 by 46 metres in total). Photographs courtesy of S.R. Marple.

Other receivers for the UHF system are located at Kiruna, Sweden and Sodankylä, Finland. The three stations enable three components of the plasma velocity to be measured and thus a full vector to be determined. Some system parameters for the radars are detailed in Table 3.3. Most of the incoherent scatter results presented in this thesis come from the mainland UHF radar and so the following discussion is primarily concerned with this facility. More information on the ESR can be obtained from Wannberg *et al*. (1997).

The mainland UHF antennae are circular paraboloids of 32 m diameter (570 m^2 collecting area). The antennae can be steered both in azimuth and elevation at a maximum rate of 80° per minute and have half-power beam widths of 0.6°. The radar operates at frequencies around 931.5 MHz and is capable of probing the ionosphere at altitudes between about 70 km and 1500 km. The EISCAT UHF radar is currently the only tristatic incoherent radar in operation. Comprehensive descriptions of the technical characteristics and capabilities of the EISCAT radars have been published in the past (e.g. Rishbeth and Williams, 1985; Folkestad et al., 1983). In 2000 the EISCAT mainland radars underwent a large technical overhaul; this included equipping the UHF with two high efficiency klystrons and extensive upgrading of the receiver systems with new digital signal processing equipment. A set of channel boards have replaced much of the old analogue equipment and up to six different signals can be received and processed simultaneously. These system changes have improved the signal to noise ratio by more than 50 % relative to the old system and led to the development of new coding schemes.

Site	Location	Dip Angle	Antenna	Frequency	Power (MW) Peak	Mean
Tromsø	69.6°N 19.2°E	77.6°	32 m Parabola (UHF). 120m × 46m Parabolic cylinder (VHF).	931 223	2.0 5.0	0.25 0.67
Kiruna	67.9°N 20.4°E	76.8°	32 m Parabola			
Sodankylä	67.4°N 26.7°E	76.7°	32 m Parabola			
Longyearbyen	78.15°N 16.05°E	82.02°	32 m Parabola 42 m Parabola	500	0.5	0.125

Table 3.3 Operational details of the EISCAT radars, both mainland and at Svalbard.

3.3.4 EISCAT experiments

Experiment time on the radar is split into two categories: Special time and Common time. Special time is divided amongst the member nations of the EISCAT association to allow tailored experiments to be run. This time is applied for in the home nation and the data collected by the Special experiments are for the exclusive use of the applicants for one year after which the data becomes available to the rest of the EISCAT community. As the name suggests, common time provide data to the whole EISCAT community and these experiments are run for at least 50% of the operating time. A range of experiment geometries and coding are used to provide the common programmes. The range of available mainland programmes from before the 2000 upgrade are listed in Table 3.4 with a brief description of their operational characteristics.

As stated earlier, the observations used in this thesis come mostly from the UHF radar and those that occur before the upgrade of 2000 use the cp1 experiment. This uses a fixed transmitting antenna pointing along the geomagnetic field direction. The basic time resolution is 5 seconds and the scheme uses alternating codes and long pulses as well as short pulses to produce power profiles. These power profiles provide a measure of the electron density to lower altitudes than the alternating code can reach. Whereas the alternating code starts from around 80 km altitude, EISCAT can observe scatter from around 65 km if there is sufficient electron density to produce a reasonable signal to noise ratio. This raw electron density can be calibrated at heights where there are common range gates with the alternating code, thus providing more accurate estimates.

Experiment	Radar	Geometry	Altitude	Latitude
cp1	UHF	Field aligned	80 - 600 km	-
cp2	UHF	Four position scan: field aligned, vertical, east and north	80 - 600 km	-
cp3	UHF	Wide scan in N-S geomagnetic plane.	140 - 950 km	62° - 76°
cp4	VHF	Northward pointing (occasional split beam to the north west)	283 - 1000 km	73° - 80.5°
cp6	VHF	Vertical	73 - 113 km	-
cp7	VHF	Vertical	80 - 2500 km	-

Table 3.4. Experiments that operate on the two mainland radars pre- 2000 AD.

Following the refurbishment in 2000 a new suite of radar experiments have been introduced on the mainland. The reliance on long pulse transmissions has diminished with a greater emphasis on the alternating code. At time of writing there are currently 8 experiments available to run on the UHF and VHF. A brief summary of these experiments is presented in Table 3.5 together with a listing of the experiments currently run on the ESR. There are a further two experiments being tested to replace cp7h and to act as a general purpose VHF experiment. The mainland data presented in this thesis post-2000 are from the cp1l.

Experiment	**Radar**	**Range**	**Comment**
tau1	VHF	100 - 1900 km	Replacement for cp4
tau2	UHF	90 – 750 km	General purpose to replace cp1l
tau3	UHF	90 – 1400 km	Modified Tau2 used for scanning
arc	UHF/VHF	90 –250 km	High time resolution for auroral studies
D-layer	VHF	60 – 130 km	High spatial resolution for D-layer
cp1l	UHF	90 – 700 km	Old cp1k converted for new system
cp4b	VHF	400 – 1800 km	Old cp4b converted for new system
cp7h	VHF	280 –2000 km	Old cp7g converted for new system
tau0	ESR	90 – 1200 km	General purpose ESR experiment

Table 3.5 Summary of experiments operating on the mainland and ESR radars at time of writing (2002).

3.4 Satellites

An important part of the research conducted in this thesis relates observations from satellites to their ionospheric signatures. This section details several satellites used in this study, including polar orbiting satellites (SAMPEX and DMSP) and geostationary spacecraft (GOES). Satellites located outside of the magnetosphere also play an important role in relating the observed phenomena to solar wind coupling processes. The data from three satellites were used in the course of this thesis to provide solar wind and particle flux parameters in interplanetary space: Geotail, WIND and ACE. Brief descriptions of the locations and instruments of these solar wind satellites are provided in section 3.4.4. Satellite orbit information is presented in the format: perigee × apogee.

3.4.1 SAMPEX (Solar, Anomalous, Magnetospheric Particle Explorer)

SAMPEX is one of the NASA small explorer satellites (SMEX). It was launched in July 1992 with a mission duration goal of three years and is still flying in 2002. It is located in a polar orbit with an inclination of 82° and flies at an altitude of 550 (perigee) × 675 km (apogee). SAMPEX was designed to study the energy, composition and charge states of four classes of charged particles: galactic cosmic rays, anomalous cosmic rays, magnetospheric electrons, and solar energetic particles. The timing of the launch meant that the latter investigation would carry from shortly after solar maximum into the declining phase of the solar cycle. In fact since the satellite has far outlived its expected lifetime it has monitored nearly a complete solar cycle. A more detailed overview of the SAMPEX satellite is given in Baker *et al*. (1993).

In total there are four instruments that make up the scientific payload of the SAMPEX satellite. The characteristics of the 4 instruments are described in Table 3.6. Comprehensive descriptions of the four instruments are available in Cook et al. (1993a and 1993b), Klecker et al. (1993) and Mason et al. (1993).

Instrument	**Details**
LEICA Low-Energy Ion Analyser	Measures the elemental and isotopic composition of nuclei from He to Ni (Z = 2 to 28) over the energy range from ~0.5 to ~5 MeV/nuc.
HILT Heavy Ion Large Telescope	Measures the elemental composition of nuclei from He to Ni (Z = 2 to 28) in the energy range from ~4 to 250 MeV/nuc.
MAST Mass Spectrometer Telescope	Measures the elemental and isotopic composition of nuclei from He to Ni (Z = 2 to 28) over the energy range from ~15 to 200 MeV/nuc.
PET Proton-Electron Telescope	Measures the energy spectra of electrons from ~0.5 to 30 MeV, and of H and He from ~ 20 to 200 MeV/nuc.

Table 3.5 Typical operating values for the four instruments on the SAMPEX satellite.

3.4.2 GOES (Geosynchronous Operational Environmental Satellites)

NOAA (National Oceanic and Atmospheric Administration) operates a series of satellites known as Geosynchronous Operational Environmental Satellites (GOES). These satellites carry a package of instruments designed to monitor space weather variations. There are three main components that are measured by the Space Environment Monitor (SEM) system: X-rays, energetic particles and magnetic fields. The majority of observations presented in this thesis are from the GOES-8 satellite that was launched in 1995. This is the first of the GOES satellites that is "3-axis stabilized" rather than spin stabilized. This section concentrates on brief descriptions of the X-ray and energetic particle sensors carried on board GOES-8.

The X-ray sensor (XRS) measures the solar X-ray flux for the 0.5-4.0 and 1.0-8.0 Angstroms wavelength bands. The two bands allow the hardness of the spectrum to be estimated. Observations from XRS provide a means for detecting the start of solar X-ray flares, though occasionally there is a low channel response to either energetic particles or X-ray production from precipitation of energetic particles. The EPS instrument measures energetic particles. This is a series of solid-state detectors with pulse-height discrimination that measures proton, alpha particle and electron fluxes. There are seven proton channels, the lowest energy (P1) responds to primarily trapped outer-zone particles; the energies are given in Table 3.6. P2 occasionally responds to trapped particles during magnetically disturbed periods however the higher channels are sensitive only to fluxes originating outside the magnetosphere. The proton data provided by NOAA is in two forms: integral and differential fluxes.

Channel	Differential (P)	Integral (I)
1	0.6-4.2 MeV	> 1MeV
2	4.2-8.7 MeV	> 5 MeV
3	8.7-14.5 MeV	> 10 MeV
4	15-44 MeV	> 30 MeV
5	39-82 MeV	> 50 MeV
6	84-200 MeV	> 60 MeV
7	110-500 MeV	> 100 MeV

Table 3.6. Lists of the GOES data energy channels supplied by NOAA/SEC

3.4.3 DMSP (Defence Meteorological Satellite Programme)

The Defence Meteorological Satellite Program (DMSP) is operated by the US air force and the program began in the mid 1960s. Originally the operational program called for two satellites to be in polar orbit at all times: one in the dawn-dusk meridian and one in 1030 LT to 2230 LT meridian. Depending on the system lifetimes there can be as many as three satellites in operation at a given time. In December 1999 the F15 satellite was launched and during the time interval of IRIS operations (post September 1994) there have been 6 operational spacecraft. The satellites fly in sun-synchronous, 101 minute orbits at ~830 km altitude. Due to an error at the launch the F10 satellite processed to later local times at a rate of 15 minutes/year. Although primarily a meteorological satellite the DMSP spacecraft also carry an array of solar terrestrial orientated sensors that measure along-track plasma densities, velocities, composition,

ion drifts and local magnetic fields. Low energy electron analysers were first carried in 1974 with additional upgrades on the F2 satellite in 1977 that allowed electron energy to be measured in the range 50 eV to 20 keV in 16 channels. Post DMSP F5 each of the satellites have carried an improved electrostatic analyser; the SSJ/4 auroral particle sensor. Curved plate detectors allow precipitating particles to enter through the instrument aperture and electrons and ions of the selected energy are deflected toward the target by an imposed electric field applied across the two plates. The two low energy detectors consist of 10 channels centred at 34, 49, 71, 101, 150, 218, 320, 460, 670, and 960 eV. The high energy detector measures particles in 10 channels centred at 1.0, 1.4, 2.1, 3.0, 4.4, 6.5, 9.5, 14.0, 20.5 and 29.5 keV. The SSJ/4 instruments on F13 and F15 have suffered degradation in the low energy ion detectors (below 1keV) making the data unreliable. SSJ/4 data are supplied at 1 second resolution. For a full description of the SSJ/4 sensor see Hardy *et al*.(1984).

3.4.4 Solar wind measurements (Geotail, ACE and WIND)

Geotail was designed to measure the flow of energy in the magnetotail in order to increase the understanding of fundamental magnetospheric processes. Since 1995 the satellite has been in an 8×30 R_e orbit at an inclination of 7.5º and a period of 4.9 days, which places Geotail outside of the magnetopause for certain periods. In this thesis data was obtained for a period when the spacecraft was traversing the magnetosheath. Two instruments from the Geotail payload were used to provide magnetic field measurements and ion dynamic pressure within this turbulent plasma. The Magnetic Fields Measurement (MGF) consists of dual three-axis fluxgate magnetometers and a three-axis search coil magnetometer. Only fluxgate

magnetometer data is presented here. Plasma data comes from the Low Energy Particle (LEP) detector, which provides measurements of ion density and the three components of the plasma velocity.

ACE (Advanced Composition Explorer) is located at the first Lagrangian point (L1). The satellite payload consists of four instruments to study energetic ions and electrons (EPAM), magnetic fields (MAG), high-energy particle fluxes (SIS) and solar wind ions (SWEPAM). Data from the last three instruments have been included in this thesis. The fixed position of ACE provides a consistent data set for monitoring the solar wind conditions during periods of geomagnetic activity. Some of the more energetic events presented in this work cause failure of the lower energy particle detectors, making solar wind observations unreliable at these times.

WIND has provided measurements of the solar wind and IMF parameters since it was launched in November 1994. The original orbit of WIND was designed as a sunward, multiple lunar swing-by with the spacecraft occasionally travelling up to 250 R_e into the solar wind at apogee whilst at other times reaching less than 100 R_e. This allowed measurements to be taken in a large portion of the upstream solar wind. In 1998, WIND spent several months at the L1 point calibrating its instruments with ACE, before undertaking a series of petal orbits with dimensions of 10×80 R_e, outside of the ecliptic plane. WIND carries a solar wind experiment (SWE) to provide bulk velocity and density data, as well as a magnetometer experiment (MFI). Also the EPACT instrument measures high-energy proton fluxes in several energy bands (4.6 to 72.0 MeV overall).

3.5 Additional Instruments

Two other instruments have been used to provide data that contributes to this thesis. These include a coherent scatter radar (CUTLASS) and pulsation magnetometers. The following two sections give brief descriptions of their operating characteristics.

3.5.1 CUTLASS (Co-operative UK Twin Located Auroral Sounding System)

CUTLASS is a twin station, high frequency, coherent scatter radar used to study the high latitude ionosphere (principally the F region). The radars are located in Iceland and Finland (Figure 3.4) and look north into a common volume over northern Scandinavia. Scatter is detected from field-aligned irregularities when the radar ray is orthogonal to the magnetic field line. This is achieved through the refraction of the HF ray in the ionosphere. The Doppler shift of the returned signal provides a measure of the line of sight velocity of the plasma and the data from the two radars can be combined to produce horizontal velocity vectors throughout the common volume. A single radar consists of sixteen beams each with seventy five 45 km range gates in standard common mode. Each beam has a dwell time of 7 seconds with the scan synchronised to start every 2 minutes. The University of Leicester operates CUTLASS as a UK National Facility, funded by the UK Particle Physics and Astronomy Research Council (PPARC). It also forms part of the Super Dual Auroral Radar Network (SuperDARN) (Greenwald *et al.*, 1995).

3.5.2 Pulsation Magnetometers

The Space Physics Group of Oulu and the Sodankylä Geophysical Observatory maintain a chain of search coil magnetometers. Unlike traditional fluxgate magnetometers, these instruments are capable of measuring geomagnetic fluctuations covering a frequency range from several mHz to 4 Hz. This includes the whole Pi/Pc (irregular and continuous pulsations) period range. Fluctuations in these ranges correspond to a number of ULF waves that occur in the magnetosphere that affect the precipitation of charged particles (Coroniti and Kennel, 1970). The pulsation magnetometers operate with a resolution of 1 nT/s. Data from two stations, Kilpisjärvi and Sodankylä, have been used in this thesis (marked on Figure 3.4).

3.6 Summary

This chapter has highlighted the instruments used to investigate the precipitation of charged particles into the D layer. The majority of observations come from the Imaging Riometer for Ionospheric Studies (IRIS) located at Kilpisjärvi, Finland, with the Sodänkylä Geophysical Observatory (SGO) chain of riometers used in support. The EISCAT radar has provided useful details of the altitude changes in electron density and other parameters that can only be obtained regularly through incoherent scatter methods. Similarly satellites such as GOES, DMSP and SAMPEX place the ionospheric observations in a magnetospheric context by direct measurement of the precipitating flux of particles. Solar wind based satellites provide measurements of the IMF and changing particle speeds that interact with the magnetosphere. Thus the history of events can be traced from the solar wind down to the ionosphere.

Chapter 4

A Review of Auroral and Polar Cap Absorption observations

4.1 Introduction

This thesis presents an investigation into energetic particle precipitation and this is achieved through the use of wide beam and imaging riometers (e.g. IRIS) which monitor the absorption of cosmic radio noise, a parameter that is directly related to the electron density in the D layer. Although the riometry technique is limited (it only provides a measure of the height integrated product of the electron density and the collision frequency) it has made some significant contributions to ionospheric physics.

Auroral radio absorption was discovered by Appleton, Naismisth and Builder (1933) during the International Polar Year of 1932-1933 when observing ionospherically reflected HF waves. They found that the intensity of the reflected signal was weakened, often considerably, during periods of magnetic and auroral activity and attributed the effect to increased ionisation at low altitudes. During the International Geophysical Year (1958-1959) the RIOMETER (Relative Ionospheric Opacity Meter using Extra Terrestrial Electromagnetic Radiation) was developed as a means to regularly measure the ionospheric absorption (e.g. Little and Leinbach, 1959). This was based upon the principal of monitoring cosmic radio noise absorption as developed by previous workers (e.g. Shain, 1951; Mitra and Shain, 1953; and Blum *et al.*, 1954). This chapter provides an introduction to observations of ionospheric absorption and how it has been used to investigate the dynamics of the lower

ionosphere, in particular two types of absorption: auroral absorption and polar cap absorption (PCA). PCA is due to the incidence of solar protons on the polar cap (first identified by Bailey, 1957) whereas auroral absorption is from the direct entry of magnetospheric electrons. The two types were originally distinguished through characteristic time variations and the geographic distribution; auroral absorption is short lived, irregular and confined to an oval near to the auroral region, whereas PCA tend to last for several days and varies smoothly across the sunlit polar cap (Hargreaves, 1969). Before reviewing auroral and polar cap absorption it is worth mentioning other types of cosmic radio noise absorption that are observed by riometers.

4.2 Summary of Absorption Types

Stauning (1996) summarised a number of types of absorption event including mechanisms for non-precipitation related absorption; e.g. F-region absorption due to low temperatures (Rosenberg *et al*., 1993; Wang *et al*., 1994; Nishino *et al*., 1997), and Electron Heating Absorption (EHA) from the E region during periods of high ionospheric convection (Stauning, 1984; Stauning and Olesen, 1989). Both of the aforementioned event types result in much weaker absorption changes than a typical precipitation event (of the order of 0.5 dB for F region absorption). Principally, there are two sources of precipitation that lead to enhanced cosmic radio noise absorption at high latitudes: the solar wind (and ultimately the sun) and the magnetosphere. As described in Chapter 1, these regions are coupled such that a change in the solar wind can produce a change in the magnetosphere. This is particularly demonstrated during large changes in solar wind speed that lead to the sudden commencement of

geomagnetic storms (SSC or Sudden Storm Commencement). The arrival of a shock front in the solar wind at the magnetopause may result in sudden compressions of the magnetosphere leading to impulse like precipitation of previously trapped high-energy particles. Events such as these tend to be short lived but are often widely extended in longitude and have been described as Sudden Commencement Absorption (SCA) (Brown *et al*, 1961; Brown, 1978; Brown and Driatsky, 1973). It has been argued that since a shock in the solar wind can produce similar short-lived results in the ionosphere without producing a geomagnetic storm, the term sudden impulse (SI) should replace SSC (Joselyn and Tsurutani, 1990), and by extension Sudden Impulse Absorption (SIA) is substituted for Sudden Commencement Absorption as a generic term for shock events.

4.3 Auroral Absorption

4.3.1 Precipitation and ionisation

Chapter 3 explained that IRIS observes absorption related to the precipitation of energetic particles. Calculations of the rate of ionization of air by beams of electrons have been made (e.g. Spencer, 1955 and Kamiyama, 1966), however most auroral applications come from semi-empirical approaches (Rees 1963; 1989). Figure 4.1 displays an example of ionisation rates for mono-energetic electrons and similar curves for protons. It becomes clear that for similar energies it is the electrons that dominate the absorption in the D region (Bailey,1955); a 200 keV electron may penetrate to 75 km but a 200 keV proton will reach only to 130 km, where the collision frequency is smaller. Eather and Burrows (1966) used H_β emission observations from the ground to indicate the contribution of ionisation from protons to

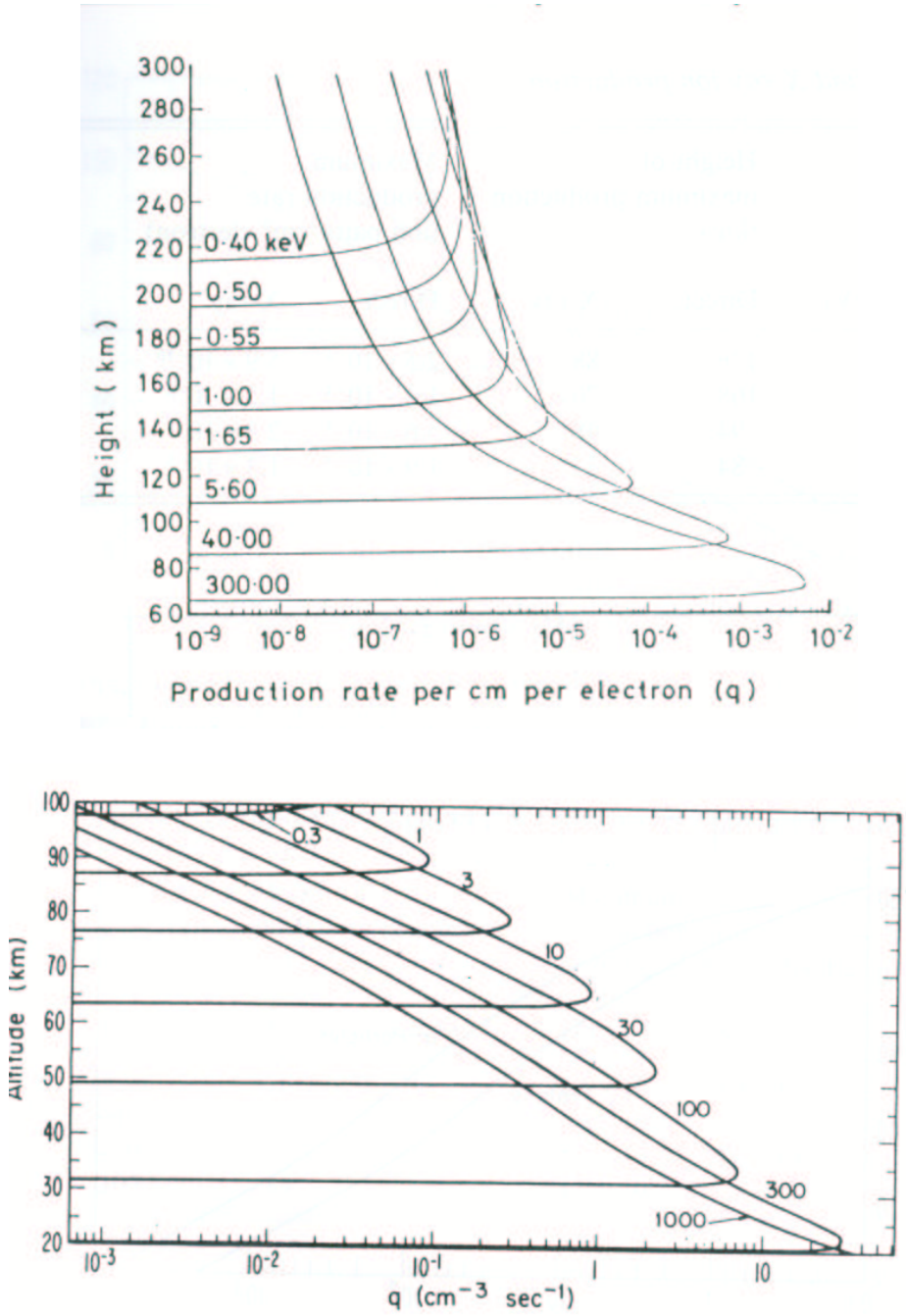

Figure 4.1. **Production rates due to monoenergetic electrons (top panel) and protons (bottom panel) for various initial energies; keV for electrons and MeV for protons (After Rees, 1963 and Reid, 1974).**

auroral absorption was negligible. Satellite observations (e.g. Hargreaves and Sharp, 1965) have found that the protons usually carry less than 10 % of the total precipitating energy.

4.3.2 Statistics of the Absorption Oval

The first question that faced workers in the riometry field was where do the particles that generate auroral absorption come from? Several workers (Holt *et al.*, 1961; Hartz *et al*.,1963; Driatsky, 1966; Hargreaves and Cowley, 1967; Foppiano and Bradley, 1984 and references therein) have investigated the statistics of auroral absorption from many latitudes and longitudes (Figure 4.2). Usually the diurnal occurrence shows two peaks, one close to magnetic midnight and the other before noon. Discrepancies arise due to the differing methods of compiling the statistics (Hargreaves, 1969). The absorption oval covers several degrees of latitude centred between 64° and 68° magnetic latitude, a few degrees equatorward of the auroral oval (Hartz *et al*, 1963; Basler, 1963; Driatsky, 1966; Hook, 1968). A notable effect is the deep minimum in the afternoon (Hargreaves and Cowley, 1967). Studies that employ direct particle precipitation measurements also demonstrate this pattern of dislocated ovals and local time variations (e.g. Hartz, 1971). Enhanced geophysical activity shifts the absorption zone to lower latitudes, affecting the night sector more than the day (Basler, 1963; Driatsky, 1966; Hargreaves, 1966; Hook, 1968). The diurnal pattern seen by a riometer is usually interpreted in terms of precipitation patterns fixed with respect to the sun, however there is possibly a longitudinal effect due to the displacement of the Earth's dipole from the spin axis. This effect has been looked for in the statistics (Hartz *et al.*, 1963 and Driatsky, 1966) but the results are inconclusive.

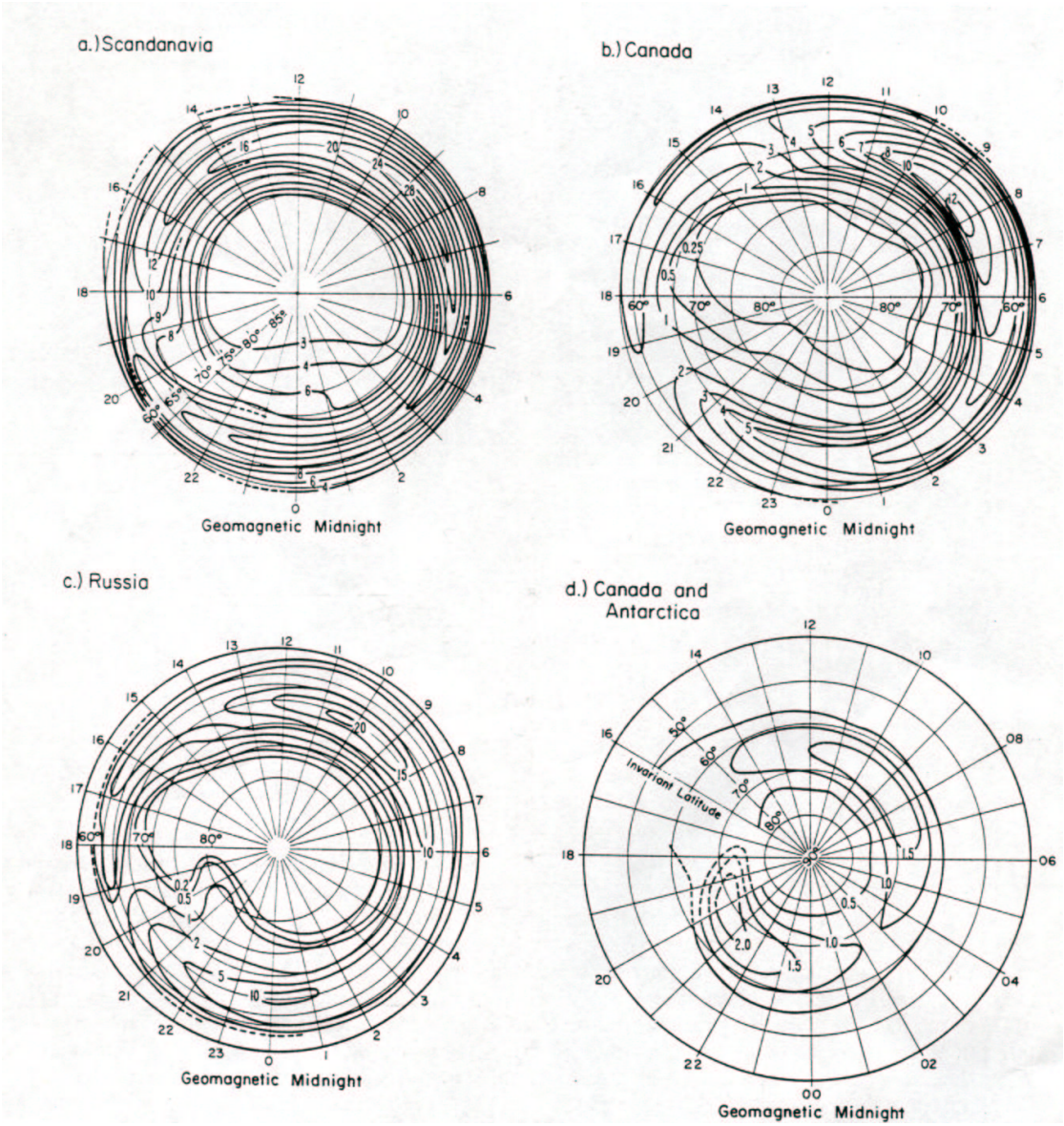

Figure 4.2. Occurrence of auroral absorption in latitude and time measured at several longitudes. (After a) Holt *et al.*,1961; b) Hartz *et al.*, 1963; c) Driatsky, 1966; d) Hargreaves and Cowley, 1967. (a) shows the percentage of time that absorption excedds 0.5 dB; (b) and (c) show the percentage of time that absorption equals or exceeds 1.0 dB and (d) gives the median intensity in dB.

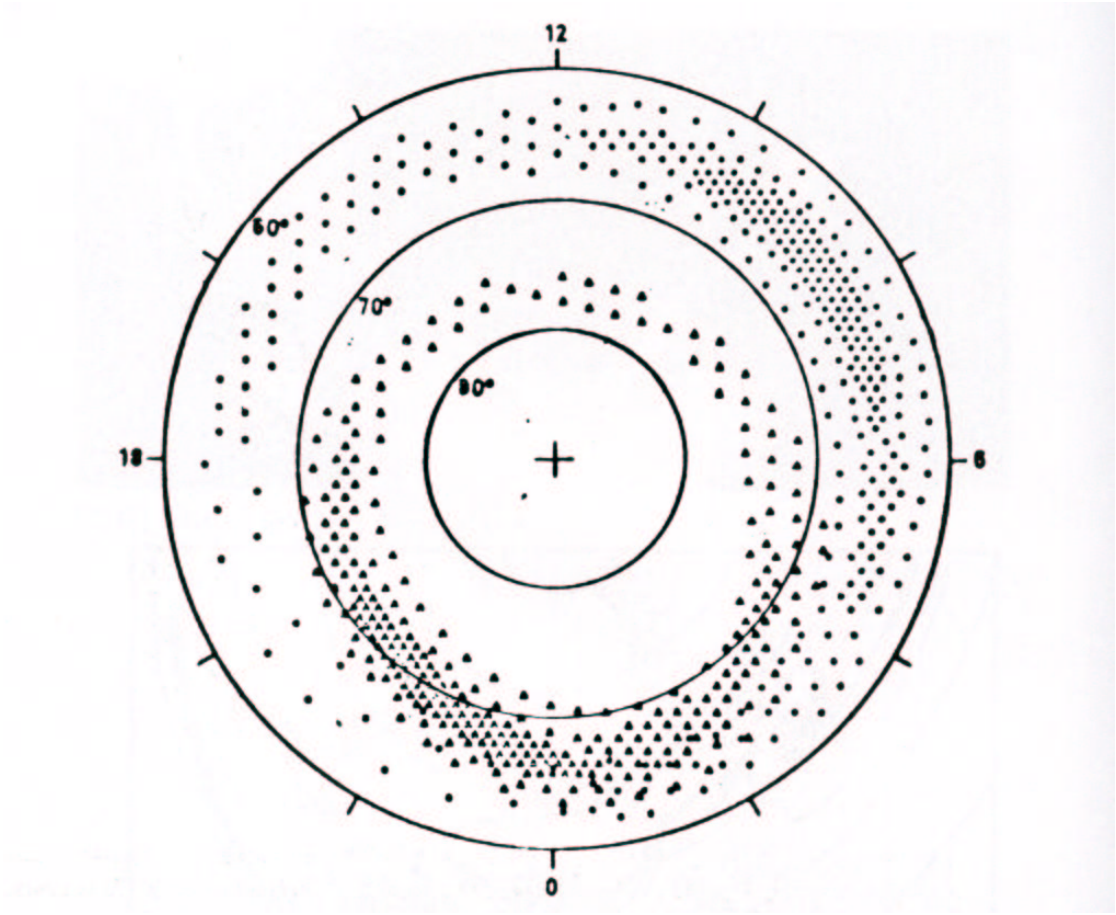

Figure 4.3. **Average pattern of electron precipitation as a function of magnetic latitude and local time. Note the two zones: auroral zone precipitation (medium energy) is represented by the triangles and high energy precipitation by the dots. The average flux is indicated approximately by the density of symbols (after Hartz, 1971).**

Driatsky (1966) reported less intense absorption in the Russian sector than in the North American sector, but differences in the solar activity at the time of observations result in ambiguity. Hargreaves *et al.* (1984) once again found little conclusive evidence of a longitudinal effect on the absorption statistics, suggesting that small changes in latitude could explain differences in the average absorption patterns.

The seasons have also been observed to affect the intensity and pattern of absorption, being 1.5 to 2 times greater in winter than in summer (Basler, 1966). It has been suggested that this is evidence of a dependency on the magnetospheric geometry (Hargreaves, 1969) but also possible changes in the ionospheric chemistry may affect the amount of electron density.

4.3.3 Substorms and Daytime absorption

The origin of the daytime maximum in absorption has been a point of study since it was first detected. Absorption in the day and night sectors have been compared by a number of workers (Parthasarathy and Reid, 1967; Hargreaves, 1967; Coroniti *et al.*, 1968) and it was found that day and night time activity tend to occur together with a delay of up to an hour before the morning absorption. The link between substorms and auroral absorption has been investigated by a number of authors (e.g. Hargreaves, 1974; Ranta *et al.*, 1981; Hargreaves *et al.*, 1997; and Hargreaves *et al.*, 2001) including phenomena such as spike events and pre-onset bays as well as the motion of absorption patches. Visual aurora and absorption have occasionally been found to coincide with good correlation (Holt and Omholt, 1962; Gustafsson and Ortner, 1962) however some studies show little matching between intense absorption and discrete forms (Kavadas, 1961). Ansari (1964) split absorption

observations into two main categories; the first consists of absorption that occurs between 20 and 02 MLT and that correlates well with luminous fluctuations in the 557.7 nm wavelength. Category two absorption is only observed post midnight, varies slowly with time and does not correlate with the luminous intensity (Figure 4.4). Later works have extended this second category to the absorption on the dayside (e.g. Stauning, 1996; Nishino *et al.,* 1999); thus the dayside absorption is taken to be an extension of the precipitation that begins on the night side. Absorption in the morning sector is a common occurrence (e.g. Hargreaves, 1969; Hargreaves and Berry, 1976) and has been linked to gradient curvature drifting electrons, injected on the night side during substorm activity (e.g. Stauning *et al.*, 1995b and Stauning, 1998), however some discrepancies between the theory and the observations still arise. Hargreaves (1968) determined that the drift velocities of the particles often did not agree with those expected for the necessary energy, and suggested that some form of propagating wave triggers precipitation of particles already present in the day sector (Figure 4.5). Jelly and Brice (1967) lend credence to this theory by observing that substorms are less likely to trigger day-side precipitation when the preceding period has been geomagnetically quiet. Hargreaves and Devlin (1990) used the EISCAT radar to investigate morning absorption and found that the energy dispersion predicted by curvature drift was not present (Figure 4.6). The debate over whether gradient-curvature drift is the primary mechanism responsible for the morning absorption is ongoing.

Finally it is worth mentioning the occurrence of ULF (Ultra Low Frequency) pulsations in the morning sector. This is a wide topic that will not be reviewed here

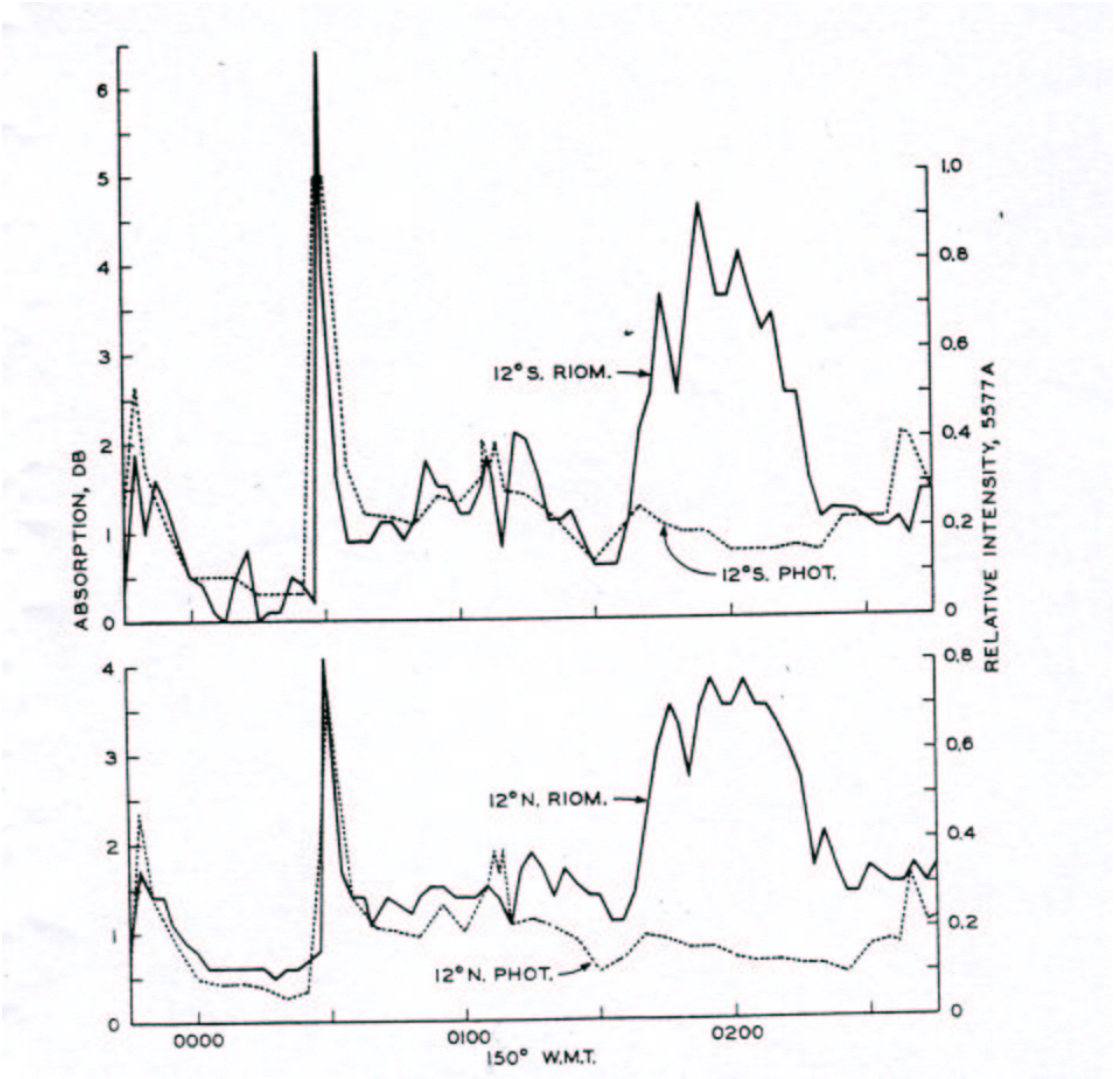

Figure 4.4. Variation of absorption measured by 12° S, N riometers and relative 557.7 nm intensity observed by 12° S, N photometers on October 25-26, 1962. The correspondence between auroral intensity and absorption is good until break up (From Ansari, 1964).

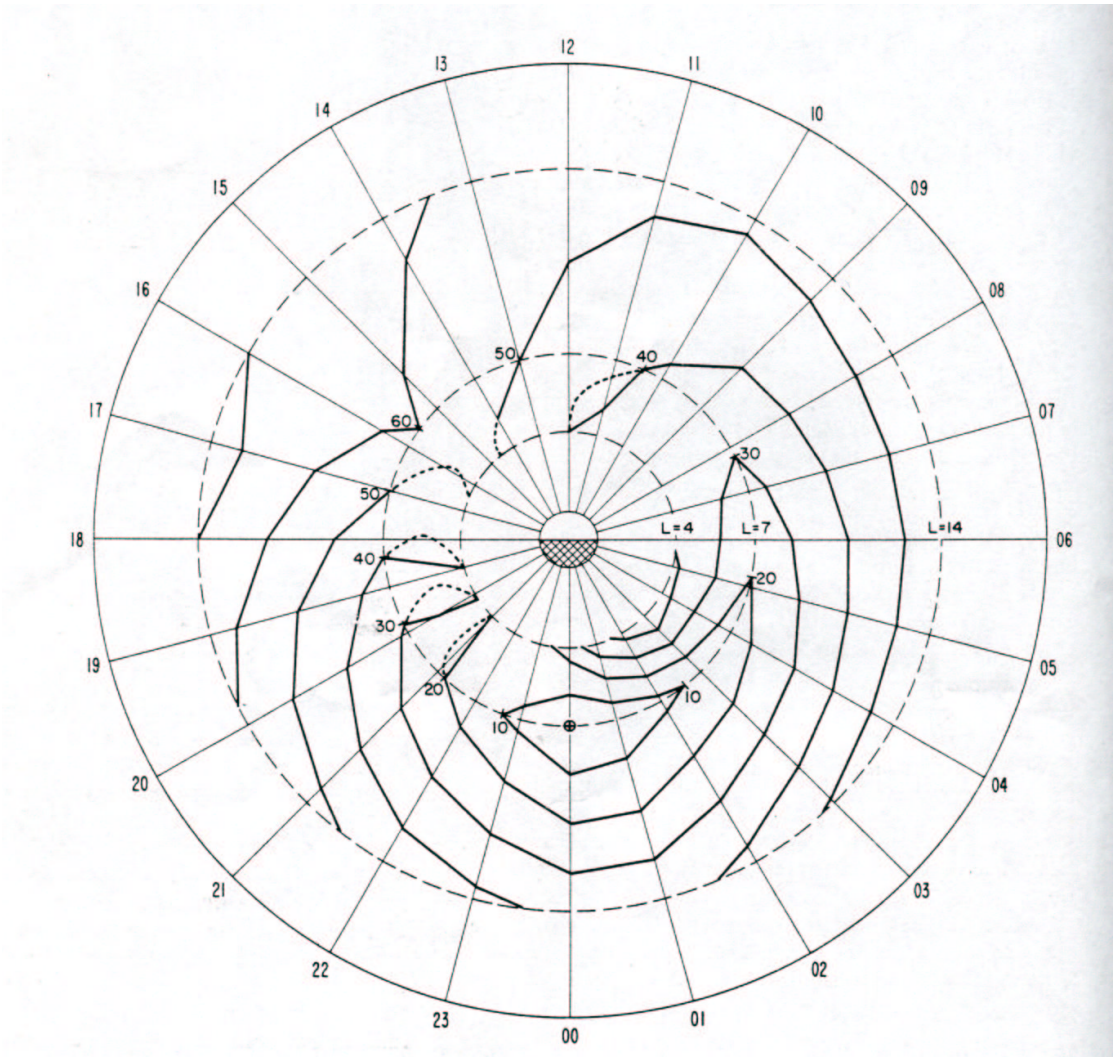

Figure 4.5. **Global movement of a median absorption onset projected to the equatorial plane. Wavefronts at ten minute intervals (From Hargreaves 1968).**

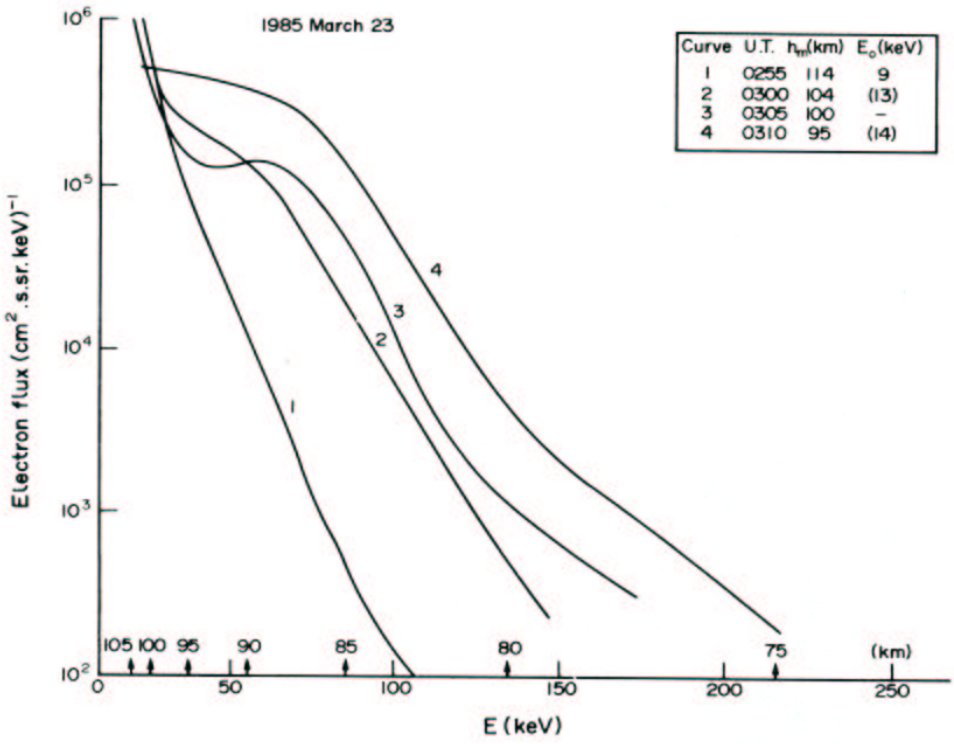

Figure 4.6. **Computed spectra of precipitating electrons corresponding to EISCAT measurements from 23 March 1985. Note that the hardest precipitation occurs some 15 minutes after onset.**

but both Stauning (1998) and Kikuchi *et al*. (1988) have observed slowly varying absorption events related to strong Pc4-5 pulsations. The links between the two are not clear but observations were first reported by Ziauddin (1960) and it has been suggested that the electron precipitation is being modulated by interaction with these longer period waves (e.g. Parthasarthy and Hessler, 1964; Barcus and Rosenberg, 1965; Coroniti and Kennel, 1970).

4.4 Polar Cap Absorption (PCA)

Having described the processes by which absorption is caused by geomagnetic radiation it is pertinent to review the next important contribution: Polar Cap Absorption. As described in Chapter 1, the open magnetosphere leads to direct access of solar wind particles to the geomagnetic cavity. These particles also display a pitch angle dependence that determines whether they precipitate into the ionosphere. Thus the low altitude polar cap and cusp regions will contain electron density that is due to the ionisation trails of solar wind electrons and ions (mostly protons). Under certain conditions very energetic particles can cross closed field lines and precipitate to lower latitudes than might be expected. This section describes the processes that produce these energetic particles and the ionospheric effects.

4.4.1 General features of polar cap absorption

Polar Cap Absorption (PCA) has come to refer to the range of ionospheric effects during the precipitation of energetic, solar originating particles; mostly protons with some heavy nuclei with energies in the MeV range (Reid, 1974). These effects were first identified following the major solar proton event of 23 February 1956, and

include the loss of signal on high-latitude VHF communication circuits (Bailey, 1957), sudden disturbance of phase and amplitude of LF and VLF radio signals (Allen *et al*., 1957; Belrose *et al*., 1956; Ellison and Reid, 1956; Pierce, 1956), as well as strong cosmic radio noise absorption.

It was found that events similar to February 1956 were relatively frequent, of the order of one per month. However other events did not necessarily produce the ground level increase in cosmic ray flux that occurred in the first event. These events were then determined to be due to bursts of particles from the sun with energies insufficient to reach ground level (Hultqvist and Ortner, 1959; Leinbach and Reid, 1959; Reid and Collins, 1959). Around the same time as these discoveries, Japanese workers (Hakura *et al*., 1958) described polar cap effects observed before major geomagnetic storms based on observations of blackouts recorded by ionospheric sounding equipment. Since then much work has been done to identify the main cause of the precipitating solar particles with arguments between those who support the propagation of solar protons following release through flares and those who favour shock acceleration of solar wind particles as the dominant mechanism (Krucker and Lin). Either way it is undisputed that energetic protons of >1 MeV are the principal cause of the polar cap absorption. Reid (1974) provides a comprehensive review of the early theory and observations surrounding Polar Cap Absorption events, including a discussion of the ionisation processes involved. As mentioned earlier one of the defining differences, as far as absorption observations are concerned, between auroral and polar cap absorption events is the spatial coverage. The following section reviews observations of how and why the polar cap absorption boundary changes in time.

4.4.2 The Cut-off Boundary

The earliest observations of PCA described the absorption region to be relatively uniform across the polar cap, reaching as far south as 60° magnetic latitude. Solar protons gain access to the magnetosphere at the pole and cross closed field lines to precipitate at much lower latitudes; this was first proposed by Störmer. Störmer theory is concerned with the motion of energetic charged particles in the magnetosphere. It was originally developed for the study of auroral particles but has proved more useful with solar protons due to their high energies. Because the solar protons are of such high energies, the magnetic field changes significantly over a single gyration, however particles travelling along the magnetic field are deviated least making the polar regions the most accessible. To reach lower latitudes a proton must cross closed field lines down to the atmosphere. Rigidity (momentum per unit charge * c/z), has been developed as a convenient measure for discussing the penetrative properties of a particle; all particles with the same value of rigidity will follow the same path in a given magnetic field. Störmer's analysis defined 'allowed' and 'forbidden' regions in the magnetosphere that could or could not be reached by a charged particle approaching the Earth from infinity. Thus there is a lower limit in latitude that is reachable by a particle of a given rigidity (the cut-off rigidity). Rigidity is usually measured in GV (10^9 Volts) and for a dipole field the relationship between the cut-off latitude and Rigidity is:

$$R_c = 14.9 \cos^4 \Lambda_c \qquad (4.1)$$

At invariant latitude Λ_c particles with rigidities greater than R_c can be observed, thus Stormer theory predicts that particles of all energies will gain access at the

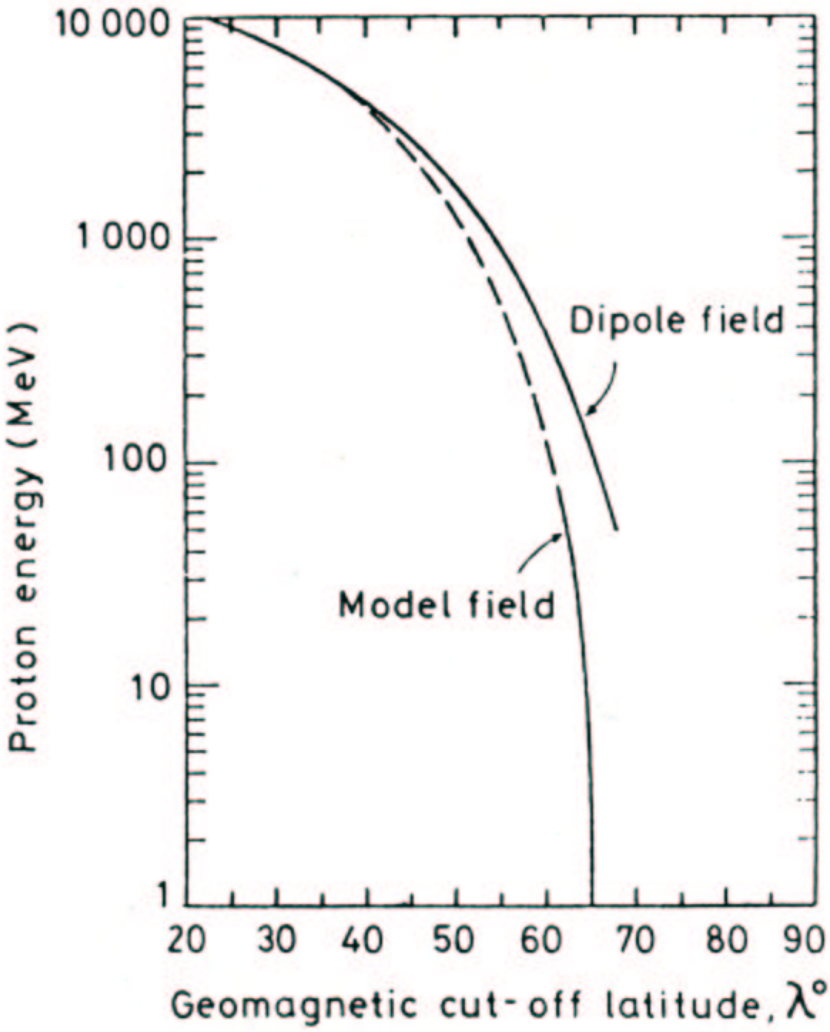

Figure 4.7. Variation of the geomagnetic cut-off latitude with proton energy for both a dipole field and a model geomagnetic field. Note that the model field reduces the latitude to which lower energy protons can reach (From Reid and Sauer, 1967).

geomagnetic pole and then the absorption will decrease steadily with decreasing latitude. Leinbach *et al.* (1965) found that the ratio of PCA at two latitudinally separated stations was about 0.8 under quiet conditions. Using a third riometer 3º equatorward, the ratio dropped to 0.3. These observations showed that PCA events display a broad polar cap plateau of roughly 50 degrees diameter with a steep edge of a few degrees in width –the cut-off boundary.

High altitude balloon experiments have been used as a means of determining particle cut-offs in the magnetosphere as far back as 1956. Waddington (1956) and Fowler *et al* (1957) used photographic emulsion experiments over Europe and North America to measure the cut-off rigidity of alpha particles. They found that the rigidity contours predicted by Störmer theory were significantly removed from the observations (± 3° latitude). Biswas *et al.* (1962) was able to construct a solar proton spectrum during the 3 September 1960 event from balloon measurements near Minneapolis (~45° geographic latitude). The lowest detected energy was ~200 MeV, however simultaneous measurements at Fort Churchill (Winkler *et al,* 1961) indicated that the spectrum extended down to at least 100 MeV. By comparing results it was clear that protons with energies >300 MeV were allowed at all latitudes from 45° upwards, however at 200 MeV only partial intensities were recorded. Further work at both sea level (e.g. Kodama and Miyazaki, 1957; Rothwell and Quenby, 1958) and aircraft altitudes (e.g. Katz *et al.,* 1958; Sandstrom,1958; Storey *et al*., 1958) together with measurements from neutron monitors (Pfotzer, 1958; Marsden and Wilson, 1958) indicated that the dipole field was inadequate to explain the observed cutoff rigidities and that the non-dipolar components of the field were important. With the increased interest in solar proton events after 1957, Freier *et al.,* (1959) were the first to measure

low rigidity solar protons at balloon altitudes following the event of 23 March 1958. These measurements and the observations from Anderson (1958) conclusively identified the particles as protons.

Polar orbiting satellites provided a boost for measuring the extent of the latitudinal cut off of both solar originating particles and galactic cosmic rays (e.g. Lin *et al* (1963); Quenby and Wenk (1962)). Stone (1964) found the quiet-time cut-off for 1.5 MeV protons to be as low as 67° invariant latitude, in conflict with Störmer theory, which predicted only energies exceeding 120 MeV could reach this latitude. For higher energy solar protons (>30 MeV) Akasofu *et al*, (1963) and Lin and van Allen (1964) reported measurements with quiet time cut-offs around 65° on average. The position of the cut-off boundary for a given energy is dependent on the position of the outer-zone trapping region (Reid and Sauer, 1967; Hoffman and Sauer, 1968; Leske *et al.*, 2001). A particle in a trapped orbit must have rigidity below the cut-off applicable to the field line around which it gyrates. Since a particle above this rigidity could reach the line from infinity, a similar particle on the field line must be able to reach infinity and thus could not be trapped (Reid and Sauer, 1967). More recently Leske *et al*. (2001) have used the polar orbiting satellite, SAMPEX, to investigate the variation of cut-off with both magnetic activity and also local time. Six separate solar proton events were used between November 1992 and November 1998. Significant variations in the cutoff locations for several particle energies (protons and helium from 8 to 64 MeV) were observed, often by ~5°-10°. These variations were compared with D_{st} and K_P indices as proxies for geomagnetic activity. In general the shapes of the time variations in the cut-offs correlate remarkably well with changing D_{st} and K_P (coefficients of 0.76 and –0.77 respectively).

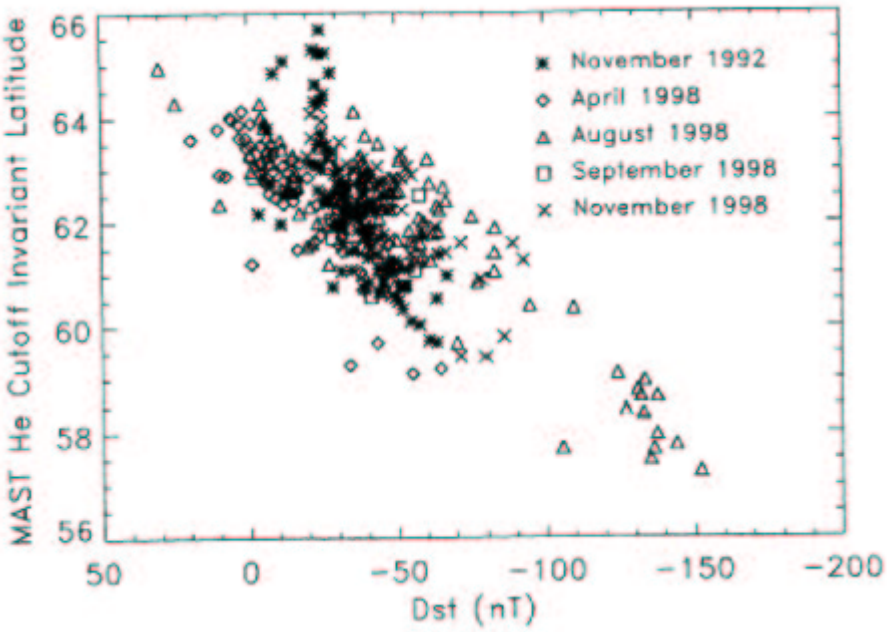

Figure 4.8. Orbit averaged cut-off invariant latitude for ~8-15 MeV/nucleon He plotted versus D_{st} to the same time as the cutoff measurement for the five time periods indicated (From Leske *et al.*, 2001)

A change in D_{st} by 200 nT or more will move the cut-off latitude by ~8°-10° for particles with rigidity of ~250-340 MV. However at certain times the indices significantly lead or lag the changing cut-off and have large deviations from the cut-offs, particularly at high values of D_{st}. The reason for this behaviour is not clear however the coarser resolution of K_P introduces an additional uncertainty. By correcting for D_{st} values, the local time dependence of the cut-off was determined. In the northern hemisphere this resulted in a circle of ~25.85±0.04° offset by 0.75±0.06° towards 2211 MLT. The southern hemisphere has a circle of similar size but the offset was greater and pointed towards an earlier local time (0.85±0.06° at 2113 MLT). Both cases point to the expected diurnal variation with a maximum cut-off latitude occurring in the morning sector and a minimum pre midnight. The observations by Leske *et al* (2001) agree with those made by Faneslow and Stone (1972) where a variation of < 2° was found with local time.

The cut-off boundary may also play an important role in the signature of absorption from riometers close to those latitudes. The following section investigates a phenomenon that has often been attributed to the diurnal variation in the cut-off: the midday recovery.

4.4.3 The midday recovery

Leinbach (1961) was the first to discover and describe the so-called Midday Recovery. This recovery is a decrease in polar cap absorption observed on the day side near the edge of the polar cap and the principal features of the recovery were defined by Leinbach (1967). Midday recoveries occur within the local time range of 0800 to 1500 with most between 1000 and 1200 LT and total duration at a single

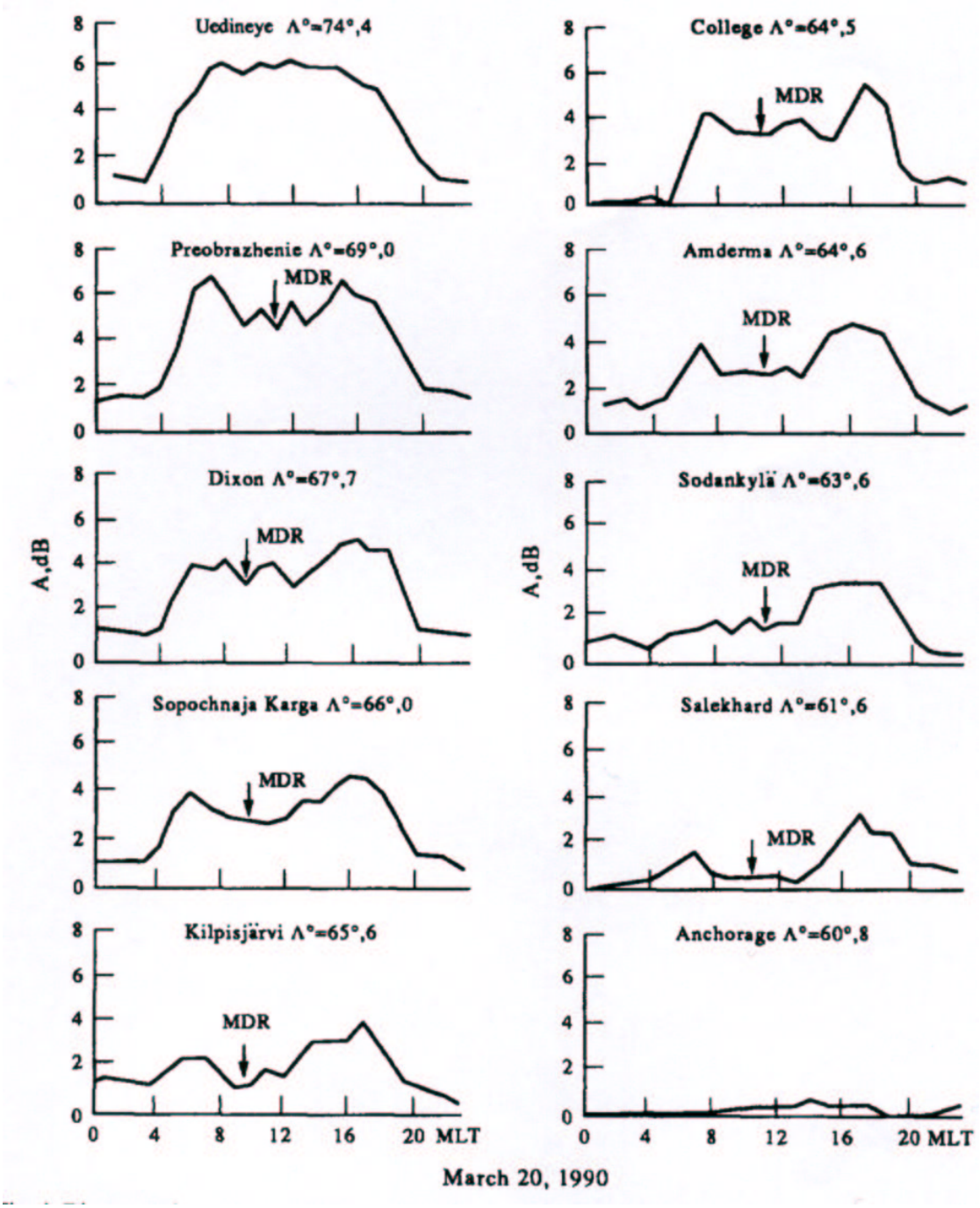

Figure 4.9. Riometer absorption on 20 March 1990 as seen at different stations of the northern hemisphere. The Midday recovery is marked on each plot when identified (Uljev *et al.*, 1995).

riometer station may be as long as 6-10 hours (Figure 4.8). . The magnitudes of the recoveries are latitude dependent, with a greater drop in absorption evident at the edge of the cut-off boundary. This remains true during magnetic storms when the cut-off boundary expands equatorward, the midday recovery also occurs at the lower latitudes. These properties suggest that the recoveries are the result of an effective increase in the rigidity of the bombarding particles during the local morning hours near to the edge of the polar cap region. Two principle mechanisms have been suggested for the reduction in absorption: The development of an anisotropic pitch angle distribution of the protons leading to reduced precipitation around noon, and a general increase in the cut-off latitude at noon due to the configuration of the magnetic field.

Taylor (1967) calculated trajectories for low energy solar protons (1.2 MeV) using the Taylor and Homes (1965) model magnetosphere. He found that protons with this energy would reach magnetic latitudes of 65°-75° only if the pitch angles at 2000 km altitude were very large. This supports the theory of a depleted loss cone for the low energy protons on the day side of the polar cap (Leinbach, 1967). Paulikas *et al* (1968) reported an anisotropic distribution of solar protons at invariant latitudes less than 75° around noon during the PCA of 2 September 1966. The increase in cut-off latitude for a given rigidity is supported by Reid and Sauer (1967). As described in a preceding section, the existence of the geomagnetic tail leads to a day night asymmetry in the trapping boundary. If the region of solar bombardment is dependent on the position of the open-closed field line boundary then a similar day night asymmetry will be seen in the cut-off latitude (Hoffman and Sauer, 1968). The anisotropy theory was also contested by Burrows (1972) after making direct

measurements of the solar proton pitch angles during several PCA using the ISIS-1 satellite. No anisotropy was detected at latitudes less than 65°.

The contributions of both processes have been studied by Uljev *et al* (1995) using a case study of the event of 19-21 March 1990. Morphological features of the event were described and in particular the area affected by the midday recovery was found to be 10° of invariant latitude with two separate regions below and above 65° latitude in which properties of the recovery are different. Above 65° a combination of anisotropic flux of protons and the diurnal variation in the cut-off latitude results in a shorter recovery and smaller amplitude. Below 65° it is suggested that the diurnal variation is dominant. These conclusions support the previously conflicting observations of Burrows (1972) and Paulikas *et al* (1968). The effect can be explained by considering the portions of the energy spectrum that result in the absorption at the different latitudes. At lower latitudes proton energies of 30-100 MeV control the absorption due to their cut-off rigidity, whereas the 1-30 MeV protons dominate above 65°. Schöler (1975) found experimental evidence that pitch angle anisotropy is a typical feature of solar protons with energy less than 30 MeV but not of higher energy protons.

However neither of the explanations can explain the occurrence of observations of the midday recovery. Leinbach (1967) identified midday recoveries in only 20% of the PCA events between 1957 and 1961. Uljev (1978) and Uljev *et al.* (1995) determined that only solar proton fluxes with a relatively soft energy spectrum (characteristic rigidity of less than 100 MV) will produce a midday recovery. Thus if hard events occur, no midday recovery will be observed. Another important factor is the level of geomagnetic activity (Driatsky, 1974). An increased level will prevent

reliable identification of the midday recovery due to the enhanced auroral precipitation. The 20% occurrence described by Leinbach has been challenged by Ranta *et al* (1995). Using observations from densely spaced riometer chains from 1989-1991, the midday recovery was found to occur in at least one station during all days of each PCA event. This supports the diurnal variation of the cut-off boundary as the dominant cause of the midday recovery, a position supported by Hargreaves *et al* (1993).

4.4.4 Chemical Effects: The diurnal variation, twilight anomaly and recombination rates

The most striking effect of the mesospheric chemistry on PCA is the diurnal variation exhibited as decay in absorption during the hours of darkness. Gillmor (1963) demonstrated that with similar proton fluxes, such as in geomagnetically conjugate stations, absorption levels were similar when both regions were sunlit. However the absorption dropped considerably at night. The cause of this day-night variation is the variation of the electron-negative ion ratio (λ), i.e. chemical in nature rather than geophysical as the diurnal change in the cut-off boundary. In Chapter 1 it was explained that in the lower D layer the attachments of electrons to neutral species is the dominant loss mechanism and as seen in Chapter 2 ionospheric absorption is dependent on the electron density, thus an increase in λ leads to a decrease in absorption. From earliest observations the night time recovery was attributed to chemical changes involving O_2 and ultimately water cluster ions (Fehsenfield and Ferguson, 1969) and particularly the process of photodetachment. Much study has been made of the transition through twilight and the rate of decay of absorption with

the solar zenith angle. It was found that approximately half of the sunset decay takes place while the shadow of the Earth moves from ground level to 40 km identifying the detaching radiation as Ultra Violet rather than visible light; the ozone layer at ~35 km altitude heavily absorbs UV. Originally O_2^- was thought to be the dominant species involved in the transition, however if UV is the influential radiation then the photodetachment takes place from a more tightly bound negative ion.

Progress in studying the chemical changes in the lower ionosphere was advanced with the introduction of incoherent scatter radar observations. In theory the excess ionisation in the D layer during solar proton events provides a good incoherent scatter signal at altitudes lower than during the more usual auroral electron precipitation events (Turunen, 1996). The EISCAT radars have been used to determine the temporal behaviour of the negative ion to electron density ratio, λ (Rietveld and Collis, 1993). During the sunset on 23 October 1989 the incoherent scatter spectrum is seen to widen with increasing solar zenith angle for all altitudes below 70 km. By modelling the spectral width values for different values of ion mass the authors illustrated a discrepancy between the measured and theoretical values. Similar observations were made by Hansen *et al* (1991) and Tepley *et al* (1981) with the measured spectra being noticeably narrower than the calculated ones. Further work by Collis and Rietveld (1998) using the EISCAT VHF radar produced similar effects with narrowed spectral widths compared to model predictions. This rules out the possibility that the radar frequency is a factor in explaining the discrepancy. The reason for this discrepancy is still unclear, but it highlights the need for detailed theory and models of the D region for interpreting incoherent scatter signals. Progress has been made in this area using detailed ion chemistry models such as the six ion scheme

by Mitra and Rowe (1972) and more recently by a 35 ion model (e.g. Burns *et al*, 1991; Turunen, 1993). This approach uses the spectral width and the raw electron density data supplied by EISCAT as inputs to determine parameters such as λ, mean ion mass, neutral temperature and ion concentrations. Comparisons of the model temperature results for the 14 August 1989 PCA event with data collected by a LIDAR at Andoya (Hansen *et al*, 1991) show a close match, including a sharp gradient above the mesopause in the temperatures. Discrepancies in the heights of the mesopause may be due to the separation of 129 km between the LIDAR and EISCAT.

In 1989 13 separate experiments on the EISCAT UHF radar partly covered seven solar proton events between March and December (Collis and Rietveld, 1990). Electron density data could be analysed from as low as 54 km altitude on one occasion. During four separate twilight periods the electron density variations were observed (23-25 October), allowing a detailed comparison of the sunset and sunrise periods. A marked asymmetry was observed as a delay in the build up of the electron density at altitudes below 70 km during sunrise. During sunset a linear dependence on solar zenith angle was found for the initial time of the electron density decrease at each altitude. Corresponding behaviour was seen during sunrise above 70 km. Chemical information was deduced from consideration of the Earth's shadow height and the delay in electron density build up. The dominant negative ion was deduced to be a high affinity ion such as NO_3^-, instead of the primary negative ion O_2^-. The thirty-minute delay in build up below 70 km was tentatively attributed to the build-up time of neutral O_2. It was concluded that either the loss of O_2^- in collisional detachment with $O_2(^1\Delta_g)$ would be the dominant loss process, or reactions of negative ions with atomic oxygen would produce O_2^- which is easily photodetached.

Reagan and Watt (1976) used the Chatanika incoherent scatter radar to estimate the effective recombination rate coefficient by combining electron density observations from the radar with proton flux data from a polar orbiting satellite during the intense solar proton event of August 1972. Hargreaves *et al* (1987) used the EISCAT UHF radar to perform a similar investigation during an event in February 1984. The altitude profile of the recombination rate was consistent with a transition from simple molecular ions to hydrated ions in the lower ionosphere. A gradual decrease of the recombination rate coefficients occurred at all altitudes during three hours around noon in both studies. This has been interpreted as a progressive change in D-region photochemistry but further interpretations were not attempted.

Effective recombination rate coefficients were also estimated by Hargreaves *et al* (1993) for the PCA of 19-21 March 1990. The calculation was performed in a similar manner as explained by Hargreaves *et al* (1987) however this time scatter from the EISCAT VHF radar was used between heights from 60 to 80 km. The estimated effective recombination rates show a large variation with time of day, increasing rapidly with night at the lower altitudes, consistent with the formation of negative ions. Just as Collis and Rietveld (1990) the authors used the Earth's shadow height to deduce that ultra violet light (UV) is responsible for the photodetachment process in the lower D region. In effect at high solar zenith angles the ozone layer at 35 km altitude acts as a filter, reducing the UV incident upon the D region at the horizon.

The EISCAT UHF electron density data has been used to derive proton energy spectra at the top of the atmosphere (Hall *et al.*, 1992). During the August 1989 solar proton event the overall time behaviour of the integrated spectra was similar to the spectra observed by the GOES-7 satellite at geostationary orbit. The authors note that

their treatment did not include the correction for other possible ionisation sources and the choice of the effective recombination rate coefficient might have led to the observed differences in detail. Other workers have used proton measurements from polar orbiting satellites to determine an empirical relationship between the precipitation flux and the absorption observed by riometers in the polar cap Davies (1990) states that polar cap absorption events are related to integral proton fluxes of energies greater than 20 MeV. Potemra (1972) determined that the absorption is proportional to the square root of the flux and is most affected by protons with energy > 15 MeV, which produce their greatest ionisation at a 65 km altitude in the D layer.

4.5 Summary

In this chapter, results relevant to the precipitation of energetic particles in the auroral zones and particularly riometer measurements have been reviewed. The observations and causes of auroral absorption have been discussed along with the phenomenon of Polar Cap Absorption. It has been shown that much work in the riometry field has been done since its inception in 1958, however with more refined technology and with the support of complementary observations from satellites, radars and other instruments much more can be done. Chapters Five, Six and Seven of this thesis present observations of auroral and polar cap absorption.

Chapter 5

Absorption in the dayside ionosphere – case study

5.1 Introduction

In this chapter an investigation of a case of dayside auroral absorption is presented. This event occurred on the 11 February 1997 and consisted of significant but slowly varying absorption in the morning sector (post 06:00 UT) continuing past 12:00 MLT into the afternoon. The EISCAT mainland UHF radar monitored the whole event providing estimates of the electron density for altitudes upward of ~65 km, supporting the observations from the imaging riometer for ionospheric studies (IRIS) at Kilpisjärvi. Due to a number of passes of DMSP spacecraft, providing spectral information, the precipitation of particles is directly observed at the same time as wave structure is remotely monitored by ground based pulsation magnetometer. By considering the chain of riometers operated by Sodankylä Geophysical Observatory the gross latitudinal movement and development of the absorbing region is investigated. Comparisons are made between the movement of the absorption patch with F layer convection derived from the CUTLASS HF radar. Finally the event is placed in a global context by considering the simultaneous night side observations of substorm activity, monitored by the CANOPUS array of instruments.

Four main topics are addressed: the solar control of precipitation; substorm related particle drifts; ionospheric flow changes; changes from electron to predominantly ion precipitation.

5.2 Observations

The following sections describe the observations taken during the event on the 11 February 2002. This includes observations of the solar wind and IMF close to Earth from the GEOTAIL satellite, ground based observations from Fennoscandia, satellite measurements of precipitating particles and night side observations from the Canadian sector.

5.2.1 Solar Wind Measurements –GEOTAIL

The interval preceding 11 February 1997 was particularly active. A large magnetic cloud had passed the Earth on the 10 February and the interplanetary magnetic field (IMF) had been highly variable throughout the preceding week with high solar wind speeds up to ~650 kms^{-1} at the L1 point. By the time of the event presented here (06:00 to 12:30 UT, 11/2/1997) the solar wind speed had slowed to around 450 kms^{-1} and continued to slow throughout the day reaching a low of 400 kms^{-1} by 11:40 UT.

Figure 5.1 shows the northward (B_z) and eastward (B_y) components of the IMF together with the dynamic ion pressure during the event. The data come from the GEOTAIL satellite (Kokobun *et al.*, 1994; Mukai *et al.*, 1994) that was moving duskward in the solar wind from (10.1, -0.8, 0.6) to (9.2, 8.7, 1.32) Earth Radii in geocentric solar magnetospheric (GSM) coordinates. This suggests that the satellite was in the magnetosheath, between the bowshock and the magnetopause. The timing

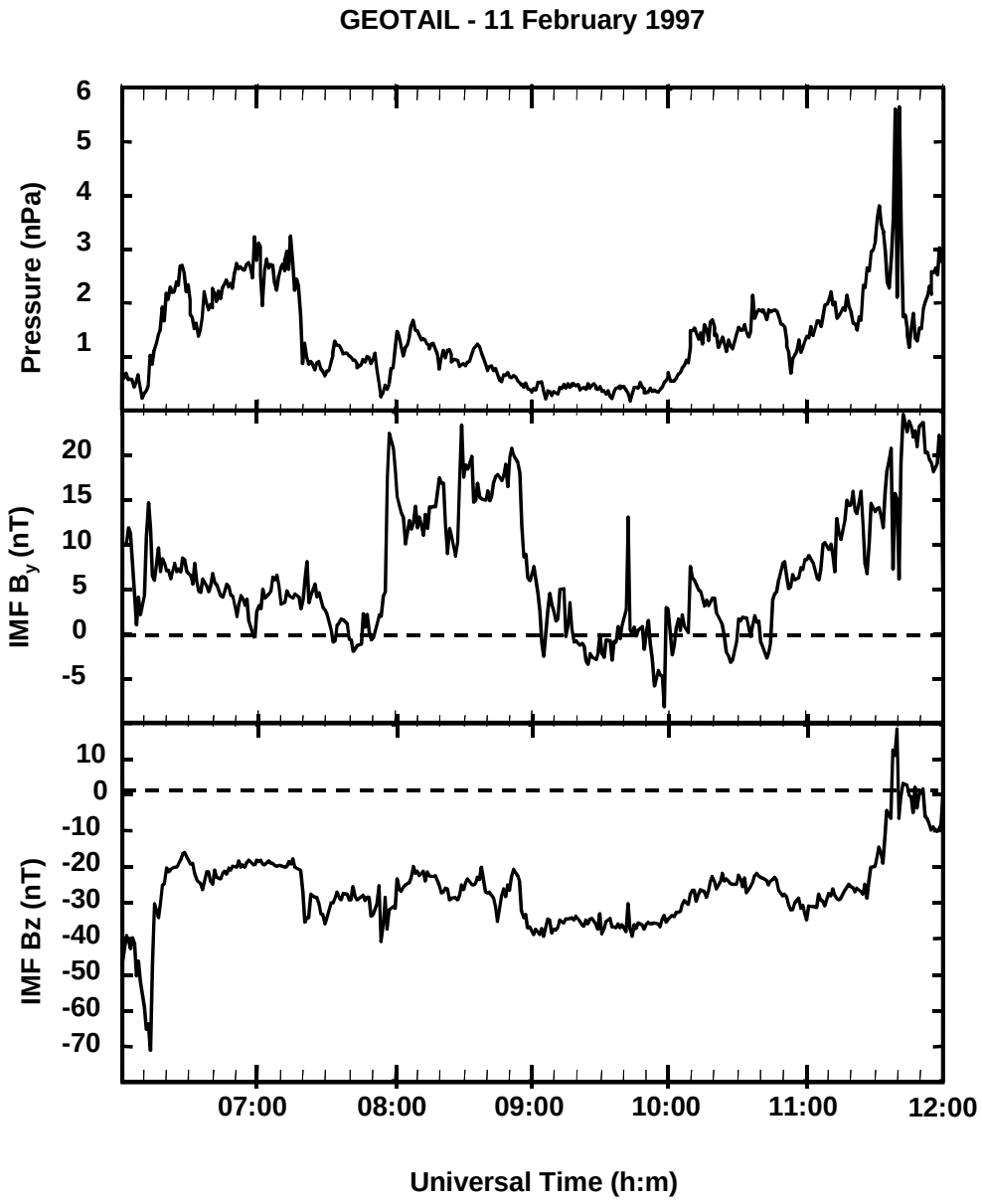

Figure 5.1: Solar Wind data taken from the GEOTAIL spacecraft. The satellite was crossing the front of the magnetopause at 10 R_e for the duration of this event. The panels illustrate (top to bottom): predominantly negative IMF B_Z, positive IMF B_Y, and the low solar wind dynamic pressure

from the magnetopause to the foot of the ionosphere is estimated to be approximately 2 minutes (Stauning *et al.*, 1995a). Data from the satellite is available from 06:00 UT to 12:00 UT.

The dynamic pressure is relatively low throughout the event, reaching a maximum of 5.8 nPa at 11:40 UT, but remaining mostly below 3 nPa. A rise of 2.4 nPa occurs over 15 minutes around 06:10 UT. A peak of 3.1 nPa occurs at 07:00 UT. A number of small steps (positive and negative) in pressure follow this first rise with a general decline to ~0.5 nPa. Pressure again increases after 10:00 UT and remains variable over short time scales, never exceeding 6 nPa by 12:00 UT. B_Y shows an eastward tendency at the start of the event with a gradual westward turning; B_Y drops from +15 to –1 nT by 07:40 UT. An abrupt eastward swing begins at 07:50 UT reaching a maximum of +23 nT at 08:00 UT. Values fluctuate between +10 and +23 nT for the next hour before once again swinging westward to –2 nT at 09:05 UT. The eastward component then varies about zero until 10:45 UT when a gradual eastward turning occurs, reaching a maximum of +25 nT at 11:45 UT.

The northward component of the IMF was strongly negative at the start of the time series. A short drop from –40 to –70 nT accompanied a drop from +12 to +1 nT in B_Y at 06:10 UT. This quickly recovered to –22 nT in the B_Z component and remained relatively steady around –20 nT until 07:20 UT. A short drop in B_Z to –35 nT preceded variations of ±8 nT about –31 nT until shortly before 09:00 UT when B_Z decreased again. Following this more southward turn (-40 nT) there was a slow northward motion of the IMF, increasing after 11:30 UT to make a northward excursion that lasted a couple of minutes at 11:40 UT.

5.2.2 Ground based Observations -EISCAT, IRIS and pulsation magnetometer

Figure 5.2 shows the time series from three ground-based instruments starting from 06:00 UT (08:10 MLT at EISCAT) on 11 February 1997. The top panel shows raw electron density values between 65 and 180 km measured by the EISCAT radar, uncorrected for the electron to ion temperature ratio. This correction is not expected to be important at E region heights and below where $T_e \sim T_i$, unless significant joule or ion frictional heating occurs. In this event the ion and electron temperatures remained at background levels for most of the duration apart from a slight increase between 11:00 and 12:00 UT which will not be discussed here. The centre panel contains the cosmic radio noise absorption from beam 16 of IRIS, measured in decibels (dB). Beam 16 intersects with the field aligned UHF radar beam in the D region. A spectrogram from the search coil magnetometer co-located with IRIS at Kilpisjärvi is presented in the bottom panel. The intensity (arbitrary units) of pulsation activity is illustrated for frequencies from 0 to 1 Hz.

A substantial enhancement in electron density occurs from 06:20 UT. This is located in a height band of ~83 to 116 km. The density enhancement maximises at $\sim 2.2 \times 10^{11}$ m^{-3} and lasts until 06:40 UT. Cosmic radio noise absorption is approximately proportional to the height-integrated product of the effective collision frequency and the electron density in the D region (chapter 2, section 2.3.3), thus there is a sharp 1 dB rise at 06:20 UT. The northernmost beam of IRIS observes an increase of 1 dB at 06:15 UT, which then expands equatorward, covering the whole field of view by 06:50 UT; apparent from an inspection of the multi-beam data. A second peak in the ionospheric electron density ($\sim 1.7 \times 10^{11}$ m^{-3}) occurs around 07:00

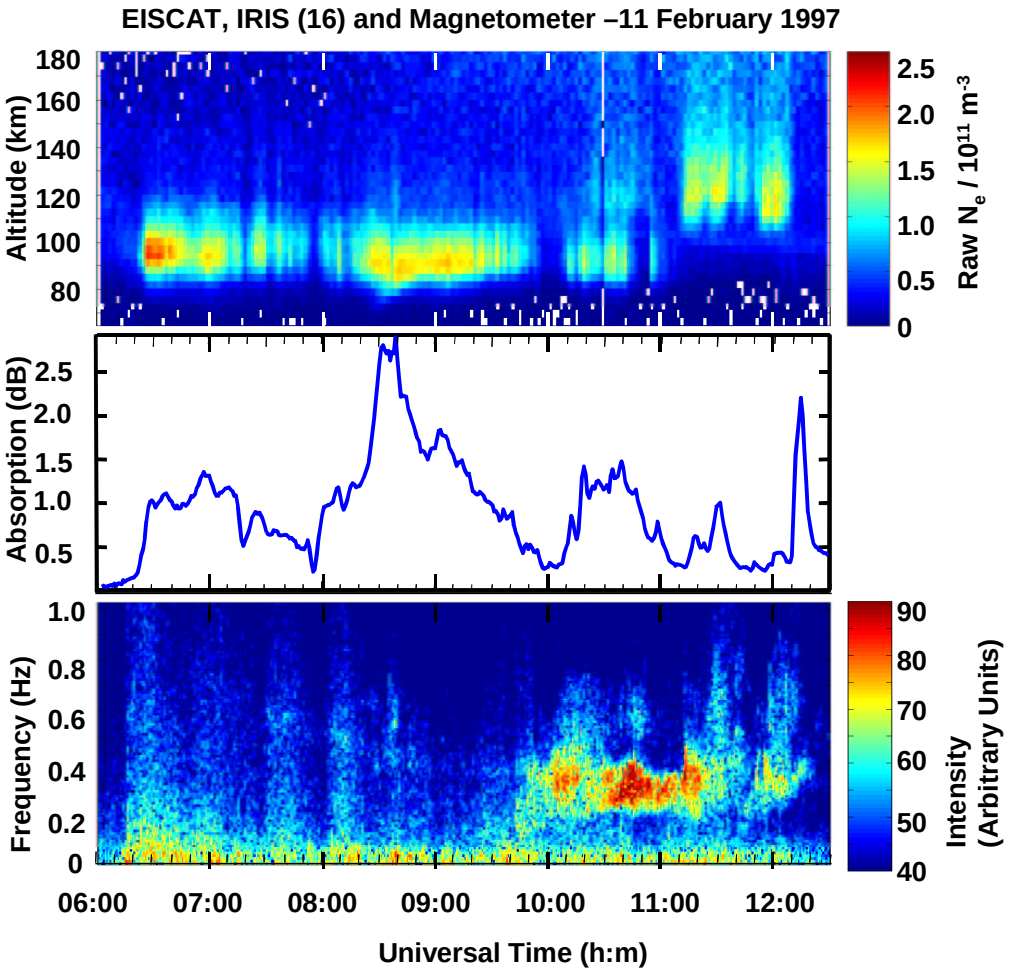

Figure 5.2: **The top panel shows the EISCAT raw electron density, scaled from the returned power. The middle panel shows the absorption time series from beam 16 of IRIS. The bottom panel is a spectrogram from the pulsation magnetometer at Kilpisjärvi with arbitrary units of intensity.**

UT. There appear to be 4 distinct bursts of structured density between 06:00 and 08:00 UT (06:30, 07:00, 07:15 and 07:30 UT) with successively decreasing maxima and narrowing height ranges. The peaks of the enhancements last for 10-15 minutes. IRIS recordsmatching peaks between 0.6 and 1.3 dB. After 08:00 UT another increase occurs (1.3×10^{11} m^{-3}) lasting for ~10 minutes. This precedes a large, long duration, increase in electron density at 08:15 UT. At 08:35 UT the density reaches to a lower altitude of ~77 km, before gradually rising to the previous altitude limits, corresponding with high absorption (3 dB). Electron densities remain greater than 10^{11} m^{-3} until 09:50 UT with an increasing lower altitude limit. This is reflected in the riometer time series as a gradual decrease in absorption. From 10:00 UT a change in the altitude spread of the electron density occurs (Figure 5.2, top panel). Enhancements range from ~80 km to 130 km altitude, with lower density values. The absorption peaks at about 1.4 dB due to the extended height range of electron density. Around 11:00 UT the ionosphere starts to lift so that by 11:12 UT most of the D region density has disappeared. Instead there are strong concentrations ($>1.5\times10^{11}$ m^{-3}) in the E region with 'tails' extending into the lower F layer. These appear to occur in 4 short and narrowly separated bursts, each lasting 10 to 15 minutes. The absorption over EISCAT is relatively low, with the exception of a short duration 1 dB spike at 11:30 UT. A sharp cut-off in electron density occurs shortly after 12:10 UT and densities then remain low until late evening. The large spike in the absorption data at 12:15 UT is due to a drifting, narrow arc that is partly covered by beam 16 but does not pass through the much narrower beam of EISCAT. At 11:12 UT the magnetometer observes structured pulsations covering the range of 0.2 to 0.5 Hz with the upper limit gradually rising to 1 Hz and the lower limit increasing to 0.4 Hz over

the next 30 minutes. This structure is repeated at 11:50 UT and coincides with northward turnings of the IMF. The first of these is clear in the data from GEOTAIL (Figure 5.1).

Throughout the precipitation event the Finnish search-coil magnetometer at Kilpisjärvi observes intense pulsations particularly in the < 0.2 Hz range (Figure 5.2, bottom panel). From 06:00-10:00 UT there are low intensity pulsations of <1 Hz, with a maximum below 0.4 Hz. There is some time coincidence with the bursts of electron density with the pulsations lasting for 10 to 15 minutes and separated by ~10 minute intervals. The weakest burst of pulsations coincides with the large increase in absorption at 08:40 UT. After 09:45 UT there are much more intense, continuous pulsations occurring in the frequency range of 0.2 to 0.6 Hz. This frequency band narrows over the next 90 minutes.

The spatial development of the absorption over EISCAT can be ascertained from the keogram in Figure 5.3. The keogram is a slice across the field of view at constant geographic longitude (19.2°). The equatorward expansion at 06:15 UT is clear and the large increase at 08:40 UT seems to occur simultaneously in all beams. A northward drift of the absorbing region is visible in the keogram after 09:40 UT with the most intense absorption being confined to the south end of the field of view, away from EISCAT. A patch of absorption at 11:10 UT drifts poleward and westward with levels exceeding 3 dB. A second patch follows at 11:30 UT, this one extending further north (66.4° Mlat). The arc of absorption at 12:15 UT meanders poleward as well, but as discussed earlier, it does not enter the EISCAT radar beam.

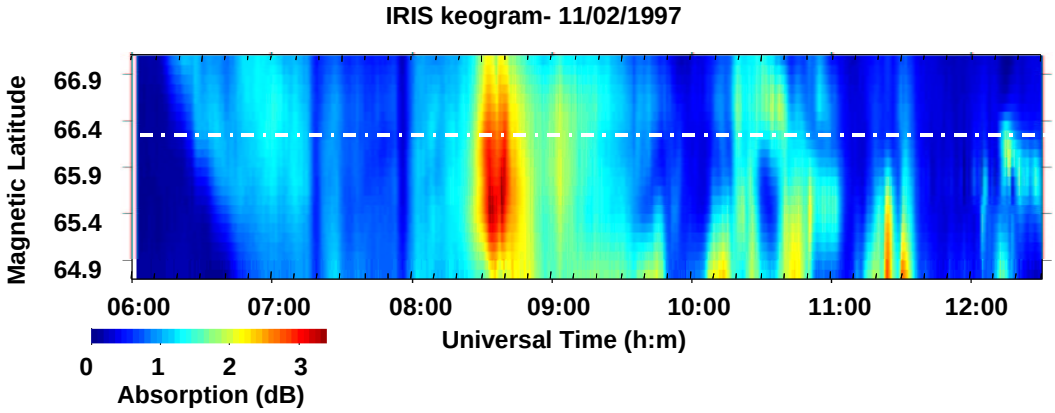

Figure 5.3: **Keogram taken at constant geographic longitude. The image is a composite from the IRIS beam data and includes beam 16 that overlaps the field aligned EISCAT radar beam in the D region. The dashed white line indicates the latitude of EISCAT.**

5.2.3 Ground Based Observations –The SGO riometer chain and CUTLASS

The motion of absorption observed in the riometer (Figure 5.3) indicates that the precipitation region is moving in the ionosphere. The F region irregularity velocities provides a window to view the convection of the magnetospheric field lines. Figure 5.4 displays the line of sight velocities from beam 5 of the CUTLASS Finland radar that passes over EISCAT. Negative values represent velocities away from the radar site and the dashed horizontal line indicates the latitude of EISCAT. The lack of data from Iceland East means that velocity vectors are not available for 06:00 to 12:30 UT, but beam 5 points approximately meridionally. The scatter is patchy for much of the event, however the velocities after 11:00 UT are high (sometimes reaching >800 ms^{-1}) and increase in the westernmost beams. The eastern beams show lower velocities at this latitude, even turning equatorward in the easternmost beam. This indicates that EISCAT is in a region of strong ionospheric return flow as the field lines convect poleward towards the cusp and across the polar cap. Velocities previous to this tend to be low (± 200 ms^{-1}) as the direction of dominant flow is most likely perpendicular to the radar line of sight.

Larger scale observations of the development of the precipitation region can be obtained from the SGO chain of riometers. Figure 5.5 is a stack plot of the riometer data, incorporating the IRIS wide beam. The top panel is from the Hornsund instrument located at the southern tip of the largest island of the Svalbard archipelago. The remaining instruments are on the mainland and are ordered in descending magnetic latitude; the Y-axis divisions are 0.5 dB. For the purpose of direct comparison, the data have been scaled according to frequency to match the level of a 38.2 MHz riometer.

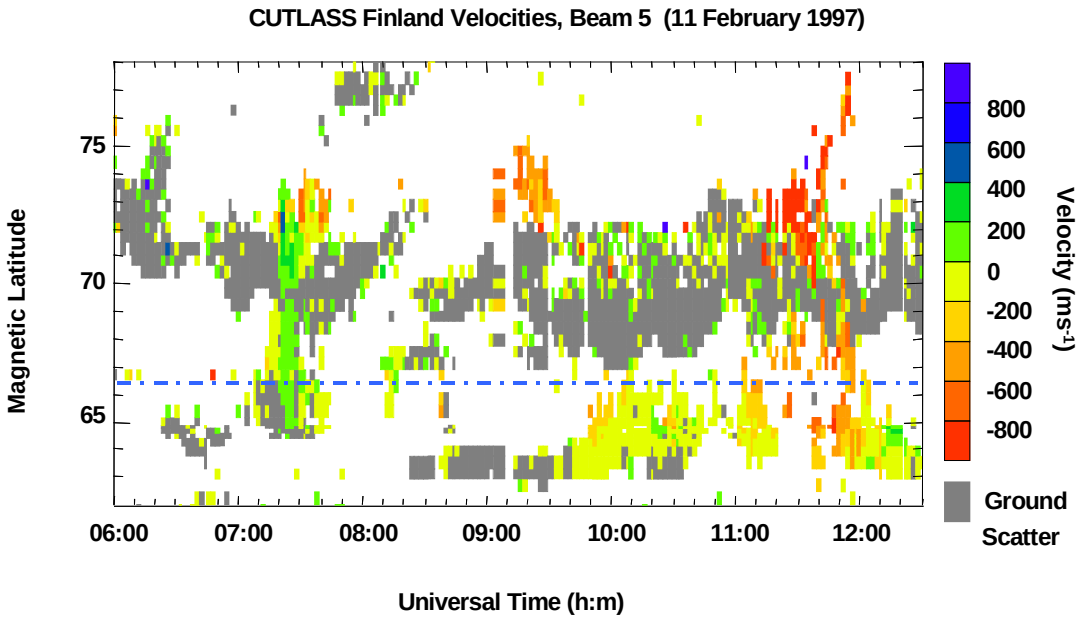

Figure 5.4: **Line of sight velocities from beam 5 of the CUTLASS Finland HF radar. Negative velocities are away from the radar site (approximately poleward). The radar was operating under normal scanning mode for this period. The horizontal dashed line indicates the latitude of EISCAT.**

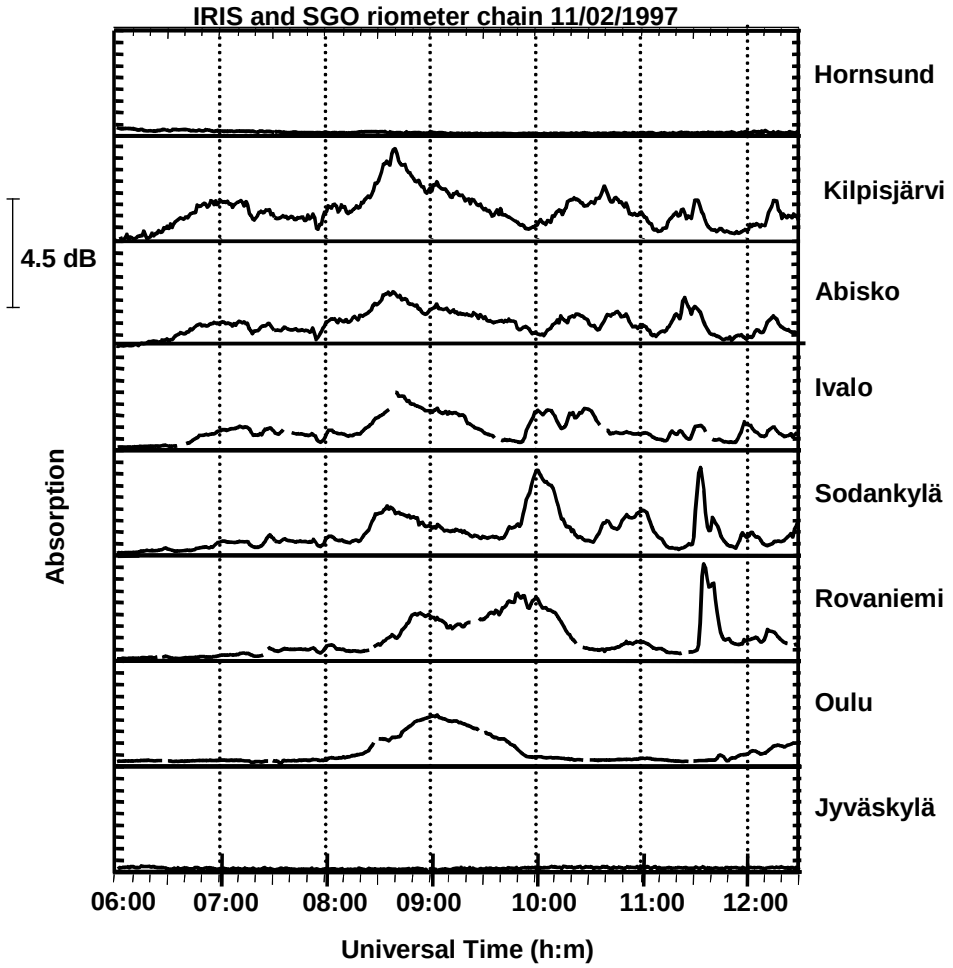

Figure 5.5: **A stack plot of riometer data comprised of IRIS and the SGO chain. The instruments are ordered by descending magnetic latitude. Hornsund and Jyvaskyla see little activity throughout the event. The spatial development of the precipitation in the ionosphere can be seen as changes in the absorption signatures at each latitude and the time delays between notable features.**

Neither Hornsund (73.8° Mlat) nor Jyväskylä (58.8° Mlat) witness absorption above 0.5 dB from 06:00 to 12:30 UT, placing a definite latitudinal limit to the precipitation. The time lag in the event onset can be seen in the riometer chain. Oulu (61.5° Mlat) does not see increased absorption until 08:00 UT. At this time the riometers from Abisko to Oulu see a rise of at least 2 dB maximising after 08:40 UT. The absorption reaches background levels again at Oulu by 10:00 UT. Post 10:00 UT the activity is more variable. Before 11:30 UT most activity is recorded in the mid to northernmost riometers; there follows two large spikes in Sodankylä and Rovaniemi (~4.5 dB) at the same time as a gradual rise begins in Oulu (1 dB by 12:30 UT).

5.2.4 Space Based Observations of Precipitation –DMSP.

Three passes of DMSP satellites occurred with 12° longitude of EISCAT between 06:30 and11:30 UT on 11 February 1997. Figure 5.6 shows particle flux-energy spectrograms from two of the DMSP. The top panel displays data from the F13 satellite split into electron and ion fluxes. The satellite crossed the magnetic latitude (Mlat) of EISCAT at 06:33 UT, 10° longitude west of the radar beam, indicated by the solid, vertical black line. The dispersed ion signatures from 06:30 to 06:32 UT indicate that the satellite is on newly opened field lines, moving south to closed field lines. By the time of crossing EISCAT (06:33 UT) there are no ion signatures, however there are relatively high fluxes of low energy electrons and low to medium fluxes of high-energy electrons (> 2.5 keV). The maximum energy deposition height of a 2.5 keV electron is ~130 km suggesting good agreement with the EISCAT data at this time. The high-energy electrons are still detected to ~65° Mlat. A pass by the F12

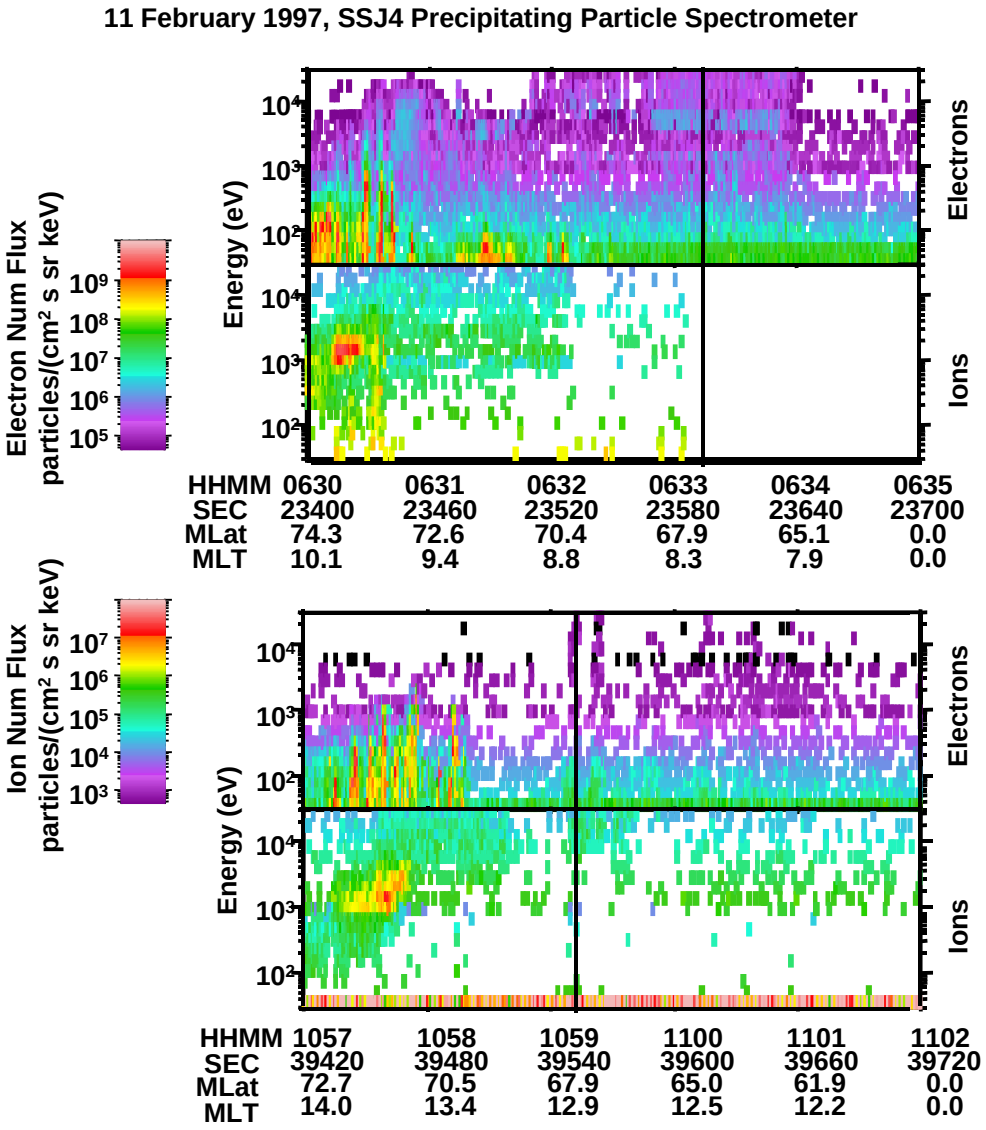

Figure 5.6: **Two passes from DMSP satellites are shown. The black vertical lines illustrate the times of crossing the magnetic latitude of EISCAT. The top panel is from the F13 spacecraft around 06:30 UT. The bottom panel is a pass by the F10 satellite close to 11:00 UT**

satellite at 09:58 UT (5° longitude from EISCAT) coincided with decay in the electron density (data not shown). Low fluxes of energetic electrons were observed together with softer electron precipitation that deposits in the lower F region, once again in agreement with the EISCAT data.

The final DMSP pass (Figure 5.6, bottom panel) is by the F10 satellite at 10:59 UT (7° longitude away). Once again there is the dispersed ion signature as the satellite travels equatorward through the cusp. There is a distinct lack of energetic electrons at this time, however there are fluxes of 10s of keV ions over a short latitude range. This coincides with the E region densities observed by EISCAT and the structured Pc1 pulsations recorded by the magnetometer. Although there is evidence of softer electrons, there are also high fluxes of energetic ions (10-30 keV) that could account for the E-region densities.

5.2.5 Night Side Observations of Substorm activity – CANOPUS.

Finally, night side observations are provided by the CANOPUS (Canadian Auroral Network for the OPEN Program Unified Study) array of instruments. Figure 5.7 shows the response of several instruments to the varying geomagnetic activity. The top panel displays the magnetic signature at Gillam, filtered for Pi2 pulsations. The scale has been limited to ±20 nT to allow easy viewing of the low intensity pulsations. The central panel shows the latitude integrated (red) and peak (black) intensity observed by the Gillam Meridian Scanning Photometer (MSP) at 557.7 nm. The bottom panel is a stack of riometers from the Churchill line; Churchill, Gillam and Island Lake from top to bottom. Due to a lack of reliable quiet day curves the signal amplitude is illustrated rather than absorption.

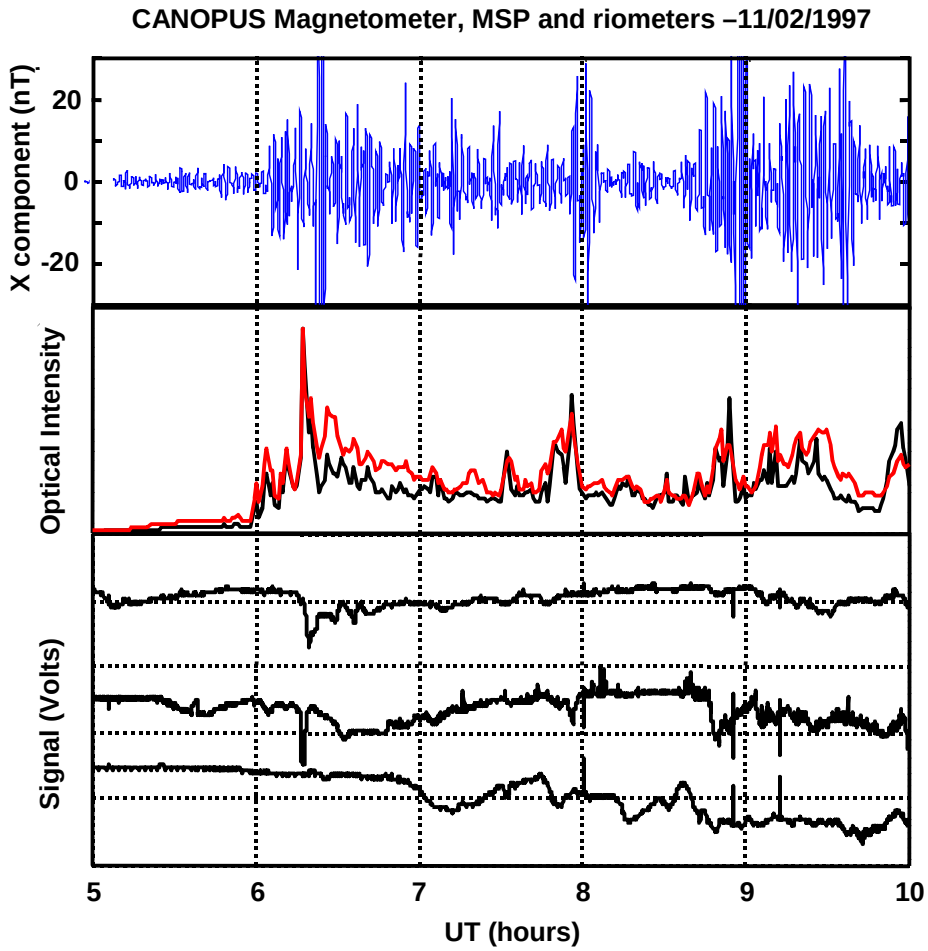

Figure 5.7: **CANOPUS night side observations illustrating elevated geomagnetic and auroral activity. The Pi2 filtered magnetic signature at Gillam is shown (top) with latitude-integrated (red) and peak (black) optical intensity at 557.7 nm from a co-located MSP (middle). The bottom panel is a stack plot of riometers from the Churchill line; Churchill, Gillam and Island Lake from top to bottom.**

Low activity occurs locally up until 06:10 UT when a large burst of Pi2 occurs, reaching a maximum at 06:20 UT. This corresponds with increased optical activity and a sharp spike in the riometer data indicating energetic precipitation. Magnetic midnight occurs at 06:30 UT at the Gillam site. Activity remains high from 06:00 UT to 10:00 UT with Pi2 fluctuations of >±20 nT and variable optical signatures in the MSP related to drifting auroral arcs. A second strong burst of activity occurs shortly before 08:00 UT (01:30 MLT) and then again around 09:00 UT (02:30 MLT) and beyond.

5.3 Discussion of Observations

Here we discuss different possibilities for explaining the origin of the absorption observed by IRIS related to the enhanced electron densities. Three main areas are addressed: the effect of the solar wind pressure, drifting electrons from substorm injection and changes in precipitation spectrum. From these topics, the precipitation on the morning of 11 February 1997 may be characterised as arising from a combination of two distinct geophysical phenomenon; the recovery phase of a small storm and drifting electrons from enhanced nightside activity coupled with solar wind pressure changes. Finally the spatial development of the absorption is considered and compared with ionospheric flows measured by coherent radar. This enables the differentiation of dominating flow regimes at different times during the event.

5.3.1 Solar Wind Pressure

The timing of the first increase in absorption coincides with the first rise in solar wind pressure at around 06:20 UT (assuming a short delay from the magnetosheath to the ionosphere), and the time structure of the absorption broadly follows the changing pressure; small changes in the pressure are reflected in changing absorption levels in IRIS. The pressure-absorption relationship breaks down after 08:15 UT (at EISCAT) when the pressure decays to <1 nPa within 30 minutes whereas the absorption continues to increase. This is due to a hardening of precipitation, as indicated by the increase in electron density at lower altitudes evident in the EISCAT data. Pressure pulses in the solar wind are well known to produce increases in auroral precipitation (Brown et al, 1961; Brown and Driatsky, 1973) through wave particle interactions in the magnetosphere, leading to enhanced ionospheric absorption (Perona, 1972). This sudden commencement absorption (SCA) is often associated with poleward moving absorption regions (Brown, 1978), however in this case the absorption spreads equatorward following onset (Figure 5.3). SCA are usually associated with pressure increases of at least an order of magnitude greater than the values observed during this event. From this it may be surmised that the solar wind pressure is not the sole cause of the electron density observed at EISCAT. The coincidence in the temporal structure of the pressure and the absorption suggests that the solar wind plays a role in the precipitation of the electrons in this case, however similar observations are needed to confirm if this is more than a coincidence. If high fluxes of trapped electrons are present fluctuations in the Earth's magnetic field will encourage the growth of resonant waves. This will lead to pitch angle diffusion amongst the particle population, resulting in scattering into the loss

cone and hence precipitation (Schulz and Lanzerotti, 1974 and references therein). A mechanism by which elevated fluxes of electrons are injected onto the relevant field lines is suggested in the following section.

5.3.2 Substorm Drifts

The electron density enhancements from 06:15 UT correspond with bursts of <0.6 Hz pulsations (Figure 5.2). On average these bursts last for 10 to 15 minutes with a ~10-minute separation suggesting a Pc5 like modulation. Kikuchi *et al.* (1988) and Stauning (1998) observed some slowly varying absorption events to be related to strong pulsations in the Pc 4-5 range. Stauning (1995b) and Stauning (1998) describe the theory that absorption in the morning sector displaying this slowly varying nature was related to the drizzle of eastward drifting electrons from substorm activity on the nightside. Those observations were from the Sondre Stromfjord IRIS at 73.5° Mlat. The CANOPUS observations (Figure 5.7) confirm that substorm activity was occurring in the Canadian sector at this time. Activity at the Gillam site started shortly after 05:00 UT. The magnetometer indicates low intensity Pi2 signatures at this time related to a small brightening in the 557.7 nm emission between 70° and 64° latitude. Major activity begins after 06:00 UT with a large Pi2 signature at 06:20 UT accompanied by a spike in the absorption from the co-located riometer at Gillam. Figure 5.8 shows the AE index (top panel) and Dst index for 11 February 1997. The period of observation at EISCAT is highlighted in red. A sharp increase in the AE index occurs around 05:00 UT before a much larger increase occurring after 06:00 UT. This reinforces the CANOPUS observations of the geomagnetic activity.

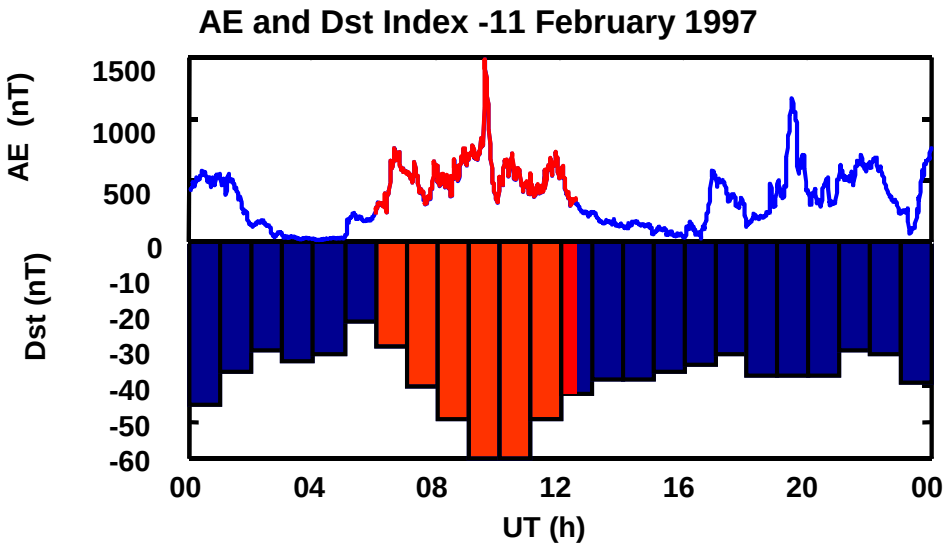

Figure 5.8: **Hourly Dst and the 1 minute AE indices for 11 February 1997. The periods in red denote the times of observation at EISCAT. The whole period was relatively active but a minimum in the Dst index occurs around 9 to 11 UT. AE shows an initial sharp increase close to 5 UT before a much larger step after 6 UT.**

The timing of the expansion of absorption at onset across the IRIS field of view gives an estimate of the energy of precipitating electrons if it is assumed that electrons are injected onto all relevant L shells simultaneously. The IRIS keogram (Figure 5.3) illustrates a distinct gradient in the precipitation at event onset. The IGRF-2000 model was used to identify two IRIS beams (beams 2 and 46) that have the same magnetic longitude, and to calculate their L-values. During the initial period of activity a time difference of about 25 minutes was observed between the appearance of absorption features in these two beams.

Assuming only small changes in the magnetic field the drift period of a particle can be expressed, following Hargreaves (1995), as:

$$P = \frac{733}{E} . \frac{1}{R} . \frac{G}{F} \qquad \text{hours} \qquad (5.1)$$

E is the energy of the particle in keV, R is the equatorial distance, in earth radii, and G/F is a function that depends on the mirror point of a particle. Close to the equator G/F=1 and increases to 1.5 for particles mirroring at the poles. It is clear that a particle will take longer to complete an orbit on a lower L shell than a similar particle at higher L. Particles which mirror at the equator are ignored for the purpose of this calculation since they are less likely to precipitate than those that mirror at the poles. Thus G/F is taken to be 1.5 for the following estimation. It should be noted that particles are injected on the nightside and precipitate after dawn, thus they complete only a fraction of an orbit. For the purpose of this calculation we make the assumption that particle injection occurs around magnetic midnight. This follows the observations of Vagina *et al.* (1996) using LANL and GOES geosynchronous spacecraft to detect dispersed particle populations and magnetic field dipolarization.

These signatures of the injection region occurred between 21:00 and 01:00 MLT with most before but close to midnight. Thus in this case the injection region is chosen to be 24:00 MLT. Assuming this injection period, a particle that precipitates at 08:20 MLT will have travelled just over 8 hours of magnetic local time. Thus a particle precipitating at 06:15 UT will have travelled 35% of its predicted orbital period and a particle precipitating at 06:50 UT will have travelled 38%. Hence, the time separation of precipitation from a single characteristic energy (E) on two field lines (R_1 and R_2) at similar magnetic longitude can be expressed as:

$$T_2 - T_1 = \Delta T = \frac{1099.5}{E} \times \left(\frac{0.38}{R_2} - \frac{0.35}{R_1} \right) \qquad (6.2)$$

Where ΔT defines the time difference of precipitation occurring on field lines R_2 and R_1. Thus for the two IRIS beams at L=6.65 and L=5.62, E ≈ 37 keV.

This method assumes that electrons are injected, simultaneously, over the range of L = 5.62 to 6.65 and at a very confined range of longitudes. EISCAT shows a maximum of electron density between 85 and 105 km altitude at 0620 UT, peaking close to 92 km. The maximum ionisation production of a 37 keV electron occurs at an altitude of ~90 km (Rees, 1963). Thus EISCAT appears to verify that the drift timing gives a reasonable estimate of the characteristic energy of the electrons responsible for the D region density enhancements.

Equation (6.1) indicates that there is an inverse relationship between the period of a gradient-curvature drifting particle and its energy. Thus, as may be expected, for a given L shell a higher energy particle will drift around the Earth at a higher velocity than a particle of lower energy. This leads to an energy dispersion signature in the particle population that can be observed by satellites (e.g. Vagina *et al.*, 1996). If this

is the case then it is reasonable to assume that at event onset, the electron density enhancements observed at EISCAT will be due to virtually mono-energetic beams of precipitating electrons. This can be tested in two ways; the first is by looking at data obtained from low orbit satellites (such as DMSP), the second method inverts the EISCAT electron density profiles to obtain an estimate of the energy spectrum of precipitation.

Hargreaves and Devlin (1990) used the second approach to study morning sector precipitation during two intervals. In both cases the events were much earlier in local time, however, the principal of energy dispersion still holds. The conclusions of that study indicate that the maximum electron density occurs a short while after onset and the spectra tend to be relatively broad. This is not consistent with the theory of drifting electrons that suggests that the maximum occurs at the onset and that the energy spectrum will be narrow due to the energy dispersion of the particle population. The method used in that previous paper has been applied to EISCAT profiles from the current study. A description of the procedure (ZABMOD) can be obtained from the appendix of Hargreaves and Devlin (1990), but in brief it is an iterative process that operates between 65 and 110 km altitude and with energies from 5.9 to 380.5 keV. For the altitudes examined in this case study it is unnecessary to assume a background electron density from solar radiation, especially during un-illuminated periods..

Figure 5.9 shows the results for two electron density profiles close to the onset of the event on the 11 February 1997. There is an initial hardening of the spectrum that occurs over a short time range (~10 minutes). Pure Gradient Curvature drift predicts that the maximum should occur at a sharp onset. It is reasonable to expect

that dispersion in the particle energies will result in a changing signature at IRIS/EISCAT as the lower energy electrons arrive at a later time. This appears to occur in the gradual rising of the lower edge in the EISCAT electron density (Figure 5.2, top panel) between 0700 and 0800 UT and also after 0900 UT, though continuing substorm activity observed by CANOPUS suggests that fresh populations are injected at later times. The increased Pi2 signature after 0615 UT suggests that substorm activity is overhead at the Gillam site (local time = 2345 MLT). The activity continues throughout the early event with the most intense Pi2 pulsations displaying similar quasi periodicity to the dayside precipitation suggesting a link to the small fluctuations in the solar wind pressure.

The pass of the DMSP F12 satellite at 06:33 UT shows that there were particles of ~30 keV present on field lines close to EISCAT (The top energy of the SSJ/4 sensor is ~32 keV). The flux at this energy is approximately 3×10^{5} $cm^{-2}.s^{-1}.sr^{-1}.keV^{-1}$ showing good agreement with the derived spectrum. This would also match the energy derived by drift timing if the longitudinal separation is considered. However the satellite also indicates that there is precipitation of electrons with energies lower than the estimated level. These particles must come from another source to the drifting electrons that produce the density enhancements at EISCAT.

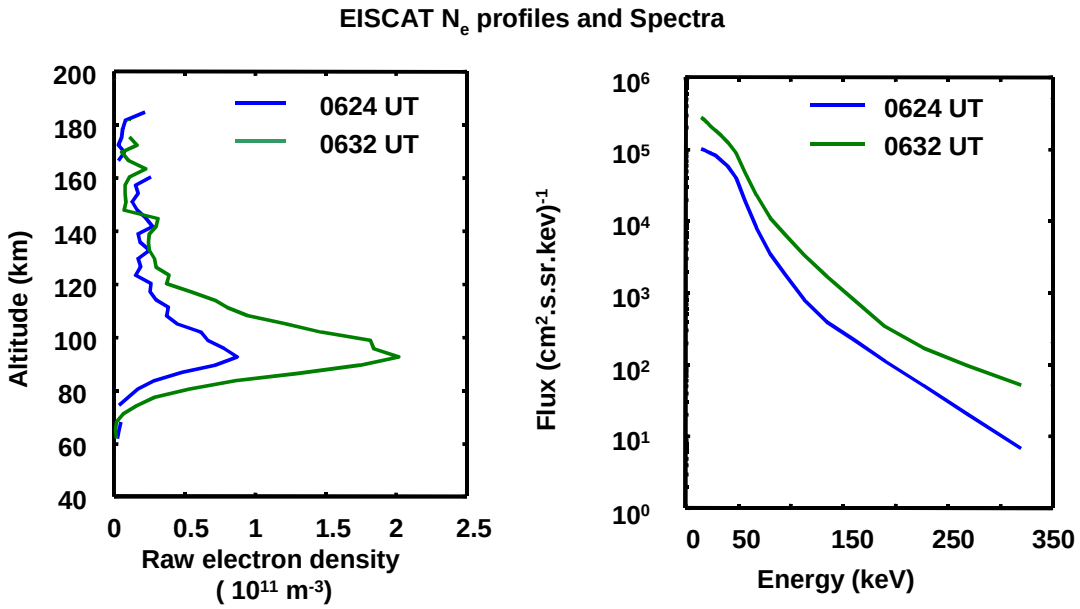

Figure 5.9: **The first panel contains EISCAT measured electron density profiles for two times close to the onset of the event. The second panel shows the corresponding modelled energy flux spectra, calculated from the profiles using the ZABMOD method. Note the hardening of the spectrum from 06:24 UT to 06:32 UT and the flux increase at high energies is much greater than at low energies.**

As stated earlier precipitation of drifting electrons has been reported at the Sondre Stromfjord IRIS (e.g. Stauning et al., 1995b; Stauning 1998) and also at the Japanese IRIS located at NyÅlesund on Svalbard (e.g. Nishino *et al.*, 1999), both at higher magnetic latitudes and closer to the polar cap boundary than the present observations. The results presented in this paper support the notion that gradient-curvature drift cannot be the only explanation for the structure and occurrence of morning sector precipitation.

5.3.3 IMF influences and Changes in Precipitation Spectrum

Nishino *et al.* (1999) observed a rectified response, during a morning absorption event, to north-south excursions of the IMF. Their observations were from the IRIS at NyÅlesund (~76.1° Mlat) and they concluded that the rectified response was due to the movement of the convection boundary and intensification of field aligned currents. In the case presented here the interplanetary magnetic field configuration was predominantly southward and no such response is observed, although a change in precipitation does occur with changing IMF over longer time scales. The point of most intense precipitation (08:40 UT) occurs as the solar wind pressure dies away and during a decrease in clock angle, due mostly to a large positive step in B_Y (~08:00 UT). This change in B_Y will result in a change in the convection pattern in the ionosphere and so alter the configuration of the geomagnetic field (Cowley *et al.*, 1991; Khan and Cowley, 2001). A change in the latitudinal spread of absorption occurs whilst B_y is positive. The rise in absorption at 08:20 UT, due to the increased lower altitude electron densities, occurs almost simultaneously from Kilpisjärvi to Oulu, though Oulu peaks later. The previous absorption had shown little effect at Oulu

(at L=4.3). Precipitation continues for a longer duration at this time (~90 minutes) than for the previous bursts in which the electron density decayed within 25 minutes on average. The distribution of absorption suggests two events occurring simultaneously; the first a continuation of the drizzle of precipitation confined to higher latitudes, the second a burst of precipitation extending from deeper in the magnetosphere and across a larger range of L shells. If the magnetosphere changes in a shorter time span than the drift period of a particle, radial diffusion of the particle could occur. Since the dayside magnetic field lines have been skewed due to the change in IMF B_Y, a drifting particle will encounter a local change of field. As the particle moves onto a lower L shell it will experience acceleration due to the stronger field and shorter field lines. Thus higher energy fluxes are produced at the lower L shells. With continuing wave particle interaction leading to pitch angle scattering into the loss cone, precipitation of higher energy electrons across a broader range of latitudes will be observed.

An alternative to this mechanism is that substorm injection is occurring across a larger range of L shells with higher energy particles being injected. The CANOPUS data show that there is increased activity shortly before 08:00 UT. The precipitation is not as enhanced as the onset at 06:00 UT, however there is a spike in both the optical intensity and in the riometer data, suggesting energetic precipitation. By assuming that maximum activity is occurring around local midnight and that the hardening of the spectrum at EISCAT is due to drifting electrons, it is possible to estimate the characteristic energy. Thus if injection occurs at 07:50 UT (estimated from the Pi2 burst at Gillam (CANOPUS)) and the electrons precipitate at 08:40 UT we would expect a characteristic energy of ~80 keV. This corresponds to a maximum

ionisation production height of ~86 km which is reasonably consistent with the altitude of peak electron density observed by EISCAT. A combination of these higher energy electrons coupled with radial diffusion could result in the deeper penetration and enlarged latitudinal spread of absorption that occurs at 08:40 UT.

After 10:00 UT (12:10 MLT) changing conditions are reflected both in the electron density profile, which shifts towards a maximum in the E-region, and in the drastic change in the geomagnetic pulsation spectrum (Figure 5.2). This change occurs as the instrument location rotates equatorward of the cusp in a region of strong return flow in the ionospheric convection pattern as indicated by the CUTLASS HF radar at Hankasalmi (Figure 5.4). This direction of flow also appears in the movement of the absorption region seen in both IRIS and the riometer chain where there is a poleward and westward flow. The DMSP pass at 10:59 UT (Figure 5.6, bottom panel) indicates the presence of higher energy ions on field lines close to EISCAT with low energy electrons suggesting that the change in density profile is due to increased ion precipitation rather than electrons. Regions of both high poleward flow and high and variable spectral width in HF radars have been shown to indicate the location of the ionospheric footprint of the cusp (Baker *et al.*,1995). Both CUTLASS and DMSP observations place the equatorward edge of the low altitude cusp to be a few degrees north (~71^{o} Mlat) of the EISCAT site. Ion precipitation is common in the cusp, and both the Boundary Plasma Sheet (BPS) and Low latitude boundary layer (LLBL) have been observed to contain ions with energies exceeding 30 keV (the upper limit of the DMSP spacecraft) (Lockwood, 1997). It is possible that the ion signatures observed at EISCAT could be related to precipitation from the LLBL or BPS and the energies seem reasonable. The magnetometer shows bands of Pc1 pulsations, which are taken

to be signatures of ion-cyclotron waves and lead to scattering of ions into the ionosphere. Narrowband waves in the Pc1 range have been detected close to the equatorward edge of the cusp near to the low-latitude boundary layer (e.g. Dyrud *et al.*, 1997) giving credence to the speculation that the ions observed at EISCAT are related to the LLBL. It is expected that the Pc1 pulsations reach a maximum intensity when the equatorward edge of the cusp is located close to the station, however in comparing the signature from the magnetometer at Kilpisjärvi (65.8° Mlat) with observations from a similar instrument at Sodankylä (63.9° Mlat) (data not shown), the lower latitude station observes more intense, but similarly structured, pulsations at this time. The distance from EISCAT to the equatorward edge of the cusp casts doubt on this being a reasonable assumption and the likelihood of the precipitation being related to the cusp/LLBL is diminished. The increase in intensification at lower latitudes coincides with increased absorption at those stations related to increased electron density. Figure 5.3 shows that the south end of the IRIS array observes higher absorption than the region around EISCAT. Thus the precipitation of energetic ions is maximising deep in the magnetosphere, at low L shells. The changes in the structure of the Pc1 signature occur at similar times to two northward excursions of the IMF. Ion precipitation was occurring before this, during the narrow band pulsations. The change in IMF may influence a change in the wave structure but appears to have little effect on the ion precipitation. The Pc1 waves do indicate that there has been a growth in electromagnetic ion-cyclotron (EMIC) waves in the magnetosphere close to around L=4.5 (Mauk and Mc Pherron, 1980; Anderson *et al.*, 1992a; Anderson *et al.*, 1992b). These result in pitch angle scattering of energetic ring current ions, which then precipitate (Gonzales *et al.*, 1994). The EMIC wave growth can be attributed to

the interaction of cold plasma with hot ions, as the plasmasphere enlarges and mixes with the ring current (Cornwall *et al.*, 1970, Cornwall, 1978). The ring current ions have been accelerated, either through injection from the tail during the ongoing substorm activity (Arnoldy and Chan, 1969) or via the transport of plasma sheet particles by enhanced convection electric field (Lyons and Schulz, 1989). Since this event occurs after a distinctly active period, it is reasonable to expect the radiation belts to be increased with high fluxes of energetic particles. This theory is reinforced by the Dst index (Figure 5.8) which shows a minimum of –60 nT occurring between 9 and 11 UT before increasing as in the recovery phase of a small to moderate geomagnetic storm.

5.3.4 Ionospheric Flows

Low velocities (< 200 ms^{-1}) were observed by CUTLASS (Figure 5.4) after onset (06:15 UT), most likely due to a predominantly zonal drift with small meridional movement. These observations are contrary to the movement of absorption observed by IRIS, which displays a distinct equatorward motion after 06:00 UT. From 11:00 UT there is a definite poleward and westward flow of the intense absorption patches to the south end of the riometer field of view (Figure 5.3). Estimates of the poleward velocities have been made for these patches both through comparisons of time series from consecutive IRIS beams and through the movement of steep absorption gradients in the IRIS images/keogram. Previous studies have shown the drift velocity of absorption patches to be consistent with the E×B drift (Nielsen and Honary, 2000). The current estimates were compared with the flow observed by CUTLASS in the region of high return ionospheric flow. The absorption

appears to drift with velocities of ~650 ms^{-1} from 11:00 to 11:20 UT after which there is then a general increase to ~900 ms^{-1}. The radar backscatter is patchy at this time but several of the radar beams (0 to 11) cut across IRIS providing a good indication of the flows. Only data from beam 5 has been displayed since this is the beam that encompasses the EISCAT beam, however data from neighbouring beams show that there are similar velocity fields across the IRIS field of view. The CUTLASS line of sight velocities pre-11:30 UT, at the latitudes of IRIS, are generally <600 ms^{-1} away from the radar. Post 11:30 UT there is a general increase with some scatter suggesting flows >800 ms^{-1}. These rough calculations suggest good agreement between the movement of the F region irregularities and the absorption patches in the E and D regions. It is therefore reasonable to suggest that the dominant drift mechanism for the precipitating particles at this time is the E×B drift, as opposed to gradient-curvature drift apparently observed at event onset (06:15 UT). If the absorption at the south end of the array is also due to ion precipitation into the E region then the tendency to drift as the E×B velocity seems reasonable. Past studies have established that the flow in the E region is often similar to that in the F region (Nielsen and Schlegel, 1985). The possibility exists that the scatter observed by CUTLASS could come from the E region irregularities that compose the electron density enhancements (Milan *et al.*, 2001). An investigation of the elevation angle of the returned HF beam suggests that this is not the case, with angles of >21° for most of the scatter in the nearer range gates. The E region densities have well defined 'tails' extending into the F region and so the radar scatter could originate from irregularities in these 'tails'.

5.4 Summary

A case study of varying precipitation in the morning sector and across noon during an active period on the 11 February 1997 is presented. The observations were made using an imaging riometer (IRIS) and a nearby incoherent scatter radar (EISCAT) together with a chain of wide beam riometers and two pulsation magnetometers, in conjunction with satellite and HF radar measurements. Through nightside observation, provided by the CANOPUS array of instruments (including a meridian scanning photometer, magnetometers and riometers) the precipitating electrons have been linked to substorm injection and subsequent gradient-curvature drift. The time separation of absorption increases across the IRIS field of view has been used to provide an estimate of the characteristic energy of precipitation assuming that gradient curvature drift is the dominant process involved. Observations of electron density from EISCAT suggest that the energy estimate is reasonable, although it is found that gradient-curvature drift alone cannot account for the spectrum of precipitation at EISCAT. A controlling influence from the solar wind has been identified in the form of small-scale pressure changes at the magnetopause, leading to increases in pitch angle scattering in an already unstable energetic population of electrons.

A small increase in particle penetration into the ionosphere has been discussed in relation to increased radial diffusion producing higher energy electrons at lower L shells. This assumption is based on a dramatic change in the geomagnetic field orientation, transmitted from the IMF, and near simultaneous increase in precipitation. This precipitation leads to enhanced absorption in the nearby riometers, and is coupled with the more energetic particles being injected at the nightside. The electron

precipitation then decreases, at the same time as an increase in ion fluxes, the latter being identified in data from the over flight of DMSP F10. The possibility that the ions arise from the LLBL or BPS has been dismissed not only because of the relatively large distance to the cusp, but also because Pc1 waves are observed to increase in intensity at lower L-shells. Instead it has been suggested that the ion precipitation is due to a growth in EMIC waves resulting in pitch angle scattering of ions into the loss cone. This has been attributed to an interaction between an enlarged plasmasphere and energetic ring current during the recovery phase of a small to moderate geomagnetic storm. At this later time (>13 MLT), IRIS was located under a region of strong poleward convection. The flows observed by CUTLASS at this time were found to be comparable with the movement of strong absorption patches as derived from the IRIS keogram unlike at the start of the precipitation (~08:30 MLT). This suggests that ExB drift is governing the precipitating particles at this time rather than L-shell separation of the drifting electrons as at event onset (06:15 UT to 06:50 UT).

Chapter 6

Statistics of the Variation of Absorption Observed using IRIS

6.1 Introduction

Understanding the variation of HF radio absorption in the auroral zone is of great use for predicting HF radio propagation conditions. By relating the absorption to other geophysical parameters it may eventually become possible to predict the response of the ionosphere to a given set of circumstances. This is especially true if the absorption can be linked to quantities that are measured in real time such as the solar wind. Constant monitoring is currently available from the ACE (Advanced Composition Explorer) spacecraft situated at the L1 point. An upstream vantage point such as this results in early warnings of possible conditions at Earth from 10 minutes to over an hour depending on the solar wind speed.

Cosmic Noise Absorption (CNA) at high latitudes acts as a proxy for energetic precipitation (see Chapter 4 for a review of absorption). By examining the variations and distribution of absorption an insight into the limits of particle motion and wave-particle interactions in the magnetosphere can be gained. Further to this the coupling between the ionosphere and magnetosphere in terms of energy deposition can be investigated. Thus a thorough understanding of cosmic radio noise absorption can

lead to estimations of the energy transferred from the solar wind that is eventually deposited into the lower ionosphere (Hargreaves, 1966).

Since September 1994 the Imaging Riometer for Ionospheric Studies (IRIS) has been operating at high latitudes in Fennoscandia providing maps of small-scale precipitation into the D layer. This chapter determines the statistics of the absorption observed by IRIS across a small range of latitudes based on magnetic local time (MLT) and investigates the dependence on parameters such as K_P and the solar wind speed.

6.2 Observations and data descriptions

Figure 3.2 displays the beam pattern for the IRIS at Kilpisjärvi projected at 90 km altitude. In Figure 6.1 the centres of the beams are plotted on a grid of magnetic latitude and longitude. Each centre has been calculated for the 1998 epoch in AACGM (Altitude Adjusted Corrected Geo-Magnetic) (Baker and Wing, 1989) co-ordinates using the IGRF-2000 model (International Geomagnetic Reference Field). IRIS is aligned with the geographical North Pole (accounting for the skew in the beam pattern) leading to each beam having a discrete magnetic latitude (Mlat). Ideally this provides a range of latitudes from 64.21° N to 67.59° N and a spatial resolution of ~0.07° latitude, however, the corner beams of the imaging riometer are inclined at a low elevation (Chapter 3), leading to large side lobes and an extended path through the ionosphere, making these unsuitable for general use. Similarly the beams adjacent to

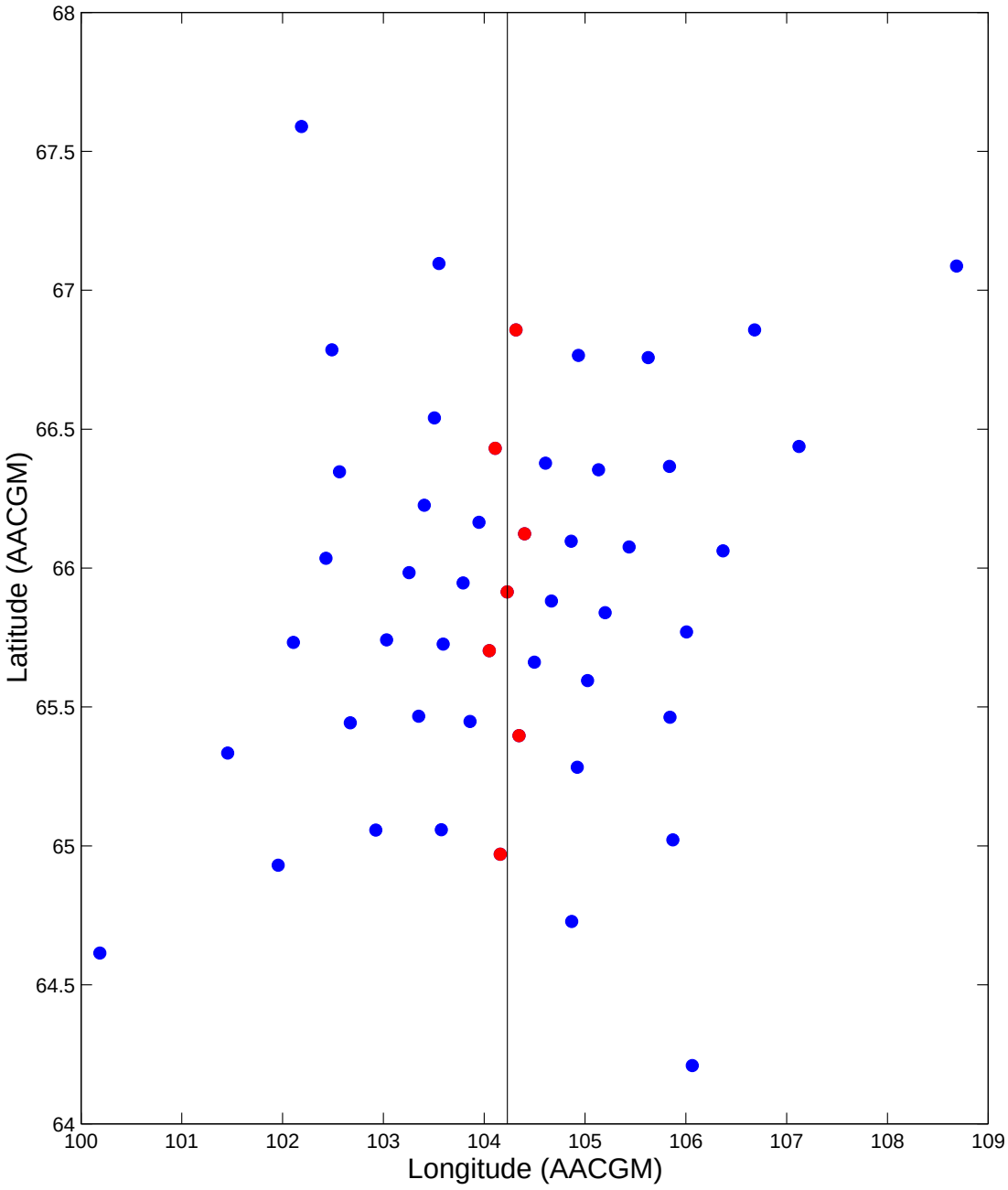

Figure 6.1. **IRIS beam centre positions in Altitude Adjusted Corrected GeoMagnetic coordinates (AACGM)**

the corners should be used with some caution (Hargreaves et al., 2002). Instead of using all the beams to produce high spatial resolution, seven beams across the centre of the array are used to provide data for this statistical study. The beam numbers and their magnetic co-ordinates are presented in Table 6.1

Beam	Mlat	Mlong	MLT at midnight UT
3	66.86	104.32	21:17
10	66.43	104.11	21:17
18	66.14	104.40	21:16
25	65.91	104.23	21:17
32	65.70	104.05	21:17
40	65.40	104.35	21:16
47	64.97	104.16	21:17

Table 6.1. The IRIS beams used to provide data for this statistical study. Magnetic co-ordinates are displayed as well as the MLT values for midnight UT at each beam centre.

The seven beams are roughly aligned along 104.2° magnetic longitude, with a maximum separation of 0.35° magnetic longitude. Magnetic Local Time (MLT) variations are less than a minute in each case. Data are taken from the epoch 1995 to 2001 inclusive, at 10-minute resolution, providing a maximum of 144 data points for each of the 2557 days. In practice data is lost due to maintenance time and hardware failures, but this accounts for less than 1% of the epoch. The most significant loss of data is due to contamination from solar radio emission and this will be described in more detail further into this chapter (section 6.2.1).

The geomagnetic data used in this study are provided by the World Data Centres for Geomagnetism (Kyoto, Japan) and Solar Terrestrial Physics (RAL, UK). The K_P index was available for the whole of 1995 to 2001 at 3-hour values. No finalised or even provisional values for AE were available for the interval; instead the quick look values are used for preliminary studies. Data are available from only 8 out of the 12 standard AE stations for only 4 years of the selected interval (1997 to 2000) and as such should be treated with caution.

Data from both the ACE (1998-2001) and WIND (1995-1998) spacecraft have been used to provide measurements of the solar wind and interplanetary magnetic field. As described in chapter 3, ACE is positioned at the first Lagrangian point (L1) whereas WIND is in a more complicated orbit. Knowing the positions of the spacecraft enable the data to be corrected for the delay time to the magnetosphere using the solar wind speed measurements. Periods when WIND passed close to the bow shock (within 10 R_e) have been discarded, though these prove to be relatively

few. Occasions when high speed streams overlap with slower solar wind have also been removed from the data set. The separation between WIND and ACE translates to little differences in the magnitudes of the field; at the distance of the satellites from the magnetopause the IMF variation with distance is represented by the tail of an exponential function (Cahill and Amazeen, 1963). At the time of writing ACE data did not cover the whole of 2001 and so the data set falls short of the absorption data by 2 months.

6.2.1 How can absorption be Negative?

Before attempting any form of statistical analysis on the riometer data an important constraint must be addressed; negative absorption. Unlike most imagers, which tend to be optical in nature, the imaging riometer operates independently of solar illumination. There is, however, a serious constraint on the use of riometer data under active solar conditions. It has long been recognised that during intense solar X-ray flares, the sun also emits radiation bursts, which can take the form of sweeps through frequencies or continuous emissions. During periods of high solar activity radio emission is virtually continuous. The processes that lead to this emission are not described here although the effects on the riometer are.

The manner in which the riometer operates has been described in Chapter 3 but an important point to highlight is that the riometer is basically a sensitive radio receiver. IRIS measures the cosmic radio noise at 38.2 MHz in the HF band and during periods of high solar activity the increased radio emission from the sun

incorporates this frequency. This signal is significantly higher than the cosmic radio noise such that during periods of daylight the receiver can reach saturation. During periods of minimal precipitation solar radio emission manifests as negative spikes (or extended negative bays) in the absorption trace. This is particularly apparent at the start of polar cap absorption events in the period between the solar flare and the arrival of the solar protons (see Chapter 7). Problems occur when precipitation is high, whether through geomagnetic processes or via solar proton entry to the magnetosphere. The solar emission boosts the radio signal received by the riometer causing a reduction in the measured absorption. So far this deviation from the true ionospheric absorption has not been quantified as no direct measure of the solar radio emission at 38.2 MHz is easily available. A further complication because of the temporal structure of the emission, which can produce false structure in the absorption leading to false interpretation of the precipitation.

Figure 6.2 shows time series of the average absorption in two rows of beams from IRIS. The top panel is from the second row of beams, judged from the north of the array, and the bottom panel displays the data from the most southerly beams (row 7); no filtering has been applied to these data. Decreases in absorption occur in both rows 2 and 7, although it is only in some of the beams of row 7 that the absorption moves below zero. These negative bays propagate eastward through the beams in both of the rows, following the track of the sun through the sky. Each of the beams has a large bay accompanied by a number of secondary spikes; the result of the strong solar signal in the weak side lobes of the beams. Whereas under usual circumstances the

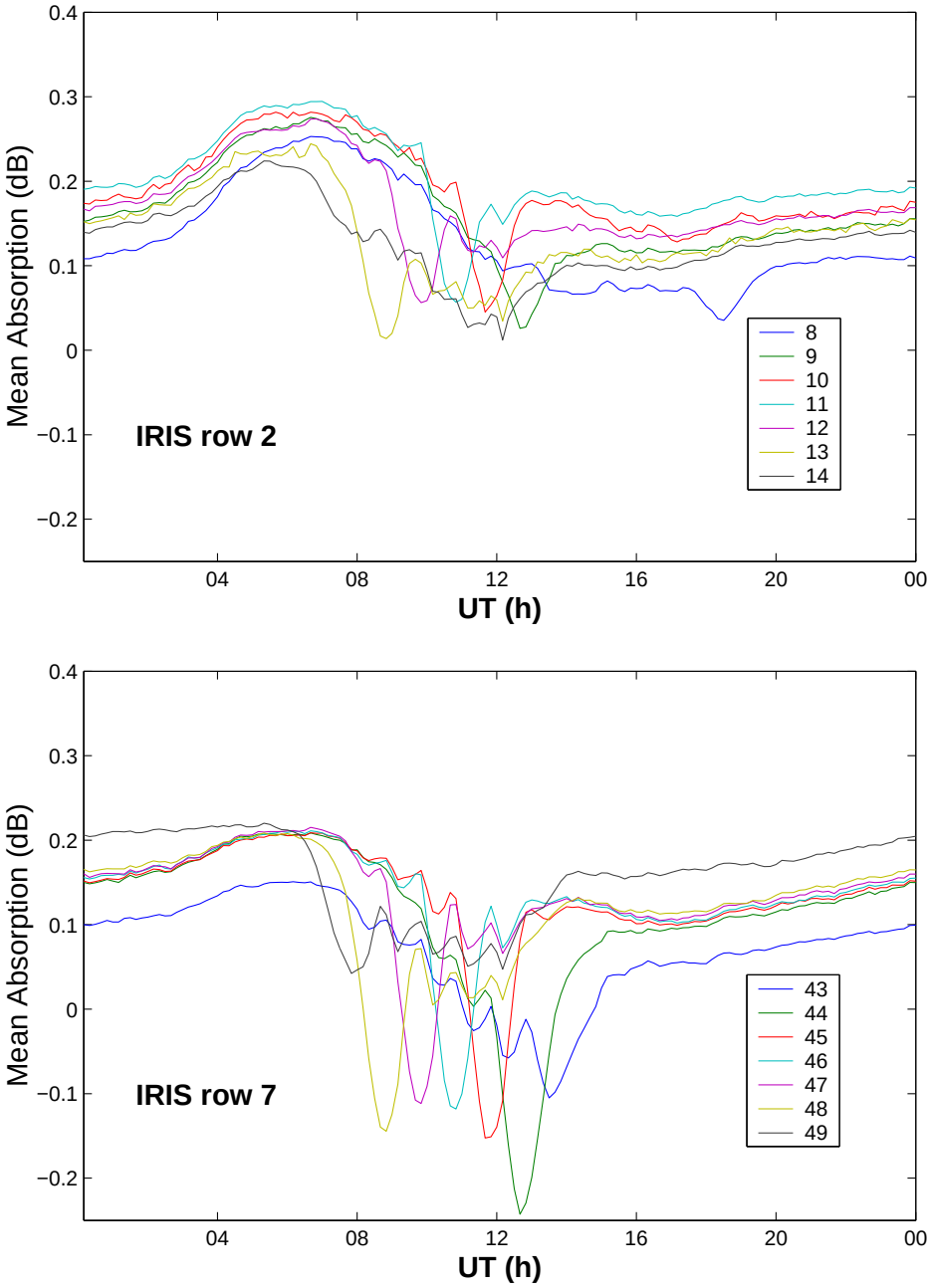

Figure 6.2. **Mean absorption in two rows of the IRIS beams. These have been calculated from 2557 days of data and include all negative data points.**

side lobes of most of the beams contribute very little to the measurements of absorption, they become increasingly important when considering solar radio emission. The cosmic radio noise signal is relatively low and the solar emission may be very high in comparison. Thus the emission detected in a side lobe of a beam may form a large amount of the signal in a northward beam. Modelled radiation patterns for beam 10 are displayed in Figure 6.3; the largest side lobe points south, in the same general direction as beam 45. For this study, if a beam records negative absorption below –0.2 dB, data from all beams are removed for that period; it is expected that this will catch the vast majority of contaminated events. The –0.2 dB limit is implemented to account for instrument sensitivity and possible errors in the quiet day curves. Times when this approach will fail are when precipitation levels are high in all beams; this occurs mostly during solar proton events. SPE lead to high levels of absorption making it unlikely that data will reach negative values, however these events are rare. For the purposes of this study all periods of enhanced solar proton bombardment have been removed, and this subject will be covered in more detail in Chapter 7. Since this chapter is concerned with the solar wind/magnetospheric effects on absorption the removal of polar cap absorption (from SPE) is actually desirable.

6.2.2 Daily Variations and Seasonal changes.

Since a range of latitudes have been selected it is possible to display the absorption data in the keogram format using averages of the absorption taken over the whole range of days. Figure 6.4 consists of two panels; the top panel displays the

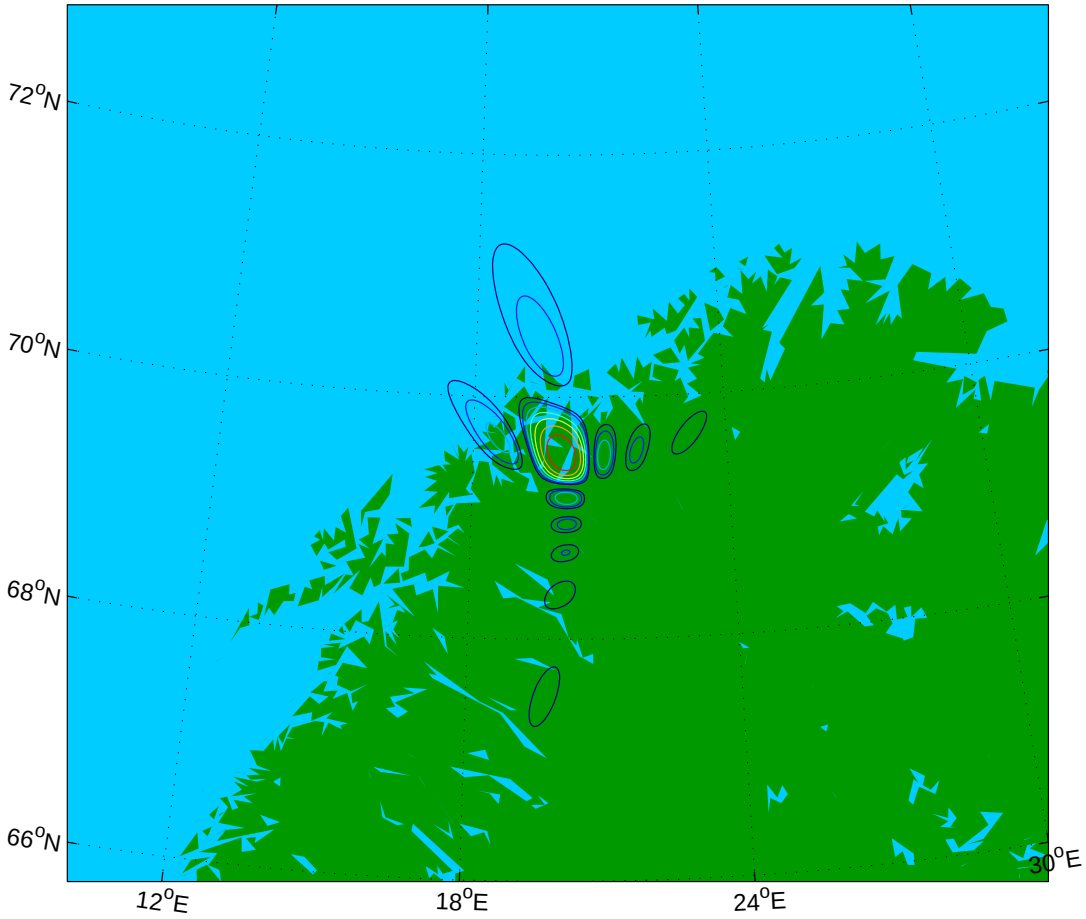

Figure 6.3. Beam patterns (at 90 km altitude) of beam 10 including the positions of side lobes. The colours indicate the strength of the beam with the red ring illustrating the traditional position of beam 10 (the 3 dB point).

mean absorption versus magnetic latitude for all magnetic local times. A distinct diurnal variation is clear with a peak in the morning sector following a rise from evening (20 MLT). The absorption peaks at 0.3 dB close to 10 MLT before decaying rapidly, dropping from 0.25 dB at 15 MLT to less than 50% of the maximum at 19 MLT. Absorption appears to be relatively uniform across the range of latitudes (65º-67º), though there appears to be a minimum in the central beam and at the edges, possibly due to problems with the obliquity factors. Absorption levels averaged over such a large number of data points tend to be low such that apparent large steps are in fact less than 0.1 dB in magnitude. Standard deviations for the absorption distribution are displayed in the bottom panel. In general these follow a similar trend to the mean absorption in the top panel, however the standard deviations are larger than the mean at some local times by up to 0.15 dB.

Figure 6.5 displays the distributions of absorption in 0.1 dB bins (centred on 0, 0.1, 0.2 etc) at selected local times for the zenithal beam. In each case the amount of negative absorption is always less than 6% of the total number of instances. By far the majority of absorption peaks around 0.1 dB with a rapid exponential-like decay to higher values. The data in Figure 6.4 still include some negative values, as explained above; the bottom panel of Figure 6.5 shows the local time variation in the zenithal beam when all negative values are discarded. The blue curve is the mean absorption and the green curve displays the standard deviation; the standard deviation and mean are less widely separated when all negative values are removed (>0.08 dB separation at maximum). Around midnight (20 to 04 MLT) the standard deviation is

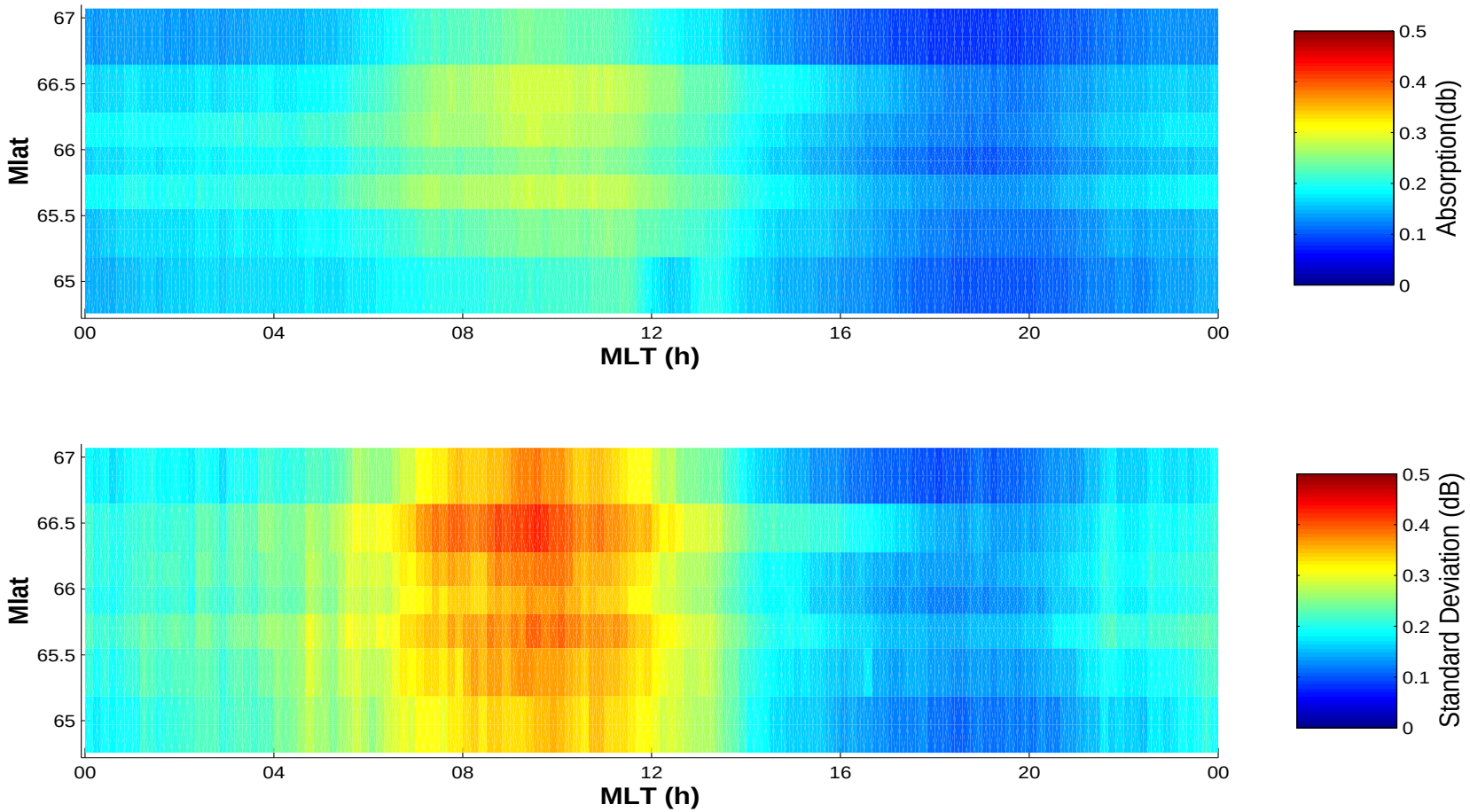

Figure 6.4. **Mean absorption (top panel) and standard deviations (bottom panel) in the ten IRIS statistical beams**

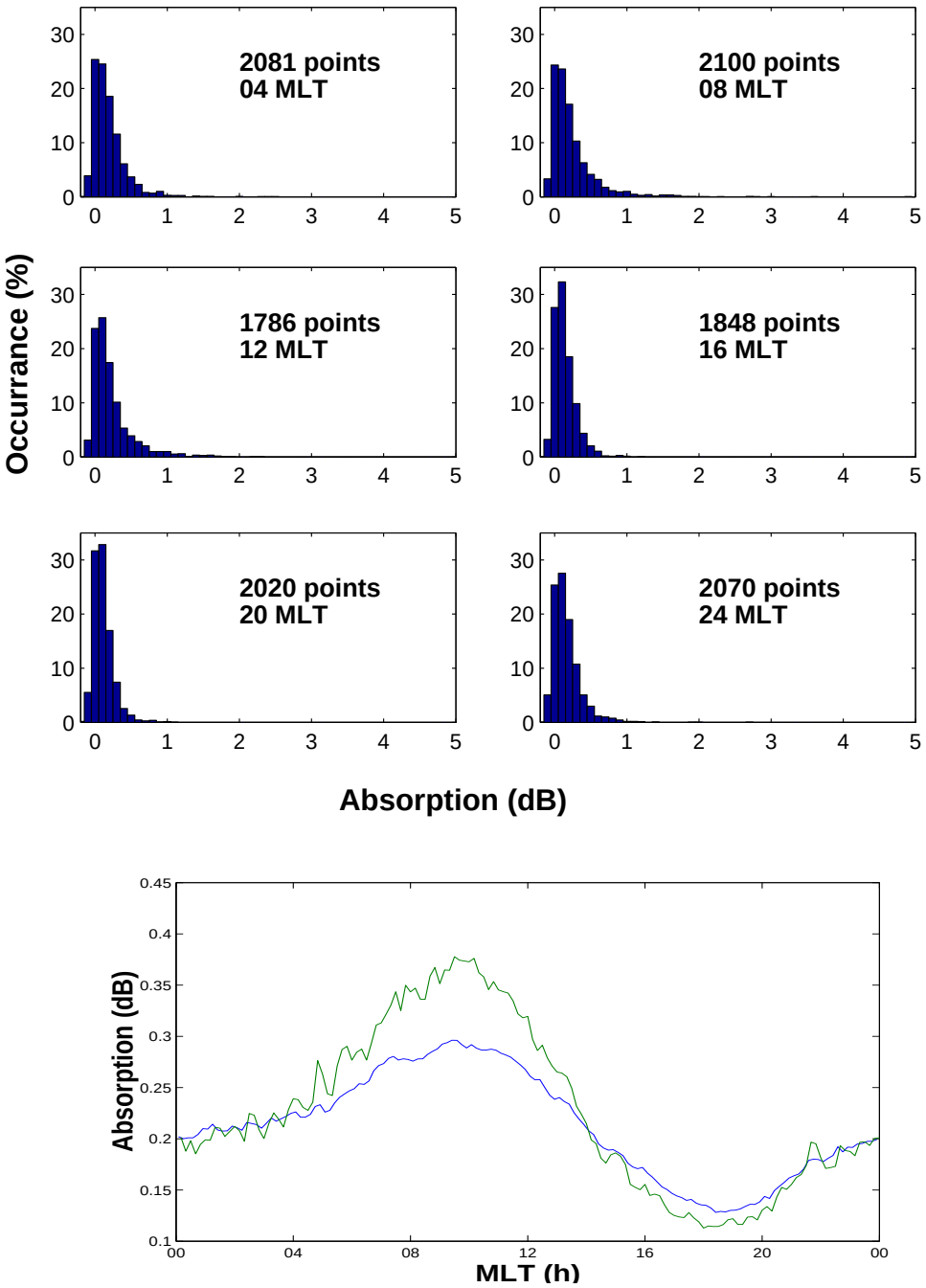

Figure 6.5. Distribution of Absorption in the zenithal beam of IRIS (epoch 1995-2001) for 6 magnetic local times. The bottom panel shows the mean and standard deviation in the zenithal beam when all negative values have been removed from the data.

approximately equal to the mean, and it is only at the extremes that this relationship deviates. The equality of the two parameters suggests that the distribution of absorption (excluding negative points) may be close to exponential in nature; the occasionally higher standard deviation in Figure 6.5 is a factor of a long tail in the distribution where there are some high absorption values.

Figure 6.6 displays the distributions in the seven beams once again binned by 0.1 dB, but this time limited to a maximum absorption of 3 dB (since this covers the largest range of values). The data have been normalized to the total number of data points in all beams at the appropriate time (displayed on each plot) and the colour scale is logarithmic. Again it is clear that there is a maximum around 0.1 dB with a sharp decay that occurs across all of the beams, although beam 10 (second from top) observes fractionally higher absorption in the daytime hours (06-18 MLT). A temporal evolution in the distribution is apparent; the occurrence at higher values increases from evening (20 MLT) into the morning sector before rapidly dropping by 16 MLT. Lower latitudes (<66°) show an extended tail in the first local time plot, somewhat repeated at 20 MLT with a lower mean absorption. In general each of the beams sees similar levels at each time.

Solar cycle 23 began with the solar minimum in 1994 and the utilised riometer data extend from close to sunspot minimum to maximum (2001), thus the dependence of absorption variation on changing solar cycle conditions can be observed. Figure 6.7 consists of two panels displaying the daily variation of absorption in each of the years 1995 to 2001; the top panel shows the mean absorption for 10-minute intervals

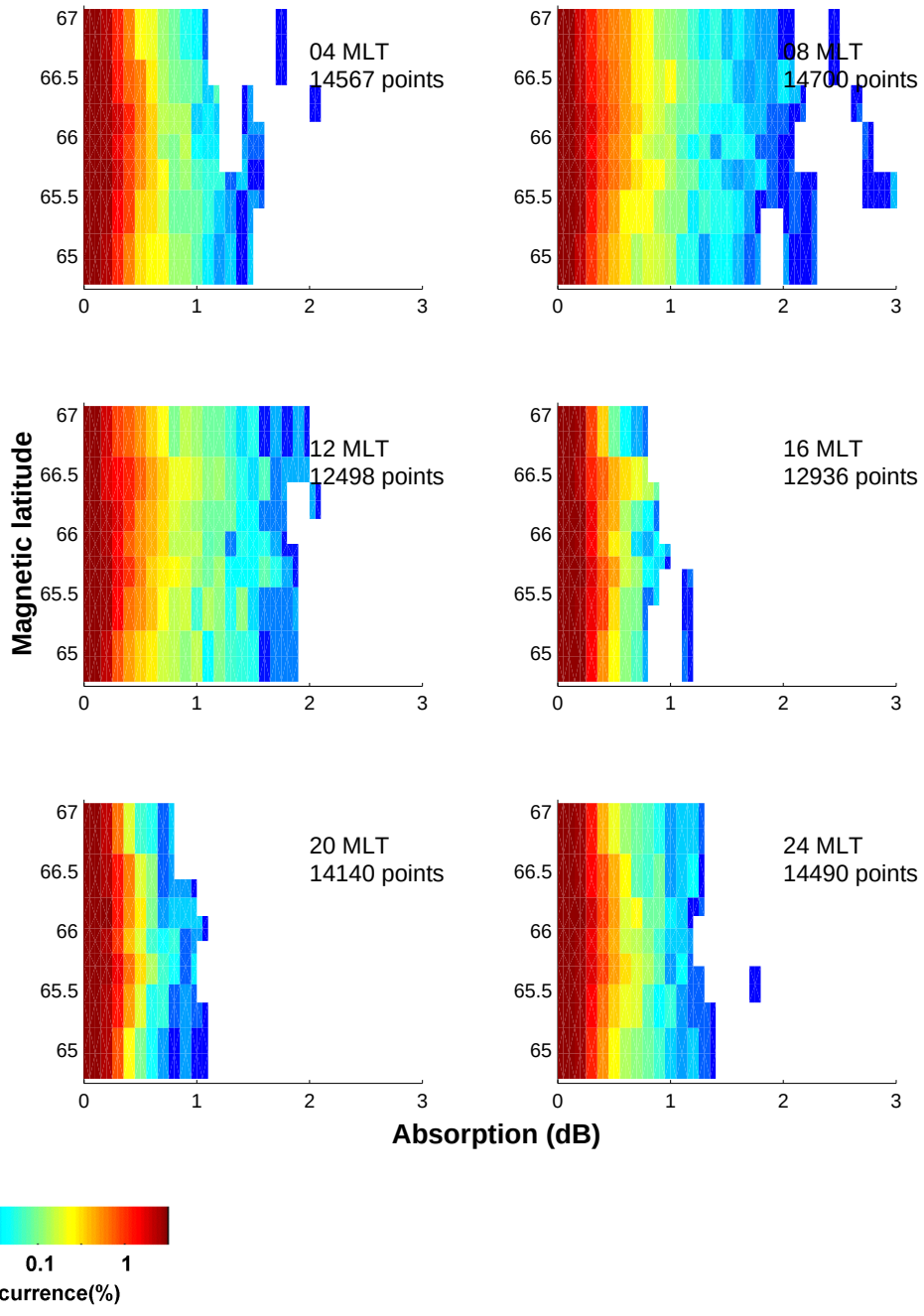

Figure 6.6 **Distribution of absorption with latitude for 6 magnetic local times (as in Figure 6.5). The total number of points are indicated in each plot.**

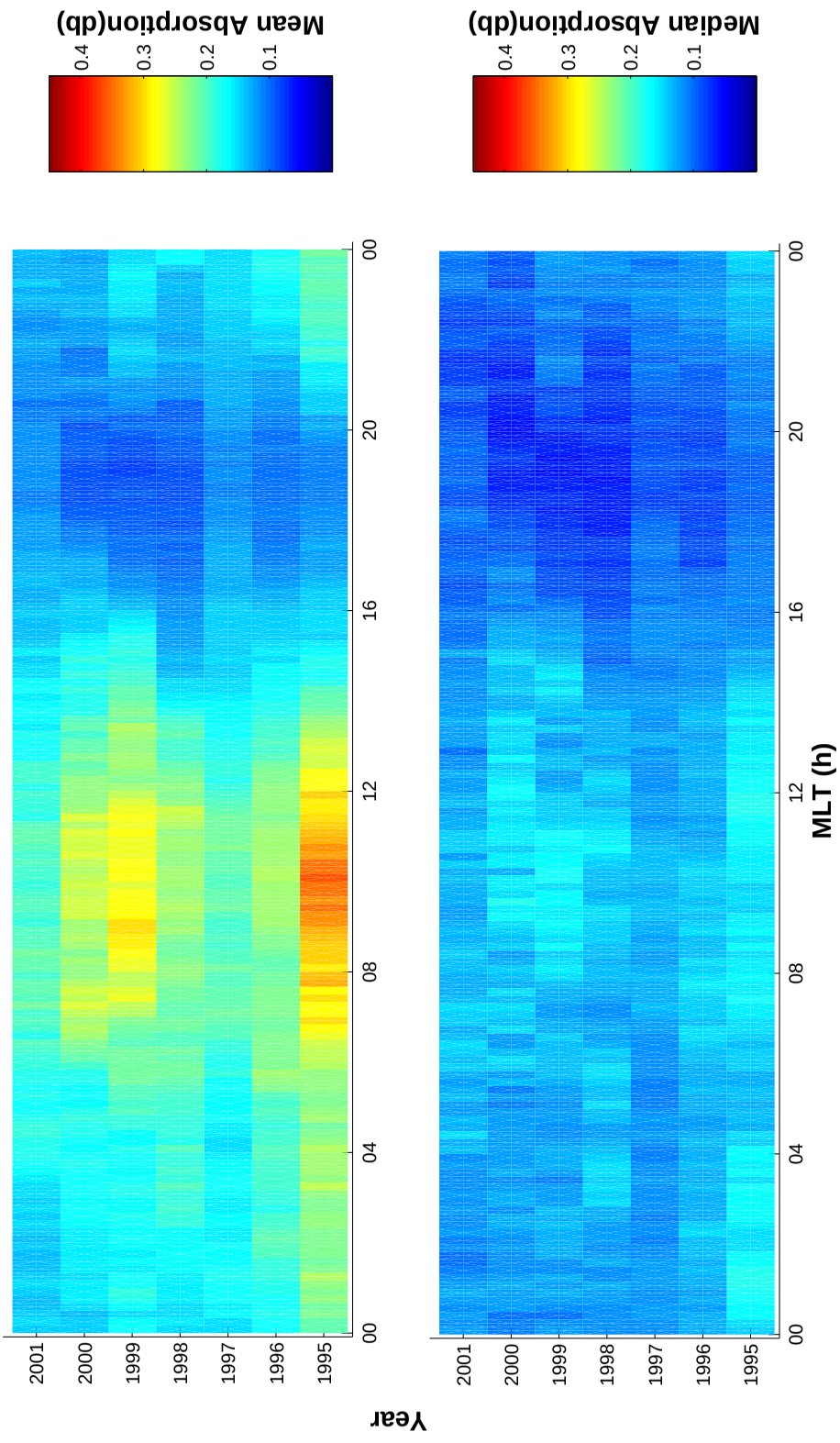

Figure 6.7. Mean and median absorption by magnetic local time for each year in the 1995 to 2001 epoch.

whereas the bottom panel shows the median absorption. The diurnal variation is obvious in the mean absorption data in 1995 reaching the highest level of 0.35 dB (at 10 MLT) whilst 2001 has the lowest maximum (0.2 dB). The median absorption demonstrates more variability between local times but the year to year trend is the same with highest levels in 1995 followed by a lull and then recovery. At 19 MLT the absorption in each year is separated by less than 0.04 dB. A maximum in 1995 (10 MLT) is very clear followed by a gradual decline to approximately half this value by 1997. The absorption then increases to a second peak of ~0.3 dB in 1999 before once again decreasing to a minimum in 2001 (~0.18 dB). The keogram of median values shows a similar yearly trend though the morning maximum has shifted to slightly later local times. A second peak is highlighted in 1995 close to midnight and the variation through the day is less smooth than for the mean values. The comparison of mean and median values indicates that in 1995 for example there were several very high values of absorption between 06 and 12 MLT, linked to discrete absorption events; this moves the mean to higher absorption levels.

After investigating absorption on a year-by-year basis the data are binned by season. Each season consists of three months of data from each of the seven years (~640 by 7 data points). Figure 6.8 contains four keograms; the panels from top to bottom represent winter (December to February), spring (March to May), summer (June to August) and autumn (September to November). Spring and autumn (panels (b) and (d) respectively) both exhibit the diurnal variation in absorption across all latitudes. There is a significant morning maximum towards the north of the array

during spring and pre-midnight there is less absorption at the poleward side of the field of view than at the same local time in autumn. The maximum in the autumnal data is smaller than that during spring and the increase of absorption in the evening is more evident in the north during autumn though the difference is only ~0.1 dB. Curiously the beam second from the top (beam 10 of IRIS) witnesses no drastic decrease in the late afternoon and evening, as is the case for spring; possible reasons for this are discussed in section 6.3.3.

Winter and summer (panels (a) and (c) respectively) present a very different picture of the changing absorption. The diurnal variation is less dramatic in the winter months with a shift in the maximum to later local times. Once again it is beam 10 that shows a strong difference from the expected trend; strong absorption (0.3-0.4 dB) occurs between 09 and 16 MLT. This is later than the maximum in the beam immediately south of this (beam 18) which peaks between 06 and 11 MLT (0.2-0.3 dB). This suggests a general poleward drift in the absorption, which intensifies with increasing latitude. The afternoon depression is later than previously observed and is displayed predominantly in the northern most beams (>66º Mlat). At lower latitudes the absorption is relatively steady, varying by less than 0.06 dB. Pre-midnight absorption is reduced in the higher latitude beams reaching levels of 0.15 dB compared with the 0.2 dB measured by beam 32 in the equatorward half of the field of view. The mean absorption during summer does not exceed 0.25 dB, though the afternoon/evening loss of absorption is still clear. The pre-midnight absorption is most evident in the poleward beams (with the exception of beam 3) and the keogram

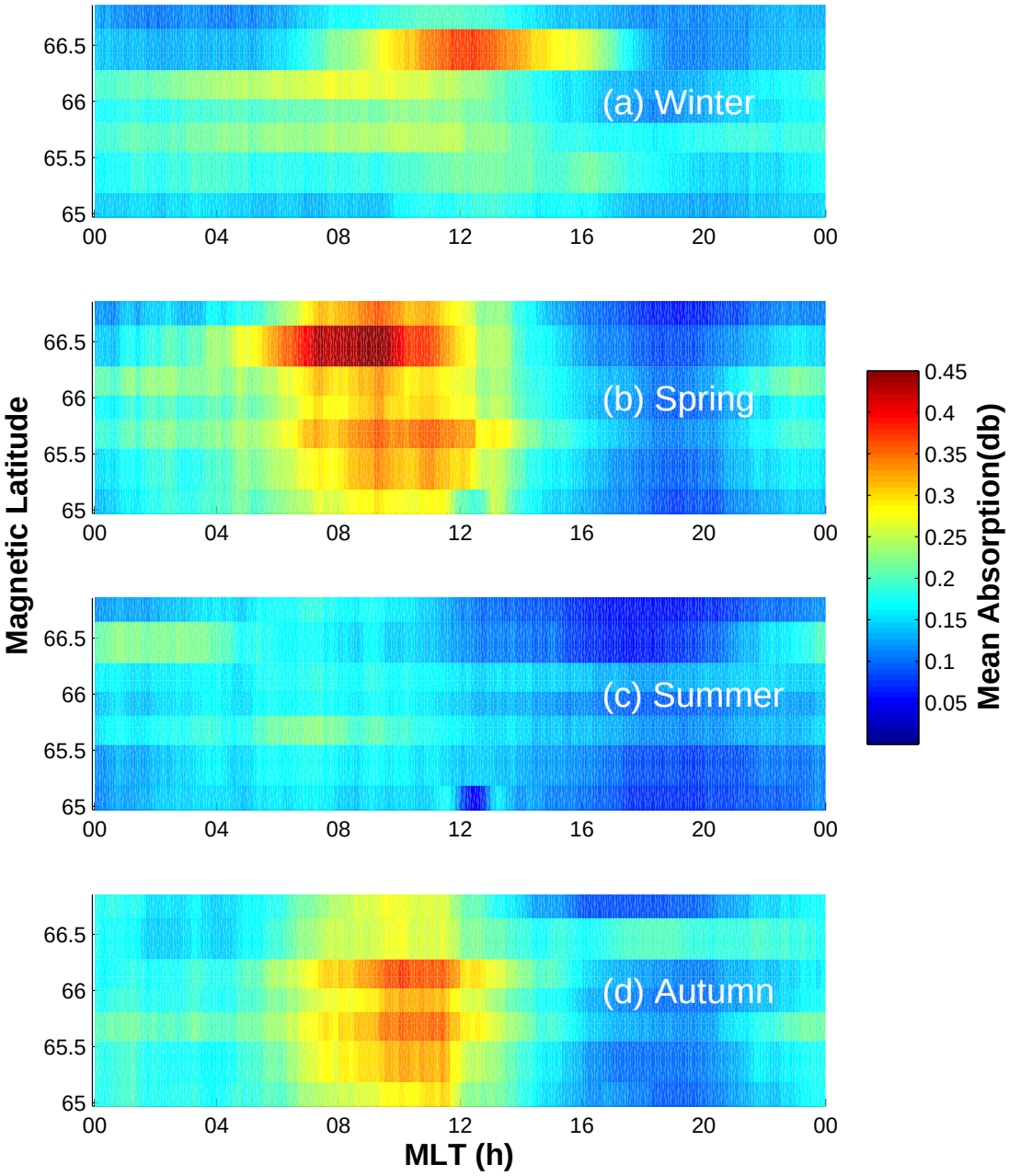

Figure 6.8. **Keograms for the mean absorption in each season calculated for the 1995 to 2001 epoch. From top to bottom the panels display: Winter (December to February), Spring (March to May), Summer (June to August), Autumn (September to November).**

gives the impression of an equatorward movement in the absorption region to later local times. In comparison with autumn and spring there is little variation and with winter there is significantly less absorption during the day, though night time (18 to 06 MLT) levels remain similar for all four seasons.

6.2.3 The Geomagnetic Effect

Since auroral absorption is primarily caused by energetic particle precipitation it is sensible to consider the effect that increased geomagnetic activity will have on the attenuation of radio waves in the auroral zone. In Figure 6.9 the occurrence distribution of the K_p index for the 1995 to 2001 epoch is presented. The distribution is skewed towards the lower values with the mode at K_p=1 and the median at K_P=2$^-$. Over 59% of the time is during quiet to low activity ($K_p < 2$). For only ~8% of the time (approximately 206 days worth of data) is activity high ($K_p > 4$), thus most observations of absorption will take place during quiet to medium activity levels. This distribution can be split into seasonal variations just as the absorption. Figure 6.10 shows four panels corresponding to winter, summer, autumn and spring (clockwise from top left). The distributions in the two equinoctial seasons display very similar patterns; the spring K_p peaks at 2$^-$ (10.3 % rather than 8.6 % in autumn). There are small increases in the autumn percentages at higher K_p (e.g. 1 % higher at K_p = 4), offset by similar levels at the very low activity levels. More marked differences are in the winter/summer distributions. The winter distribution appears to be broader than the summer. The low activity is much reduced in winter (3.5% lower

occurrence in both the 1^+ and 2^- K_p levels) whereas the number of examples of very low activity is much increased (4.2 % difference for K_p = 0). For higher activity winter has a higher occurrence of the 3^- to 4 K_p level, a total of 3.5 % difference in this medium to active conditions range. In general the distributions are broadly similar in the equinoctial seasons and both are significantly broader than the solstitial seasons.

Figure 6.11 displays the results of sorting the absorption into bins of K_p; the data are at 3-hour resolution to match the index and five levels of K_p have been chosen to provide a reasonable number of data points in each bin. The top panel displays the variation of the mean absorption from the zenithal beam (25) and the centre panel shows the median values. Both are spread across the range of magnetic local times. The bottom panel shows the number of data points in each local time bin. Each set of curves is colour coded to indicate the geomagnetic activity range they correspond to; this information is provided in the legend. The lowest index values are for Kp<1 (blue curve) where the mean absorption reaches a maximum of 0.11 dB at 15 MLT with a minimum of 0.06 dB at midnight; an insignificant difference. Median values tend to be consistently lower by a factor of ~0.02 dB. The green curve ($1 \leq Kp < 2$) illustrates the absorption variation with quiet conditions, peaking at 12 MLT (0.18 dB for the mean absorption). Instead of midnight, the minimum has shifted to evening (18 MLT). Once again the median values are consistently lower. Unsettled conditions are represented by the red line ($2 \leq K_p < 3$) and this displays broadly the same pattern as the previous activity level but here the absorption peaks around 09 MLT (mean=0.31 dB,

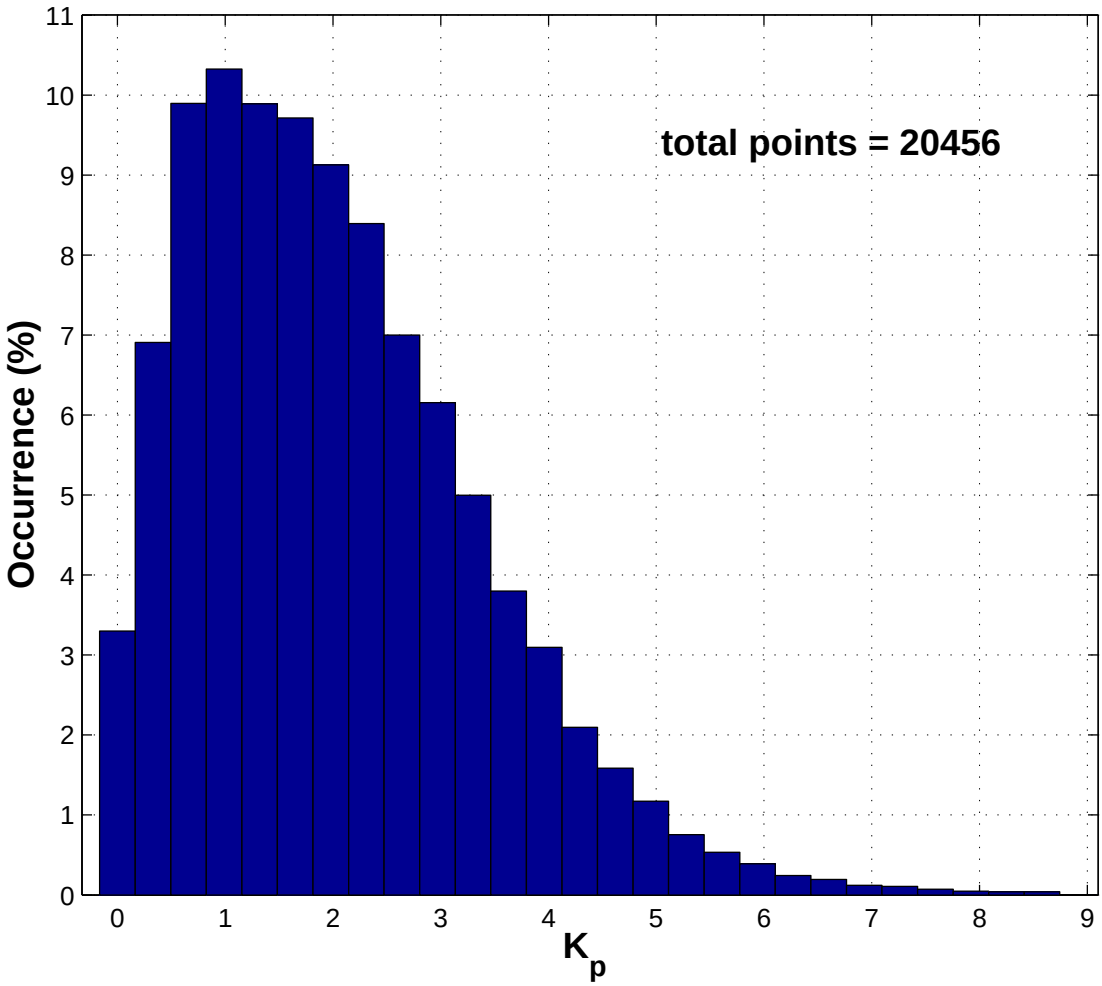

Figure 6.9. Distribution of 3-hour K_P from the 1995 to 2001 epoch. Occurrence is presented along the y-axis. The total number of data points are displayed on the plot.

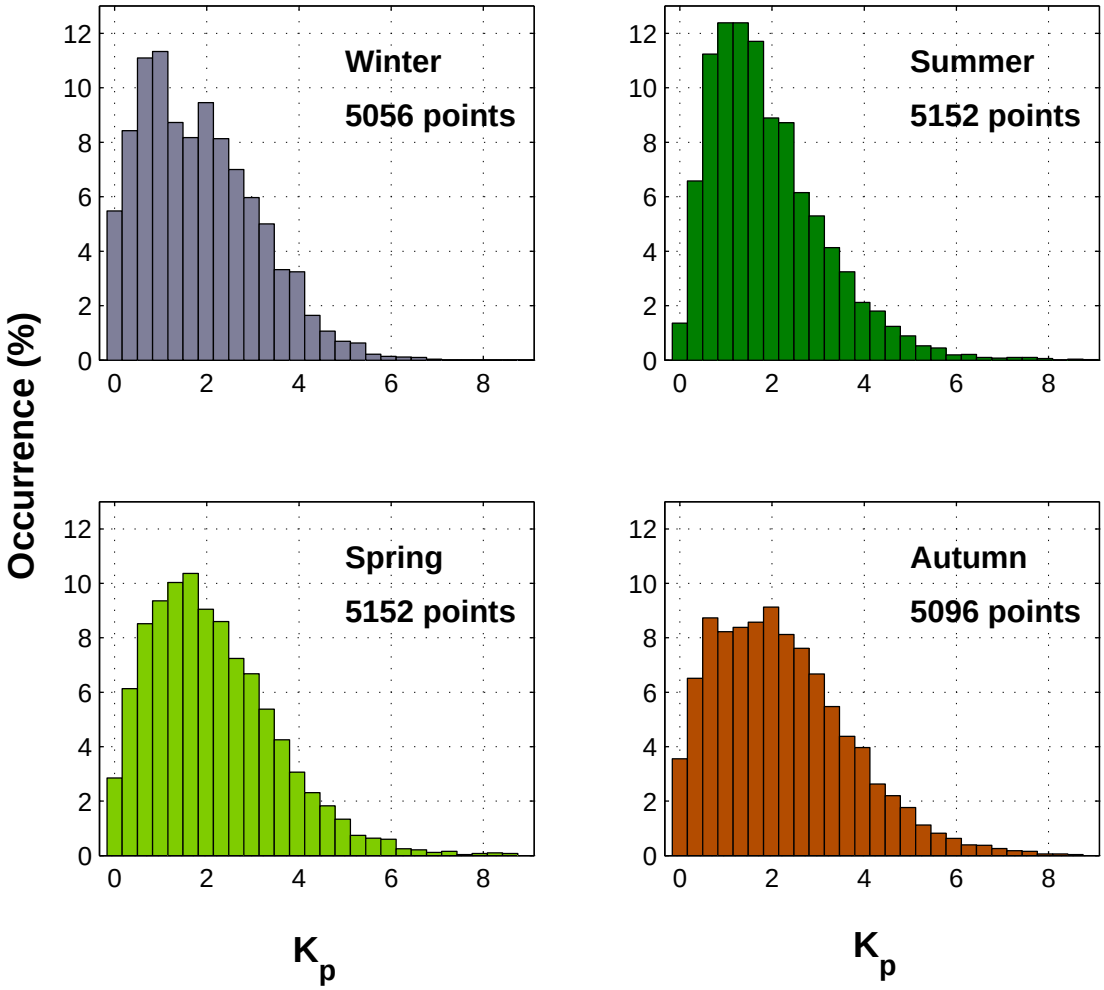

Figure 6.10. The occurrence of K_P in the four individual seasons, defined in the same manner as for Figure 6.9. The total number of points for each season is labelled on the graphs.

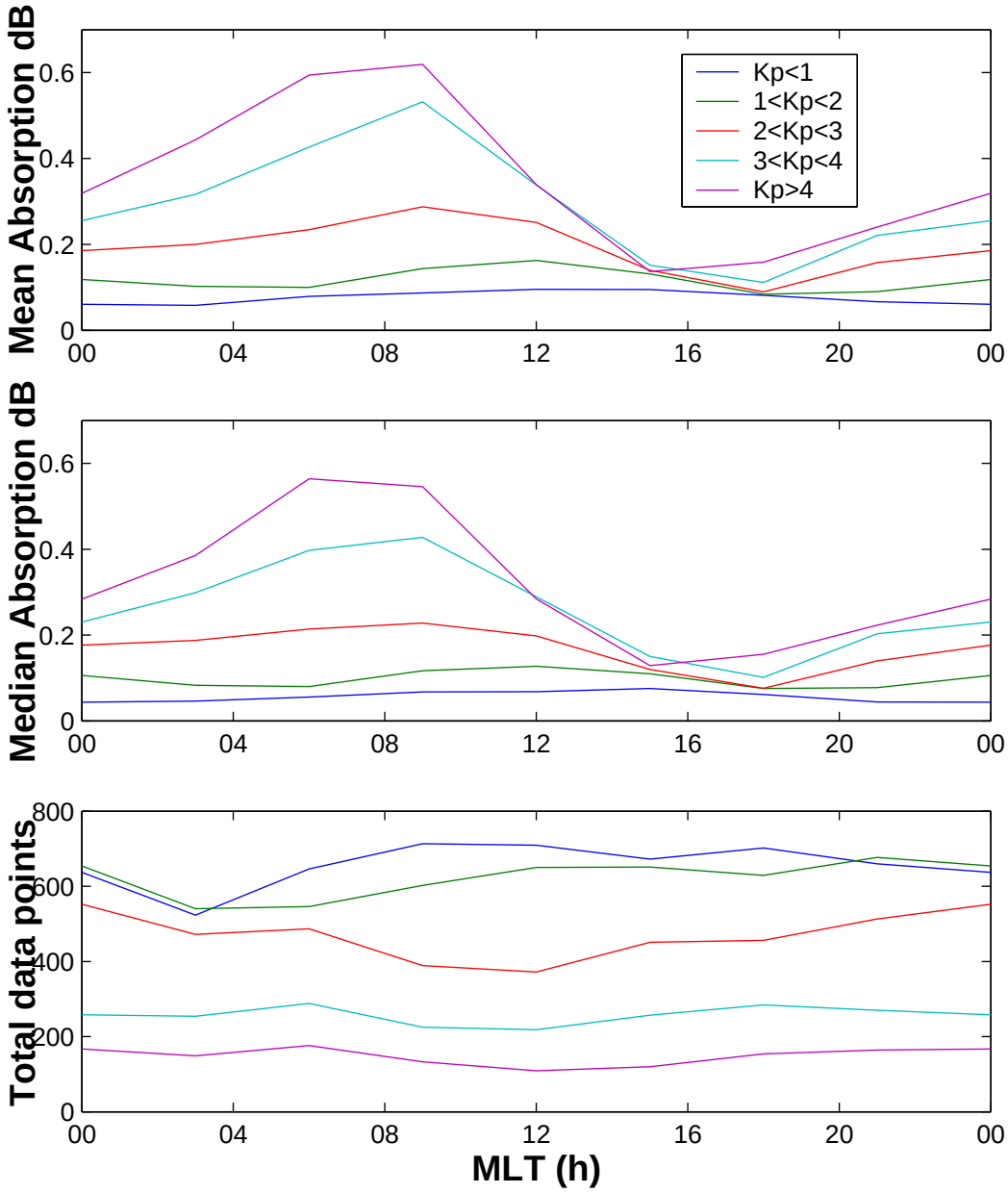

Figure 6.11. Daily variation of absorption in the zenithal beam binned by K_P. The top two panels represent the mean and median absorption respectively and the bottom panel demonstrates the variation of data points in each bin.

median=0.26 dB). During moderate geomagnetic activity ($3 \leq K_p < 4$) the mean absorption reaches a maximum of 0.5 dB (at 09 MLT) but dips to 0.13 dB in the afternoon. The mean and median values show little difference in the temporal structure. The final K_p bin uses all values of the index equal to or above 4 (purple curve). In this case the mean absorption maximises at 0.67 dB at 09 MLT and drops to 0.17 dB by 15 MLT. The median absorption peaks earlier in this range (06 MLT) but otherwise follows a similar pattern to the mean absorption. Only for the highest K_p range does the number of data points dip close to 100 and as would be expected it is the lowest activity bins that have the largest number of data points. Morning absorption levels show an increase with successively higher magnetic activity and in each case the point of minimum absorption lies between 15 to 18 MLT (except for $K_P < 1$ when it is at 00 MLT) and shows only small differences between the curves (~0.08 dB); at 09 MLT the variation is markedly higher with the lowest level being ~30% of the highest value. A diurnal variation is apparent in all but the lowest activity level, which changes by only 0.02 dB with the maximum occurring close to 15 MLT. This maximum point moves to earlier local times with each successively higher range of activity, until it reaches 09 MLT.

By considering the distribution of absorption at each level of K_p more information on the dependence of absorption on geomagnetic activity can be discerned. Figure 6.12 is composed of eight images displaying the absorption against K_p for each local time point. Occurrence is colour coded as a percentage with red being the highest (4.5%) and white indicating zero; percentages are plotted to 0.1%

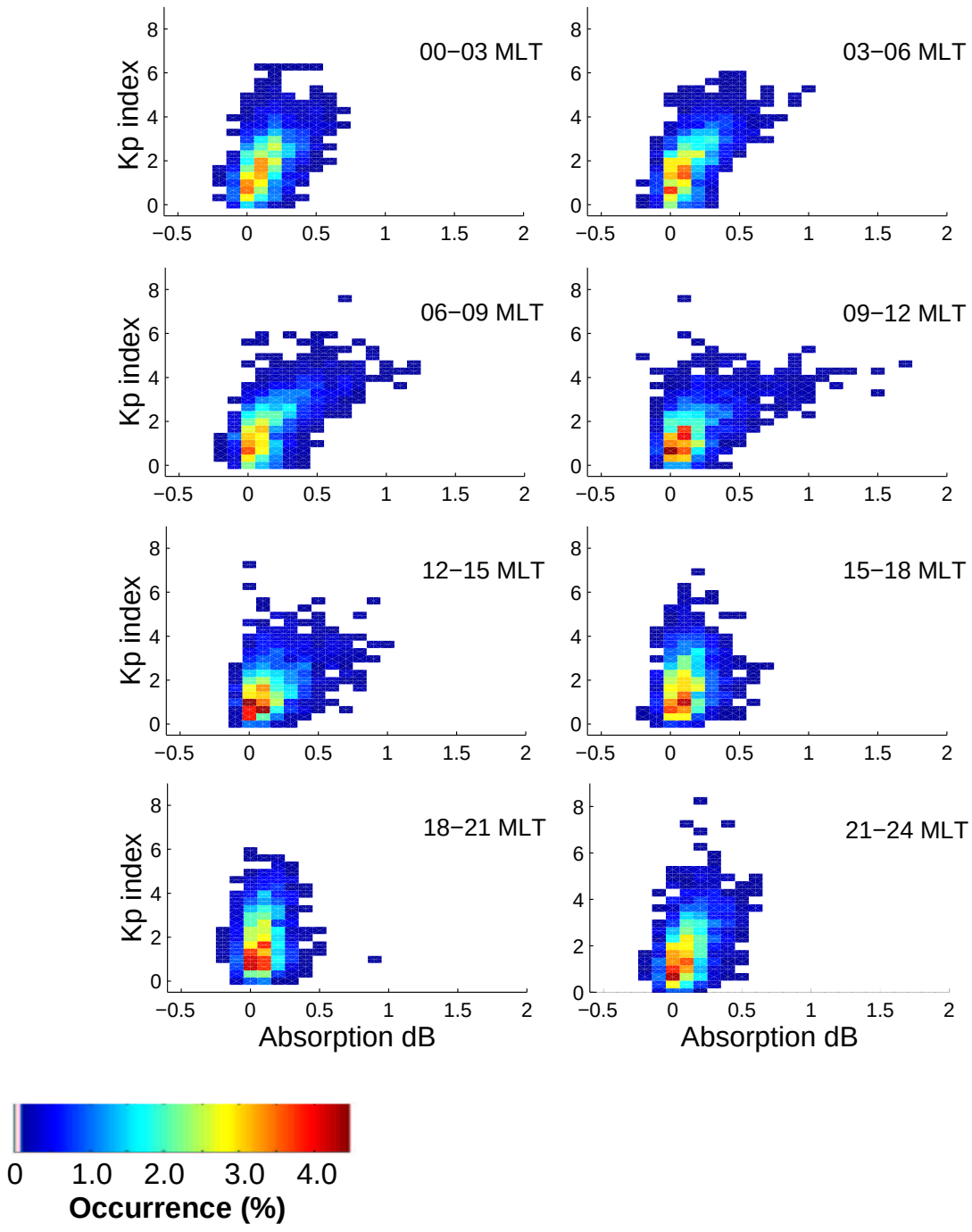

Figure 6.12. Distribution of absorption with K_P in the zenithal beam, calculated for 8 magnetic local time ranges.

accuracy. Absorption has been sorted into 0.1 dB bins taken from –0.1 to 5 dB. The x-axis of each of the plots has been limited to 2 dB since all absorption higher than this falls well below the 0.1% level. In every case the highest percentage is at the low K_p values and around zero; those negative values that have been included make up less than 4% of the total number of points at each local time. The 00 MLT plot (a) indicates a tilt in the data to higher absorption at higher K_p, but the absorption is restricted to lower than 0.7 dB. By 03 MLT (b) the absorption has extended to 1 dB at the top end of the K_p range, though the majority of absorption is within 0.4 dB. At the next time step (c), absorption levels have exceeded 1 dB though the occurrence is still very low and by 09 MLT (d) a maximum of 1.7 dB at the 0.01% level is recorded. This occurs at $K_p = 5^-$ and the spread of K_p values at 0.5 dB has increased from the previous time step. The next image (e) represents the 12-15 MLT time range and in this case the absorption has shrunk to a maximum of 1 dB again, but at 0.5 dB there are a broad spread of K_p values represented (1^- to 6^-). The shrinking absorption has continued into 15 MLT (image f) and again to 18 MLT (g) where the majority of absorption is safely within 0.5 dB. In the final image (h) at 21 MLT the absorption has once again started to tilt to higher K_p levels. So with each successive time step the distribution curves over to increasing absorption until 09 MLT. After this the absorption recedes such that by 18 MLT the absorption is restricted to 0.5 dB across the range of K_p. The absorption displays most curvature at 09 MLT and is most linear at 18 MLT.

Due to the restricted resolution of the K_p index it is desirable to observe how the absorption is affected on smaller time scales using a different indicator of geomagnetic activity. The obvious choice for examining absorption in the context of the auroral regions is to use the AE index. However as discussed in Section 6.2, there are restrictions imposed due to the quality of the data at this time. Three levels of activity have been used in Figure 6.13 to determine mean absorption keograms; these levels reflect large differences in the auroral activity. Once again absorption is plotted against magnetic latitude and magnetic local time; the activity is indicated on the plot by the AE values. The top panel shows mean absorption for AE < 150; the diurnal variation is readily apparent reaching a maximum of 0.28 dB at ~09 MLT across most of the beams and the midnight sector absorption peaks at 0.18 dB. In the middle panel the absorption is for $150 \leq AE < 300$ and a significant rise in absorption levels occurs during the morning sector; this effect is repeated for $AE \geq 300$. In each case there is no evidence of a latitudinal difference in the absorption data and no local time shift with increased activity. The pre-midnight values show little difference between the middle and bottom panels. Figure 6.14 uses the same AE bins but this time displays curves for the zenithal beam for the occurrence of absorption ≥ 1 dB; a parameter that has often been used in investigations of absorption statistics (e.g. Foppiano and Bradley, 1984). For the data in the lowest activity range (blue curve) there are two peaks, the largest in the morning sector at 2.4 % and the second at midnight (0.4 %). At the next level of activity (green curve) the morning peak has increased to 6 % whereas the peak at midnight is still at 0.4 %. By the highest level of activity (red

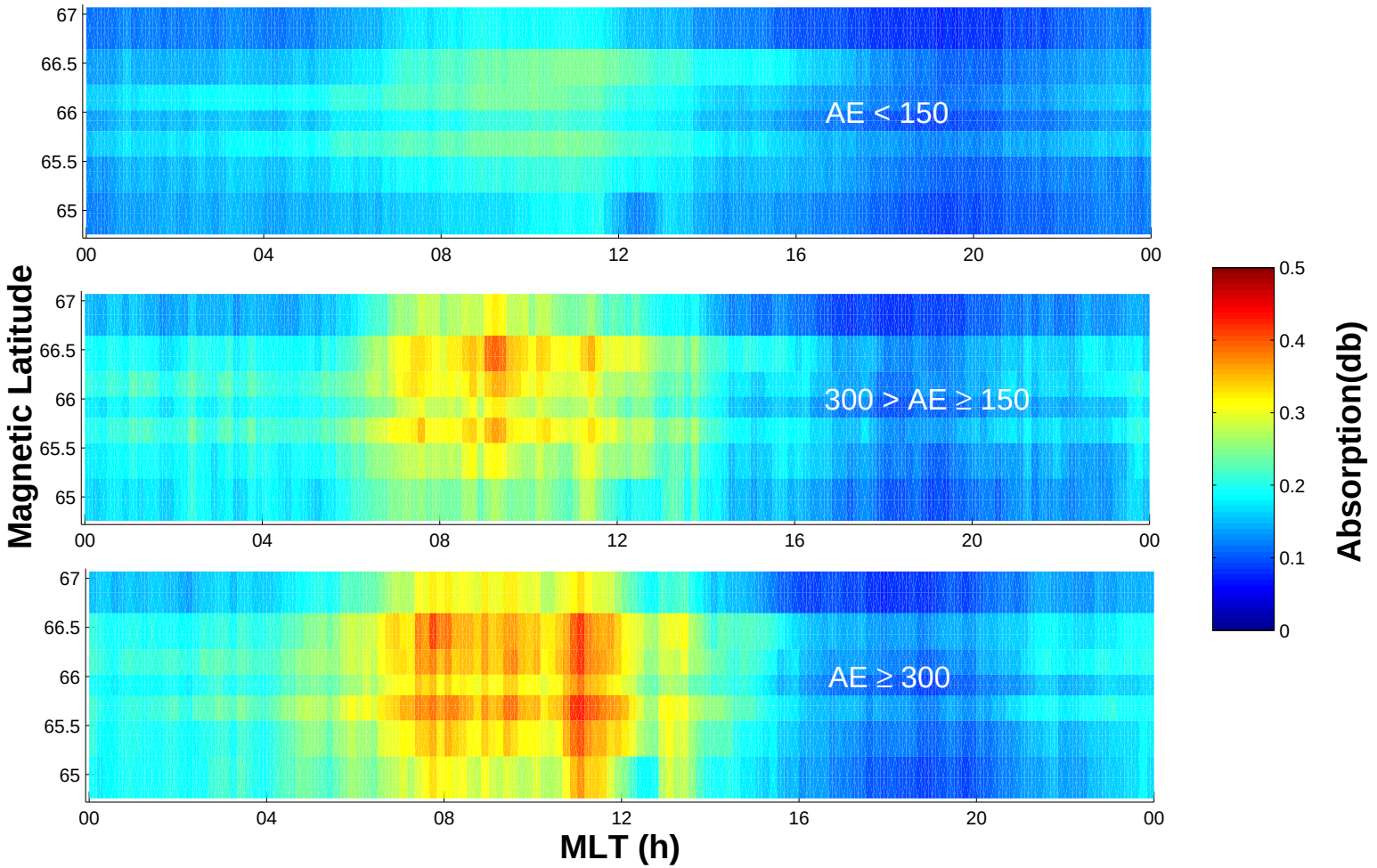

Figure 6.13. **Keograms of mean absorption for the epoch 1997 to 2000 (inclusive) for three ranges of the AE index.**

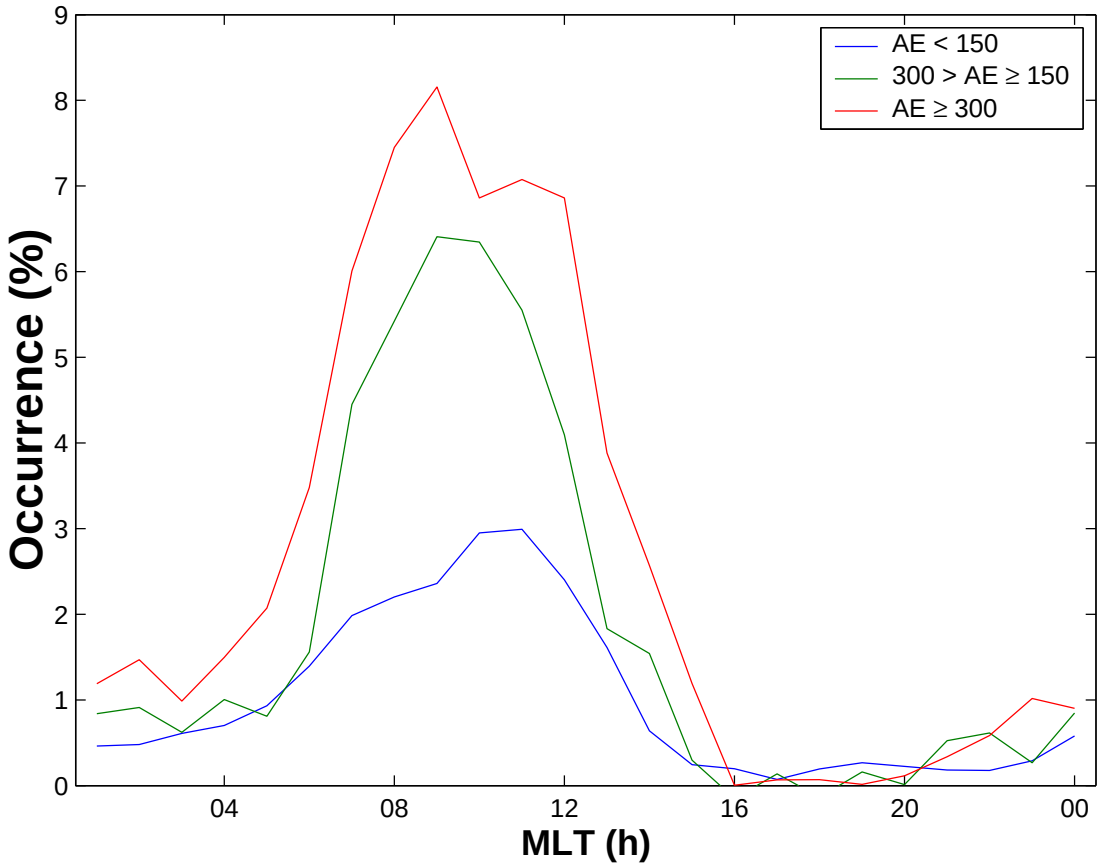

Figure 6.14. The occurrence of absorption exceeding 1 dB at the three ranges of AE from Figure 6.13. This parameter is often referred to as Q(1)

curve) the morning peak has shifted to an earlier local time (09 MLT) and reached an 8 % chance of occurring. In all three instances the afternoon minimum is clearly present and reaches 0 % at 18 MLT.

6.2.4 IMF induced variations in absorption

So far the dependence of energetic precipitation (with auroral cosmic radio noise absorption as a proxy) on season and geomagnetic activity has been presented. In this section the focus will shift to the interplanetary magnetic field, which is known to produce changes in the geomagnetic activity and particle precipitation in the ionosphere. Figure 6.15 consists of two distribution plots for the IMF B_Y and B_Z components. The data are at 5-minute resolution and have been sorted into 0.5 nT bins. The top panel presents the occurrence of the B_Z illustrating a normal distribution with $B_Z = 0$ for 7.4% of the time from 1995 to 2001; thus for roughly 46% of the time the IMF was southward. The B_y distribution is significantly different being broader and lower. Rather than perfectly normal, the distribution might be represented by the sum of two Guassian distributions; one centred at +2 nT, the second at –1 nT. The overall outcome is that there is a slight bias in the IMF data to eastward (+ive) values.

The absorption data for 1995 to 2001 is now sorted by IMF clock angle quadrant; Figure 6.16 displays four keograms of the results of this binning. Each shows the variation of the mean absorption with magnetic local time at each of the latitudes provided by the spread of IRIS beams. The top two panels present data for northward IMF, the first (a) is for eastward IMF whilst the second (b) is for westward

values. Both show very similar distributions, with the now familiar diurnal variation across all latitudes. For the western values there is a slight increase in the absorption around midnight over the eastern counterpart, this leads to a second minimum in the data at 04 MLT before an apparent earlier increase to the high morning values. The absorption peaks at 0.35 dB for the eastward IMF and at 0.3 dB for the westward. The usual minimum is still in the evening sector (~20 MLT) where the absorption dips to almost zero.

After considering the northward IMF, the next two panels use data from southward-directed field. Panel (c) is for southeast conditions and panel (d) is for southwest. A large rise in absorption levels over the northward IMF is evident. Absorption greater than 0.25 dB begins before midnight and stretches around to the morning sector, increasing to a plateau of ~0.38 dB at 06:30 MLT in panel (d) and 0.32 dB in panel (c). Following the usual rapid drop in the afternoon sector, the absorption reaches a minimum of ~0.1 dB in both cases, however this now occurs at about 19 MLT. The general trend of absorption appears to be earlier increases for westward IMF over the eastward values and a shift of the minimum to earlier hours. Southward IMF also leads to mean absorption values at least two times higher than those during northward IMF conditions.

Figure 6.17 uses the occurrence of absorption above 1 dB in the zenithal beam binned by IMF B_Z in steps of 2 nT. For the northward IMF ($B_Z > 0$) the occurrence is always below 4.2 % and displays no trend with increasing/decreasing values of B_Z. When the IMF turns southward there is a drastic change in the occurrence. Each

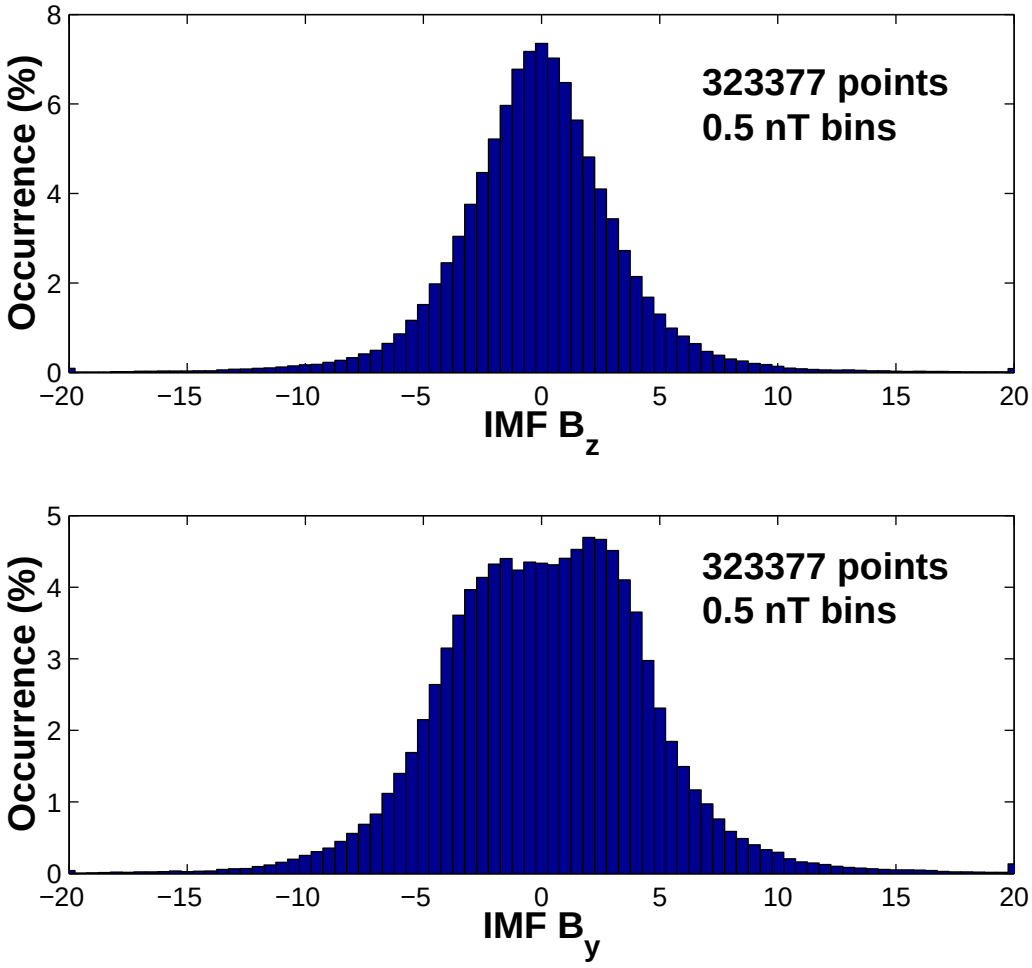

Figure 6.15. **Distribution of the B_Z and B_Y interplanetary magnetic field components. The top panel shows the northward component (B_Z) which follows a normal distribution. In the bottom panel the eastward (B_Y) component demonstrates a bias to the east over the west.**

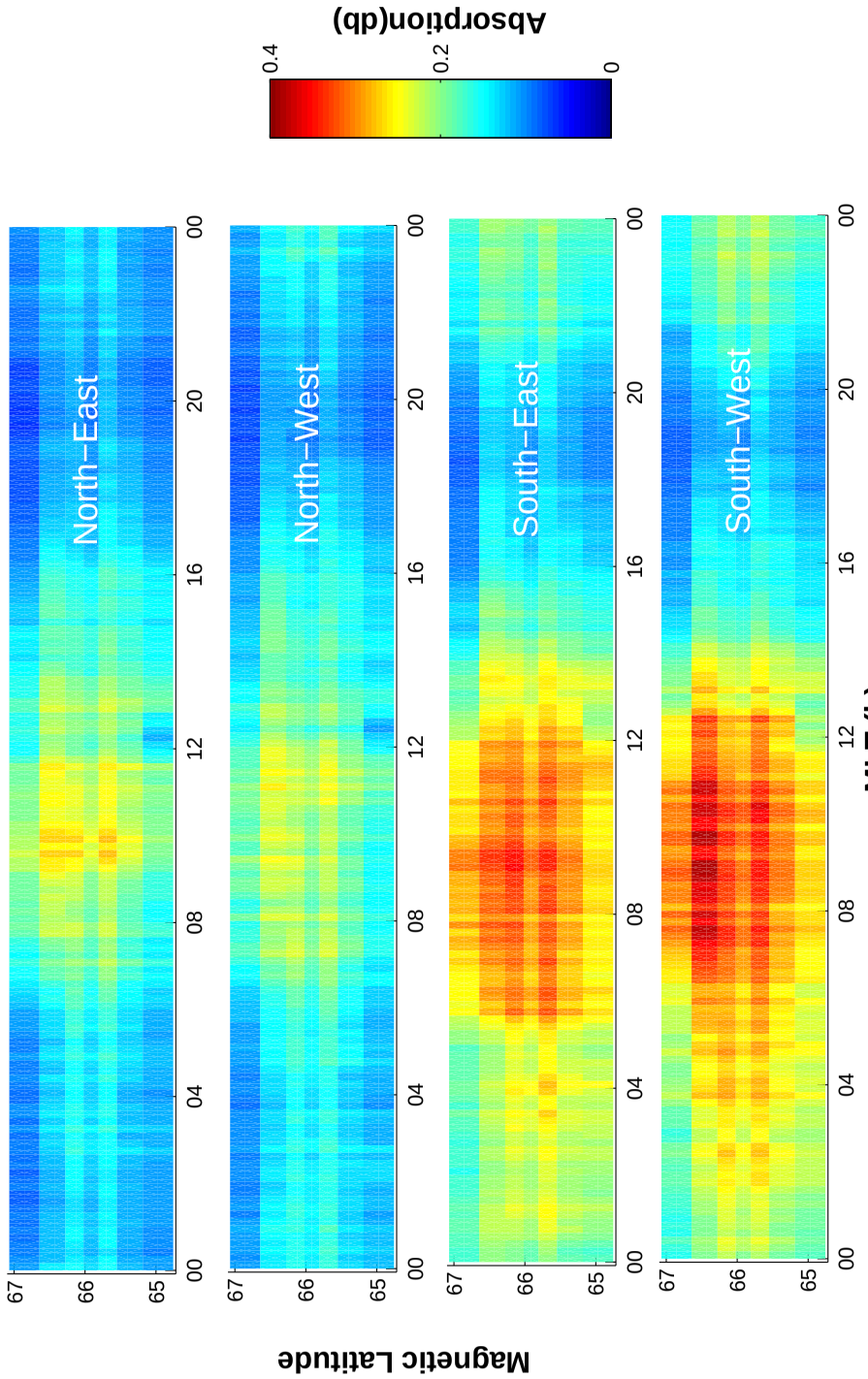

Figure 6.16. **Keograms of the mean absorption after the data has been binned into the 4 quadrants of the IMF clock angle.**

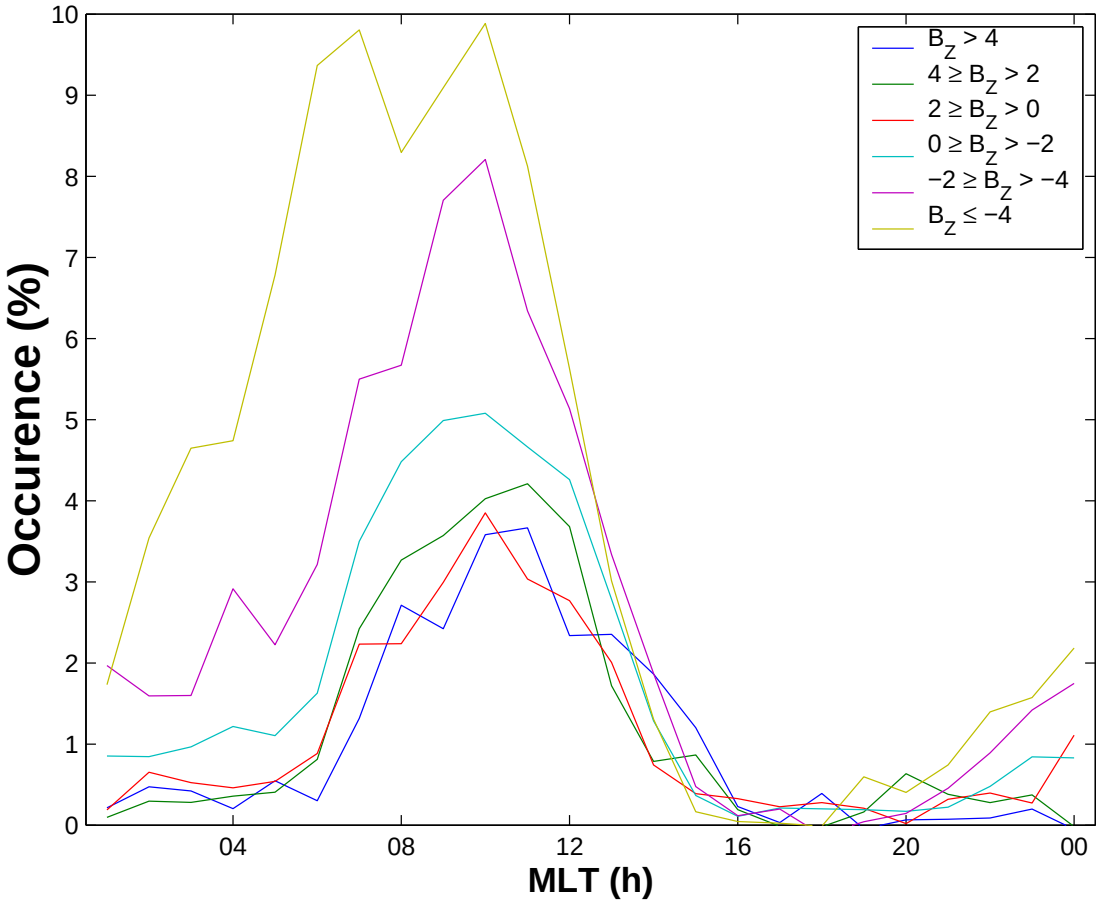

Figure 6.17. Occurrence of absorption exceeding 1 dB (Q(1)) for six ranges of IMF B_Z. Data are presented as hourly averages.

successively lower value of B_Z leads to a higher occurrence of the ≥ 1 dB absorption, such that for $B_Z \leq -4$ the occurrence peaks above 9 %.

6.2.5 Solar Wind effects

The second extra-terrestrial effect most likely to ring changes in the magnetosphere is the solar wind. Shocks from high-speed interactions lead to geomagnetic storms and the pressure on the magnetosphere is thought to influence the wave particle interactions that produce precipitation. The dynamic pressure has been calculated using the formula:

$$P_{dyn} \sim m.\rho.v^2 \qquad (6.1)$$

Where *m* represents the average mass of the main constituents, usually taken to be protons, and ρ is the proton number density. Figure 6.18 presents the occurrence distribution of solar wind pressure. Data have been sorted into 1 nPa wide bins and the percentage occurrence is plotted against the pressure. Values can exceed 100 nPa during high-speed streams and CME interactions with the magnetosphere, however the majority of pressure remains lower than 20 nPa (99% of the total) with only 3 nPa being the mode value. The second panel shows the distribution zoomed into the 0-20 nPa range, close to a Maxwellian distribution; very little pressure occurs above 5 nPa (<20%).

Figure 6.19 shows three keograms of the same format as Figure 6.4, this time binned by solar wind pressure; each of the ranges is displayed in the panel. All three

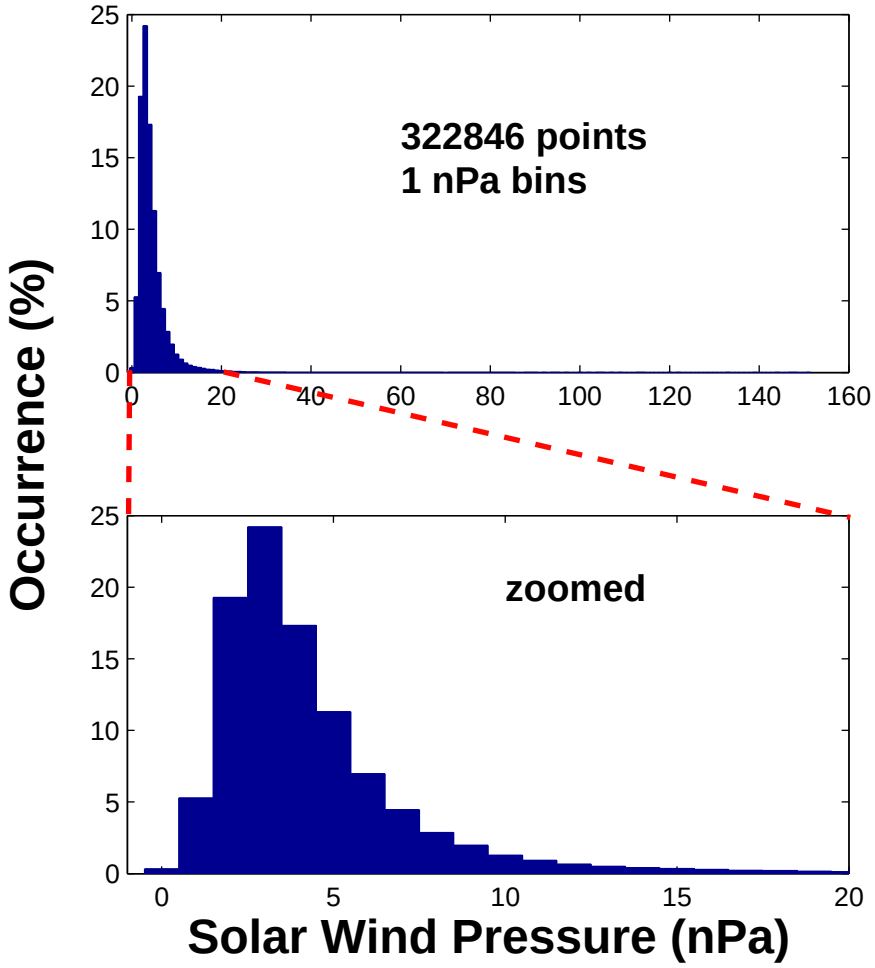

Figure 6.18. **Distribution of solar wind pressure values from 1995 to 2001 inclusive. Dynamic pressure is less than 20 nPa for over 90% of the time as demonstrated by the bottom panel**

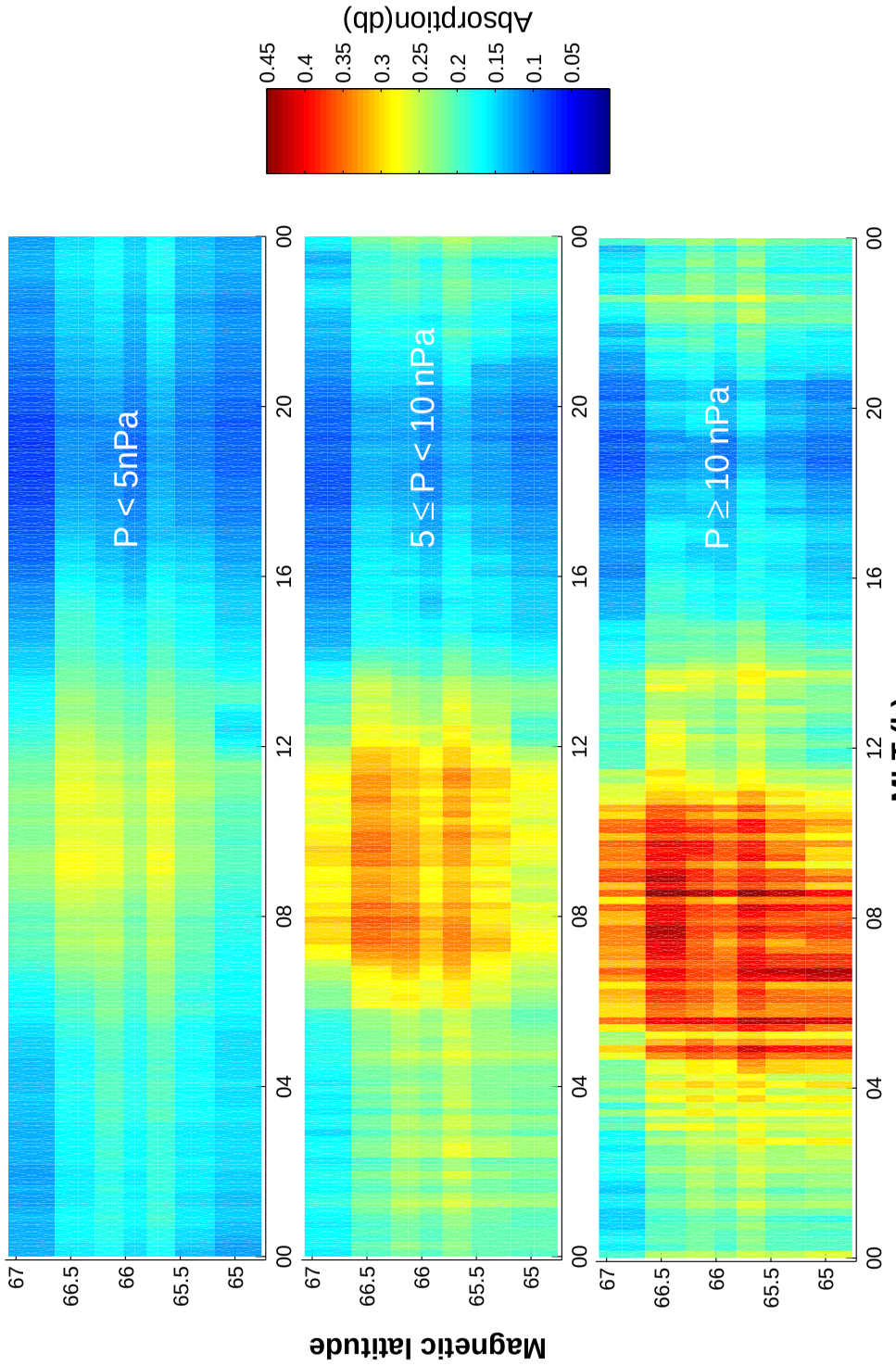

Figure 6.19 Keograms of the mean absorption arranged by solar wind pressure in three ranges.

show a diurnal variation with maximum in the morning sector and minimum in the evening. For the lowest pressure (top panel) the mean absorption peaks at 08:30 MLT (0.3 dB), remaining high until 12 MLT when it starts to decrease reaching 0.1 dB by 18 MLT. For $5 \leq P_{dyn} < 10$ nPa (middle panel) the maximum value occurs at 07:30 MLT, levelling until midday and then decreasing. Dynamic pressure over 10 nPa produces an absorption peak much earlier, pre-dawn at 04:45 MLT, before dropping just before midday. The minimum once again occurs around 18 to 19 MLT. With increasing pressure thresholds the absorption in the midnight sector also increases by 1.5 dB across the three distributions. In the first two plots the absorption appear higher in the morning sector at the higher latitudes. By the final plot, absorption is relatively uniform across the array.

Finally observations of mean absorption values are linked to the changing solar wind. Figure 6.20 provides the solar wind velocity distribution. This ranges from 250 to 900 km/s in 10 km/s bins. A small bump appears in the tail of the velocities at ~550 km/s, possibly due to the removal of high-speed data that overtake slower streams. By far the most commonly occurring velocities lie between 300 and 500 km/s. Figure 6.21 consists of five magnetic local time keograms that show the latitudinal variation of the mean absorption for successively high solar wind speeds. For velocities less than 300 km/s (top panel (a)) the absorption appears sporadic and low, never exceeding 0.2 dB. At the next level of velocity (b) a diurnal variation has reappeared though absorption is still low (>0.25 dB). In the middle panel (c) the mean absorption is from values corresponding to solar wind velocities between 400 and 500 km/s.

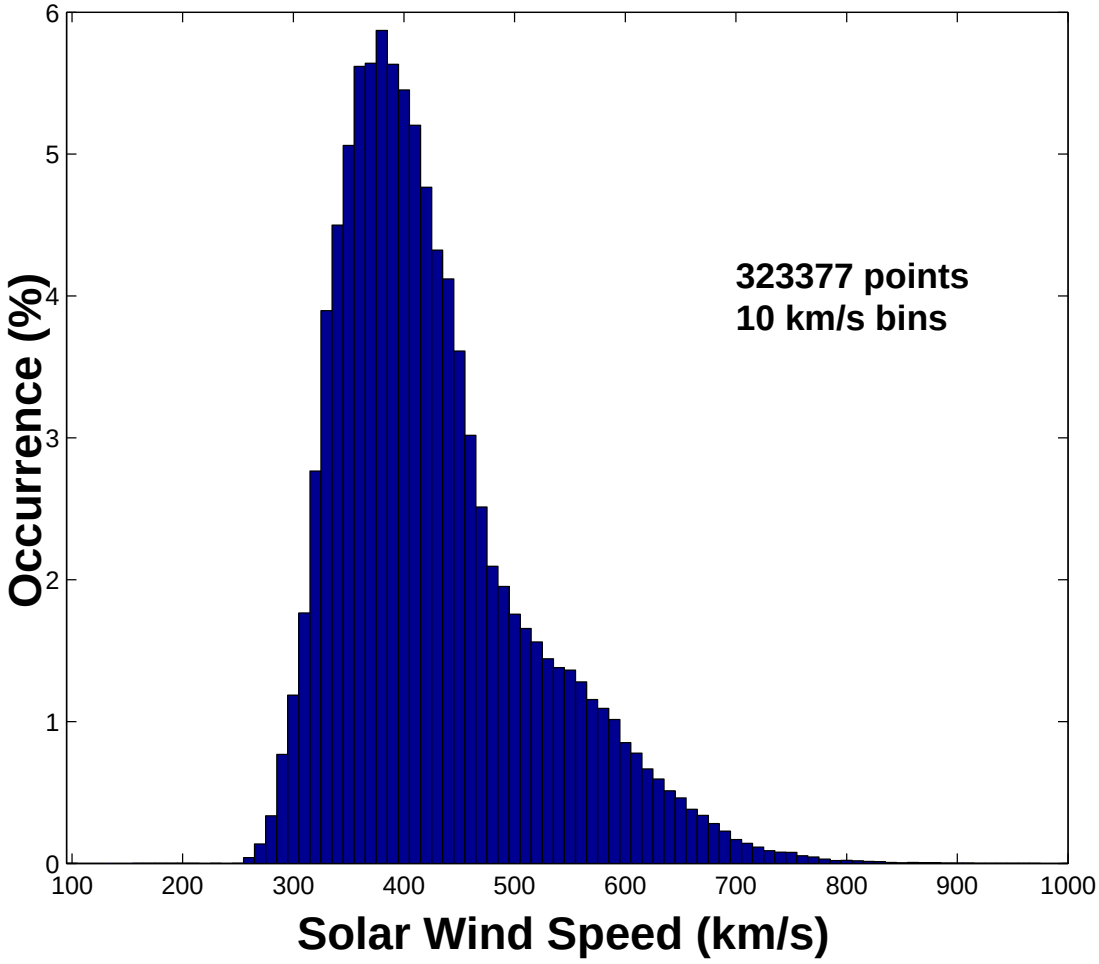

Figure 6.20. **Distribution of solar wind velocity from 1994 to 2001 (10 minute resolution) in 10 km/s bins. The bump in the tail of the distribution is likely due to the periods of missing data when high and low speed streams interact.**

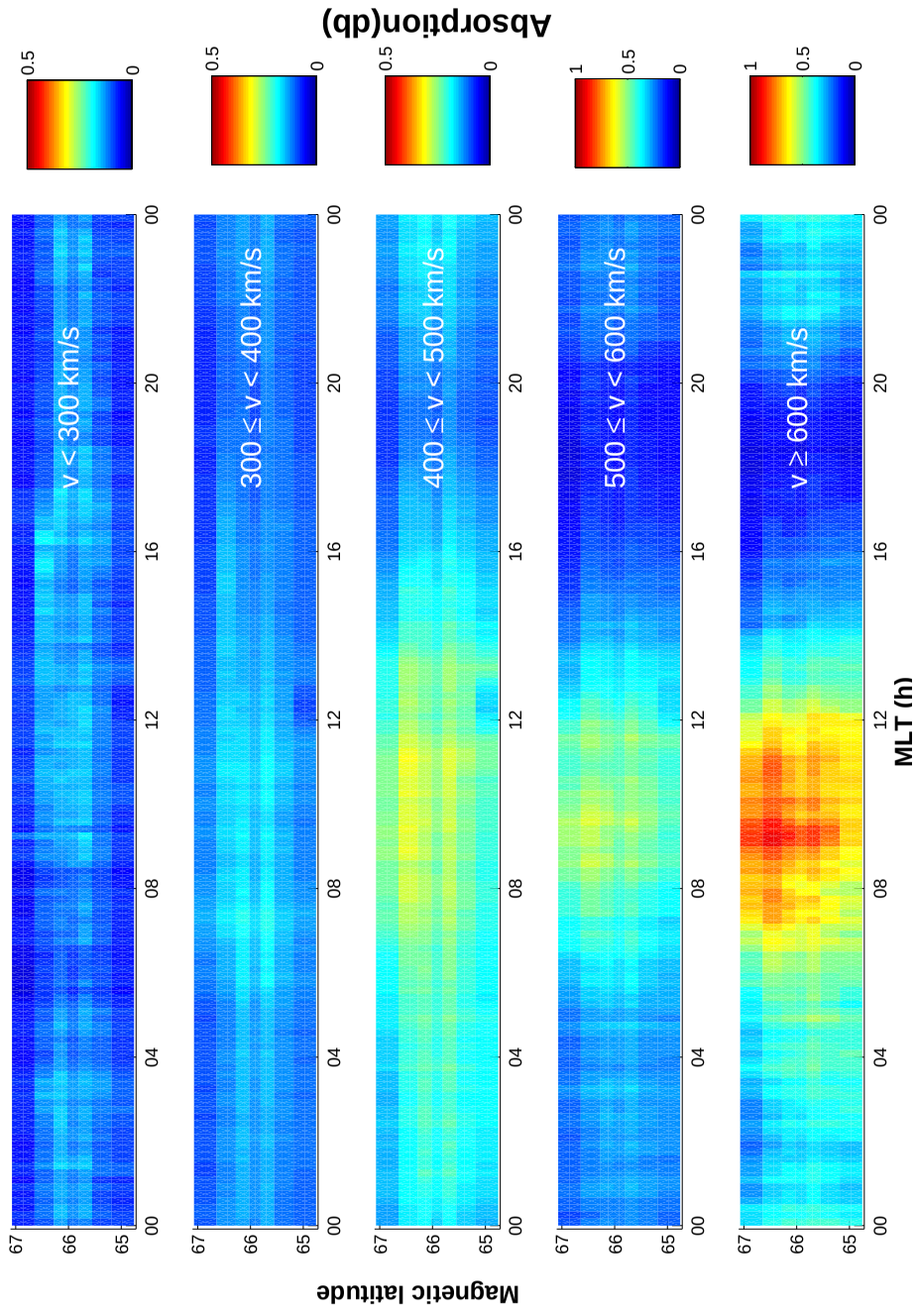

Figure 6.21. **Mean absorption keograms for 5 ranges of solar wind speed. Note the different colour bars between the first three and last two plots.**

Absorption appears to be stronger at the higher latitudes during both the morning (0.3 dB) and evening (0.2 dB) sectors. It must be noted that for velocities greater than 500 km/s the absorption colour scale extends twice the previous range. The fourth panel covers velocities between 500 and 600 km/s. Once again the mean absorption is higher at the north end of the array, reaching 0.6 dB in the morning. This pattern is repeated for $V \geq 600$ km/s (bottom panel) with absorption reaching close to 0.8 dB. No shift in local time occurs and the minimum value is consistently low (0.1 dB) in the afternoon/evening sector. The difference between absorption levels for each velocity range is more apparent in Figure 6.22 where absorption curves are plotted for the zenithal beam. In each case the absorption is variable from one time point to the next, regardless of the number of points that are used to derive the mean value. For $V < 300$ km/s (blue curve) the absorption fluctuates around 0.1 dB with no structure whereas for those velocities between 300 and 400 km/s (green curve) a distinct diurnal variation can be seen. This is more pronounced with increasing velocity, however the absorption level always dips to between 0.08 and 0.14 dB from 17 to 20 MLT. The general trend is that high velocity leads to high morning and medium pre-midnight absorption with a strong minimum around dusk.

In order to further study the dependence of absorption on solar wind speed, the distribution of absorption against solar wind speed is calculated for a number of time spans in the day. Figure 6.23 repeats the format of Figure 6.6 with the absorption this time averaged over local time ranges (indicated on each plot with the number of data points) for solar wind speed steps of 25 km/s. The occurrence ranges from 0.01 to 10

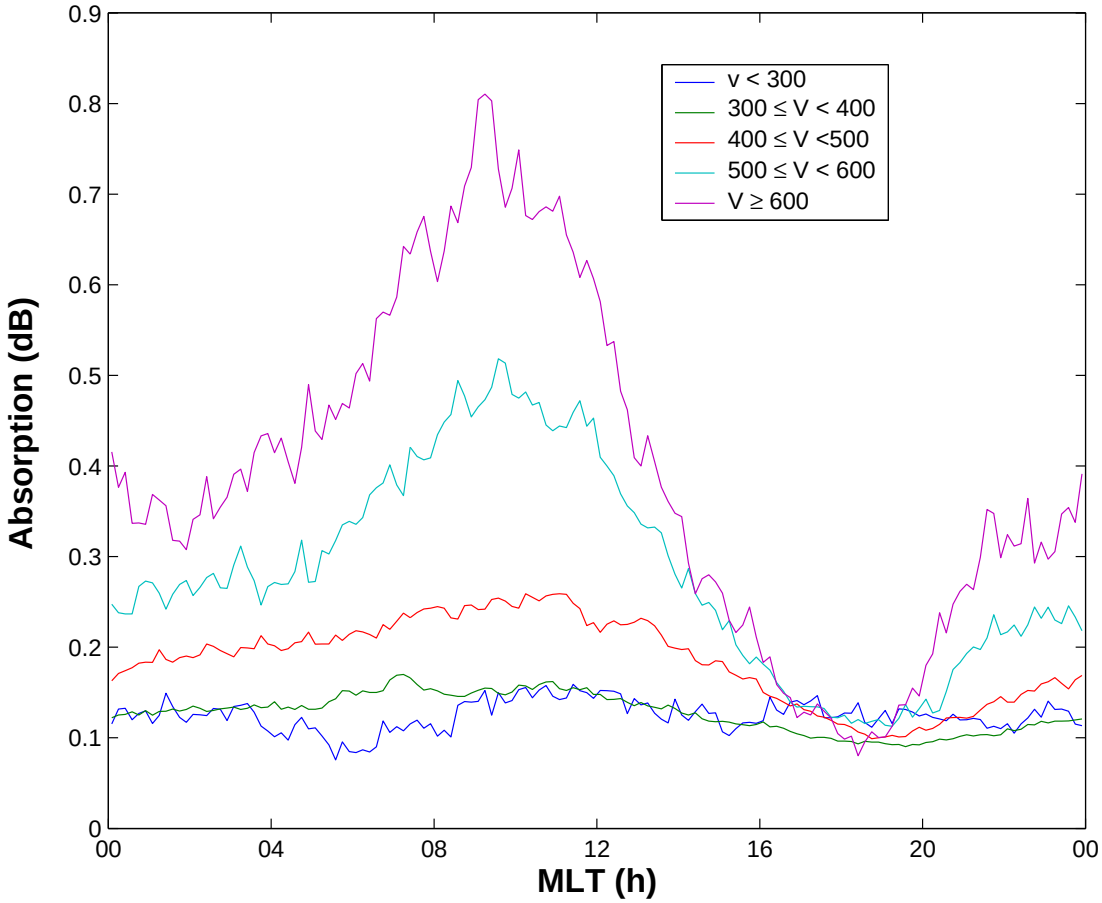

Figure 6.22. Magnetic local time variation of absorption in the zenithal beam for the five ranges of solar wind speed used in Figure 6.21.

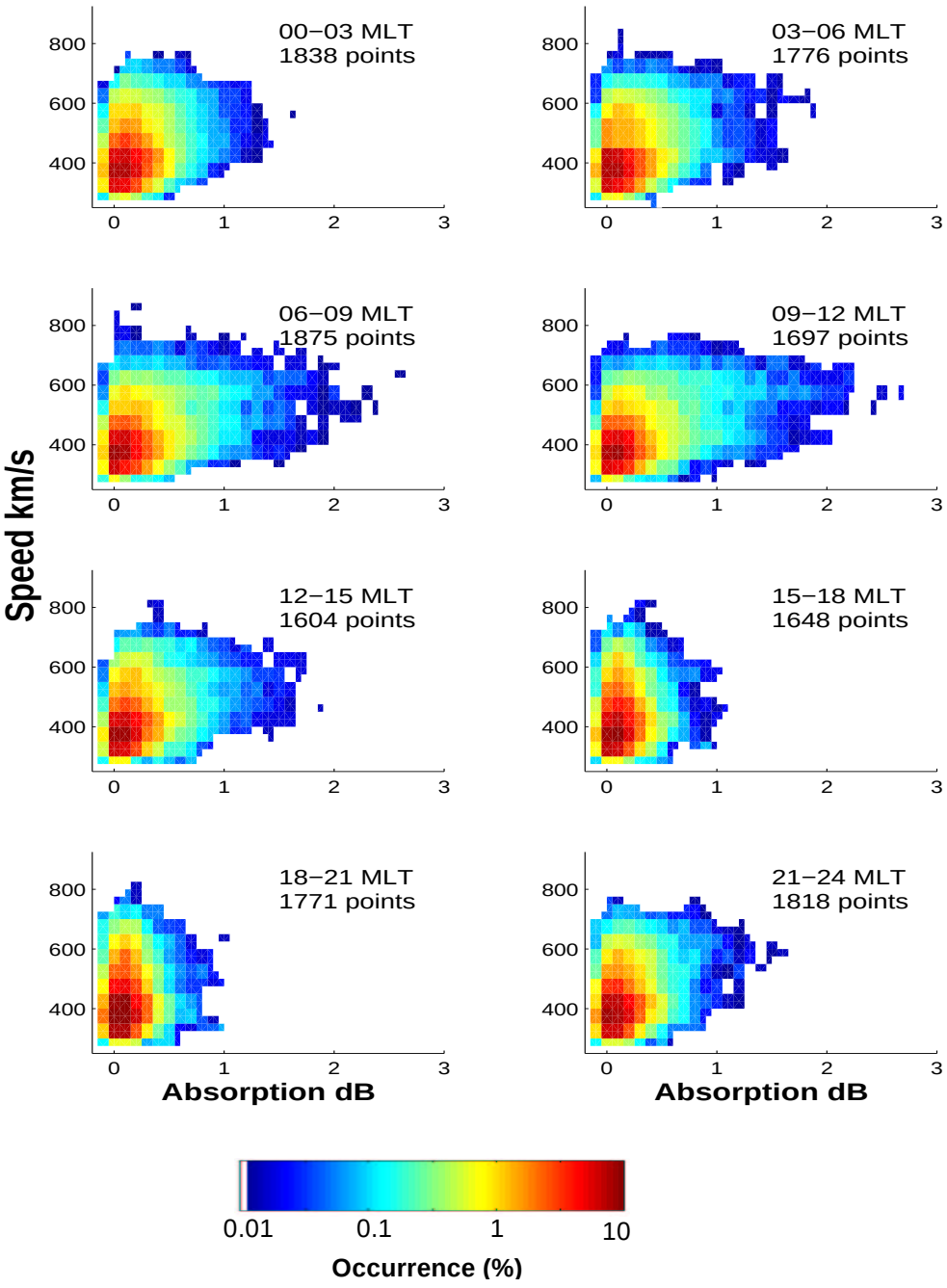

Figure 6.23. Distribution of absorption in the zenithal beam with the solar wind speed, calculated for the 1995 to 2001 epoch. Note that the colour scale is logarithmic.

% and the colour scale is logarithmic. From 00 to 03 MLT the strongest absorption occurrence is for low solar wind speeds and absorption below 0.5 dB (to the 1% threshold). Between 400 and 675 km/s the absorption extends to 1.3 dB at the ~0.03 % level. At the next time range (03 to 06 MLT), the absorption within this range has extended to 1.6 dB, though at lower solar wind speeds it is confined to ~0.5 dB. Entering the post-dawn sector (06 to 09 MLT) the absorption at the 0.03% level has reached over 2 dB and there are accompanying increases at the lower and higher solar wind speeds. By 09-12 MLT the absorption is peaking at 2.6 dB, though for the lowest occurrence plotted the 1 dB mark has been passed by values corresponding to 300 km/s. After midday (12-15 MLT) the absorption recedes again (1.8 dB) continuing this trend into the late afternoon (16-18 MLT) where most of the absorption is confined within 1.1 dB at all solar wind speeds. Post dusk and the distribution has shrunk to the lowest level with the absorption at the lowest identifiable level never exceeding the 1 dB mark. This is followed by a recovery as midnight approaches with a broader distribution at ~600 km/s, peaking at 1.7 dB. It should be noted that the diagrams do not display the total number of points available so that in each case a small number of absorption events will reach higher levels than suggested.

6.3 Examining the variations in Absorption - Discussion

As mentioned in the introduction to this chapter auroral absorption often acts as a proxy for the varying precipitation of energetic electrons. Chapter 4 pointed out that

this is not the only cause and that significant heating of the D and E layer can produce absorption (Stauning, 1984) although the occurrence of this type of absorption has not yet been quantified. That said, the values of heating related absorption tend to be lower than those measured due to particle precipitation and it is expected that the latter will strongly dominate in the type of statistical analysis undertaken here. By linking the auroral absorption to other parameters insights into both geophysical mechanisms and predictions of HF absorption can be obtained. Observations from the IRIS instrument lead to a number of topics that are addressed in this section:

i. Distribution of absorption, both in time and in space

ii. Seasonal and solar cycle effects (if any)

iii. The relationship to geophysical parameters (e.g. K_P and AE indices)

iv. The dependence on extra-terrestrial effects (e.g. solar wind speed and IMF)

v. Errors and inconsistencies that may arise.

To begin the latitude variation is investigated and the errors associated with the assumptions related to the imaging riometer are discussed.

6.3.1 Quiet-day curves, Height and Obliquity

Unlike previous statistical studies this investigation is unique in that it is the first to use an imaging riometer instead of a wide beam or chain of wide beam instruments. The apparent immediate advantage is that changes on a small latitude scale can be examined. Above and beyond this, a measure of consistency is available;

the data all come from the same instrument and have been processed in the same manner (e.g. same quiet day curve determination). However there are also some potentially serious drawbacks to using the multi-beam capacity of IRIS due to necessary assumptions that are made in interpreting the data.

At this stage the first point of error must be addressed. Although the method of quiet day curve generation (see Chapter 3) is the same for all beams, it is still a source of possible error. Hargreaves *et al*. (1985) pointed out that the uncertainty in the quiet day curve has the greatest relative effect on the smallest absorption values. The largest percentage of absorption measured by IRIS occurs close to zero, thus the largest error will appear due to these low values. The technology employed in riometers has advanced considerably since the instruments were first invented (Little and Leinbach, 1959) and currently the devices in IRIS are accurate to within 0.05 dB (S.R. Marple, private communication). Integrating over time and assuming that the quiet day curves are as accurate as possible improves this accuracy somewhat (Browne *et al*., 1995).

Figure 6.6 showed little regular variation in the occurrence of absorption with latitude across the seven beams used in this study. The results from past investigations (e.g. Hargreaves, 1966; Hargreaves *et al.*, 1985; Foppiano and Bradley, 1984) suggest that absorption should decrease to the south across the magnetic latitude of IRIS. This effect is not apparent in the data presented in either Figure 6.4 or Figure 6.6 and this may be explained by the movement of the absorption oval across the field of view with changing geomagnetic activity (Hartz *et al.* 1963; Basler, 1963; Driatsky, 1966;

Schluka, 1965). Instead of a steady change certain beams appear to see high absorption whilst adjacent beams to the north and south see a reduced level. Figure 6.13 uses the AE index to bin the absorption data and produce keograms. Here again there is little or no movement to lower latitudes with increasing activity, just simple increases in the mean absorption across all latitudes probably due to the restricted field of view offered by IRIS.

Another important point to consider is the difference in the beam configurations. As described in Chapter 3 the beam pattern of IRIS is produced by a phased array of dipole antennas and the beams are all inclined at some angle to the zenith. Table 6.2 shows the zenith and azimuth angles for the 10 beams used to produce the keograms in this study together with their respective beam widths and the obliquity factors that are routinely ascribed to correct for the angular differences. The beam parameters are symmetrical about the centre beam (25) due to the square symmetry of the beam pattern. Since the riometer gives no height information the latitude distribution of beams (Table 6.1) uses an assumed height for the absorption (90 km); a standard method in riometry that has been employed since the technique was first invented. Chapter 5 demonstrated that the absorbing layer in a single event can range from 75 to 120 km altitude, though with diminishing effectiveness at larger heights. Chapter 3 explained that Cosmic Noise Absorption (CNA) is proportional to the height-integrated product of the electron density and the effective collision frequency; this is likely to increase exponentially at lower altitudes making it the

Beam Number	Zenith	Azimuth	Beam Width	Obliquity Factor
3	49.2º	-18.6º	15.09º	1.502
10	33.1º	-26.6º	13.73º	1.187
18	14.2º	0.0º	12.83º	1.031
25	0.0º	0.0º	12.6º	1.00
32	14.2º	180º	12.83º	1.031
39	33.1º	153.4º	13.73º	1.187
47	49.2º	161.4º	15.09º	1.502

Table 6.2. Statistical beams and the corresponding parameters that define them. The zenith angles display symmetry about the centre beam as do the beam widths and obliquity factors.

controlling factor in the relationship. The low elevation (high zenith) angles of some of the beams combined with the often localized nature of auroral absorption leads to discrepancies between neighbouring beams. The obliquity factor is introduced to attempt to correct for this problem however this does not account for the different beam widths which mean some beams integrate over a larger volume along a given path. Recently it has been highlighted that the obliquity factor for a wide beam in comparison with a narrow beam is actually dependent on the amount of absorption observed due to the localised and small nature of absorption patches within the beams (Hargreaves and Detrick, 2002). Adding this extra level of complexity is unfeasible in this study, and instead the original IRIS obliquity factors are used. Errors in the obliquity factors may arise since it is impossible to distinguish the height and extent of absorption through single beam riometry but these are likely to be small on an absorption event of up to a few dB. If the height of absorption varies randomly from event to event then this error should cancel out just like random noise, however it may reinforce if there are particular conditions that reoccur producing very similar precipitation spectra. Thus a beam with too small a factor will have a higher mean absorption than the zenithal beam (obliquity factor = 1) and too high a factor will lead to a lower mean absorption value. The same should hold true for median values and the occurrence of absorption exceeding some threshold (Q); the two other parameters commonly used in describing absorption statistics (Hargreaves, 1969).

Thanks to the symmetry about the centre of the IRIS beam pattern it should be possible to compare beams with the same obliquity factor to get a general idea of the

trend of absorption across the latitudes. Three different spacings are possible and the differences in latitude with each pair (based on 90 km altitude) are: 1.89º, 1.03º and 0.44º for beams 3 and 47, 10 and 39, and 18 and 32 respectively. From the observations of Hargreaves *et al.* (1986), the variation of occurrence over such a small latitude range should amount to no more than a few percent. With increasing geomagnetic activity the north-south gradient should decrease as the centre of the absorption oval moves closer to the latitude of IRIS. Figure 6.24 shows the results of this comparison for the occurrence of absorption ≥ 1 dB for the three different levels of AE used in Figure 6.16; the data have been corrected as if for a 30 MHz riometer to allow easy comparison with similar investigations and grouped into 3-hour periods. AE increases from left to right and the beam spacing decreases from top to bottom; the beams are identified by the colour of the curve, blue is for poleward and green is for equatorward. The lowest separation between the curves is for the most narrowly spaced beams (18 and 32) which vary by two percent at most, this is hardly surprising with such a low spacing between them (0.44º). At the highest separation (1.89º) there is a transition from a south to north dominance in the post-dawn sector. This agrees with the observations of Hargreaves and Cowley (1967) and Hargreaves *et al*. (1986) who determined a region of higher occurrence at higher latitudes in the morning sector. A suggestion was made by the authors that the enhancement in the middle of the day at lower latitudes was likely due to energetic electrons from the outer radiation belt rather than the usual drift of substorm injected particles. At the higher activity level the difference between the equatorward and poleward values in the morning

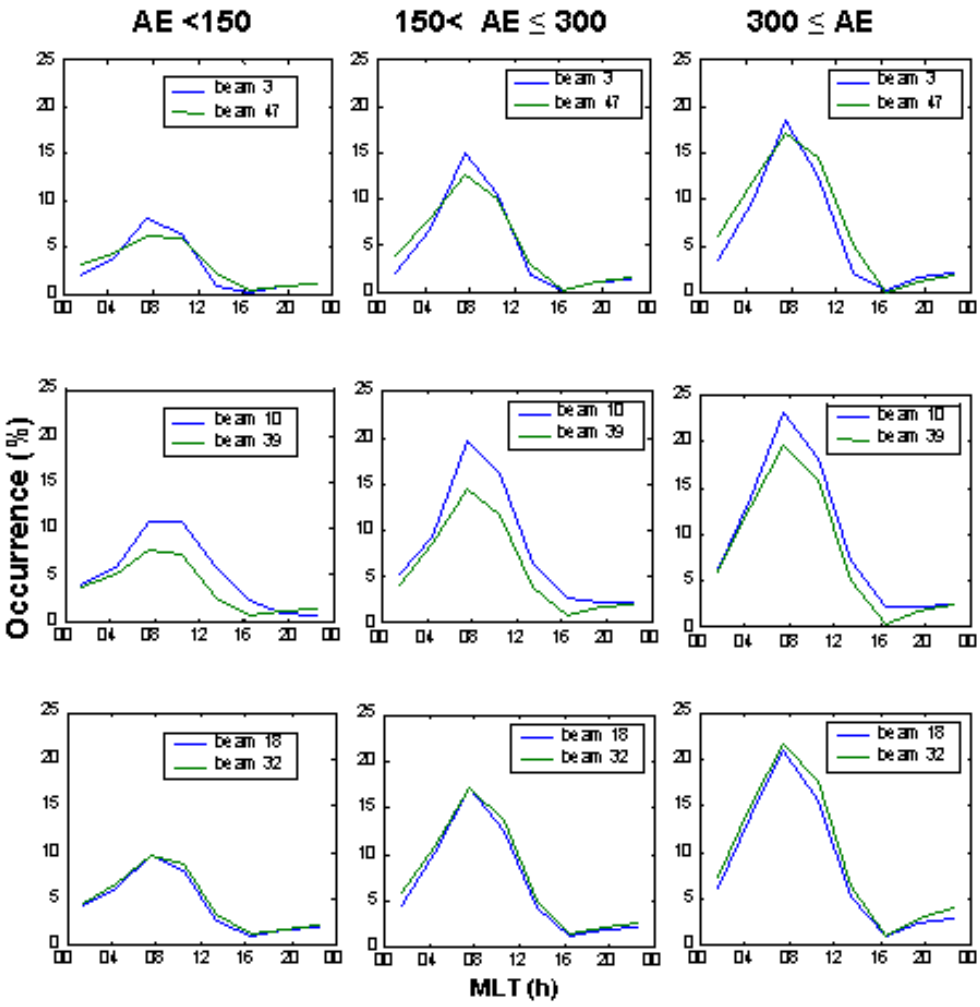

Figure 6.24. **Comparisons of beams with equal zenith angles for three levels of AE index (as in Figure 6.13); hourly averages are presented. The spacing of the beams decreases from the top plot to the bottom and from left to right the AE increases.**

sector is much reduced with the southern beam dominating at an earlier time, perhaps indicating an equatorward shift in the maximum of the absorption oval. For beams 10 and 39 there is a significant separation with the poleward beam having consistently higher occurrences. Figure 6.8 shows that beam 10 has a higher mean absorption compared with the other beams in the same time intervals. This suggests that data from this beam should be treated with caution as values may be over inflated. A preliminary investigation can find no drastic errors in the data on a case by case study, although if the data are marginally higher in each case this would noticeably effect the overall statistics.

The error from the quiet day curve is expected to be minimal although the obliqueness of some of the beams and their associated errors need to be considered in statistical studies. Methods to combat the obliquity factor problem are currently being implemented at Lancaster (S.R. Marple, private communication) based upon the recent findings by Hargreaves and Detrick (2002). It should be noted that the obliquity factor error is small in individual events and depends on the level of absorption; it is the cumulative error that leads to problems in the statistical analysis and in the future this is likely to be resolved leading to better estimates of the average absorption. That said, the imaging capability of the riometer gives an impression of the general trends in the spread and motion of the absorption region. The remaining sections in this chapter will examine the diurnal variation and the relationship between absorption (in the central zenithal beam) and K_P and solar wind speed.

6.3.2 Diurnal Variations and distributions

The local time dependence of absorption is a well known phenomena (Holt *et al.*, 1961; Hartz *et al.*,1963; Driatsky, 1966; Hargreaves and Cowley, 1967). Previous studies found that the strongest absorption occurs in the morning sector extending back towards midnight and slightly beyond. The studies by Driatsky (1966) and Hargreaves and Cowley (1967) showed that the absorption close to midnight showed a peak rather than the smooth decay into the evening sector indicated by other authors. The relative size and appearance of the maxima (pre-noon and pre-midnight) depends on the method by which the statistics are compiled (Hargreaves, 1969). By choosing a discrete event based approach the absorption peak close to midnight is enhanced over the morning counterpart. Absorption in the pre-midnight sector is attributed to the precipitation of electrons directly associated with substorm activity (e.g. Ansari, 1965; Ranta *et al*., 1981; Hargreaves, 1974; Hargreaves *et al*, 2001) and the precipitation in the morning sector has often been associated with the eastward drift of electrons (see Chapter 5) following substorm injection. Thus in the past it is the absorption around midnight that has been considered to be of premier geophysical importance (Hargreaves, 1969), however for practical purposes (e.g. HF communication circuits) the morning values are of much more interest. Auroral absorption directly associated with substorm activity often takes the form of short duration, spike events (Ansari, 1964; Hargreaves *et al.*, 2001). In the morning sector absorption is higher and more slowly varying. Since the current study uses 10-minute resolution data to determine

the mean values at each magnetic local time it is less sensitive to the short duration spikes so de-emphasizing the midnight peak.

The data presented in this chapter have come from seven years of continuous monitoring in the auroral zone; past statistical studies have used a much reduced time span such as a single year (e.g. Hargreaves, 1966) although the study by Hargreaves *et al.* (1985) used 11 years of hourly data from the Finnish riometers (Ranta (1972-1983). Figure 6.4 clearly demonstrates the diurnal variation observed in all of the beams, with a strong morning peak following a smooth rise from the pre-midnight sector. Gross features in the distributions should correlate well between individual studies however any comparisons between the different statistical studies must take into account the method by which the data were collected.

The keogram format is based upon the mean absorption at each local time in each bin. Figure 6.5 (bottom panel) illustrated that when all negative values are removed the absorption and standard deviation converge for a large percentage of the day. As mentioned in section 6.2.2 this is suggestive of an exponential distribution of the occurrence and Figure 6.5 uses 6 local time samples to show that this appears to be the case. It must be remembered that these data are from a 38.2 MHz riometer and so before comparing with results from other riometers operating at different frequencies the data must be scaled correctly.

Foppiano and Bradley (1984) found that the cumulative amplitude probability distributions of riometer absorption could be fitted by a log-normal distribution rather than an exponential as suggested by Hargreaves (1966). Figure 6.25 presents the

cumulative amplitude distribution ,Q, for the same samples as Figure 6.5. Each of the curves displays some exponential-like behaviour but by fitting curves of the empirical expression:

$$Q = ce^{-kA} \qquad (6.2)$$

where c and k are constants and A is the absorption. It is clear that the data does not strictly obey an exponential relationship at all times. Hargreaves *et al.* (1984) found that the log-normal distribution was a good fit to both hourly and monthly distributions but that since it predicted zero probability of zero absorption suggested it should be used with caution and only at the ranges that it had been tested over. The data in Figure 6.5 clearly demonstrate that the occurrence of absorption (at least at 38.2 MHz) favours values close to zero; unsurprisingly since the majority of absorption is substorm related. Interestingly the best fits to the exponential expression occur within the afternoon/evening sector (12-20 MLT). This is the time when the mean absorption approaches its minimum level, close to 0.1 dB (16 MLT). Thus it may be surmised that for low ranges of absorption (> 0.5 dB) an exponential distribution more accurately describes the cumulative amplitude, whereas for high levels the log-normal distribution is more accurate. These distributions have been chosen since they fit the data, however no theoretical explanation is clear. Wave particle interactions in the magnetosphere that lead to precipitation are intrinsically linked to the distributions of auroral absorption and so some purely speculative ideas governing the particle motion at various local times are considered in section 6.3.6. A

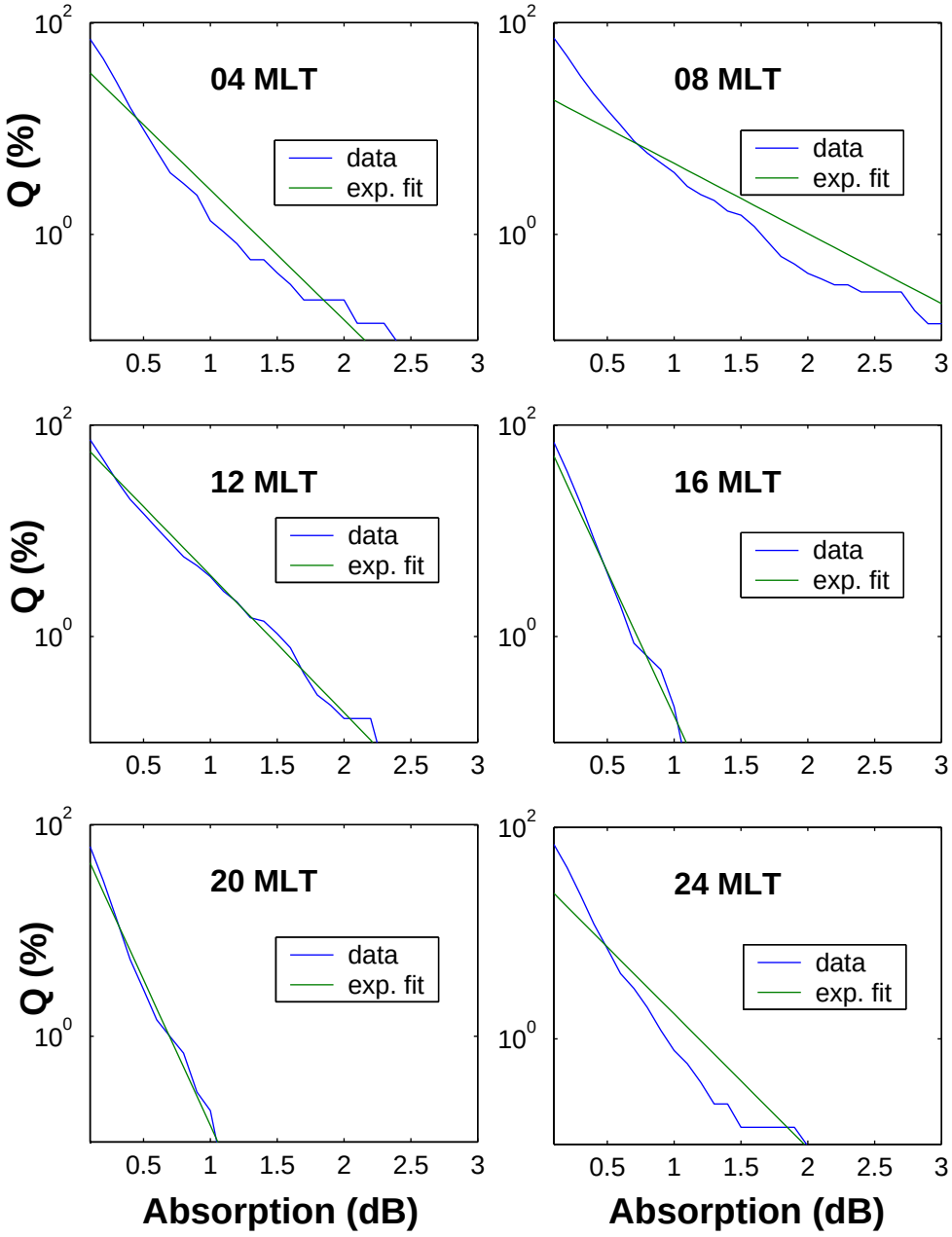

Figure 6.25. Cumulative Amplitude Distributions for 6 magnetic local times (as in Figure 6.5). The blue line represents the data and the green line is an exponential fit of the form: $Q = ce^{-kA}$

clearer picture will be found when satellite observations at all local times are compared with the riometer results.

6.3.3 Seasons and the Geomagnetic influence

By binning the absorption data into the four seasons (Figure 6.8) some notable differences in the mean absorption appears. Winter shows a generally higher level of absorption than summer and the diurnal variation is less obvious. Spring and autumn display similar characteristics though there appears to be a poleward bias in the spring data. Some of the differences may be ascribed to the unusually higher levels that appear in beam 10 during absorption events (see Section 6.3.1), indeed beam 10 shows distinctly strong absorption in both summer and spring. To determine whether the differences in the mean absorption are significant a significance test is applied to the data. The Kolmogorov-Smirnov (K-S) test is a significance test that in this case compares two continuous data sets to determine whether they might belong to the same distribution (von Mises, 1964). Figure 6.26 displays the results of applying the test to the season-binned data, significance levels of <0.01 represent a strong significance suggesting that the data are not from the same distribution; i.e. the differences displayed in the distributions are of statistical significance. The top panel compares the winter and summer keograms and suggests that the distributions are significantly different at virtually all local times. There are some periods of similarity in the morning sector in the lower latitude beams and also in the two northernmost beams; this does not mean the data are from the same distribution, but rather that no

significant conclusion can be drawn from this data. The second panel compares the equinoctial months and in this case the majority of the day suggests little significant difference between the distributions, the largest exception being in beam 10 in the morning and evening sectors. This is yet another example of how beam 10 stands out from the remaining imaging beams. No problems with the IRIS hardware have been found to account for the high values in the beam but curiously the effect appears to move to different local times with season, in anti-phase with the time when scintillation is likely to affect the main beam. The possibility that scintillation from Cassiopeia is significantly affecting a side lobe of beam 10 can not be ruled out. Although the effect of Beam 10 is the clearest in the data it cannot explain the significant distribution differences in other beams at other local times suggesting a distinct seasonal difference.

High absorption values observed in the mid-latitude ionosphere during winter are described as the winter anomaly (Hargreaves, 1995). At mid-latitudes ionospheric absorption is due to the ionisation by solar illumination and thus it is counter-intuitive to expect the absorption to increase during winter when the ionosphere is dark. Rocket measurements have pinpointed the immediate cause of the anomaly as electron density enhancements between 60 and 90 km (Geller and Sechrist, 1971). Various suggestions have been put forward to explain the winter anomaly including changes in stratospheric temperature (Shapley and Beynon, 1965), transport of NO from higher latitudes and the precipitation of electrons from the radiation belts. It is important not to confuse the data presented here as an example of the winter anomaly; the data are

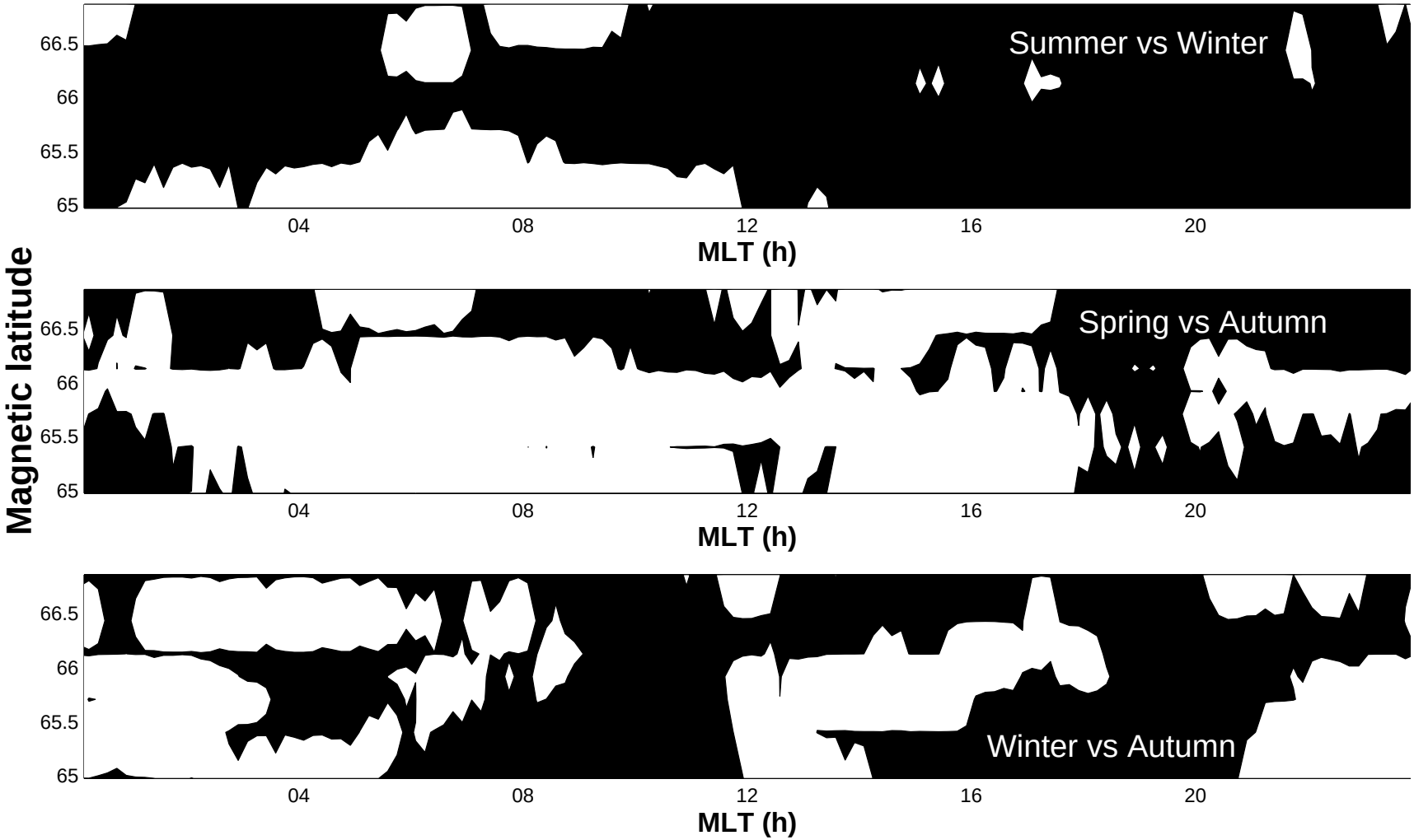

Figure 6.26. **Kolmogorov-Smirnov significance tests on the Season data. Top panel compares summer and winter; middle panel compares spring and autumn; bottom panel compares winter and autumn. Black indicates significance <0.01 and white indicates significance >0.01.**

from higher latitudes than those usually associated with the anomaly and the mean absorption in winter very rarely exceeds the equinoctial values.

The cause for the increase in winter over the summer values is most likely geophysical in nature. Figure 6.10 compared the distributions of K_P in each of the seasons and found that the winter had a slightly higher occurrence in the higher activity levels than summer (3.5 % difference). Spring and autumn K_P occurrence values at higher activity are broadly similar and are above either of the solstitial seasons. These differences should be enough to explain the variation in the mean absorption between the season keograms, pointing to the fact that any seasonal variation is actually geomagnetic in origin and thus the absorption is most likely still related to the precipitation of energetic electrons. It has been demonstrated that there is a semi-annual variation in the occurrence of geomagnetic storms (Russell and McPheron, 1973) dependent on the geometry of the IMF with the Earth's magnetosphere. Spring and autumn form two peaks in the variation with a minimum over winter and another over summer; the summer minimum is the deeper of the two.

Magnetospheric influence on auroral absorption was established long ago in the early days of riometry (e.g. Parthasarathy and Reid, 1967). Figure 6.11 highlights the dependence of the absorption on activity as defined by the K_P index. Both the mean (top panel) and median (bottom panel) show significant increases in the morning and midnight sectors with higher activity. The mean absorption is consistently higher than the median due to a few high occurrences of high absorption skewing the mean value. Interestingly the median absorption in the highest activity range peaks at an

earlier magnetic local time than the corresponding mean absorption. For $K_P > 4$ the morning absorption is ~6 times higher than for the lowest K_P range yet around 15-18 MLT the absorption is gathered within less than 0.1 dB for all activity levels. The afternoon minimum appears to be a strongly defined characteristic of the daily absorption and will be returned to later in this chapter (section 6.3.5).

Meanwhile it is worth concentrating on the distribution of the absorption data; Figure 6.12 shows how with increasing MLT the distribution extends to higher absorption values at lower K_P until the afternoon when a recovery occurs. A relationship linking geomagnetic activity with absorption for a given local time and latitude is desirable for prediction purposes. Past authors have attempted to predict auroral radio absorption based upon statistical measurements (e.g. Agy, 1972; Herman and Vargas-Villa, 1972; Foppiano, 1975; Vondrak *et al.*, 1978; Masi, 1980 and Foppiano and Bradley, 1984) including terms based upon sunspot number, linking the absorption to the solar activity cycle. Hargreaves (1966) determined relationships between the absorption and K_P and A_P indices and later works (e.g. Hargreaves *et al*., 1984 and Hargreaves *et al.*, 1986) confirmed this reliance on geomagnetic activity, suggesting that a geomagnetic term should replace the sunspot dependence in any prediction model.

The investigation by Hargreaves found a linear relationship between the log of the median auroral absorption and K_P that was heavily dependent on time of day:

$$\log_{10} A_m = I + S.K_P \qquad (6.3)$$

A relationship between the log of absorption and the K_P value seems reasonable since the K_P index is itself quasi-logarithmic. Results from that investigation for two latitudes are presented in table 6.3. The time bands are presented in universal time and the data come from two riometers in the northern hemisphere: Great Whale River (55.03º, -77.83º geographic) and Baie St. Paul (47.37º, -70.55º geographic), operating at 29.85 MHz. The two stations are separated by 38 minutes of magnetic local time (Baie St. Paul leads Great Whale River) The corrections to magnetic local times are presented in the second field calculated using the IGRF model for 1964.

	UT	**00-06**	**06-12**	**12-18**	**18-24**
Latitude	**MLT (67.8º)** **MLT (60.0º)**	**18:53-00:52** **19:31–01:30**	**00:53–06:52** **01:31–07:30**	**06:53-12:52** **07:31–13:30**	**12:53–18:52** **13:31–19:30**
67.8º	**I** **S**	0.134 0.113	0.086 0.216	0.064 0.284	0.281 0.080
60.0º	**I** **S**	-1.068 0.284	-0.949 0.338	0.155 0.061	0.090 0.096

Table 6.3. Intercept (I) and slope (S) in $Log_{10}(A_m) = I + S.K_P$. After Hargreaves (1966).

Figure 6.12 demonstrated that there is a changing distribution in the absorption at different levels of K_P at each magnetic local time, and the scatter of absorption appears to curve over at times. Figure 6.27 plots the logs of the median and mean absorption values for each K_P level at the same magnetic local times as for the distributions in Figure 6.12. The two colour coded lines display first order quadratic fits to the data for the mean (blue) and median (red) values. For K_P levels where less than 50 data points occur in each local time bin the mean and median values are excluded in the fit. Either side of the mean values the two dashed black lines show the positions of one standard deviation from the mean value. Table 6.4. shows the values of the intercepts and slopes for this set of fits, and for comparison the values in brackets represent corrections for radio absorption at 29.85 MHz. The differences between the curves in each time bin suggest that the local time dependence is very significant and so using large separations (e.g. 6 hours) is inadvisable.

A quantitative comparison between the two estimates of the absorption-K_P relationship is difficult; the differing choices of magnetic local time ranges cause problems and since no direct observations were made at same latitudes such a comparison becomes increasingly unreliable. Estimates of the values of the fits could be ascertained by interpolating between latitudes through assuming an appropriate spatial distribution; the most often selected distribution is the Guassian fit to the Q(1) parameter (e.g. Hartz *et al.*,(1963); Holt *et al.*, (1961); Hargreaves, 1966 and Foppiano and Bradley, 1985) (Q(1) describes the probability of absorption exceeding 1 dB). However the factor of the longitudinal separation of the riometer stations in the

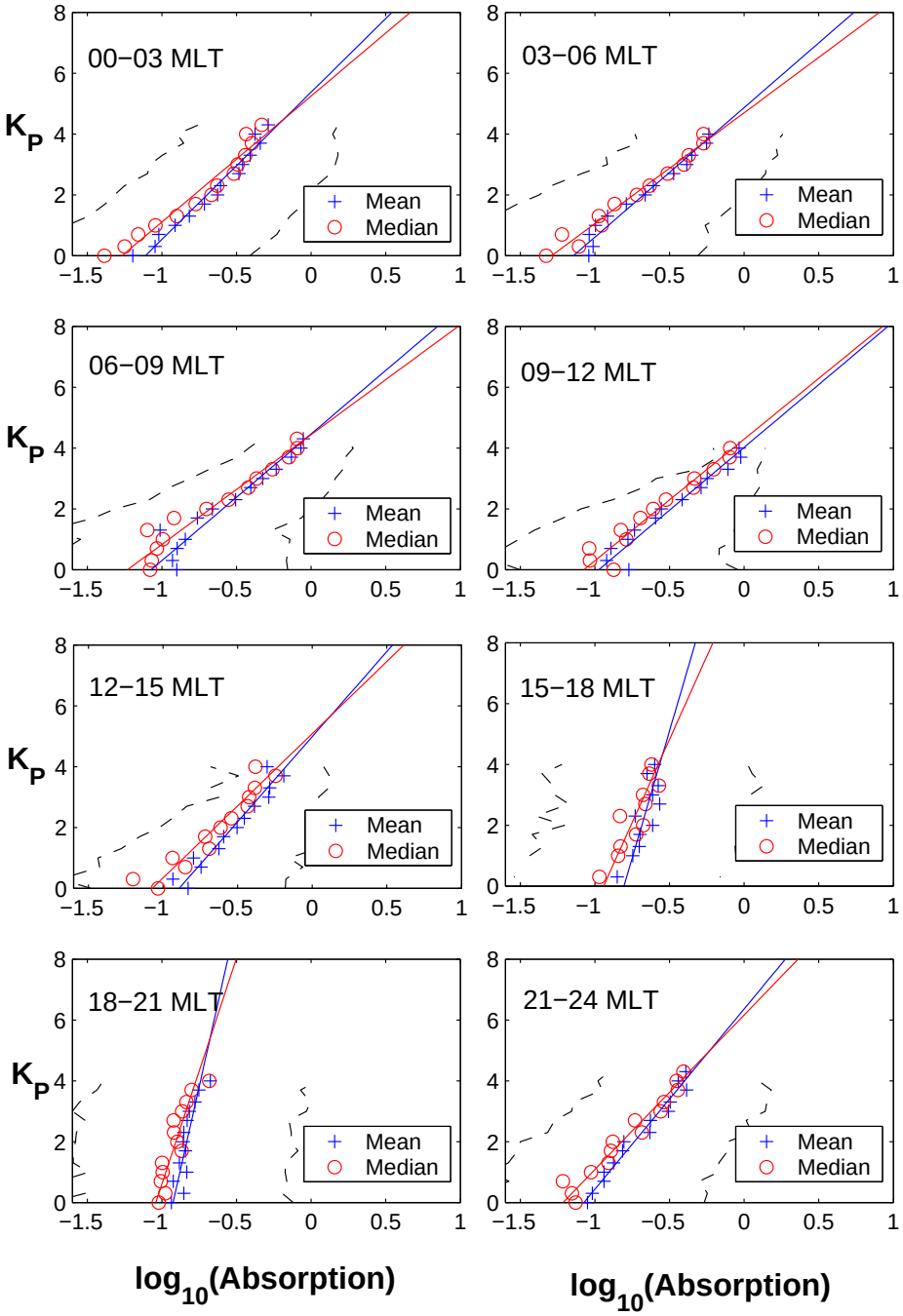

Figure 6.27. **Log of the mean (blue crosses) and median (red circles) values of absorption in each K_P bin plotted against the corresponding K_P. The two straight lines are linear fits to the data and the dashed black curves represent the log of ±1 standard deviation about the mean.**

MLT	Mean		Median	
	Gradient (S)	**Intercept (I)**	**Gradient (S)**	**Intercept (I)**
00-03	0.184 (0.184)	-1.291 (-1.082)	0.215 (0.215)	-1.441 (-1.231)
03-06	0.213 (0.214)	-1.327 (-1.117)	0.240 (0.240)	-1.454 (-1.245)
06-09	0.236 (0.236)	-1.280 (-1.070)	0.270 (0.270)	-1.436 (-1.226)
09-12	0.217 (0.216)	-1.148 (-0.938)	0.224 (0.238)	-1.247 (-1.037)
12-15	0.151 (0.151)	-1.067 (-0.856)	0.172 (0.172)	-1.231 (-1.021)
15-18	0.062 (0.062)	-1.047 (-0.837)	0.075 (0.075)	-1.140 (-0.930)
18-21	0.063 (0.063)	-1.164 (-0.954)	0.088 (0.088)	-1.284 (-1.074)
21-24	0.142 (0.142)	-1.247 (-1.037)	0.163 (0.163)	-1.375 (-1.165)

Table 6.4. Gradient and Intercept values for fits to equation 6.3 for both mean and median absorption for data in Figure 6.30. Values in brackets display the fits for 29.85 MHz absorption; there is no difference in the slopes only in the intercept as the correction simply scales the data by the same value.

original and present investigation produces a large uncertainty. Qualitatively, by comparing the values of the gradients of the fits (S) for similar magnetic local times the IRIS results fit within the limits imposed by the two latitudes of the wide beam riometers (except in the ~13-19 MLT range). A bias in S towards the northward riometer values appears at each time range and since this is the smallest separation in latitude (65.91º to 67.8º) it appears promising for the current results.

Interestingly the point where the comparison breaks down is in the 13-19 MLT time range, this spans the rapid decline to and slow rise following the afternoon/evening minimum (~18 MLT). By weighting the latter half of the time period more than the former a better comparison of S is found, suggesting that the minimum is controlling the result in the 18-24 UT bracket (from Hargreaves, 1966). The dominance of the minimum is unsurprising considering the little effect that geomagnetic activity has on this recurring phenomenon and it is a clear example of how careful selection of temporal bins is essential to avoid smearing across very different characteristics. Large differences in the intercept values (I) may be the result of the expected longitudinal effect. Current values of I are significantly lower than those from the past study. More investigations of this nature are needed at different sites spread in longitude to determine whether such an effect exists and if so how large the magnitude of the differences.

In an attempt to test the relationship between absorption and K_P the coefficients of the fit are applied to the K_P data from 1995 to 2001. Correlation coefficients are determined for the observed and estimated data sets for both the mean

and median absorption fits and the residuals for each are computed. The results from the fit are presented in table 6.5.

	Correlation Coefficient	**Mean of residuals**	**Standard deviation of residuals**
Mean	0.391 (0.532)	-0.129 dB (-0.093)	0.348 dB (0.167)
Median	0.358 (0.528)	-0.099 dB (-0.056)	0.396 dB (0.165)

Table 6.5. Correlation coefficients and residual information for absorption values derived from K_P levels and compared with observed values in the epoch 1995-2001. Values in parenthesis are from fits to data over the range where reliable means and medians were calculated.

In both cases (mean and median) the correlation coefficient over the whole data set is rather poor though better for the mean relationship. The mean ratio of the observed and estimated data sets is better for the median values (0.73) than the mean (0.6). and the residuals (observed – estimated) indicate that the relationship overestimates the absorption on average but that the values are quite reasonable. However the standard deviations of the residuals reflect the wide distribution of absorption and show that for some periods there is a marked difference. At times the

estimated absorption is >1.7 times the observed value; for an observation of 0.5 dB this translates to an error of 0.3 dB at 38.2 MHz. Translating this to 15 MHz (around the operating frequency of the CUTLASS radar for example) 0.5 dB becomes ~7.3 dB and the difference is 4.4 dB! For the range of data represented by the well defined calculated mean and median values the correlation and accompanying parameters are much improved; the spread of the residuals is reduced to a much more reasonable level suggesting a better representation. Thus although this approach to determining absorption appears to be severely limited over the current range of activity levels, with more high activity observations to constrain the fitted curves a better measure of the relationship is likely attainable.

To address the current uncertainty associated with the log-linear relationship, a different empirical relationship is now suggested. The occurrence plots in Figure 6.12 suggested a measure of curvature that increased with magnetic local time until 12-15 MLT, and Figure 6.27 showed a distinct curve to the mean and median values at some of the local times. A quadratic is fitted to the mean and median values in each K_P bin. This fitted relationship takes the form:

$$A_m = aK_P^2 + bK_P + c \qquad (6.4)$$

where a, b and c are constants. Figure 6.28 displays the local time results of this fit to the data with surprisingly good results over the range of available data. The black dashed lines show the ±1 standard deviation from the mean for each K_P bin. At 15-18 MLT there is a significant failure to fit the quadratic curves in a meaningful fashion; this is at the minimum in the diurnal variation and the range of absorption values

hardly increases as the activity level rises, the distribution of points suggests a more linear fit with a steep gradient. This will be improved when more data at the highest and lowest K_P values become available. Table 6.6 displays the coefficients for each local time for the mean and median absorption; neither the linear nor the squared term dominate to any significant level in each of the time ranges except in the 00-03 MLT and 12-15 MLT sectors. At these times it is clear that the relationship is mostly linear with a small non-linear contribution at high K_P.

Testing this relationship in the same manner as for the log-linear fit results in a notably higher correlation between the observed and the modeled data for the entire epoch. Restricting comparisons to the range of calculated medians leads to slightly better results but not as markedly improved as with the log-linear fit. Once again the absorption based on K_p is higher on average than the observed quantity though the mean residual is marginally closer to zero. The standard deviation of the residuals is also smaller; all pointing to the quadratic providing a better estimate of the absorption. The values of the correlation coefficients are presented in Table 6.7 where they are shown to be approximately the same. With that in mind, a better choice for determining the absorption would be to use the coefficients associated with the median value due to the improved spread of residuals. Although by gaining higher activity observations the fits can be better restrained it is clear that at least for the current data set the quadratic fit provides better solutions than the log-linear.

MLT	Mean			Median		
	a	**b**	**c**	**a**	**b**	**c**
00-03	0.008	0.072	0.055	0.003	0.087	0.022
03-06	0.040	-0.023	0.083	0.029	0.017	0.049
06-09	0.058	-0.058	0.123	0.052	-0.036	0.077
09-12	0.066	-0.046	0.141	0.057	-0423	0.115
12-15	0.009	0.090	0.105	0.007	0.084	0.061
15-18	-0.010	0.072	0.118	-0.005	0.057	0.090
18-21	0.006	-0.008	0.130	0.007	-0.007	0.102
21-24	0.012	0.032	0.080	0.014	0.020	0.061

Table 6.6. Coefficients for the quadratic fit to the mean and median absorption values at 8 magnetic local times.

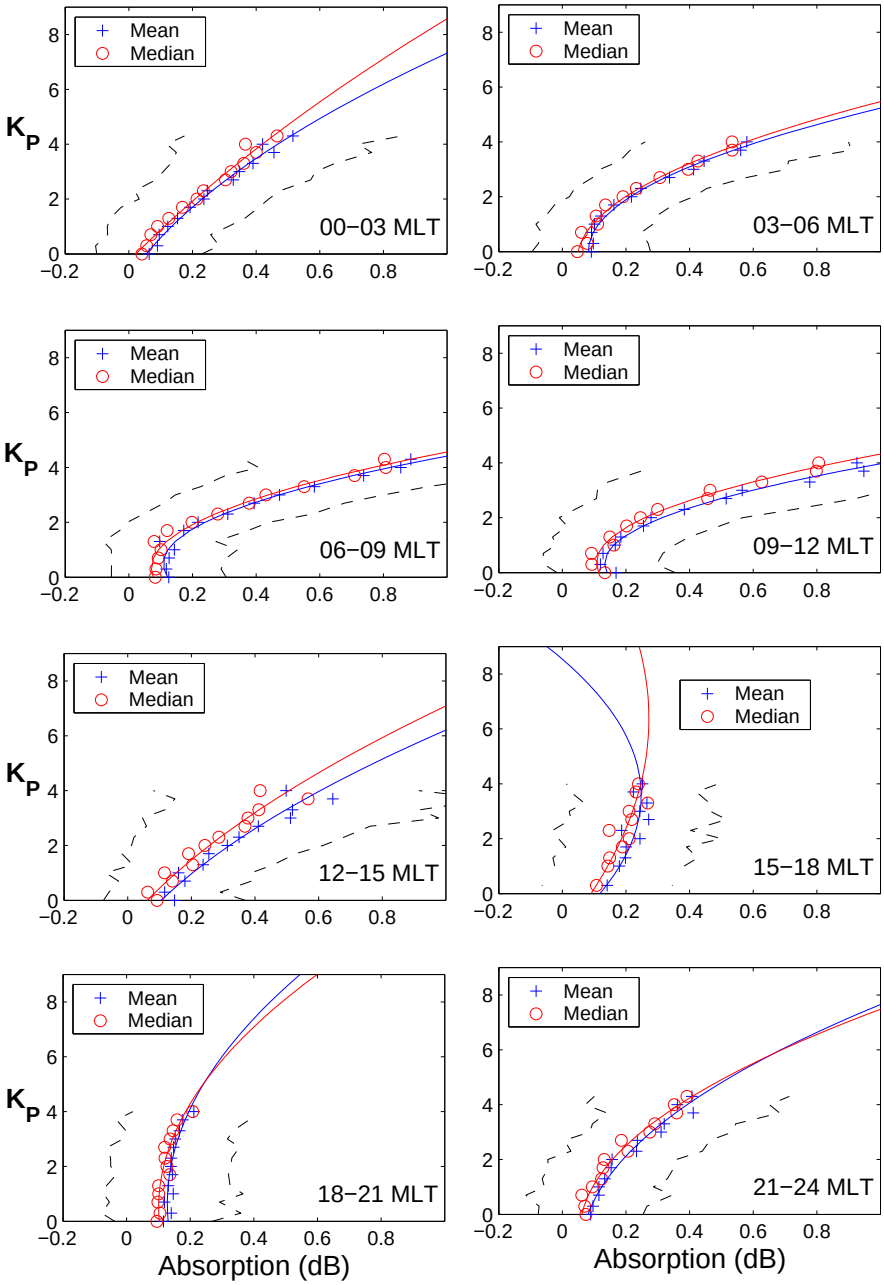

Figure 6.28. Local time plots of the median (red circles) and mean (blue crosses) absorption against the K_P. The curves represent quadratic fits to the data points and once again the black dashed lines are ± 1 standard deviations about the mean.

Figure 6.12 demonstrated that the absorption suffers from a wide distribution in each K_p bin but the occurrence is much higher towards the lower end of the absorption scale. This does not exclude high absorption events by any means, but even with high values of K_P there will be many occasions when absorption is low. Similar geomagnetic conditions will not necessarily return similar absorption levels. When the nature of auroral absorption is considered this becomes less surprising; radio absorption at high latitudes is principally due to the precipitation of energetic particles (electrons >15 keV) and so if no particle population is existent in the magnetosphere then no absorption will occur. Thus for periods of high geomagnetic activity in close succession the high-energy particle populations may be depleted leading to a significantly reduced absorption level. Many factors will control this including the type of pitch angle diffusion occurring in the pertinent region of the magnetosphere. Weak diffusion will lead to a slow, gradual movement of electrons into the loss cone whereas strong diffusion will dump large fluxes into the ionosphere, quickly depleting the population on the field line. In order to make reliable absorption predictions some term dependent on the recent time history of the magnetic activity must be included in any empirical relationship.

Another important point to note is the variability of absorption on small time scales, especially in the night side ionosphere; using K_P (a three hour index) as an indicator of the absorption activity does not truly capture the dynamic nature of auroral

absorption. Figure 6.13 displays keograms for three levels of geomagnetic activity based on the auroral electrojet index (AE), which is produced at a much higher

	Correlation coefficient	**Mean of residuals**	**Standard Deviation of residuals**
Mean	0.507 (0.538)	-0.117 dB (-0.096)	0.230 dB (0.167)
Median	0.508 (0.536)	-0.080 dB (-0.060)	0.215 dB (0.163)

Table 6.7. Correlation coefficients and residual information for absorption values derived from K_P levels and compared with observed values in the epoch 1995-2001.

temporal resolution and is specific to the auroral zone rather than a planetary index such as K_P.

The increasing AE values lead to notable increases in the mean midnight to morning absorption levels and once again the late minimum exhibits only small differences from one plot to the next. The occurrence of absorption ≥1 dB (Q(1)) for each of the AE ranges shows a similar pattern (Figure 6.17). The AE data covers a

smaller time span than the K_P, extending from 1997 to 2000 inclusive and as mentioned in section 6.2 these are only quick look data, unconfirmed and derived from only 8 of the 12 stations. As such any results obtained should be treated with due caution. Once the data have been confirmed and a longer period is available AE should prove a satisfactory indicator of geomagnetic activity, suitable for attempting a similar process described above for K_P.

Having examined the statistical relationship between auroral absorption and geomagnetic activity it is worth considering the effect that the drivers of magnetospheric activity have on the variation of absorption: the IMF and the solar wind.

6.3.4 Links to the Interplanetary Magnetic Field

With the launch of the Wind spacecraft in 1994 and subsequently the ACE satellite in 1998 a valuable resource was made available to solar-terrestrial scientists; consistent and reliable solar wind and IMF data became available for a long period. At the time of writing both ACE and Wind are still operational and recording data. For previous statistical studies of the absorption oval solar wind data were available for short periods or could be estimated from the geomagnetic activity indices (e.g. Hargreaves, 1966). The current work has access to the spacecraft data allowing direct comparisons of the absorption variation in response to these important driving parameters.

Figure 6.16 used the four quarters of the IMF clock angle to bin the absorption from each of the 7 IRIS beams. There are large differences in the mean absorption between a northward IMF and a southward with smaller differences between east and west conditions. The mean absorption doubles when the IMF is southward in the morning and midnight sectors whereas it once again remains very low in the evening sector. A westward IMF appears to favour an earlier increase in absorption pre-dawn, perhaps due to the skewing of the field lines (Cowley *et al.*, 1991; Khan and Cowley, 2001) leading particles to precipitate at an earlier local time. To determine whether this is significant the data are subjected to the Kolmogorov-Smirnov significance test. Once again a returned value of less than 0.01 suggests a strong significance. In Figure 6.29 the top panel compares a positive IMF B_Z with the negative; B_Y is held constant. A strong significance (< 0.01) is shown from ~20 MLT to ~12 MLT suggesting that the data in this band are from very different distributions. Ranging across the by-now familiar diurnal minimum in all beams there is a band of apparently insignificant data, suggesting that whereas the midnight and morning absorption is highly dependent on the IMF, the low absorption values in the afternoon/evening are not. The diurnal minimum does not depend on the orientation of the IMF. The bottom panel compares the eastward (positive B_Y) and westward (negative B_Y) IMF with a constant B_Z, in this case southward. There are some small patches in the keogram that display a possible significance but these are isolated and non continuous as in the previous example. Some of these points cluster in the morning sector, pre 04 MLT, however it is clear that no significant conclusion can be drawn about the possibility of B_Y having an effect on the absorption. Discarding the B_Y parameter as insignificant for these

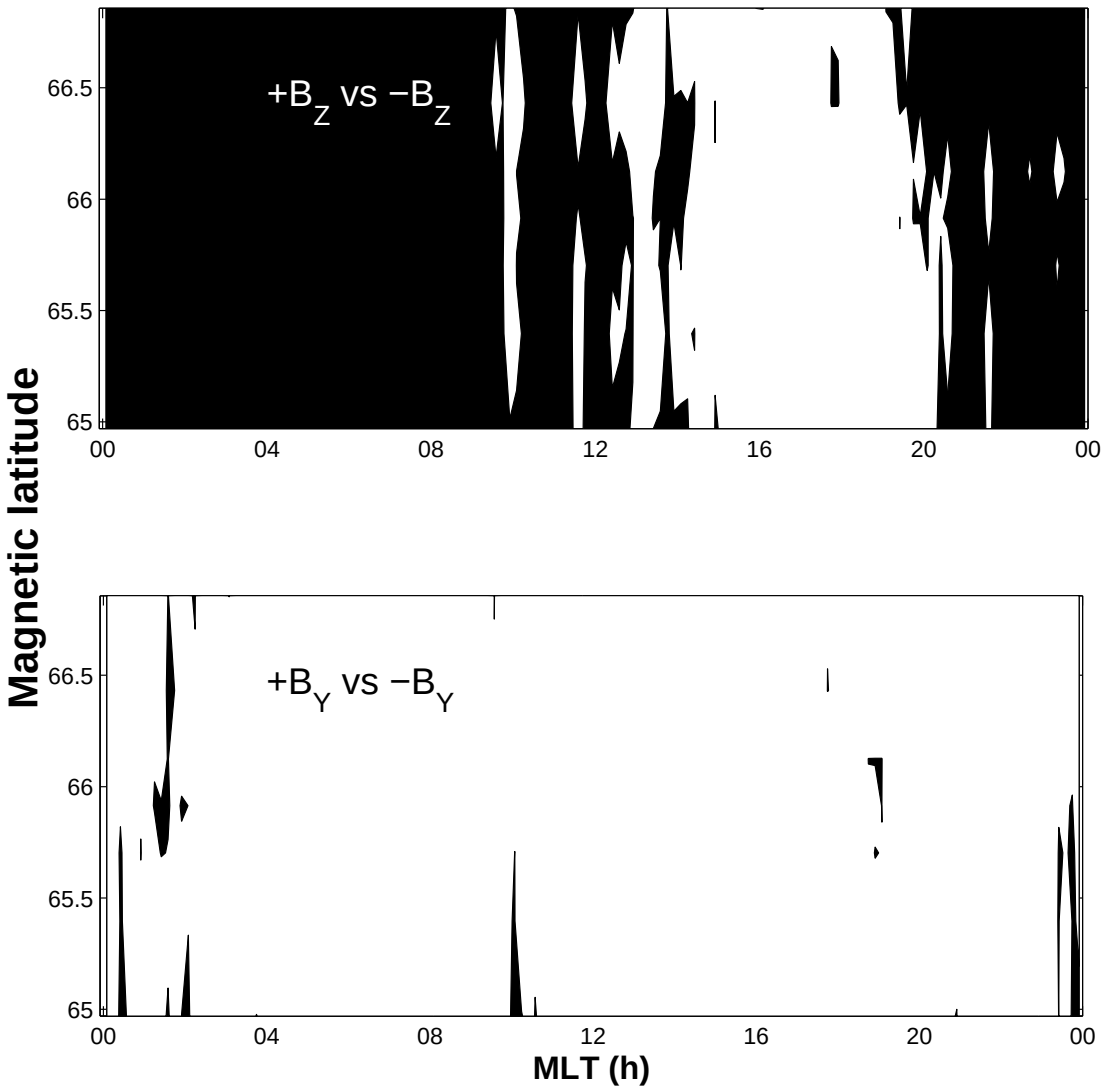

Figure 6.29. **The results of a Kolmogorov-Smirnov significance test between IMF northward and southward conditions (top panel) and IMF eastward and westward conditions (bottom panel). The colour scale reflects values above (black) and below (white) the significance level (0.01).**

purposes, the zenithal absorption can be binned by B_Z in order to further investigate the dependence. Figure 6.17 shows that when the Q(1) parameter is binned by B_Z there is a definite effect for negative values both around midnight and in the morning sector. Northward IMF does not seem to radically affect Q(1) as southward does; the curves for positive B_Z cluster below a 4 % maximum and do not follow any trend. Those curves for $B_Z < 0$ display a definite trend with increasingly higher values of Q(1) for successively negative values of B_Z. Thus the absorption distribution is obviously dependent on the Z component of the IMF just as should be expected since absorption is substorm dependent. This approach does not account for transient effects in the absorption such as those reported by Nishino *et al.* (1999) for a rectified response to north/south movements in the IMF. That example was related to increases in field aligned currents close to the open/closed field line boundary whereas the general increase here is likely related to the occurrence of substorm activity for negative IMF.

6.3.5 The Solar Cycle and the Solar Wind

Geomagnetic activity has long been identified with changing conditions in the solar wind, thus it is reasonable to suggest that the absorption will have a dependence on some defining parameter. Chapter 5 described how pressure pulses in the solar wind lead to enhancements in absorption due to the growth of wave particle interactions in the magnetosphere. The two types of absorption associated with pressure pulses are briefly described in Chapter 3 as Sudden Commencement Absorption (SCA) and

Sudden Impulse Absorption (SIA). These follow drastic changes in the solar wind pressure and are typically large-scale events (Ranta and Ranta, 1990). Tsurutani *et al.* (2001) illustrated the effects that solar wind shock waves have on the magnetosphere leading to enhanced wave activity and loss cone instabilities (e.g. Anderson and Hamilton, 1993; Lauben *et al*.,1998), which result in diffuse precipitation and the intensification of field aligned currents (Araki, 1994; Lysak *et al.*, 1995). One of the conclusions from Chapter 5 was that small changes in the solar wind dynamic pressure could affect the precipitation that causes the absorption in the dayside auroral zone. Figure 6.18 showed that the distribution of the dynamic pressure in the 1995 to 2001 epoch peaked at 3 nPa at 24 % and that the probability of high pressure events (>20 nPa) occurring is very small. Thus any dependence on solar wind pressure as displayed by Figure 6.21 is unlikely to be related to the large shocks associated with SCA and SIA. An increase in the morning and midnight levels is evident in the keograms over just this small range of pressure events.

Tsurutani *et al.* (2001), noted that long after the passage of interplanetary shocks in two separate events there was an appreciable aurora at dawn, dusk and midnight recorded by the Ultra Violet Imager carried by the POLAR spacecraft. This was attributed to a viscous interaction between the solar wind and the flanks of the magnetosphere producing either a Kelvin Helmholtz instability (Rostoker *et al.,* 1992) or cross-field diffusion of magnetosheath plasma via ELF/VLF boundary layer wave interactions (Lakhina *et al.,* 2000; Tsurutani and Lakhina 1997). Either way small changes in the dynamic pressure, brought about through slight variations in the solar

wind speed could result in increased precipitation; this is demonstrated in Figure 6.21 where the increased level of solar wind velocity produces large changes in the mean absorption in the morning and midnight sector. This is further emphasized in Figure 6.22 which displays the mean absorption for the zenithal beam; for speeds greater than 300 km/s there is a detectable effect on the absorption level. When the data is binned into the eight magnetic local time sectors used to distinguish K_P (Figure 6.23) the changing distributions become clear; although the majority of the absorption still clusters about 0.1 dB there is a broadening of the distribution with increasing solar wind speed. At high velocities the distribution appears to shrink again but this is an artefact created by low numbers of data points at the greater speeds (Figure 6.20).

Since the solar wind is credited as being the driving force behind geomagnetic activity it seems reasonable to link the absorption to the energy input from the solar wind. The study by Hargreaves (1966) attempted to estimate the total energy of precipitated particles. This relied on the empirical relationship derived by Hargreaves and Sharp (1965) linking the absorption to the square root of the total energy of the precipitated electrons combined with an expression for the solar wind velocity based on K_P/A_P:

$$V_{sw} = 67.2.K_P + 330 \qquad (6.5)$$

Measurements of the solar wind were made by the Mariner 2 space probe to derive this relationship (Snyder *et al.*, 1963), though more sophisticated variations using the AE index and including terms for the IMF effects now exist (Hargreaves, 1995). With the data available from the ACE and WIND spacecraft it is now possible to attempt to

link directly auroral absorption with the solar wind velocity. By compiling mean and median absorption values from 50 km/s wide bins a similar method to earlier can be applied to the data. Figure 6.30 shows the results of the binning with a linear fit to the data of the form:

$$A_m = a.V_{sw} + b \qquad (6.6)$$

The data points in the pre-noon sector show some measure of curvature but this is not repeated to any notable effect in the other local time bins and does not compare with the bending recorded for the K_P bins. By applying the fit to the time series of the data again a measure of the correlation can be found. Table 6.8 presents the correlation coefficients which prove a better result than with the K_P log-linear fit and with a much reduced spread of the residuals. Whereas for the mean values the modelled absorption is again overestimated, the median values are generally smaller than the observed absorption. When the relationship is computed for only those velocities where reliable mean and median values are available there is no discernable difference in the correlation.

The current equation (6.6) will produce unrealistic values for low solar wind velocities(> 200 km/s) in most cases, however in the previous half solar cycle there have been no occurrences of the solar wind dropping below ~250 km/s. Values of absorption calculated for a solar wind velocity less than 250 km/s should be discounted as extremely unreliable as should values in excess of 800 km/s. It is highly

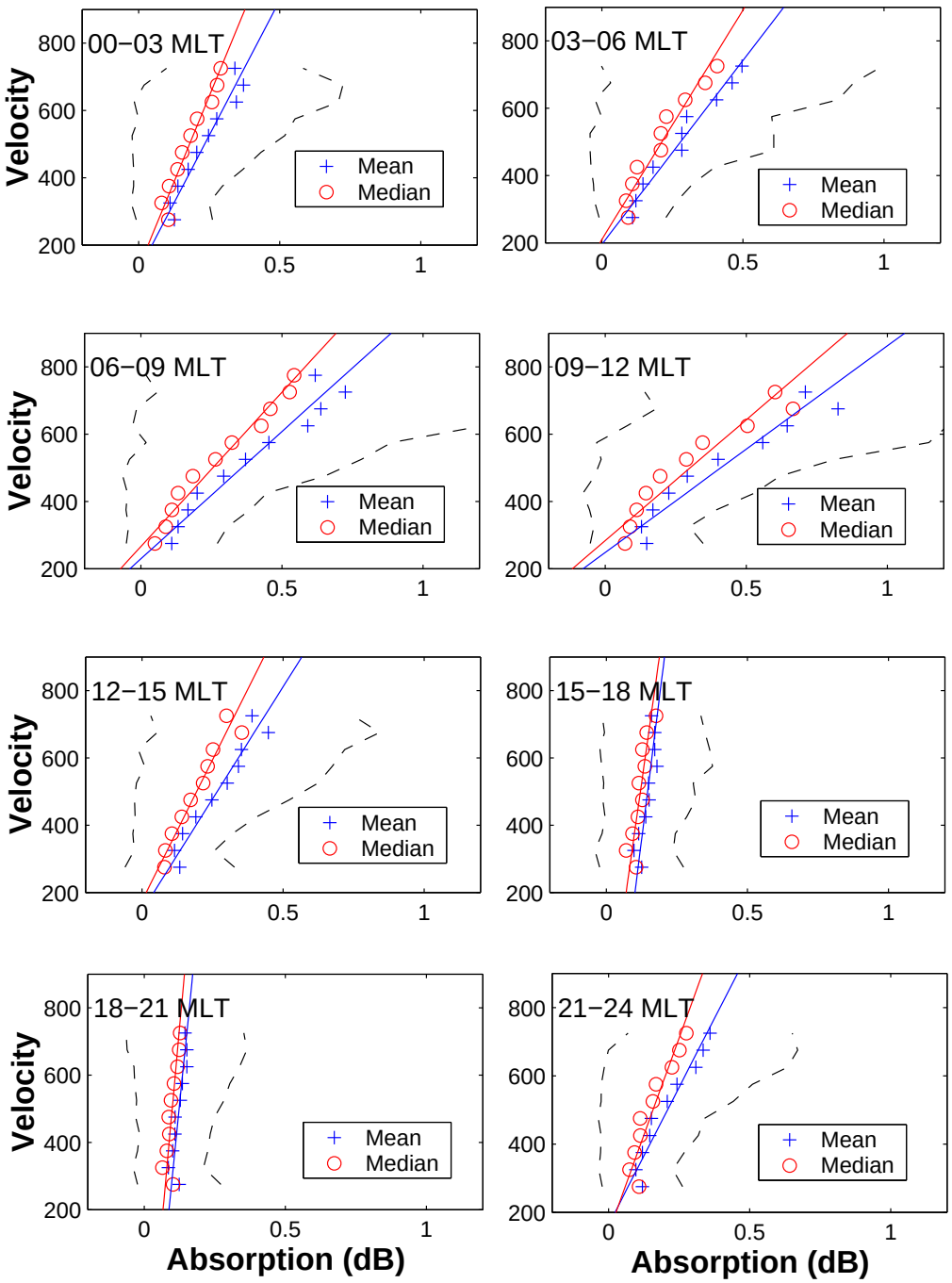

Figure 6.30. **Absorption versus solar wind velocity for 8 magnetic local time ranges. Mean and median values are calculated for each 50 km/s bin and straight line fits derived. Dashed black lines represent ± 1 standard deviation about th e mean**

	Correlation coefficient	Mean of residuals	Standard Deviation of residuals
Mean	0.477	-0.017 dB	0.187 dB
Median	0.479	0.034 dB	0.190 dB

Table 6.8. Correlation coefficients and related parameters for a linear fit of the mean and median absorption to the solar wind velocity over the 1995-2001 epoch.

likely that at the large velocities other mechanisms of absorption such as the SCA and SIA will dominate due to the infrequency of these high speeds.

A final attempt is made to fit the data to see if the correlation can be improved over ~0.48. Figure 6.31 shows the results of plotting the log of the absorption against the log of the solar wind and fitting an equation of the form:

$$\log_{10} A_m = a.\log_{10} V_{sw} + \log_{10} b \qquad (6.7a)$$

$$A_m = b.V_{sw}^{a} \qquad (6.7b)$$

The correlation for this fit is only marginally higher (e.g. 0.485 for the mean values) and no difference is found when the data are limited to the range of velocities over

which the fit is calculated. Similar results are obtained when a quadratic is fitted instead of the linear equation. Thus the simple linear fit to the solar wind data is the best that can be achieved but results in a relatively weak correlation. It is believed that the important factor that is necessary to improve upon these results is to combine the effects of the IMF with that of the solar wind and to include some term that takes account of the recent time history of the solar wind/IMF. This 'priming' factor would be related to the storing of energy in the magnetotail prior to release during substorm onset. Much further work is needed before a reliable prediction model for auroral absorption can be created based on a solar wind parameter though existing absorption models (e.g. Foppiano and Bradley, 1983; Greenberg and LaBelle, 2002) have changed from using a solar cycle related term (usually sunspot number) to a geomagnetic dependent value. This is eminently sensible as a study of the diurnal variation of absorption in each year at IRIS (Figure 6.7) demonstrates no consistency with the trend of the solar cycle. Indeed absorption is highest in 1995, just following a solar minimum. 1995 also happened to contain a series of high speed solar wind streams (Mathie and Mann, 2000); a phenomenon usually occurring in the declining phase of the cycle. This is more evidence that the absorption is closely linked with variations in the velocity rather than any parameter determined by the temporal position in the solar cycle.

6.3.6 The recurrence of the afternoon/evening minimum

It is worth considering the strongest, recurring feature in the diurnal variation of the absorption: the afternoon/evening minimum. Whether the absorption is sorted by coincident K_P, AE or the solar wind velocity there is a large rapid decrease in absorption in the afternoon sector before the slow rise begins in the evening. The empirical fits to the data at this time show a very steep gradient caused by a narrow distribution of absorption over small values. What are the defining mechanisms (or lack thereof) for this minimum? There are two options; the first is that the wave particle interactions that lead to particle precipitation (Coroniti and Petschek,1966) are severely reduced between noon and dusk in the magnetosphere the second is that there is a limit to how far substorm injected electrons can drift around the magnetosphere at auroral L shells. Of course the answer could well be some combination of the two. Past work has demonstrated that at auroral invariant latitudes the drifting particles are within the quasi-trapping region (Roederer, 1970) where the drift loss cone surrounds the bounce loss cone (close to noon). As particles enter the noon sector any pitch angle diffusion leads to particles moving towards the loss cone and consequently they are lost through radial diffusion and precipitation. Without significant pitch angle diffusion particles will complete a full circuit of the Earth being stably trapped. Satellite observations of energetic precipitation produce an average pattern that also reflects a minimum close to dusk (e.g. Hartz and Brice, 1967). Kennel and Petshcek (1966) suggested that there is a limiting particle density on a field line that governs pitch angle diffusion and precipitation. Thus if enough particles

are lost by ~18 MLT there will be a stably trapped population with only small levels of precipitation. So following substorm injections electrons drift eastward towards dawn, the pitch angle distribution is anisotropic following the injection of fresh particles leading to enhanced precipitation in the morning sector. As the particles approach midday those within the drift loss cone will be lost, further reducing the number density on a given field line and causing the population to tend towards stability. At higher activity levels more particles will be injected onto the field line and the rate of loss will also increase (Kennel and Petschek, 1966). Thus by dusk, very little precipitation will be occurring regardless of the geomagnetic activity. Space craft observations of the pitch angle distributions of energetic particles will play an important role in determining the real mechanics behind the dusk minimum. Hartz (1971) determined from satellite observations that precipitation decreased in the afternoon sector at the energies responsible for auroral absorption (e.g. > 20 keV electrons). This effectively limits the cause to a magnetospheric origin rather than an ionospheric effect (e.g. the complex chemistry of the D-layer).

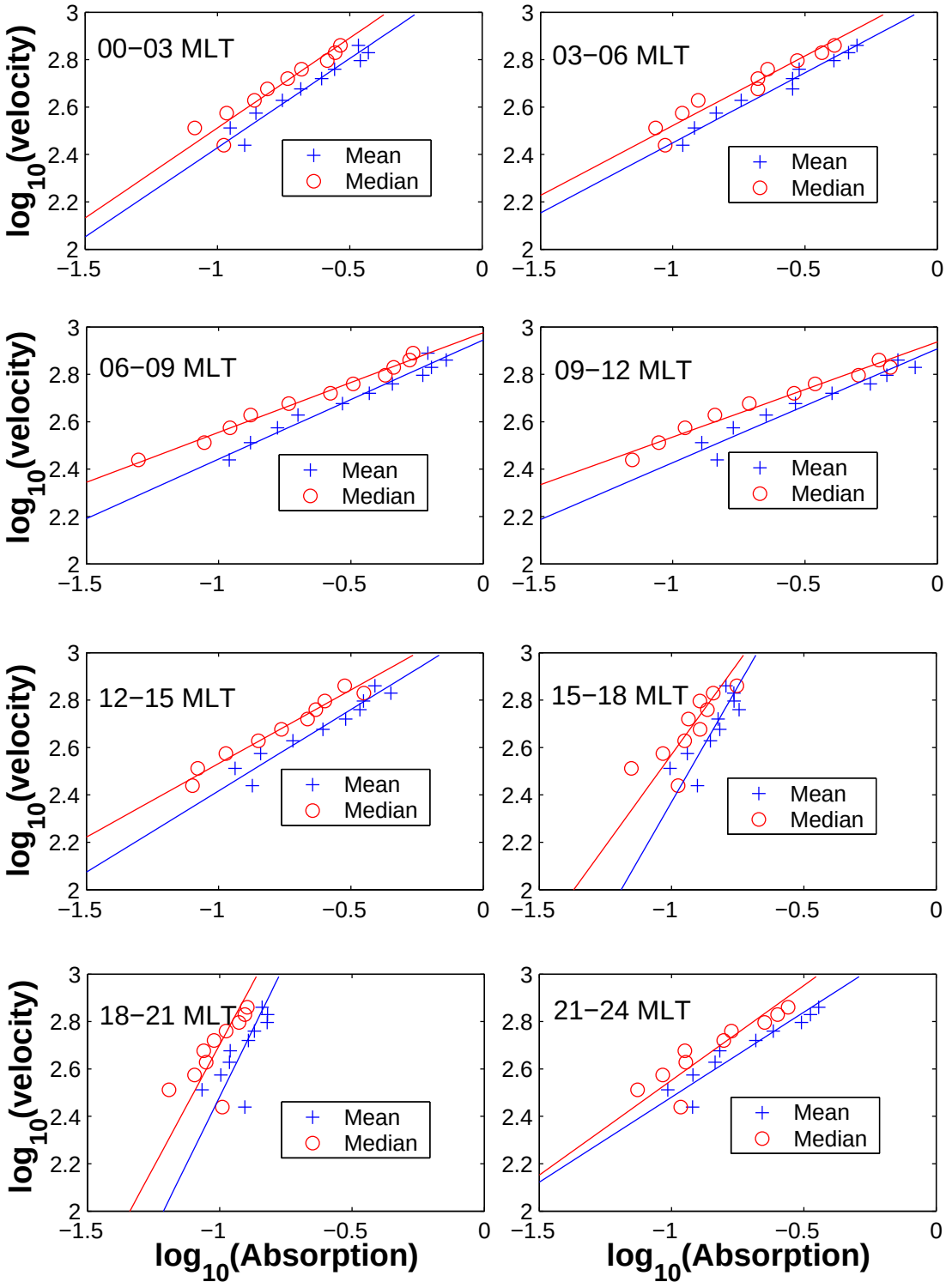

Figure 6.31. Log of absorption versus the log of solar wind velocity for 8 magnetic local time ranges (as in Figure 6.30).

6.4 Summary

For the first time data have been combined from 7 years of continuous observations of the auroral absorption from a single instrument (IRIS) and the spatial extent of the distinct problem of solar radio contamination has been examined for all beams. A definite diurnal variation becomes apparent when the data is averaged and this is characterised by a peak in the morning sector (~10 MLT) and a deep minimum around 18 MLT. This minimum appears to be independent of any geophysical or solar wind controlling factor that effects the absorption in the morning and around midnight and is likely linked to limits of anisotropy in the pitch angle distribution of the electrons.

It is agreed that a log-normal fit to the cumulative amplitude distribution of absorption (Q) is satisfactory for mid to high values, however at low absorption an exponential fit is better. Statistically, low values occur most often and particularly in the afternoon/evening, thus the log-normal distribution reflects reasonably strong precipitation.

The apparent seasonal effect on the observed auroral absorption has been attributed to differences in the amount of geomagnetic activity in the four seasons. This does not discount the possible effect of a poleward extension of the winter anomaly, although it should be noted that consistently enhanced D-region electron density effects will be removed from the data during quiet-day curve generation.

A non-linear empirical relationship between absorption and K_P has been identified and coefficients computed. This appears to fit the data reasonably well and

is superior to the log fit that had been previously proposed. The local time dependence of absorption is so clear that the possibility that different types of fits to the data in each MLT bracket should not be discounted. Any future investigation of this nature should take this into account.

The variation of absorption relies heavily on the changing solar wind levels rather than any solar cycle indicator (e.g. sunspot number). A linear relationship between absorption and solar wind velocity has been derived for the first time and it appears to give the best results of any type of fit. A southward IMF plays a significant role in precipitation in the auroral zone but the eastward component has no statistical effect on the mean absorption.

The limitations of the imaging riometer for a study such as this have been expounded upon and include errors that are introduced through the non-uniform nature of the beam sizes and the uncertainty of the distribution of absorption events in oblique beams. Some of the beams (particularly beam 10) exhibit unusually high values possibly due to some small inconsistencies in the quiet day curves; the possibility of a hardware problem has been investigated and although no drastic problems were located it can not be ruled out. The motion of the enhanced absorption in the season binned data suggests that the ambiguity may be related to scintillation in a side lobe of the beam as it displays a sidereal variation that moves in anti phase with the position of Cassiopeia in the main beam. Further investigation is necessary to determine the true cause of the problem in beam 10.

Chapter 6

This study can be considered as a portion of a possible absorption prediction model based upon latitude, longitude, geophysical and/or solar wind parameters. Although apparently reasonable fits to the mean and median absorption can be found for both K_P and the solar wind speed, the variability of the absorption still leads to problems. Low absorption is still likely even when geophysical activity is high, because absorption is highly dependent on the population of energetic particles in the magnetosphere; without fluxes of electrons (>15 keV) no appreciable absorption is possible. Thus current global models of absorption based on only K_P values are unreliable. Methods to improve such a model must take into account past levels of geomagnetic activity, absorption and some other measure of the energy stored in the magnetotail (e.g. B_Z). A detailed study of how absorption responds during geomagnetic storms would be especially useful, linking the observations to past levels of activity as indicated not only by K_P and D_{st} but also the IMF and solar wind speed. If this is done then with the large array of riometers available in both hemispheres and the catalogue of data, a suitable global empirical model could be defined.

Chapter 7

Polar Cap Absorption Events

7.1 Introduction

Solar energetic particle events (SEP) are major space weather phenomena. Large clouds of energetic protons (with some heavier ions and electrons) are released from active regions on the sun and upon reaching Earth can have severe consequences for both satellites and other facilities on the ground. In the following chapter the relationship of solar flares to solar proton events (SPE) is discussed with reference to 25 years worth of GOES satellite data. Various parameters of both the solar proton flares and the SPE are compared and contrasted; these include the temporal and spatial occurrence of flares that produce measurable proton fluxes at Earth.

The bombardment of energetic protons on the atmosphere lead to significant increases in electron density in the lower ionosphere, which in turn produces attenuation of HF radio waves. A simple empirical relationship between the proton flux measured at geostationary orbit and the absorption measured in the auroral region is derived. The effects of enhanced geomagnetic activity are explored as well as the effects that high solar radio activity have on the absorption.

7.2 Solar Proton Events and Flares

Solar Proton Events (SPE) events are thought to originate from two sources: acceleration of particles during solar X-ray flares and shocked solar wind particles, driven by coronal mass ejections; arguments continue as to which is the dominant mechanism. Protons in the MeV energy range remain the dominant species in both cases and most events can be reliably linked with X-ray flares; usually M class or above. Whatever the generating mechanism, these energetic particles travel through interplanetary space and occasionally interact with the Earth's magnetosphere and ionosphere. As described in Chapter 4, SPE lead to increased levels of ionisation in the sunlit lower ionosphere. These events are monitored by the Space Environment Centre (SEC), a branch of NOAA (National Oceanographic and Atmospheric Administration), who assign a level to each event based upon the flux of protons above 10 MeV. Table 7.1 describes each of the five classifications of radiation storm (SPE) together with the threshold PFU (particle flux unit). In addition, the fifth column of the table indicates the number of events that occurred between 1995 and 2001 (The time period for the PCA observations in this chapter).

7.2.1 SPE and PCA identification

The proton data that comprise the observations in this chapter have been collected from the GOES range of satellites (Chapter 3). SEC maintain a list of all solar proton events that have occurred since April 1976 together with associated flares and CME's. The proton flux in geostationary orbit fluctuates regularly, although a

solar proton event is defined to occur only when the flux of protons with energies above 10 MeV is greater than or equal to 10 $(cm^2.s.sr)^{-1}$ (i.e. PFU(>10 MeV) $\geq$ 10). Thus the criterion for identifying solar proton events is well established. Since 1976 there have been 197 separate cases of the proton flux exceeding the threshold level and 165 of these have reliable coincident flare identifications. Some of the events actually include multiple particle populations when fresh injections occur before an event has dropped back below the threshold.

It is the bombardment of solar protons on the ionosphere that lead to Polar Cap Absorption (PCA) events. Thus the occurrence of PCA are intrinsically linked to SPE, although not every solar proton event results in PCA due to a number of factors. Ranta *et al*. (1993), found that only the medium to strong events (>100 PFU) lead to appreciable changes in the absorption in the polar cap and auroral zones. SPE with PFU<100 result in variations of daily absorption between 0 and 1.5 dB measured at 30 MHz; this corresponds to absorption levels less than 0.93 dB at 38.2 MHz. This is still significantly higher than the majority of auroral absorption as determined in Chapter 6.

PCA events have been identified in the IRIS data set from 1995 to 2001 by considering those periods of elevated solar proton flux. Events that display uniform rises in absorption across the IRIS field of view during a SPE have been selected, reinforced by high correlation with the >10 MeV integral flux measured by GOES 8. With short time spans it becomes much harder to determine whether absorption is due to the flux of solar protons or whether it is precipitation from closed field lines, so most short duration events have been excluded. Using a reliable riometer located in

the polar cap, away from the trapping regions, can alleviate this problem, although this is not always practical; those riometers that are currently located within the northern

Strength		**PFU (>10 MeV)**	**Effects**	**# Events (1995-2001)**
S1	*Minor*	10	No effect to satellites or biological, some effect on HF propagation in polar region.	25
S2	*Moderate*	10^2	No biological effect, infrequent single-upset events, small effect on HF propagation in polar region.	11
S3	*Strong*	10^3	High latitude aircraft receive low level radiation exposure, single upset events and slight reduction in solar panels on satellites, Degraded HF radio propagation.	3
S4	*Severe*	10^4	Elevated radiation exposure to aircraft at high latitude. Degraded solar panels, noise on imaging systems, HF radio blackout in the polar regions.	3
S5	*Extreme*	10^5	High radiation exposure to aircraft at high latitudes. Satellites may be rendered useless, permanent damage to solar panels possible, complete blackout of HF communications in the polar regions.	0

Table 7.1 Radiation Storm levels as defined by the Space Environment Centre. 5 levels of storm are described together with some of the physical effects upon satellites and HF radio in the polar regions. The final column describes the number of events between 1995 and 2001 (inclusive).

hemisphere polar cap are often close to the cusp on the dayside (Stauning 1998) or are not always operating reliably (Nishino, private communication).

Table 7.2 lists the start and end times of observed SPE (1995 to 2001) together with the peak PFU. Maximum absorption values are included together with the corresponding PFU in parenthesis. Some of these values are due to auroral absorption during active periods. The remaining two columns identify the originating X-ray flare class and its position in helio-latitude and longitude. Those solar proton events which lead to confidently identified PCA events are highlighted in bold. It is worth noting that of the 27 PCA events 10 have maximum PFU of less than 100 though in general the corresponding absorption signatures for those SPE are low. Thus Ranta *et al*.(1993) are correct in suggesting only low ionospheric impact for small PFU events but it is still possible to clearly identify increases in absorption for these values. The lowest maximum absorption appeared during the solar proton event that started on 24 April 1999; this reached a peak of 0.5 dB with a corresponding PFU of 23 protons/(cm^2.s.sr). For a 20 MHz radio wave this would result in 1.82 dB attenuation.

7.2.2 Heliodistribution of Solar Proton Flares

The two panels in Figure 7.1 illustrate the helio-distribution of solar proton flares in solar longitude and latitude (top) and the occurrence of flares by longitude (bottom). Each of the flares is an X-ray flare of C class or higher that produces a solar proton event at Earth's geostationary orbit (~6.6 R_E) as measured by the GOES satellites. The data are provided by SEC and comprise 165 events measured from

SPE onset Date and time	SPE end Day/UT	Max. PFU	Max Abs. (with PFU)	Flare	Flare location
1995-10-20 08:25 UT	**20/23:40 UT**	**63**	**1.77(55)**	**M1/0F**	**S09W55**
1997-11-04 08:30 UT	**05/13:40 UT**	**72**	**1.8 (34)**	**X2/2B**	**S14W33**
1997-11-06 13:05 UT	**09/12:05 UT**	**490**	**3 (385)**	**X9/2B**	**S18W63**
1998-04-20 14:00 UT	**24/15:50 UT**	**1700**	**5.9 (1540)**	**M1/EPL**	**S43W90**
1998-05-02 14:20 UT	**04/03:35 UT**	**150**	**3.1 (11)**	**X1/3B**	**S15W15**
1998-05-06 08:45 UT	**07/01:40 UT**	**210**	**1.6 (225)**	**X2/1N**	**S11W65**
1998-08-24 23:55 UT	**29/12:10 UT**	**670**	**4.4 (55)**	**X1/3B**	**N30E07**
1998-09-25 00:10 UT	25/02:30 UT	44	3.7 (10)	M7/3B	N18E09
1998-09-30 15:20 UT	**02/08:30 UT**	**1200**	**3.1 (721)**	**M7/3B**	**N23W81**
1998-11-08 02:45 UT	08/02:45 UT	11	1.8 (10)	M2/2N	
1998-11-14 08:10 UT	**16/09:55 UT**	**310**	**3.2 (138)**	**C1/BSL**	**N28W90**
1999-01-23 11:05 UT	23/16:45 UT	14	0.7 (11)	M5	N27E90
1999-04-24 18:04 UT	**25/14:50 UT**	**32**	**0.5 (23)**		**NW limb**
1999-05-05 18:20 UT	06/05:50 UT	14	0.7 (11)	M4/2N	N15E32
1999-06-02 02:45 UT	03/14:10 UT	48	1.1 (33)		W limb
1999-06-04 09:25 UT	**05/05:15 UT**	**64**	**1.5 (47)**	**M3/2B**	**N17W69**
2000-02-18 11:30 UT	18/14:05 UT	13	0 (11)	M1/2N	S29E07
2000-04-04 20:55 UT	**06/01:55 UT**	**55**	**1.2 (29)**	**C9/2F**	**N16W66**
2000-06-07 13:35 UT	**09/03:25 UT**	**84**	**2.1 (77)**	**X2/3B**	**N20E18**
2000-06-10 20:45 UT	**11/11:30 UT**	**46**	**1.4 (16)**	**M5/3B**	**N22W38**
2000-07-14 10:45 UT	**19/23:30 UT**	**24000**	**15.3 (24000)**	**X5/3B**	**N22W07**
2000-07-22 13:20 UT	23/23:10 UT	17	0.5 (15)	M3/2N	N14W56
2000-07-28 10:50 UT	28/13:10 UT	18	1.5 (14)		
2000-08-11 16:50 UT	11/17:40 UT	17	0.8 (13)		
2000-09-12 15:55 UT	**15/21:40 UT**	**320**	**2.9 (241)**	**M1/2N**	**S17W09**
2000-10-16 11:25 UT	17/02:10 UT	15	1.4 (10)	M2	N04W90
2000-10-26 00:40 UT	26/10:00 UT	15	1.3 (10)	C4	N00W90

2000-11-08 23:50 UT	**13/07:45 UT**	**14800**	**9.6 (11400)**	**M7 multiple**	**N00-10W75-80**
2000-11-24 15:20 UT	**29/02:00 UT**	**942**	**3.6 (197)**	**X2/3B**	**N20W05**
2001-01-28 20:25 UT	30/00:35 UT	49	0.9 (36)	M1/1N	S04W59
2001-02-29 16:35 UT	01/06:00 UT	35	1.3 (28)	X1/1N	N24W12
2001-04-02 23:40 UT	**06/13:40 UT**	**1100**	**4.1 (1020)**	**X20**	**N14W82**
2001-04-10 08:50 UT	**13/10:55 UT**	**355**	**2.4 (145)**	**X2/3B**	**S23W09**
2001-04-15 14:10 UT	**17/17:00 UT**	**951**	**2.8 (625)**	**X14/2B**	**S20W85**
2001-04-18 03:15 UT	**20/08:20 UT**	**321**	**4.7 (52)**	**C2**	**S20-limb**
2001-04-28 04:30 UT	**28/05:20 UT**	**57**	**0.7 (35)**	**M7/2B**	**N17W31**
2001-05-07 19:15 UT	08/17:30 UT	30	2.0 (11)		NW limb
2001-06-15 17:50 UT	**16/12:10 UT**	**26**	**0.6 (24)**		**W limb**
2001-08-10 10:20 UT	10/14:40 UT	17	0.4 (13)	C3	Centre disk
2001-08-16 01:35 UT	**18/18:45 UT**	**493**	**2.6 (446)**		**Far back**
2001-09-15 14:35 UT	15/15:45 UT	11	1.0 (11)	M1/N1	S21W49
2001-09-24 12:15 UT	**30/17:10 UT**	**12900**	**6.0 (2710)**	**X2/2B**	**S16E23**
2001-10-01 11:45 UT	**05/03:30 UT**	**2360**	**5.7 (2040)**	**M9**	**S22W91**
2001-10-19 22:25 UT	19/22:55 UT	11	0.3 (10)	X1/2B	N15W29
2001-10-22 19:10 UT	23/01:15 UT	24	0.5 (18)	X1/2B	S18E16
2001-11-04 17:05 UT	**10/07:15 UT**	**31700**	**10.2 (26300)**	**X1/3B**	**N06W18**
2001-11-19 12:30 UT	20/14:20 UT	34	2.3 (16)	M2/1N	S13E42
2001-11-22 23:20 UT	**27/21:00 UT**	**18900**	**11.9 (3580**	**M9/2N**	**S15W34**
2001-12-26 06:05 UT	28/10:45 UT	779	0.6 (117)	M7/1B	N08W54
2001-12-29 05:10 UT	29/22:50 UT	76	0.2 (16.7)	X3	S26E90
2001-12-30 02:45 UT	04/23:55 UT	108	1.2 (88)	M9	West limb

Table 7.2. Solar Proton Events recorded by GOES (1995-2001). Events highlighted in bold produced observable Polar Cap Absorption (PCA).

April 1976 to July 2002. The events marked in red are the 41 recorded SPE that occurred between 1995 and 2001 (inclusive), encompassed by the operating period of IRIS. All of the proton flares occur within a band of ±50º latitude but are split into two latitudinally separated distributions both centred at ~20º. The northward distribution is spread more evenly in longitude whereas the southward distribution bunches towards a centre of 15º-20º solar longitude.

The bottom panel of Figure 7.1 presents the percentage occurrence of solar proton flares binned by 20º longitude. Flares that are classed as being beyond the limb are placed within the ±90º bins unless an estimation of the position has been made by SEC. The majority of the events originate in the western hemisphere of the Sun; ~75% of solar proton flares occur westward of 20° east. At this resolution two peaks appear in the data; the first at –10° and the second in the centre of the western half of the facing sun, at 50°.

The third peak in the most westward bin is an artefact of the binning of flares from the far side. Those events displayed in red are for events between 1995 and 2001. The data have been normalized to the total number of solar protons flares such that the ratios of the columns reflect the fraction of events within that data bin. The westward bias is clear, with many of the recent events occurring near or beyond the western limb. Two other peaks are still apparent although the central peak is slightly further westward.

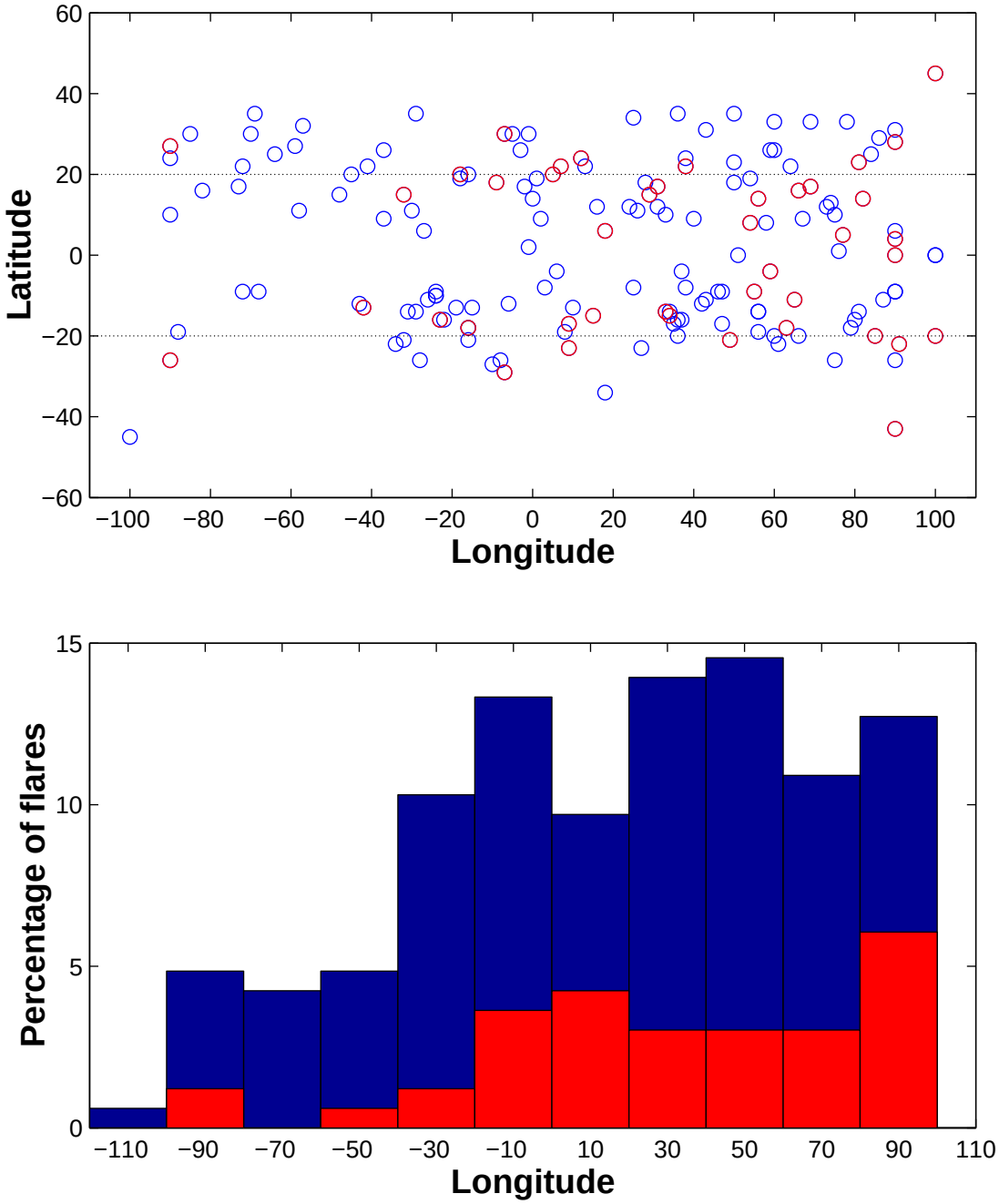

Figure 7.1. **Heliodistribution of solar proton flares (1976-2002). The top panel marks the positions of each flare in solar longitude and latitude (east is negative). The bottom panel shows the distribution in longitude in 20º bins. Red data are for events between 1995 and 2001.**

Figure 7.2 is split into 3 panels; the top panel (a) displays the delay time between the flare and the start of the SPE at Earth versus the longitudinal position. This is calculated from the point where the X-ray flux exceeds the lower limit for a C class flare. For delays of less than 1500 minutes the values tend to lie between -50 and 100 degrees with the majority in the western hemisphere. For longer delays the flare site exhibits a more eastward location. The middle panel shows the variation in maximum SPE PFU with longitudinal position of the proton producing flare. Although there is the expected trend towards the west there is a generally even spread of points across the longitudes. The bottom panel shows the maximum x-ray flux against the maximum PFU for each solar proton event. No direct correlation is obvious but in general low X-ray fluxes are not linked to the higher range PFU.

7.2.3 Solar Proton Events and PCA

Figure 7.3 shows the monthly distribution of solar proton events measured by GOES from 1976 to 2002. This includes events that are not well correlated with solar flares but may instead originate from solar wind shocks. Two distributions are plotted; the blue bars indicate the distribution of all the GOES data from 1976 to 2002 whereas the red bars demonstrate the percentage observed in the years of IRIS operations (1995 to 2002). The data are normalized to the total number of events from 1976 to 2002,

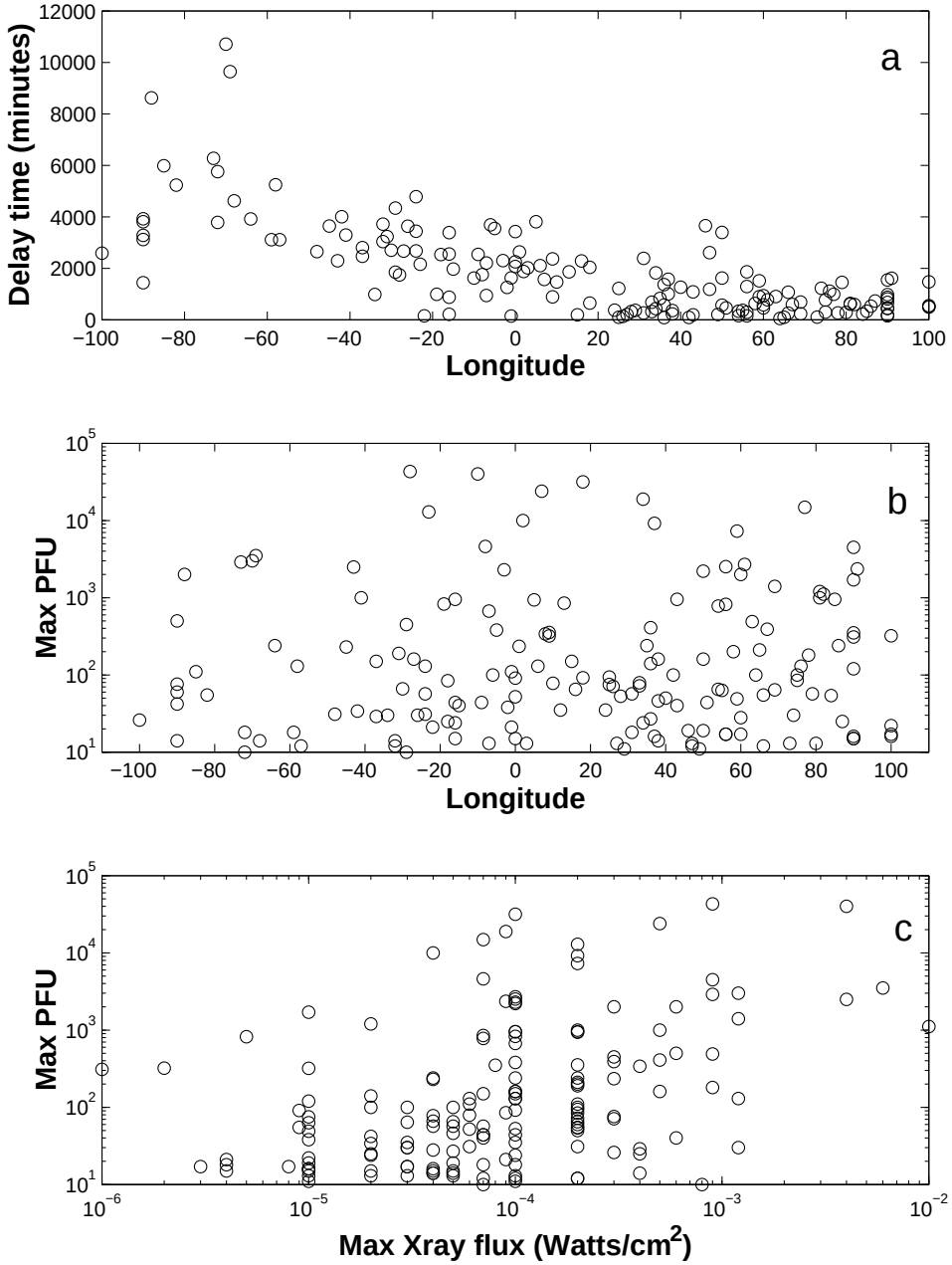

Figure 7.2. **Panel (a) displays the delay time between the flare and the solar proton event observed at Earth as a function of solar longitude. Note the increase with eastern hemisphere flares. Panel (b) compares the maximum PFU against the position and finds no correlation. In Panel (c) the maximum PFU is plotted as a function of the maximum X-ray flux. An upper limit to the PFU is indicated.**

thus the ratio of observations in each monthly bin gives the percentage of events observed in a given month. Two peaks appear in the principle distribution, the first in April (11.8%) with a broad rise and decay, and the second in November (11.3%) with a quick rise time and even quicker decay. This leads to two minima centred about winter (5.8%) and late summer (5.9%). 17.2% of events occur during the winter months (December to February) and 25.2 % occur in the summer. The broader spring peak contains 31.7 % of the recorded events whereas the autumn months (September to November) recorded 25.9 % of the events with the maximum occurring in the latest month as oppose to the central month of spring. The second panel displays the distribution of Polar Cap Absorption events observed by the IRIS at Kilpisjärvi (red bars) and the green bars are the ratio of PCA to SPE (1995 to 2001) observed in each month. These events have been identified on the basis of the uniform coverage of the array with similar signatures in other riometers of the SGO chain during an SPE. The seasonal variation is clear in this plot with a severe winter minimum of zero.

7.3 Discussion on the relationships between flare, SPE and PCA

Figure 7.1 demonstrated that solar flares which lead to solar proton events favour certain areas on the surface of the sun with respect to the Earth. A bias in the data towards the west is not unexpected; many observations of SPE have concluded that western hemisphere flares are more likely to lead to increased protons levels at Earth (e.g. McCracken, 1962; 1969). The explanation usually given for this is that protons emitted from a western hemisphere flare will propagate along the

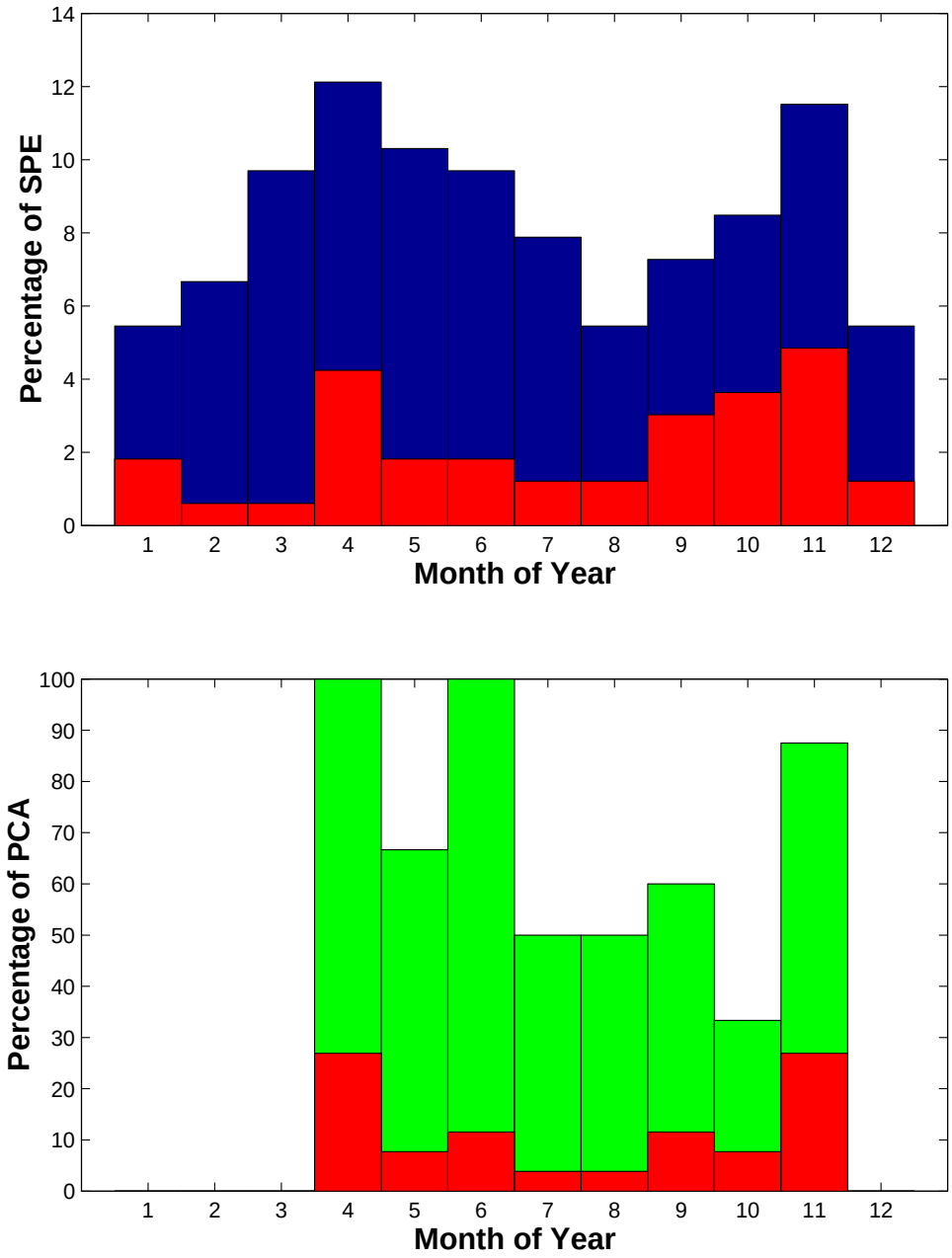

Figure 7.3. **The top panel displays the percentage of SPE binned by month of the year from 1976 to 2002 (blue bars) and 1995 to 2001 (red bars). Data from 1995 to 2001 are normalized to the total amount since 1976. The bottom panel displays the occurrence of PCA (red bars) from 1995 to 2001 whereas the green bars demonstrate the distribution when normalized to the number of SPE events.**

interplanetary field lines towards Earth; the Parker Spiral (Chapter 1) suggests that flare sites in the west are better connected with the position of the Earth and magnetosphere although diffusion of protons across field lines has also been observed (Warwick, 1963, King and Williams, 1970). Thus direct travel along field lines appears to be favoured by the protons and diffusion would explain some of the events that originate from eastern flares. The diffusion mechanism should take a longer time than simple propagation along the field line and panel (a) of Figure 7.2 indicates that the average delay time of an SPE rises with increasing eastward longitude of the flare site; however the distribution can be quite wide (between –60º and –80º the delay time varies from 2 to 7 days. All of this assumes that the IMF behaves as a Parker spiral at all times, although close to solar maximum when SPE are more common (Shea and Smart, 2002) the IMF is disordered and good connection between the Earth and the Sun may be lost. Figure 7.4 uses all the flare associated SPE from 1976 to 2002 and bins the delay times into years from solar maximum it is clear that in the falling portion of the solar cycle the delay time peaks; thus for a highly variable IMF solar protons are unable to propagate cleanly to the Earth.

The bottom panel of Figure 7.1 showed two primary peaks in the distribution of flares; one slightly east of the centre of the sun. It has become clear in recent years that X-ray flares are not the only producers of solar particles and the transition through the IMF can alter the energy spectrum of the distribution. Two main classes of solar energetic particle event can be defined (e.g. Reames, 1999); flare associated and CME

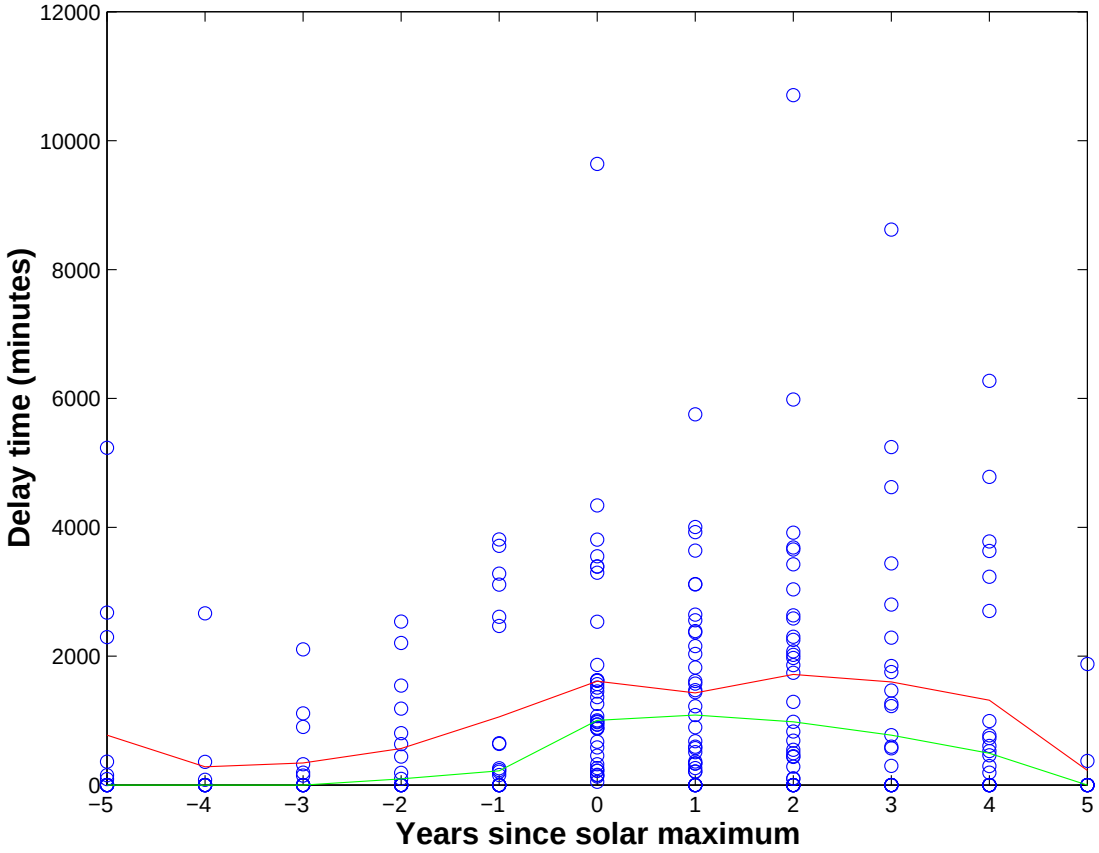

Figure 7.4. Delay times for SPE from 1976 to 2002 plotted as a function of the solar cycle. There is an increase at solar maximum and in the declining phase that is consistent with a disordered IMF.

associated. Flares close to the centre of the disc will release protons that are subsequently driven through the solar wind by the shock of the associated CME (Krucker and Lin, 2000). This will also have the effect of accelerating the protons creating different particle populations, and thus a CME related SPE may involve two stages: protons arrive shortly after the flare, a second population is injected just before the impact of the CME with the magnetosphere leading to a sudden commencement. This is a pattern often observed in the PCA/SPE (Davies, 1990). Smart and Shea (1996) used data from the IMP-8 spacecraft for solar proton events between 1973 and 1996 to determine a longitudinal bias in the flare positions. Some significant differences appear when comparing the data presented here with that of the previous study. The first is that Smart and Shea were able to allocate longitude values to flares which erupted from beyond the western limb of the Sun, thus smoothing the final peak into a successive drop in occurrence. Secondly the peaks in the data do not coincide with those obtained from SEC measurements. This may be explained partly by the different time periods that the data sets cover; 1973 to 1995 (170 events) for the previous investigation, and 1976 to 2002 (165 events) for the present study. In general both distributions display similar characteristics with a westward bias to the data but with two main peaks; one near the centre of the disk and the other to the west. Smart and Shea (1996) suggested that the distribution could be represented by the composite of two Guassian distributions. Due to the low numbers of events in each data bin, this is probably not a significant assumption, although due to the infrequent nature of solar

proton events it is hard to obtain sufficiently large, reliable, datasets to make good statistical analysis.

Figure 7.3 presented the monthly distribution of solar proton events (panel a). The double peaked nature of the occurrence shows a bias towards the equinoctial seasons when it is thought that the orientation of the IMF produces a favourable connection to the Earth (Chapter 6). The distribution of PCA will obviously be determined by the occurrence of SPE, although other factors also play a role. No PCA is observed during the winter months regardless of the few SPE that occur. Without solar UV electrons and neutral species tend to form negative ions Similarly the ratio of PCA to SPE tends to even the distribution out slightly with some notable exceptions in April, June and November. As mentioned earlier a study performed by Ranta *et al.*, in 1993 separated solar proton events into three categories: Strong (PFU >1000), Medium (100<PFU<1000) and Weak (PFU<100). The yearly distribution of these events were described from 1976 to 1989, indicating that the weak SPE have a much higher occurrence than their stronger brethren. The total number of events also broadly followed the sunspot number trend, which was reinforced in a study by Shea and Smart (2002). Ranta *et al.* (1993) examined the ionospheric effects of SPE from 1981 to 1989 using a chain of riometers located in Fennoscandia. By considering the daily mean absorption values a threshold in the PFU value of SPE was determined at 100 PFU; lower than this and no significant effect was had on the ionosphere. The reliance of absorption in the lower D region (<80 km altitude) on UV radiation also acts as a factor for determining whether PCA are observed. A dark polar cap leads to

absorption from particles that deposit energy above ~75 km (<10 MeV) with some contribution from the weak ionisation tails of the harder particles. At lower altitudes the electrons combine with neutral molecules to form negative ions (see Chapter 4) which do not contribute to the absorption; this explains the absence of PCA during the winter months demonstrated in the bottom panel of Figure 7.3. All observations used in this Chapter come from the northern hemisphere and so during the winter months the ionosphere is dark. Readings from riometers in the Antarctic would provide a useful test on whether this is true as it is assumed that the occurrence of PCA would minimise in the northern summer months. The identification of polar cap absorption used in this study (spatial coverage during SPE) leads to observations of PCA with PFU < 100 but greater than about 50, in conflict with the findings of Ranta *et al*. (1993) Thus if the ratios of the PCA to SPE are calculated for events of maximum PFU > 50 then the distribution might be expected to be level at close to 100% in every month (except winter). This is indeed the case but is insignificant due to the small number of events that have occurred to date.

Finally the maximum X-ray flux was compared with the maximum PFU of each of the events (panel c, Figure 7.2). No direct correlation appeared (correlation coefficient = 0.2), however an upper limit to the PFU is apparent; the distribution of PFU broadens with increasing X-ray flux. Thus low X-ray flux flares (e.g. 10^{-5} watts/cm^2) can produce up to a certain level of PFU (10^3 PFU). Due to the low numbers of events no conclusions can be drawn about the data at particularly high and low X-ray fluxes.

7.4 Relationship between integral proton flux and absorption

It has been established that solar proton events detected at Earth often lead to polar cap absorption. Figure 4.1 illustrates ionisation rates due to incident mono-energetic protons. Thus solar protons from 1 to 100 MeV will deposit energy between 35 and 100 km altitude. Traditionally, auroral absorption occurs at heights close to 90 km; during PCA the majority of absorption happens at lower altitudes

Intuitively, one might expect a linear relationship between the precipitating flux of energetic particles and the resulting electron density, however this is not the case. The equation relating a flux of particles with an ionisation profile in the atmosphere has been calculated by M.H. Rees (1964). In general terms the production (or ionisation) rate, q, is proportional to the incoming flux.

$$F \propto q \tag{7.1}$$

Chapter 1 (section 1.5.1) described the principle of Chapman layers and it can be shown that an alpha-Chapman layer can represent the D layer:

$$q = \alpha_{eff} N_e^2 \tag{7.2}$$

and so

$$F \propto N_e^2 \tag{7.3}$$

Where α_{eff} is the effective recombination coefficient. When considering a fixed observing frequency ionospheric absorption is approximately proportional to the

height-integrated product of the electron density and the effective collision frequency (ν_{eff}). Thus:

$$A \propto N_e \nu_{eff} \quad (7.4)$$

$$A \propto \sqrt{F} \quad (7.5)$$

Where F is the integral flux and the collision frequency is assumed to be constant with time at all altitudes; hence the absorption is proportional to the square root of the flux.

7.4.1 The role of the solar zenith angle and geomagnetic activity

During SPE the majority of absorption is from the extra ionisation caused by the incident energetic protons, however during geomagnetically active periods, significant electron precipitation is also thought to contribute to the absorption within the auroral zones. As described in Chapter 4, the lower D region is sensitive to UV and during dark periods electron density is lost to form negative ions so reducing the attenuation of HF radio waves. This suggests that there are two main criteria for determining a relationship between the integral proton flux and the absorption: the events used must be 'clean' (little or no contributions from geomagnetic radiation), and the ionosphere must be sunlit in the absorbing region. The second condition is the easiest to satisfy in practical terms. If the solar zenith angle is considered as a direct proxy for solar illumination, the variation of absorption with this angle can be included. Thus a limiting angle, χ, can be determined and only absorption that occurs for solar zenith angle < χ should be used in forming a relationship.

'Clean' events do occur when geomagnetic activity is already low and if any CME associated with the solar flare is directed away from Earth. These cases tend to be rare, however, so a method to filter the closed field line precipitation out of the data sets is needed. Using high latitude observations is one method, however contamination is still possible. If one assumes that the 'closed' contributions are small in scale size then observations from different riometers can be averaged to give a better estimate. The PCA tends to be uniform over relatively large areas so the absorption signal will reinforce whilst the small features drop in magnitude. This assumption holds for quiet to moderate activity, however too high activity will still affect the signal. For very intense PCA events the effect from 'closed' precipitation should be negligible above the background levels.

When the integral proton flux (for >10 MeV) is correlated with the measured absorption for all SPE in 1995 to 2001 the correlation is relatively variable with a mean correlation of 0.53. This low correlation is likely due to diurnal variation of PCA that is unreflected in the proton flux data; night time recoveries in the absorption are ionospheric in nature, being the product of electron attachment to neutral species (see Chapter 4). Removing absorption values that occur when the lower ionosphere is dark should lead to a better correlation

Figure 7.5 displays the correlation coefficient between absorption and the integral proton flux for the seven channels of the GOES 8 satellite, based on a sliding scale of solar zenith angle limit. Underneath the correlation curves are the number of data points that contribute to each sample. At 60^{o} three of the energy thresholds are

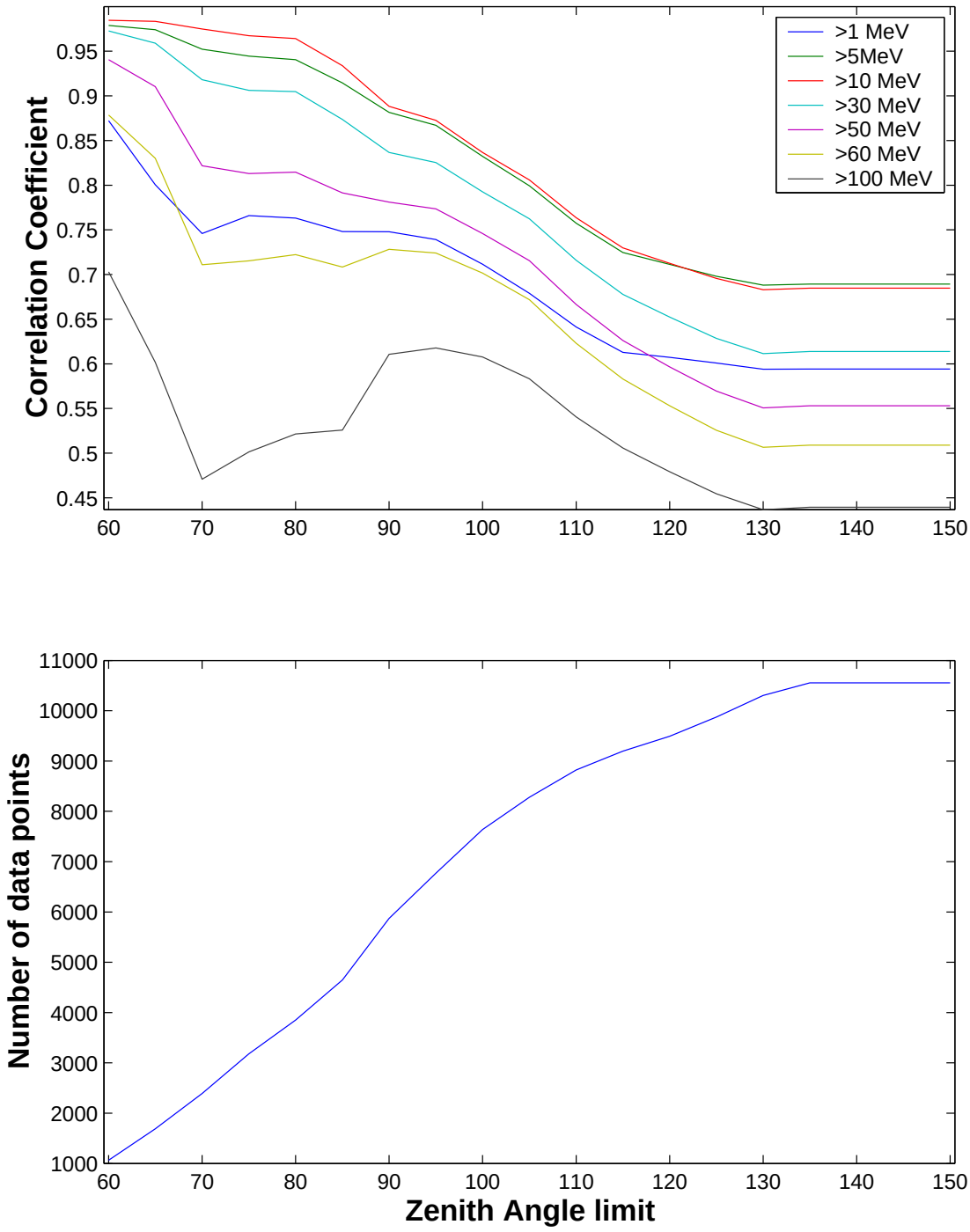

Figure 7.5. **Variation of correlation coefficients with a sliding scale of solar zenith angle limit. The bottom panel displays the number of data points used in each of the correlations, increasing as the zenith limit increases.**

close to a correlation of 1; >10 MeV, >5 MeV and >30 MeV, in order of dominance. As the zenith angle limit increases, the correlation coefficients decrease; the four highest energy thresholds decorrelate rapidly and these show considerably less correlation than the three lowest energy channels. Both >10 and >5 MeV decorrelate at a similar rate; slowly until 80 degrees and after 80º the decrease in correlation becomes steeper the correlation coefficient dropping below 0.9 at 88º. The decorrelation then continues at a greater rate across a larger range of solar zenith angle limits with the levels dropping to 0.680 and 0.685 respectively by 130º zenith angle limit.

Figure 7.6 uses a fixed solar zenith angle limit of 80 degrees and varies the level of geomagnetic activity as described by the K_P index, once again a sliding limit. This provides another series of correlation curves; in this case the >10 MeV flux still correlates with the absorption the best and the levels remain relatively high across the range of K_P. This suggests that the variation in absorption is not highly dependent on the geomagnetically originating radiation, however this only considers the temporal structure variation and higher K_P may still lead to a general increase in absorption (as demonstrated in Chapter 6).

It has become obvious that when considering the effectiveness of high energy protons on the cosmic radio noise absorption it is those particles with energies in excess of 10 MeV that are most significant close to the polar cap. It is harder to estimate an upper limit to the effectiveness by considering the integral channels, but

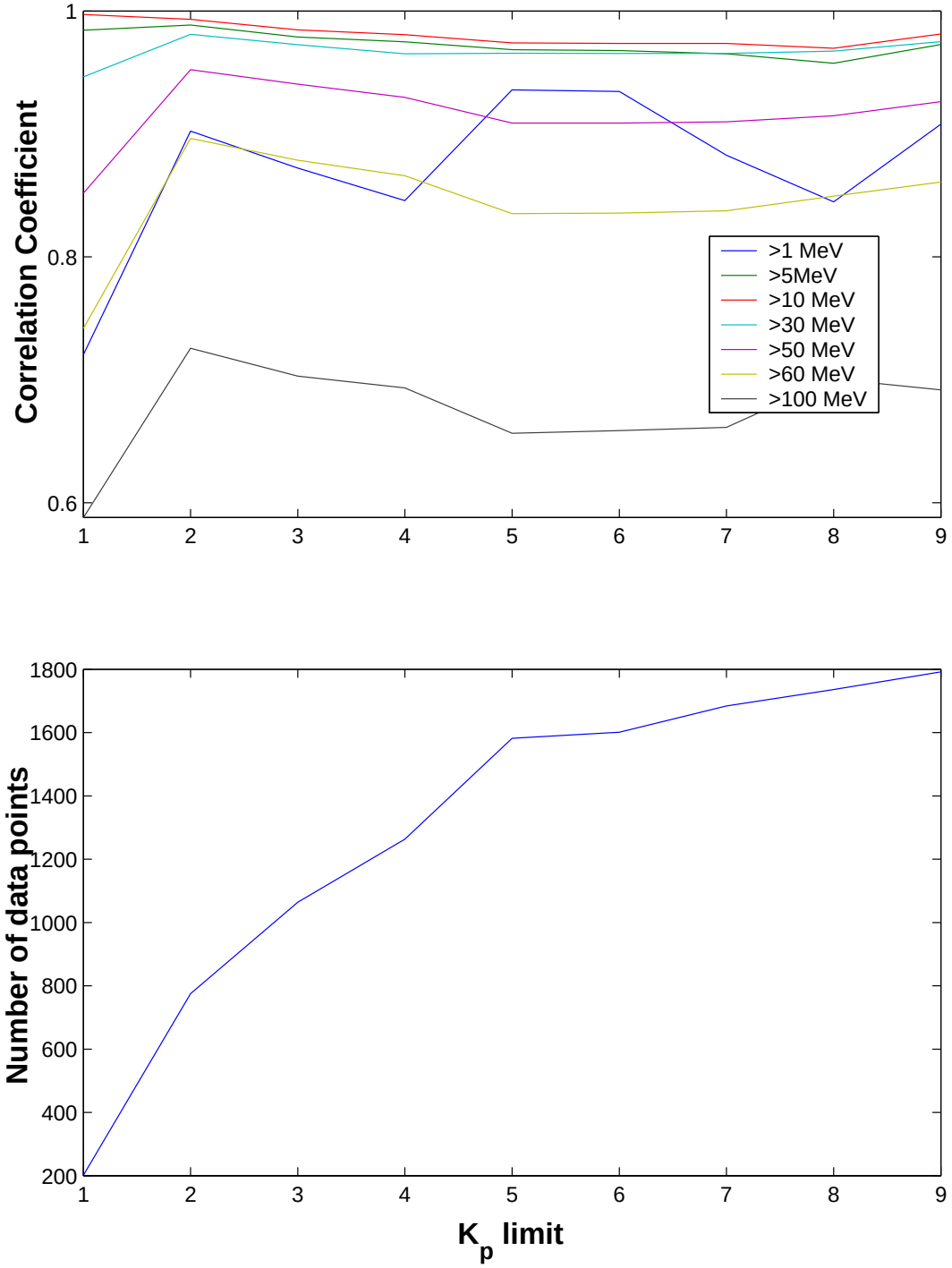

Figure 7.6. Variation of correlation coefficients with a sliding scale of K_P limit The bottom panel displays the number of data points used in each of the correlations, increasing as the limit increases.

since the dependence appears to be limited to some finite band of energies it is worth considering the differential fluxes from the GOES 8 satellite.

Figure 7.7 displays the zenith limit versus the correlation coefficient calculated for the differential fluxes with the absorption at Kilpisjärvi. The energy ranges were presented in Table 3.6 and each curve is colour coded to the values presented in the legend. At the lowest zenith limit both the 15-44 MeV and 39-82 MeV display a high correlation (0.962) though by $\chi = 72^{o}$ the higher energy has dropped to 0.911 and been surpassed by the 8.7-14.5 MeV range. With increasing solar zenith angle limit the correlation decreases for each energy band but the rate is different in certain cases; the 15-44 MeV band decorrelates at a higher rate than the 8.7-14.5 MeV channel. At a solar zenith limit of ~130º the two energies share a correlation coefficient of 0.71 and similarly the 39-82 MeV and 4.2-8.7 MeV channels converge. This suggests that the absorption at higher zenith angle depends more on the low energy protons than the higher values (15-44 MeV); a reasonable conclusion when the formation of negative ions is considered. If electrons are quickly lost in the lower D-layer (< 75 km altitude) the high-energy portion of the proton spectrum becomes less effective at producing absorption, rather the low energies (e.g. 5 to 10 MeV) will dominate the structure in the upper D layer.

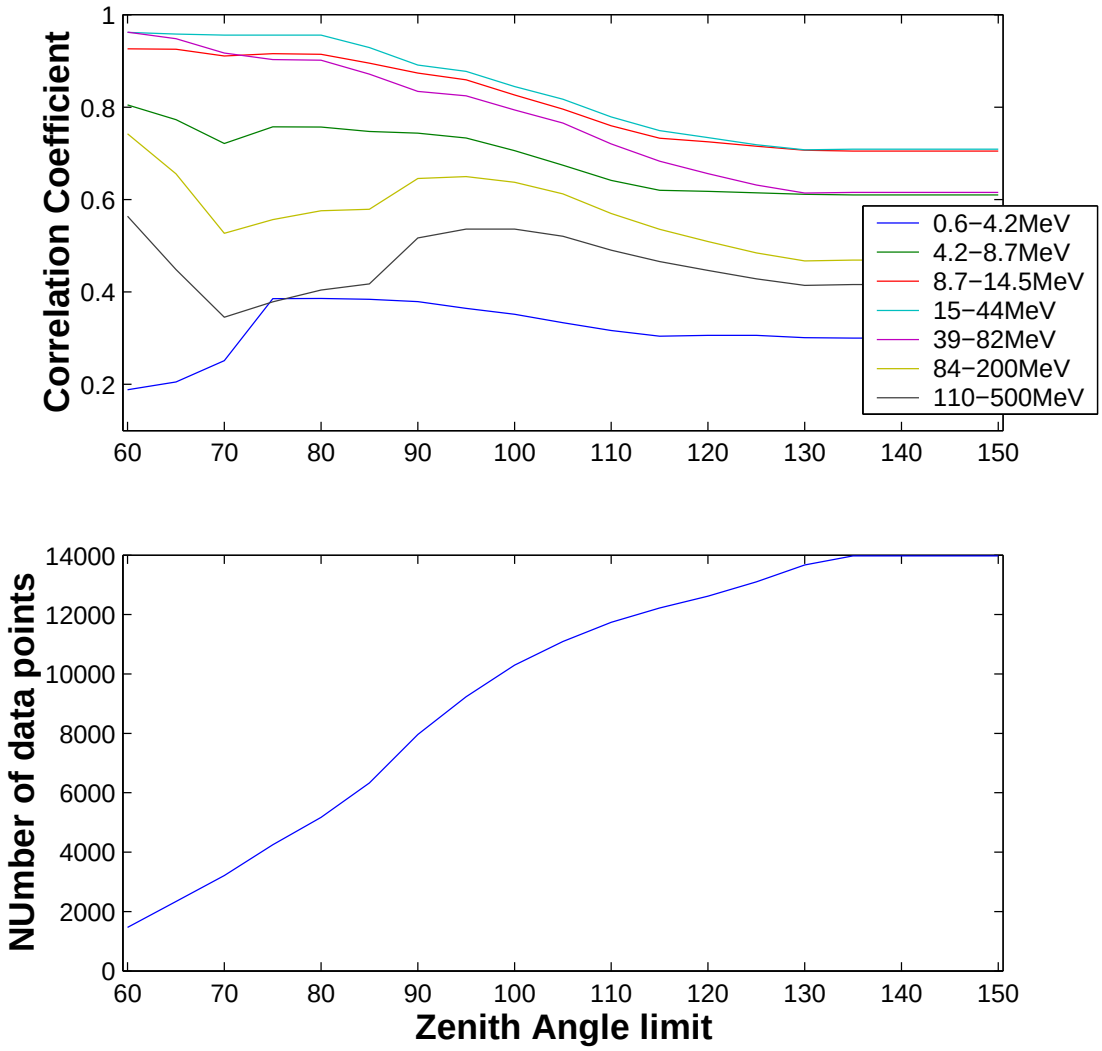

Figure 7.7. Variation of correlation coefficients with a sliding scale of solar zenith angle limit. This time the top panel display the differential flux channels from GOES 8. The bottom panel displays the number of data points used in each of the correlations, increasing as the limit increases.

7.4.2 An empirical flux-absorption relationship

The hypothesis presented at the start of this section suggested that the relationship between absorption and flux is relatively simple and non linear; absorption going with the square root of the integral flux. Coefficients have been computed before for differing energy thresholds (e.g. Davies, 1990 and Potemra, 1972) and absorption (usually at 30 MHz), often using limited data recordings. Potemra (1972) used data collected from 93 passes during three markedly different events, finding the best correlation between protons greater than 8.4 MeV and absorption at 30 MHz. The long duration observations of both IRIS and GOES have provided a larger database for determining the absorption-flux relationship. By using a geosychronous satellite instead of a polar orbiter continuous observations during SPE are possible rather than being limited to the polar passes of an orbiting spacecraft.

Equation 7.5 can be tested by plotting the logarithms of the daytime IRIS data (zenith angle < 80°) and the corresponding >10 MeV proton flux. Figure 7.8 displays the result. A line of the form :

$$\log_{10} A = C \log_{10} F + K \qquad (7.6)$$

is fitted to the data where C represents the power to which the flux must be raised in order to be linearly proportional to the absorption. In this case C = 0.53, thus the assumption that absorption is proportional to the square root seems eminently reasonable. To test this the bottom panel of Figure 7.8 displays the residuals (observed – calculated absorption) as a function of the flux; at high flux levels the fit breaks

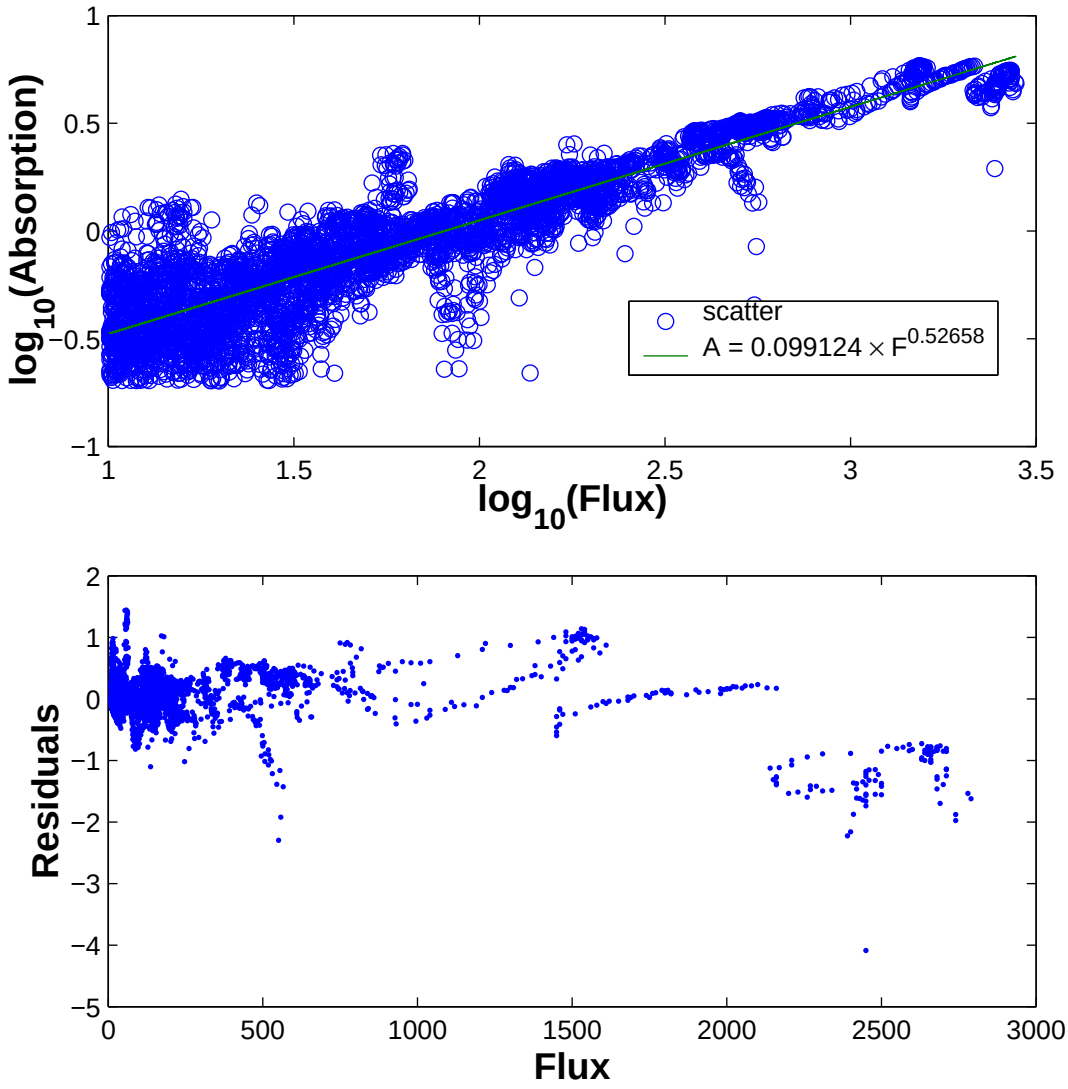

Figure 7.8. **Scatter plot of the logarithm of absorption against the logarithm of the integral flux (>10 MeV). The green line is the line of best fit to the data. Bottom panel shows the residuals of the fit displayed as absorption against the flux.**

down with a definite negative trend in the data, however the data is reasonably fitted below √F=30 although there is a large region of scatter at the lowest values that imposes quite a significant error (approximately ±1 dB). Since the original hypothesis suggested that absorption should vary with the square root of flux an attempt is made to fit the data in the form:

$$A = C\sqrt{F} + K \qquad (7.7)$$

Figure 7.9 displays the scatter of absorption with the square root of the >10 MeV integral flux (top panel). The line of best fit is displayed in green and the fitted function is displayed in the legend. The error associated with absorption due to inconsistencies in the quiet day curves can be as high as 0.2 dB; this would make the constant in the fitted equation insignificant. Thus as the flux of protons approaches zero, so too would the absorption, assuming no electron precipitation. Once again the residuals are plotted in the lower panel and vary mostly between 1 and –1 dB for most of the flux levels except at the higher values where the relationship once again breaks down somewhat. The absorption and the square root of the flux have a correlation coefficient of 0.957. As a check for determining whether a different energy level might produce a better result lines have been fitted to both the >1 MeV and > 100 MeV integral fluxes. In these cases the correlation coefficients are 0.753 and 0.511 respectively with much wider variance in the residuals. The >100 MeV protons do not contain enough of the structure related to the absorption for a good correlation and the protons from 1 to 10 MeV contain too much structure that is not exhibited by the slowly varying absorption.

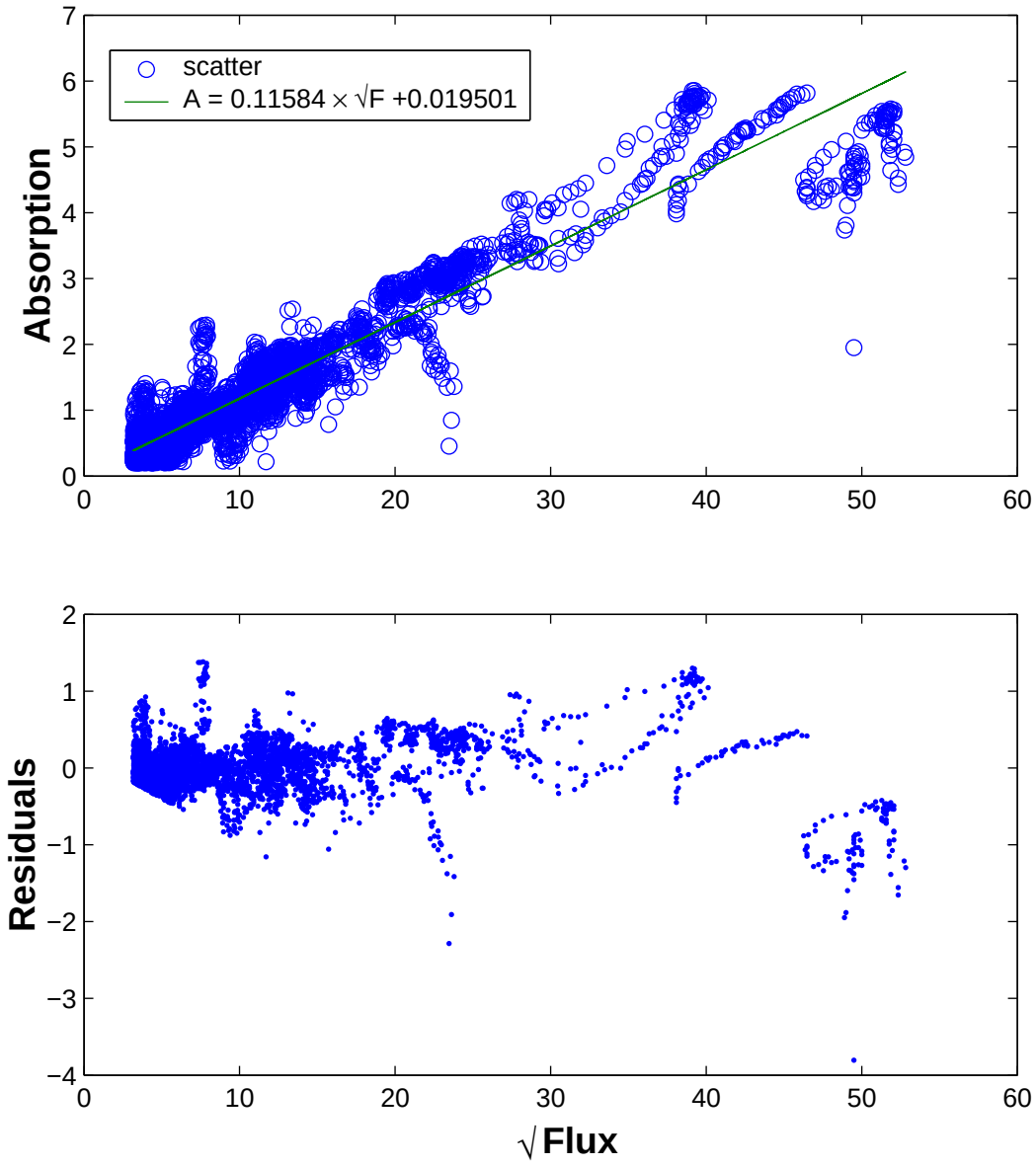

Figure 7.9. Scatter plot of the absorption versus the square root of the integral flux (>10 MeV). The green line is the line of best fit to the data. Bottom panel shows the residuals of the fit displayed as absorption against the square root of the flux.

7.5 Discussion on the Flux-absorption relationship

It has been shown that a good correlation exists between the integral flux of protons measured at geostationary orbit and the absorption observed in the auroral zone. Previous workers (e.g. Potemra, 1972) have found this to be the case with riometers located in the polar cap and the flux of protons measured by polar orbiting satellites. The best relationship is found for protons with energies greater than 10 MeV which display a high correlation (> 0.9). Although initially promising the fit does contain some problems; a good correlation is found but there are some significant errors on the calculated absorption at low fluxes (±1 dB) as well as a systematic trend away from the fit at high values of flux. At this point it is appropriate to consider the factors which may be affecting the fit. One parameter that may upset the computation is the effective collision frequency which had been assumed to be constant in time. The dominant collision regime in determining absorption is between electrons and neutral species and this electron-neutral collision frequency depends on two factors: the concentrations of the various atmospheric constituents and the temperature of the electrons. As the altitude decreases in the ionosphere the neutral atmosphere thickens and the collision frequency increases exponentially. A second product of the increase in density is the thermalization of the electrons. At lower altitudes the temperature of the electrons can be considered as equal to that of the neutral species; cases where this does not hold are in intervals of Joule heating, where electron temperatures are raised. In general the collision frequency profile can be

considered to be constant for a given polar cap absorption event, unless significant Joule heating occurs.

Thus it is clear that for comparable electron densities the absorption will be greater at a lower altitude due to the effects of the electron-neutral collision frequency. This phenomenon may become important in the flux-absorption relation when there are drastic differences in the spectrum of proton precipitation throughout events and from one event to the next. When considering solar protons it is important to remember that the energies are very high (>1 MeV) and extend well into the hundreds of MeV. A 'hard' spectrum will result in energy deposition at lower altitudes (e.g. 50 km) that, whilst possibly leading to smaller electron density values than at greater heights (e.g. 80 km), will still result in a higher integral absorption due to the increasing collision frequency, i.e. although the 'softer' protons occur in greater fluxes and produce more ionisation, the more energetic protons will still provide a considerable contribution to the absorption.

To test the dependence on spectrum Figure 7.10 plots the difference between the residuals against the ratio of the >30 to >10 MeV proton fluxes. As the ratio increases more of the protons are at the higher energy levels; there are few example of the flux being made up of predominantly > 30 MeV particles. As the ratio approaches 1 there is a wide spread of absorption (just over 1 dB) but there are few data points to draw meaningful conclusions. Most significantly is that even when the ratio is low (< 0.3) there is a wide distribution in the absorption suggesting that the errors in the fit are much less dependent on the precipitation spectrum than might have been expected.

Geomagnetic activity was shown to have little effect on the correlation of absorption and the flux but Chapter 6 demonstrated that the absorption is related to K_P, although not in a clear linear fashion. With high geomagnetic activity auroral electrons will contribute to the absorption although in general the levels are likely to be a small percentage of the total absorption from the solar protons; this may not be the case when there is a geomagnetic storm sudden commencement which will lead to high absorption. Figure 7.11 presents the ratio of absorption versus the K_P level; the calculated absorption has been computed for all data including high K_P. The two coloured lines represent the mean and median values for each K_P bin and these both tend to be centred on a ratio of 1.1. The distributions of the ratio in each K_P bin are very large especially in the active range; low occurrence in the high and low K_P bins limits the range of data. Thus the geomagnetic activity can play a major role in determining the level of absorption, but does little to effect the correlation; this is explained by the slowly varying nature of auroral absorption on the dayside; few sharp discontinuities will appear to disrupt the correlation.

So far the hardness of the spectrum has been discounted as a cause for the problems in the fit to the absorption, but the geomagnetic activity could be a contributing factor. Another parameter that will play a significant role is the level of solar radio emission. As described in Chapter 6 this is hard to quantify but PCA (and SPE) are more common close to the maximum of the sunspot cycle, however the sun also becomes more active in emitting radio frequency waves (Hargreaves , 1995; Davies, 1990). Solar flares themselves are often accompanied by radio bursts or

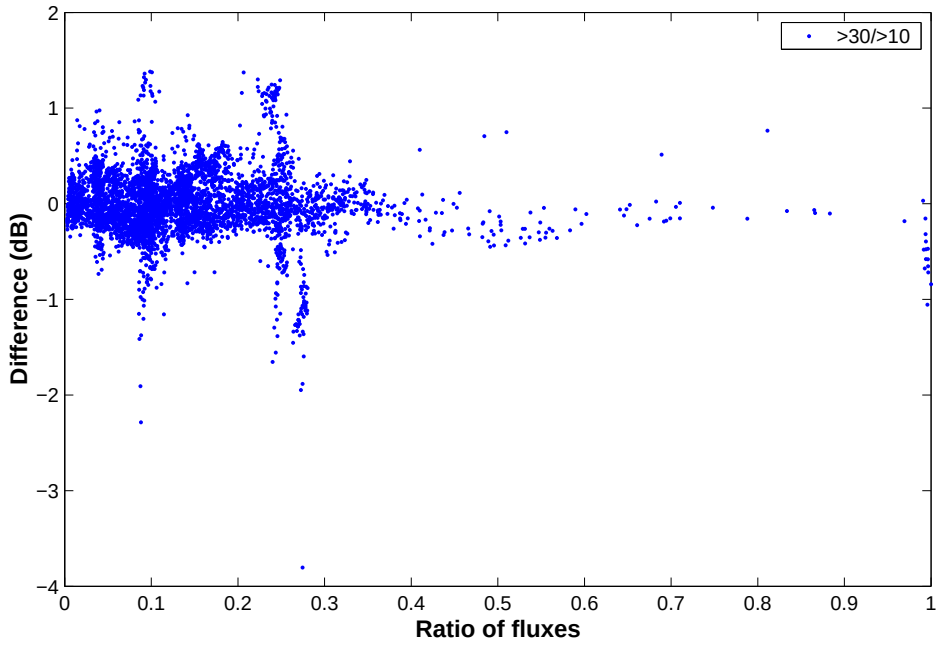

Figure 7.10. **Residuals of the absorption-flux fit as a function of the ratio of integral fluxes (>10 to >30 MeV).**

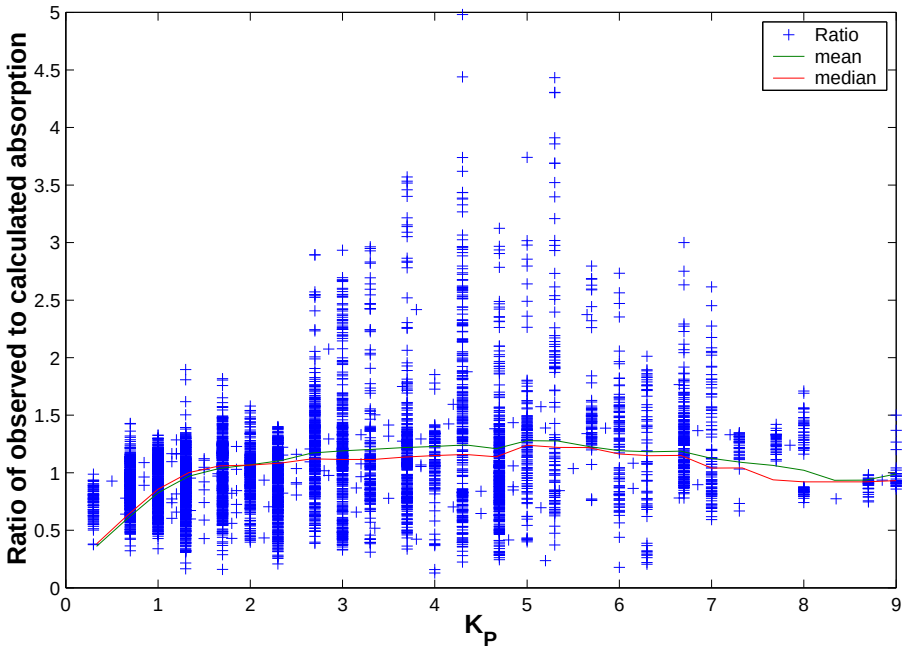

Figure 7.11. **Ratio of observed to calculated absorption as a function of K_P**

sweeps and these can reduce the amount of observed absorption on a specific frequency from the true level in the ionosphere. A method to minimise this effect is to introduce a riometer at low latitudes, away from the auroral zone, which will monitor the solar emission and through modelling of the antenna patterns a correction can be applied to IRIS.

The problems with the fit are best demonstrated when comparing time series of the observed absorption with the calculated absorption. Figure 7.12 displays all twenty seven PCA events from 1995 to 2001 combined together into a single time series with the night time values removed; on some occasions the computed absorption underestimates the observed values (e.g. 0 to 2000 minutes) whereas at other times it is overestimated (e.g. 14000 to 16000 minutes). The first example was from the PCA event of April 1998 which was very slowly varying and occurred during a period of general solar inactivity, the second example was a PCA in September 2001. There are distinct spike structures in those cases where the absorption is overestimated indicating solar radio emission was occurring, though it is hard to identify the total extent. The flux relationship contains data from contaminated events which is why it fails to reach the levels of the quiet PCA event. At other times (e.g. between 3000 and 4000 minutes) there are increases in the observed absorption that are from auroral absorption and sudden impulse absorption.

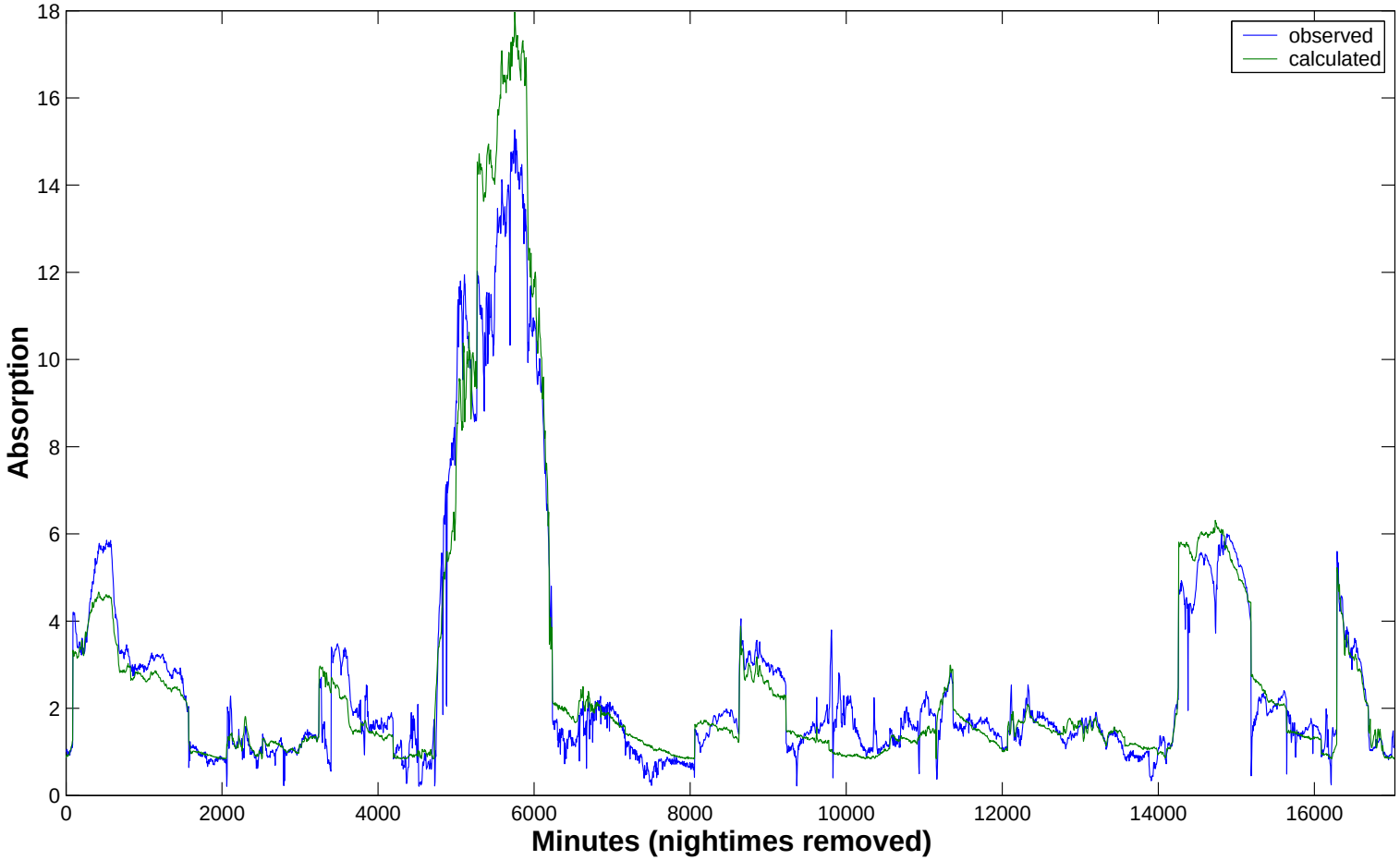

Figure 7.12. Time history of PCA events in observed (blue) and calculated (green) absorption. All values of absorption for solar zenith angle > 80º have been removed.

7.6 Summary

This chapter highlights the relationship between solar protons and the absorption observed in the auroral zone. The relationship between the flare, SPE and PCA have been examined and limits to the positions of Earth affecting proton flares have been determined. Delay times between the flare and SPE at Earth have been shown to depend both on the solar cycle (and hence the structure of the IMF) and the position of the flare on the sun. No dependence on the position of the maximum PFU is found suggesting that although some protons from eastern flares may bypass the Earth, there is sufficient diffusion across the IMF to produce high fluxes of protons regardless of the flare's longitude. There is no direct correlation between the maximum PFU and the maximum of the X-ray flux, although there appears to be defined upper limits to the number of protons >10 MeV that a flare of particular class can produce. The occurrence of SPE shows two peaks, one in spring and the other in autumn, both at times when it is thought that the Earth is better connected to the Sun via the orientation with respect to the IMF. Distributions of PCA show that events do not occur in the northern winter months; with the ionosphere in darkness there is a reduction in the electron density through chemical interactions.

Good correlation between the square root of the integral flux and absorption exists and it is determined that the absorption is mostly dependent on the flux of protons >10 MeV even though lower energy protons (e.g. energies >500 keV) will still deposit within the absorbing D layer. This is due to the exponential increase in collision frequency at the lower altitudes dominating the absorption process. The

correlation between the square root of the flux and the absorption is unaffected by increased geomagnetic activity but the difference between the calculated and observed absorption can be as great as 4 dB, thus the electrons play little part in the changing the structure of the absorption but can raise the maximum values. The hardness of the spectrum of proton precipitation is demonstrated to have little effect on the absorption.

A linear fit to the absorption and the square root of the integral flux provides a reasonable empirical relationship. At very low flux values there is a significant error (±1 dB) and at high fluxes the relationship break down. The reasons for these errors are likely due to geomagnetic activity and solar radio emission and less to do with the spectrum of precipitation. The effect of solar radio emission and auroral absorption on the relationship is clear when comparing time series of the calculated absorption with the corresponding observed absorption.

Chapter 8

Summary and Conclusions

8.1 Introduction

Auroral absorption is an important indicator of the presence of energetic fluxes of electrons that deposit energy into the atmosphere and Polar Cap Absorption demonstrates the massive effects that space weather can have on the ionosphere. Both of these phenomena have been investigated in this thesis; auroral absorption was considered both in a statistical sense (Chapter 6) and by examining a case study of enhanced daytime absorption (Chapter 5). These two approaches highlighted the benefits of using instruments both singly and as part of an array of diagnostics. Polar Cap absorption was investigated in Chapter 7 where a number of riometers and satellites were able to shed light on the relationship between the ground measurements and the proton flux and the effects of the magnetosphere.

8.2 Summary of Principal Results

The following two sub-sections will summarise the main conclusions from the preceding data chapters. Firstly the results from Chapters 5 and 6 on auroral absorption will be described followed by a summary of the conclusions from Chapter 7 on Polar Cap Absorption.

8.2.1 Auroral Absorption

In Chapter 5 a case study was presented that linked observations of varying precipitation in the morning sector with measurements of substorm activity on the nightside. The time separation of absorption enhancements across the IRIS field of view provide an estimate of the characteristic energy of precipitation if it is assumed that gradient curvature drift of electrons is the primary process involved in the electron transport. This is the first time that such a measurement has been made with just a single imaging riometer. EISCAT measurement appear to support the energy estimation, however ambiguities in the precipitation spectrum suggest that gradient-curvature drift alone cannot account for the electron density enhancements at EISCAT. Small-scale solar wind pressure changes ($\Delta P_{dyn} < 10$ nPa) at the magnetopause have been identified as being a possible controlling factor in the precipitation although further observations are necessary to support this.

A simultaneous rise in absorption across a range of latitudes occurs at the same time as an increase in particle penetration into the ionosphere and shortly after a sharp change in the IMF direction. It is suggested that radial diffusion of energetic particles to lower L shells plays a part together with an increase in the energy of injected particles in the nightside. Following this a drastic change in the electron density profile occurs as the enhancements in concentration become confined to a higher altitude; this is attributed to a change in the dominant species of precipitation from electrons to ions. The possibility that the ions are from the LLBL (Low Latitude Boundary Layer) or BPS (Boundary Plasma Sheet) has been dismissed not only because of the relatively large distance to the cusp, but also because Pc1 waves are observed to increase in intensity at lower L-shells. This suggests that the ion precipitation is due to a growth in EMIC (Electromagnetic Ion Cyclotron) waves resulting in increased pitch angle scattering of ions into the loss cone.

This is attributed to an interaction between an enlarged plasmasphere and energetic ring current during the recovery phase of a small to moderate geomagnetic storm.

Finally the movement of patches of absorption are related to the flows observed by the CUTLASS HF radar. Early in the event there was little correlation between the motion of the absorption patches and the velocities derived from the radar, instead the F region irregularities moved azimuthally whereas the precipitation footprint was expanding equatorward After 13 MLT IRIS was located under a region of strong return flow and the changing location of the ground signature of the precipitation region is comparable with the motion of the ionospheric irregularities. This suggests that E×B drift is governing the precipitating particles at this time rather than L-shell separation of the drifting electrons as at event onset (0615 UT to 0650 UT).

Although providing some useful information about how absorption can vary within a single event and how many instruments can fully define the processes involved, it is important to consider the gross characteristics of the absorption. To this end a statistical analysis of the distribution of absorption in both time and space was presented in Chapter 6; data were combined from 7 years of continuous observations of auroral absorption from IRIS The expected diurnal variation was produced in the mean of the absorption characterised by a peak in the morning sector (~10 MLT) and a deep minimum around 18 MLT. This minimum appeared to be independent of any geophysical or solar wind controlling factor that effects the absorption in the morning and around midnight and is likely linked to limits of anisotropy in the pitch angle distribution of the electrons.

An apparent seasonal effect on the observed auroral absorption has been attributed to differences in the amount of geomagnetic activity in the four seasons. This does not discount the possible effect of a poleward extension of the winter anomaly, however it should be noted that consistently enhanced D-region electron density effects will be

removed from the data during quiet-day curve generation. The high levels in spring and autumn support the theory that geomagnetic activity is higher around the equinox; the deep minimum of activity in summer is reflected also in the absorption data.

In order to improve the current state of knowledge regarding absorption models in the high latitude ionosphere a non-linear empirical relationship between absorption and K_P was identified and coefficients computed. This fits the data reasonably well and is superior to the logarithm fit that had previously been proposed. No good theoretical explanation is available for this relationship but it indicates that the link between K_P and auroral absorption contains a measure of non-linearity. The local time dependence of absorption is so clear that the possibility that different types of fits to the data in each MLT bracket should not be discounted. Any future investigation of this nature should take this into account.

Since the level of geomagnetic activity varies with the solar wind parameters the variation of absorption also relies heavily on the changing solar wind levels rather than any solar cycle indicator (e.g. sunspot number) and so a linear relationship between absorption and solar wind velocity is derived; for the first time based on direct satellite measurements. A southward IMF plays a significant role in precipitation in the auroral zone but the eastward component has no statistical effect on the mean absorption.

The limitations of the imaging riometer for a study such as this have been expounded upon and include errors that are introduced through the non-uniform nature of the beam sizes and the uncertainty of the distribution of absorption events in oblique beams. Some of the beams (particularly beam 10) exhibit unusually high values possibly due to inconsistencies in the quiet day curves or perhaps related to a hardware problem with the riometers.

This study can be considered as the start point for deriving a possible absorption prediction model based upon latitude, longitude, geophysical and/or solar wind parameters. Low absorption is still likely even when geophysical activity is high since absorption is highly dependent on the population of energetic particles in the magnetosphere. Methods to improve the current absorption prediction models must take into account past levels of geomagnetic activity, absorption and some other measure of the energy stored in the magnetotail (e.g. B_Z).

8.2.2 Polar Cap Absorption

The second type of absorption of significant importance in particle precipitation is PCA. Chapter 7 concerned itself with two aspects of PCA; how are the solar proton events related to conditions in the Sun/IMF/solar wind and also what is the relationship between the proton flux and the absorption ground signature?

The distribution of the originating location of solar proton flares has been shown to lie between ±50º solar latitude with a narrow bay across the centre. There is a definite westward bias in the occurrence but with the number of events so small (165 in 25+ years) its is unreasonable to draw too many conclusions about the distributions. Suffice to say there appears to be a bias towards two peaks; one centred at 10º east and the second (higher and broader) close to 50 west. These results agree with the findings of past investigations that western hemisphere flares are more likely to lead to proton events at the Earth, probably due to the magnetic field orientation.

An increase in delay time between flare and SPE onset is found for flares in the eastern solar hemisphere. This may be related to the time it takes for protons to diffuse across the field lines as the bulk of the population is lost into space, whereas for better magnetically connected western flares, the majority of the proton population easily

reaches the magnetosphere. No dependence on the position of the maximum PFU is found suggesting that although protons from eastern flares may bypass the Earth, there is sufficient diffusion across the IMF to produce high fluxes of protons regardless of the flare's longitude. There is no direct correlation between the maximum PFU and the maximum of the X-ray flux, although there appear to be defined upper limits to the number of protons >10 MeV that a flare of particular class can produce.

The occurrence of SPE shows two peaks, one in spring and the other in autumn, both at times when it is thought that the Earth is better connected to the Sun via the orientation with respect to the IMF. Winter appears to be a stronger minimum than the summer. Distributions of PCA suggest that events rarely occur in the northern winter months; this is because with a dark ionosphere there is a reduction in the electron density through attachment processes.

A good correlation between the square root of the integral flux (> 10 MeV) and the absorption from the IRIS wide beam has been determined. This led to an empirical relationship between the two parameters; at low fluxes a large error occurs and at high fluxes the relationship breaks down. The reasons for these problems have been identified as solar radio emission and auroral absorption contaminating the relationship. The hardness of the spectrum of precipitation is demonstrated to have little effect on the absorption.

8.3 Future Work

8.3.1 Morning Absorption and simultaneous night side observations

Chapter 5 introduced some features of morning absorption that failed to fit the current theory of the curvature drift and precipitation. Theory suggests that a clear energy dispersion signature should be observed on a single L shell as an event progresses, but this

does not always appear to be the case with a hardening of the precipitation shortly after onset. The reason for this is likely due to the ongoing night time activity, with fresh populations of particles being injected and subsequently drifting. This should be observed as pulses of eastward travelling absorption. The water is further muddied by not knowing the longitudinal extent of the injection region so particles injected simultaneously will reach a point in the morning sector with a slight time separation although they may be of similar energy. The mechanism of precipitation of the drifting particles is also in need of clarification with particular reference to the L shell dependence of the observed absorption. It takes a longer period for particles on a lower L shell to drift around the earth and so statistically a particle of given energy on a lower L shell is more likely to precipitate due to the larger number of bounces it will perform along the field line. So far, the limited observations of precipitation are inconclusive as to whether absorption at higher L values continues to later local times than that observed at lower L shells.

There are now available several arrays of riometers in the northern hemisphere stretching from the Canadian sector (CANOPUS) through Greenland (Danish Meteorological Institute chain) and Iceland (Japanese and DMI imaging riometers) to Scandinavia (DMI, STELab and Lancaster's IRIS's and the SGO chain). The progression of absorption from injection close to midnight through to the mid morning sector can be traced to an extent that was not previously possible. The ability to place the absorption in a magnetospheric context is also available with the number of satellites now available such as DMSP, SAMPEX, LANL and Cluster giving direct measurements of the particle energy spectrums. In particular the X-ray imager PIXIE, part of the payload of the Polar spacecraft, could be used in conjunction with the riometer data to monitor the movement and development of the precipitation region. A number of events of high morning absorption levels have already been identified in the IRIS data set (see Table 8.1) and by

using the CANOPUS riometers and magnetometers the time and possibly the location of substorm onset can be pinpointed. Thus a superposed epoch analysis of the development of absorption can be performed which would aid in identifying absorption mechanisms and in determining the role played by gradient-curvature drift if any.

Start Time	End Time	Duration hh:mm:ss	Mean Absorption (dB)	Max. Absorption (dB)
1995-01-30 06:39:00	1995-01-30 08:46:00	02:07:00	1.21	2.19
1995-02-03 06:03:00	1995-02-03 10:35:00	04:32:00	1.47	3.68
1995-02-08 06:34:00	1995-02-08 07:51:00	01:17:00	1.05	1.34
1995-02-13 06:10:00	1995-02-13 09:41:00	03:31:00	2.39	5.45
1995-02-27 09:52:00	1995-02-27 11:33:00	01:41:00	1.38	2.62
1995-03-01 08:29:00	1995-03-01 10:36:00	02:07:00	1.29	2.42
1995-03-13 09:59:00	1995-03-13 11:36:00	01:37:00	1.19	2.04
1995-03-16 06:18:00	1995-03-16 08:30:00	02:12:00	1.47	2.04
1995-03-29 07:47:00	1995-03-29 08:48:00	01:01:00	1.12	1.81
1995-03-29 08:49:00	1995-03-29 09:55:00	01:06:00	1.71	2.69
1995-04-08 09:11:00	1995-04-08 11:00:00	01:49:00	1.08	1.96
1995-04-11 10:04:00	1995-04-11 11:08:00	01:04:00	1.26	2.78
1995-04-27 07:22:00	1995-04-27 09:26:00	02:04:00	2.18	4.99

Table 8.1. A sample of morning absorption events identified in the IRIS data.

8.3.2 Large Scale statistics: latitude, longitude and altitude

The PIXIE camera would also play an important role in further study of the absorption oval on a statistical basis. The statistical study of absorption in Chapter 6 is incomplete since it only considers the absorption from a very confined range of latitudes. In order to more fully test absorption models such as that of Foppiano and Bradley (1983), a similar analysis could be performed on each of the stations mentioned above. The separation of the Canadian riometers and in comparison with the SGO chain should cast light on the longitude effect that is expected (Chapter 4). A detailed study of how absorption responds during geomagnetic storms would be especially useful, linking the observations to past levels of activity as indicated not only by K_P and D_{st} but also the IMF and solar wind speed. If this is done then with the large array of riometers available in both hemispheres and the catalogue of data, a suitable global empirical model could be defined. It is worth repeating here that the variation of absorption in magnetic local time is such that it is worth binning the data by much smaller time spans (less than 3 hours) and finding fits to the geomagnetic indices.

A new approach to absorption statistics would concentrate on the observations of the EISCAT radars. By considering the altitude gated electron density, statistics of the profiles of the concentration can be drawn based upon similar parameters to those used in Chapter 6 (e.g. K_P and solar wind speed). Two latitudes are now available by considering both the mainland radar and the ESR, and absorption profiles can be derived by using modelled collision frequencies calculated from the MSIS (Mass Spectrometer Incoherent Scatter) model. This should aid in understanding how and if the height of the absorbing layer varies and possibly resolve some of the problems that arose from the oblique nature of the IRIS imaging beams.

8.3.3 Beyond Polar Cap Absorption.

Although statistically rather small, 53 examples of Solar Proton Events (SPE) occurred from 1995 to 2001; a further 18 have occurred up to and including September 2002. Throughout this duration there has been constant monitoring by the GOES, POES and SAMPEX satellites providing measurements of both integral and differential fluxes of protons >10 MeV. The relationship derived in Chapter 7 is a simple measure that is quick and useful for predicting absorption in the polar cap however further information about the deposition of energy can be derived by using the spectrum of precipitation (e.g. Figure 8.1) to determine the ionisation profiles. For very energetic SPE the highest energy particles will penetrate deep into the atmosphere to altitudes below 50 km and sometimes to the ground (ground level events). Due to the changing chemistry at these lower altitudes, processes that contribute to ionospheric absorption will no longer occur. EISCAT has been operating for several of the PCA during 2001 and can measure electron density profiles from the ionising protons.

During the PCA of April 2001 incoherent scatter radar measurements were made by both EISCAT and ESR. This is the first time that dual measurements have been made during a solar proton event from instruments both deep in the polar cap and also close to the cut-off boundary. This was repeated in September 2001 and this time the radar observed the start of a geomagnetic storm part way through the event.

Since electron density decreases with height, incoherent scatter radars are limited to a minimum height of operation due to signal-to-noise constraints as well as operational limitations. The measurements from EISCAT will provide a constraint on the satellite-based computations in producing absorption estimates. From comparisons between the modelled absorption and the observed absorption, the lower altitude boundary height of

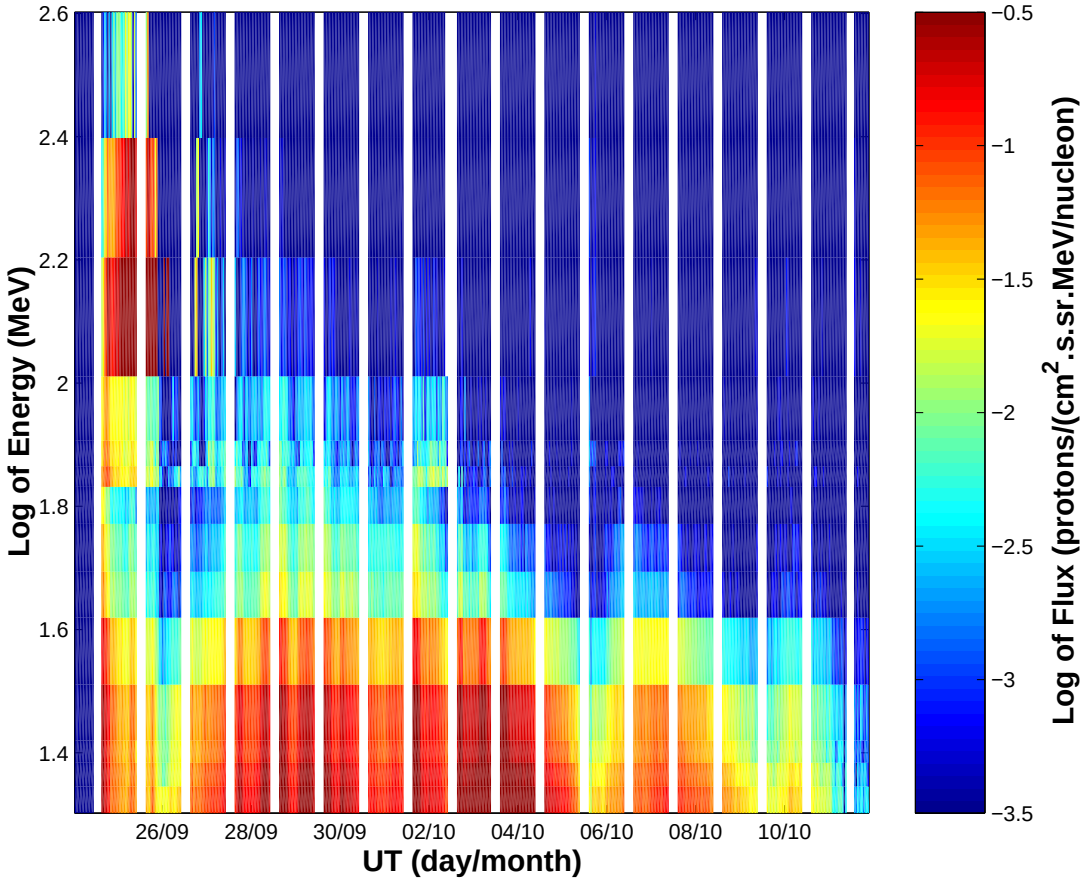

Figure 8.1. **Precipitation spectra for the PCA event of September 2001. Data are from the SAMPEX satellite and are averages of the values poleward of 70º magnetic latitude. The white lines indicate where the satellite grazes the south polar cap.**

the absorption processes can be estimated. This will differentiate the energy deposition between two regions; the ionosphere and the lower neutral atmosphere.

Similarly with the latitudinal spread of riometers, the absorption variation through the cut-off boundary can be examined and compared directly with satellite measurements of the particle cut-offs. Thus by correlating the cut-off with the absorption normalized to the peak in the polar cap it should be possible to define the cut-off boundary for a range of energies. This method has advantages over the satellite data as the riometer will pass through all local times and so eventually it will be possible to differentiate any variations in the cut-off boundary that are dependent on geomagnetic activity and those that are simply dependent on the position relative to the magnetotail (Chapter 4). The dependence on $D_{st,}$ and to a lesser degree $K_{P,}$ is well documented (e.g. Leske *et al.,* 2001) but there is also a reliance of the extent of absorption on B_Z. Figure 8.2 shows a preliminary example of an event that compares the variation of B_Z with the normalized absorption. Southward turnings show a reasonable correlation with equatorward expansions of absorption. This is not totally unexpected as when the polar cap expands equatorward then the solar protons will have greater access to the magnetosphere, however no workers so far have attempted to use B_Z as a proxy for the cut-off boundary.

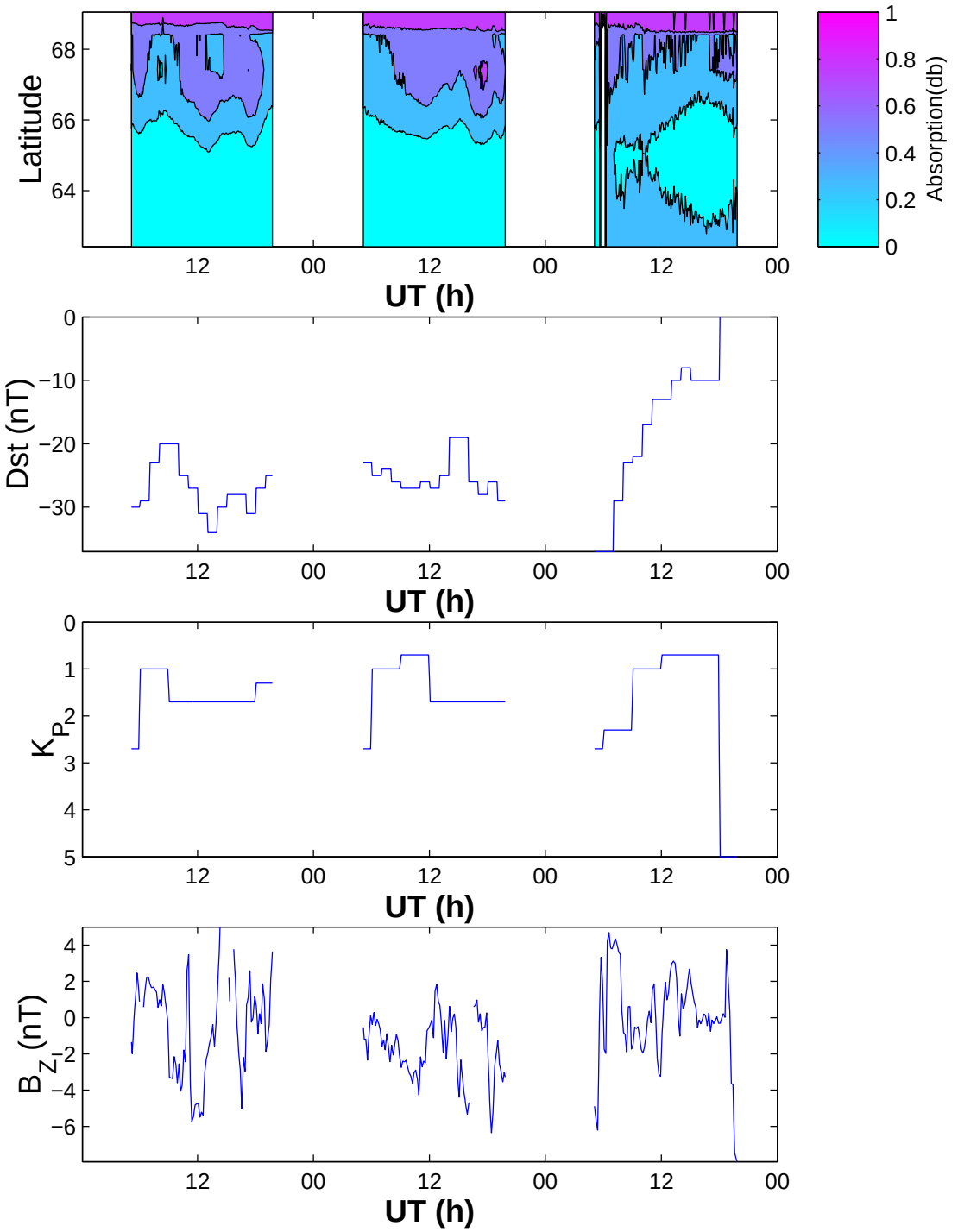

Figure 8.2. **Example of a PCA showing contours of the normalized absorption (top panel) and the variation of three parameters, K_P, D_{st} and B_Z.**

8.4 Concluding Remarks

There is now a wealth of data available not just from IRIS but also from the other imaging and chains of riometers in both hemispheres. Only a small part of this data set has been used in this investigation in which some of the processes of auroral and polar cap absorption and related precipitation have been examined. These are topics that previous workers have addressed but with added contributions from other ground based instrumentation and satellites it has been possible to place the absorption in a magnetospheric context. With the closer collaborations that are currently being formed throughout the riometry community its is possible to enhance considerably the current state of knowledge of geomagnetic processes that lead to energy deposition in the lower altitudes of the ionosphere.

References

Aggarwal K.M., N. Nath, C.S.G.K. Setty, Collision frequency and transport properties of electrons in the ionosphere, Planet. Space Sci.,.27, 753-768, 1979.

Agy, V., A model for the study and prediction of auroral effects on HF radar, Proc. AGARD conference “Radar propagation in the Arctic, ADARD-CP-97, 32-1, 1972.

Akasofu, S.I., Space. Sci. Rev., 2, 91, 1963.

Alfven, H. and C-G. Falthammar, Cosmical Electrodynamics, Oxford University Press, 1963.

Allan, A.H., Crombie, D.D., and Penton, W.A., J. Atmos. Terr. Phys., 10, 110, 1957.

Anderson, B. J., Erlandson, R. E., and Zanetti, L. J.: A statistical study of Pc 1–2 magnetic pulsations in the equatorial magnetosphere 1. Equatorial occurrence distribution, J. Geophys. Res., 97, 3075–3088, 1992a.

Anderson, B. J., Erlandson, R. E., and Zanetti, L. J.: A statistical study of Pc 1–2 magnetic pulsations in the equatorial magnetosphere 2. Wave properties, J. Geophys. Res., 97, 3089–3101, 1992b

References

Anderson, B.J., and D.C. Hamilton, Electromagnetic ion-cyclotron waves stimulated by modest magnetospheric compressions, J. Geophys. Res., 98, 11369, 1993

Anderson, K.A., Phys. Rev. Letters, 1, 335, 1958.

Ansari, Z.A., The aurorally associated absorption of cosmic noise at College Alaske, J. Geophys. Res., 69, 4493, 1964.

Appleton, E.V., R. Naismith and G. Builder., Ionospheric investigations in high latitudes., Nature, 132, 340, 1933.

Araki, T., A physical model of geomagnetic sudden commencement. In Engebretson, M., Takahashi, K.T., Scholer, M. (Eds.). Solar Wind Sources of Ultra-Low-frequency Wave pulsations., AGU., 1994

Arnoldy, R. L. and Chan, K. W.: Particle substorms observed at the geostationary orbit, J. Geophys. Res., 74, 5019–5028, 1969

Bailey, D.K., J.Geophys. Res., 62, 421, 1957.

Baker, D.N.,.Mason, G.M., Figueroa, 0. G. Colon., Watzin, J.G. and Aleman, R.M An Overview of the Solar, Anomalous, and Magnetospheric Particle Explorer (SAMPEX) Mission. IEEE Trans. Geosci. & Remote Sens., 31, 531-541. 1993.

References

Baker, K. B. and Wing, S.: A new magnetic coordinate system for conjugate studies at high latitudes, J. Geophys. Res., 94, 9139– 9143, 1989.

Baker, K. B., Dudeney, J. R., Greenwald, R. A., Pinnock, M., Newell, P. T., Rodger, A. S., Mattin, N., and Meng, C.-I.: HF radar signatures of the cusp and low-latitude boundary layer, J. Geophys. Res., 100, 7671–7695, 1995.

Barcus, J.R., and T.J. Rosenberg, Observeations on the spatial structure of pulsating electron precipitation accompanying low frequency hydromagnetic disturbances in the auroral zone, J. Geophys. Res., 70, 1707, 1965.

Basler, R.R., Radio wave absorption in the auroral ionosphere, J. Geophys. Res., 68, 4665, 1963.

Basler, R.P., Annual variation of auroral absorption, J. Geophys. Res. 71, 982, 1966.

Belrose, J.S., Devenport ,M.H and. Weekes, K, J.Atmos. Terr. Phys., 8, 281, 1956.

Biswas, S., Freier, P.S and Sten, W., J. Geophys. Res. 67, 13, 1962.

Blum, E-J., J-F. Denisse and J.L. Steinberg, Influence de l'ionospherè sur la réception du rayonnement galactique de fréquence 29.5 Mc/s., Comptes Rendus des Seances de L'Academie des Sciences, 238, 1095,1954.

References

Brice, N., Fundamentals of very low frequency emission generation mechanisms, J. Geophys. Res., 69, 4515-4522, 1964.

Brown, R. R.: On the Poleward Expansion of Ionospheric Absorption Regions Triggered by Sudden Commencement of Geomagnetic Storms, J. Geophys. Res., 83, 1169–1171, 1978

Brown, R. R. and Driatsky, V. M.: Further Studies of Ionospheric and Geomagnetic Effects of Sudden Impulses, Planet. Space Sci., 21, 1931–1935, 1973.

Brown, R. R., Hartz, T. R., Landmark, B., Leinbach, H., and Ortner, J.: Large-Scale Electron Bombardment of the Atmosphere at the Sudden Commencement of a Geomagnetic Storm, J. Geophys. Res., 66, 1035–1041, 1961

Browne, S., Hargreaves, J. K., and Honary, B.: An Imaging Riometer for Ionospheric Studies, Elect. Comm. Eng. J., 7, 209–217, 1995.

Burns, C.J., E. Turunen, H. Matveinen, H. Ranta, and J.K. Hargreaves, Chemical modelling of the quiet summer D- and E-region using EISCAT electron density profiles. J. Atmos. Terr. Phys. 51, 983-989, 1991.

References

Burrows, J.R., A review of the magnetosphere characteristics of solar flare particles. Proceedings of COSPAR symposium on solar particle event of November 1969., 61-93, 1972.

Cane. H. V. A 30 MHz Map of the Whole Sky. Australian J. Phys.,. 31, 561-565. 1978.

Collis, P. N. and Hargreaves, J. K.: Co-ordinated Studies Using Imaging Riometer and Incoherent Scatter Radar. J. Atmos. Sol. Terr. Phys., 59, 873–890, 1997.

Collis, P. N., Hargreaves, J. K., Howarth, W. G., and White, G. P.: Joint Imaging Riometer – Incoherent Scatter Radar Observations: A Four-dimensional Perspective on Energetic Particle Input to the Auroral Mesosphere, Adv. Space Res., 20, 1165–1168, 1997.

Collis, P.N., and M.T. Rietveld, Mesospheric observations with the EISCAT UHF radar during polar cap absorption events: 1. Electron densities and negative ions. Ann. Geophys., 8, 809-824, 1990.

Collis, P.N., and M.T. Rietveld, Mesospheric observations with the EISCAT UHF radar during polar cap absorption events: 3. Comparison with simultaneous EISCAT VHF measurements., Ann. Geophys., 16, 1355-1366, 1998.

Cook, W.R., A.C. Cummings, J.R. Cummings, T.L. Garrard, B. Kecman, R.A. Mewaldt, R.S. Sdesnick, E.C. Stone, and T.T. von Rosenvinge, MAST: A Mass

Spectrometer Telescope for Studies of the Isotopic Composition of Solar, Anomalous, and Galactic Cosmic Ray Nuclei. IEEE Trans. Geosi, and Remote Sens., 31, 557-564. 1993a.

Cook, W.R., A.C. Cummings, J.R. Cummings, T.L. Garrard, B. Kecman, R.A. Mewaldt, R.S. Selesnick, E.C. Stone, D.N. Baker, T.T. von Rosenvinge, J.B. Blake, and L.B. Callis, PET: A Proton/Electron Telescope for Studies of Magnetospheric, Solar, and Galactic Particles. IEEE Trans. Geosci. and Remote Sens.,. 31, 565-571. 1993b

Cornwall, J. M.: On the role of charge exchange in generating unstable waves in the ring current, J. Geophys. Res., 87, 1188–1196, 1978.

Cornwall, J. M., Coroniti, F. V., and Thorne, R. M.: Turbulent loss of ring current protons, J. Geophys. Res., 75, 4699–4709, 1970.

Coroniti, F. V. and Kennel, C. F.: Electron precipitation pulsations, J. Geophys. Res., 75, 1279–1289, 1970.

Coronitti, F.V., R.L. McPherron, and G.K. Parks, Studies of the magnetospheric substorm. 3. Concept of the magnetospheric substorm and its relation to electron precipitation and micropulsations., J. Geophys. Rtes., 73, 1715, 1968.

References

Cowley, S.W. H., Morelli, J. P., and Lockwood, M.: Dependence of convective flows and particle precipitation in the high latitude ionosphere on the X and Z-components of the interplanetary magnetic field, J. Geophys. Res., 96, 5557–5564, 1991

Davies, K., Ionospheric Radio, Peter Peregrinus Ltd., 1990.

Detrick, D. L. and Rosenberg, T. J.: A Phased-Array Radiowave Imager for Studies of Cosmic Noise Absorption, Radio Science, 25, 325–338, 1990.

Dougherty J.P., and D.T. Farley, A theory of incoherent scattering of radio waves by plasma: 3. Scattering in a partly ionised gas. J. Geophys. Res. 66, 5473, 1963.

Driatsky, V.M., Study of the space and time distribution of auroral absorption according to observations of the riometer network in the arctic, Geomagnetism and Aeronomy, 6, 828, 1966

Driatsky V.M., Nature of anomalous absorption of cosmic radionoise in the high-latitude lower ionosphere, Leningrad. Hydrometeoizdat, 223 (in Russian), 1974.

Dyrud, L. P., Engebretson, M. J., Posh, J. L., Hughes, W. J., Fukunishi, H., Arnoldy, R. L., Newell, P. T., and Horne, R. B.: Ground observations and possible source regions of two types of Pc1–2 micropulsations at very high latitudes, J. Geophys. Res., 102, 27 011–27 027, 1997.

References

Eather, R.H., and K.M. Burrows., Correction to Excitation and ionization by auroral protons, Australian J. Phys., 19, 717, 1966.

Ellison, M.A. and J.H. Reid, J. Atmos. Terr. Phys., 8, 291, 1956.

Faneslow, J.R., and E.C. Stone, Geomagnetic cutoffs for cosmic-ray protons for seven energy intervals between 1.2 and 39 MeV, J. Geophys. Res., 77, 3999-4009, 1972.

Fehsenfeld, F.C., and E.E. Ferguson, J. Geophys. Res., 74, 2217, 1969.

Folestad, K., Hagfors, T. and Westerlund, S., EISCAT: an updated description of technical characteristics and operational capabilities. Radio Sci., 18, 867-879, 1983.

Foppiano, A.J., A new method for predicting the auroral absorption of HF sky waves. CICR Interim Working Party 6/1. Docs. 3 and 10. International Telecommunication Union., 1975.

Foppiano, A.J., and Bradley, P.A. Prediction of auroral absorption of high-frequency waves at oblique incidence, Telecommun. J., 50, 547-560, 1983.

Foppiano, A.J., and Bradley, P.A., Day to day variability of riometer absorption, J. Atmos. Terr. Phys., 46, 689-696, 1984.

References

Foppiano, A.J. and P.A. Bradley, Morphology of background auroral absorption., J. Atmos. Terr. Phys. 47, 663-74, 1985.

Fowler, P.H., C.J. Waddington, P.S. Freier, J. Naugle, and E.P. Ney, Phil. Mag. 2, 157, 1957.

Freier, P.S., E.P. Ney and J.R. Winckler, Balloon observations of solar cosmic rays on March 26, 1958J. Geophys. Res. 64, 685, 1959.

Geller, M.A. and Sechrist, C.F., Coordinated rocket measurements on the D-region winter anomaly. II. Some implications, J. Atmos. Terr. Phys. 33, 1027,1971.

Gonzales, W. D., Joselyn, J. A., Kamide, Y., Kroehl, H. W., Rostoker, G., Tsurutani, B. T., and Vasyliunas, V. M.: What is a geomagnetic storm?, J. Geophys. Res., 99, 5771–5792, 1994

Greenberg, E.M., and LaBelle, J., Measurement and modeling of auroral absorption of HF radio waves using a single receiver., Rad. Sci. 37, 6-1-6-12, 2002.

Greenwald, R. A., Baker, K. B., Dudeney, J. R., Pinnock, M.,Jones, T. B., Thomas, E. C., Villain, J. P., Cerisier, J. C., Senior, C., Hanuise, C., Hunsucker, R. D., Sofko, G., Koehler, J.,Nielsen, E., Pallinen, R.,Walker, A. D. M., Sato, N., and Yamagishi, H.: DARN/SuperDARN: A global view of the dynamics of the high-latitude convection, Space Sci. Rev., 71, 761–796, 1995.

References

Hagfors T. Density Fluctuations in a plasma in a magnetic field with applications to the ionosphere. J. Geophys. Res. 66, 1699, 1961.

Hall, C., A. Brekke, . A.P. van Eyken, U. –P. Hoppe, and E.V. Thrane, Incoherent Scatter Radar Observations of the middle atmospheric response to a PCA, Adv. Space. Sci., 12, 10289-10294, 1992.

Hakura, Y., Y. Takenoshita, and T.Otusuki, Rep. Ionosph. Res. In Japan, 12, 459, 1958.

Hansen G., U.-P. Hoppe, E. Turunen and P. Pollari, Comparison of observed and calculated incoherent scatter spectra from the D-region. Radio Sci. 26, 1153-1164, 1991

Hardy, D. A., Yeh, H. C., Schmitt, L. K., Schumaker, T. L., Gussenhoven, M. S., Huber, A., Marshall, F. J., and Pantazis, J.: Precipitating electron and ion detectors (SSJ/4) on the block 5D/Flights 6–10 DMSP satellites: Calibration and data presentation, Tech. Rep. AFGL-TR-84–0317, Air Force Geophys. Lab., Hanscom Air Force Base, Mass., 1984.

Hargreaves, J.K., On the variation of auroral radio absorption with geomagnetic activity, Planet. Space. Sci. 14, 991-1006, 1966

Hargreaves, J.K., Auroral Motions Observed with Riometers: Latitudinal Movements and a Median Global Pattern. J. Atmos. Terr. Phys. 1461-1470. 1968.

References

Hargreaves, J. K.: Auroral Absorption of HF Radio Waves in the Ionosphere: A Review of Results from the First Decade of Riometry, Proceedings of the IEEE, 57, 1348–1373, 1969.

Hargreaves. J.K, Dynamics of Auroral Absorption in the Midnight Sector - The Movement of Absorption Peaks in Relation to the Substorm Onset. Planet. Space Sci., 1427-1441. 1974.

Hargreaves, J. K.: The Solar-Terrestrial Environment, Cambridge University Press, 1995.

Hargreaves, J. K. and Berry, M. G.: The eastward movement of the structure of auroral radio absorption events in the morning sector, Ann. Geophysicae, 32, 401–406, 1976.

Hargreaves, J.K. and F.C. Cowley. Studies of Auroral Absorption Events at Three Magnetic Latitudes - I. Occurrence and Statistical Properties of the Events. Planet. Space Sci.., 1571-1583. 1967.

Hargreaves, J.K. and D.L. Detrick. Application of Polar Cap Absorption Events to the Calibration of Riometer Systems. Rad. Sci., 37, 7-1-7-11. 2002.

Hargreaves, J. K. and Devlin, T.: Morning Sector electron precipitation events observed by incoherent scatter radar, J. Atmos. Terr. Phy, 52, 193–203, 1990

References

Hargreaves, J.K. and R.D. Sharp, Planet. Space. Sci.m 13, 1171, 1965.

Hargreaves, J.K., M.T. Feeney, and C.J. Burns, Statistics of auroral radio absorption in relation to prediction models, , Proc. 36th symposium of the electromagnetic wave propagation panel, AGARDS-CP_382, 1-10, 1985.

Hargreaves, J.K., Feeney, M.T., Ranta, H., and Ranta, A., On the prediction of auroral radio absorption on the equatorial side of the absorption zone, J. Atmos. Terr. Phys., 49, 259-272, 1987.

Hargreaves, J.K., Ranta, A., Annan, J.D. and J.C. Hargreaves. Temporal Fine Structure of Nightime Spike Events in Auroral Radio Absorption, Studied by Wavelet Method. J. Geophys. Res. - Space Physics,.24621-24636. 2001.

Hargreaves, J.K., H. Ranta, A. Ranta, E. Turunen, T. Turunen., Observations of the Polar Cap Absorption Event of February 1984 by the EISCAT Incoherent Scatter Radar. Planet. Space Sci., 35, 947-958, 1987.

Hargreaves, J.K., A.V. Shirochkov and A.D. Farmer, The polar cap absorption event of 19-21 March 1990: recombination coefficients, the twilight transition and the midday recovery, J. Atmos. Terr. Phys, 55, 857-862, 1993.

References

Hartz T.R., Particle precipitation patterns, in The radiating atmosphere., Reidel, 225-38, 1971.

Hartz, T.R., and N.M. Brice, Planet. Space. Sci., 15, 301, 1967.

Hartz, T.R., L.E. Montbriand and E.L. Vogan, A study of auroral absorption at 30 Mc/s, Can . J. Phys, 41, 581, 1963.

Herman, J.R and R. Vargas-Villa, Investigation of auroral ionospheric and propagation phenomena related to the Polar Foz II experiment., Analytical Systems Corporation, Report ASCR-72-62, 1972.

Hess, W.N., The radiation Belt and Magnetosphere, Blaisdell, 1968.

Holt, O., B Landmark, and F. Lied, Analysis of riometer observations obtained during polar radio blackouts, J. Atmos. Terr. Phys., 23, 229, 1961

Hoffman, D.J. and H.H. Sauer, Magnetospheric cosmic-ray cutoffs and their variations, Space. Sci. Rev., 8, 750-803, 1968.

Holt, O., and A. Omholt, Auroral luminosity and absorption of cosmic radio noise, J. Atmos. Terr. Phys., 24, 467, 1962

References

Hook, J.L., Morphology of auroral zone radiowave absorption in the Alaska sector, J. Atmos. Terr. Phys., 30, 1341, 1968.

Hultqvist, B., and J. Ortner, Nature, 183, 1179, 1959.

Jelly, D., and N.M. Brice, Changes in van Allen radiation associated with polar substorms, J. Geophys. Res., 72, 5919, 1967.

Joselyn, J.A. and B.T. Tsurutani, Geomagnetic Sudden impulses and storm sudden commencements: a note on terminaology. EOS, 71, 1808, 1990.

Kamiyama, H., Ionization and excitation by precipitating electrons, Rept. Ionosphere Space Res. Japan, 20, 171, 1966.

Katz, l., P. Meyer, and J.A. Simpson, Nuovo Cimento, Suppl. II, 8, 277, 1958

Kavadas, A.W. Absorption measurements near the auroral zone, J. Atmos. Terr. Phys., 23, 170, 1961.

Kennel C.F. Consequences of a magnetospheric plasma, Rev. of Geophys.,.7, 379-419, 1969.

Kennel, C.F., and Petschek, H.E., Limit on Stably Trapped Particle Fluxes, J. Geophys. Res., 71, 1-27,1966.

References

Khan, H. and Cowley, S. W. H.: Effect of the IMF By component on the ionospheric flow overhead at EISCAT: observations and theory, Ann. Geophysicae, 18, 1503–1522, 2001.

Kikuchi, T., Yamagishi, H., and Sato, N.: Eastward propagation of Pc4–5 range pulsations in the morning sector observed with scanning narrow beam riometer at L = 6.1, J. Geophys. Res. Lett., 15, 168–171, 1988.

King J.H. and D.J. Williams, Isotropic solar proton diffusion-a statistical study. Transactions of the American Geophysical Union, 51, 798, 1970.

Kivelson, M.G., and C.T. Russel, (Eds.), Introduction to Space Physics, Cambridge University Press, 1995.

Klecker, B., D. Hovestadt, M. Scholer, H. Arbinger, M. ErtI, H. Kaestle, E. Kuenneth, P. Laeverenz, E. Seidenschwang, J.B. Blake, N. Katz, and D.J. Mabry, HILT: A Heavy Ion Large Area Proportional Counter Telescope for Solar and Anomalous Cosmic Rays. IEEE Trans. Geosci. and Remote Sens, 31, 542-548. 1993.

Kodama, M. and Y. Miyazaki, Rept. Iono. Space Res. Japan, 11, 99, 1957.

Kokubun, S., Yamamoto, T., Acuna, M. H., Hayashi, K., Shiokawa, K., and Kawano, H.: The Geotail Magnetic Field Experiment, J. Geomag. Geoelectr., 46, 7–21, 1994.

References

Krishnaswamy,S., D.L. Detrick, and T.J. Rosenburg, The inflection point method of determining riometer quiet day curves, Radio Science, 20, 123-136, 1985.

Krucker, S. and Lin, R.P., Two Classes of solar proton events derived from onset time analysis, The Atrophysical Journal, 542, 61-64, 2000.

Lakhina G.S., B.T. Tsurutanim, H. Kojima, H. Matsumoto, “Broadband” plasma waves in the boundary layers., J. Geophys. Res., 55, 27791-27831, 2000

Lauben D.S., U.S. Inan, T.F. Bell, D.L. Kirchner, G.B. Hospodarsky, J.S. Pickett, VLF chorus emissions observed by POLAR during the January 10, 1997, magnetic cloud, Geophys. Res. Lett., 25,2995-2998, 1998.

Leinbach, H., Some Observations of daytime recoveries during polar cap absorption events, Arkiv. Geofysik, 3, 427-429, 1961.

Leinbach, H., Midday Recoveries of Polar Cap Absorption, J. Geophys. Res. 72, 5473-5483, 1967.

Leinbach, H. and G.C. Reid, Phys. Rev. letters, 2, 61, 1959.

Leinbach, H., D. Venkatesan and R. Parthasarathy., Planet. Space Sci., 13, 1075, 1965.

Lemaire, J., Adv. Space. Res., 2, 3, 1982

References

Leske R.A., R.A. Mewaldt, E.C. Stone, T.T. von Rosenvinge., Observations of geomagnetic cutoff variations during solar energetic particle events and implications for the radiation environment at the space station, J. Geophys. Res., 30011, 2001.

Lin, W.C., D. Venkatesan and J.A. van Allen, J. Geophys. Res., 68, 1593.

Little, C.G., and H. Leinbach, The riometer – a device for the continuous measurements of ionospheric absorption, PROC. IRE, 37 315-320, February 1959.

Lockwood, M.: Relationship of dayside auroral precipitations to the open-closed separatrix and the pattern of convective flow, J. Geophys. Res., 102, 17 475–17 487, 1997.

Lyons, L. R. and Schulz, M.: Access of energetic particles to storm time ring current through enhanced radial diffusion, J. Geophys. Res., 94, 5491–5496, 1989.

Lysak, R.L., Y. Song, J.C. Grieger, Coupling of the magnetopause to the ionosphere by means of Alfven waves and field aligned currents., The physics of the Magnetopause, AGU, 1995.

Machin, K.E., M. Ryle, D.D. Vonberg, The design of an equipment for measuring small radio-frequency noise powers, Proc. IEE, 99, pt3, 127, 1952.

References

Marple, S.R., and F. Honary, Removal of Solar Radio Emission and Determination of riometer Quiet Day Curves, in preparation, 2002.

Marsden, P.L. and J.G. Wilson, Nuovo Cimento, Suppl II, 8, 228, 1958.

Masi, J.L. Radar Studis from Point Barrow, Alaska, Ph.D. thesis, University of London, England., 1980.

Mason, G.M., D.C. Hamilton, P.H. Walpole, K.F. Heuerman, T.L. James, M.H. Lennard, and J.E. Mazur, LEICA: A Low Energy Ion Composition Analyzer for the study of Solar and Magnetospheric Ions. IEEE Trans. Geosci. and Remote Sens., 31, 549-556. 1993.

Mauk, B. H. and McPherron, R. L.: An experimental test of the Ion cyclotron instability within the Earth's magnetosphere, Phys.Fluids, 23, 2111–2127, 1980.

McCracken, K.G., The Cosmic Ray Flare Effect 3. Deductions regarding the Interplanetary Magnetic Field, J. Geophys. Res., 67, 447-459, 1962.

Milan, S. E., Lester, M., Sato, N., and Takizawa, H.: On the altitude dependence of the spectral characteristics of decametrewavelength E-region backscatter and the relationship with optical auroral forms, Ann. Geophysicae, 19, 205–217, 2001.

References

Milogradov-Turin .J, F.G. Smith, A survey of the radio background at 38 MHz. Monthly Notices of the Royal Astronomical Society,161, 269-79, 1973.

Mitra A.P., J.N. Rowe, Ionospheric effects of solar flares. VI. Changes in D-region ion chemistry during solar flares. J. Atmos. Terr. Phys., 34, 795-806,. 1972.

Mitra, A.P. and C.A. Shain, The measurement of ionospheric absorption using observations of 18.3 mc/s cosmic radio noise, J.Atmos. Terr. Phys., 3, 203, 1953

Mukai, T., Machida, S., Saito, Y., Hirahara, M., Terasawa, T., Kaya, N., Obara, T., Ejiri, M., and Nishida, A.: The low energy particle (LEP) experiment onboard the Geotail satellite, J. Geomag. Geoelectr., 46, 669–692, 1994.

Nielsen, E. and Honary, F.: Observations of Ionospheric Flows and Particle Precipitation Following a Sudden Commencement, Ann. Geophysicae, 18, 908–917, 2000.

Nielsen, E. and Schlegel, K.: Coherent radar Doppler measurements and their relationship to the ionospheric electron drift velocity, J. Geophys. Res., 90, 3498–3504, 1985.

Nishino, M., Nishitani, N., Sato, N., Yamagishi, H., Lester, M., and Holtet, J. A.: A Rectified Response of Daytime Radio Wave Absorption to Southward and Northward

Excursions During Northward Interplanetary Magnetic Field: A Case Study, Advances in Polar Upper Atmosphere Research., 13, 139–153, 1999.

Parks, G.K., Physics of Space Plasmas: An introduction, Perseus Books, 1991.

Parthasarathy R. abd V.P. Hessler, Periodic covariance of radiowave absorption, earth currents and other associated phenomena in the auroral zone, J. Geophys. Res., 69, 2867, 1964.

Parthasarathy, R. and G.C. Reid, Magnetospheric Activity and its consequences in the auroral zone, Planetary Space Sci., 15,917, 1967.

Paulikas G.A., J.B. Blake, S.C. Freden, Low energy solar cosmic ray cutoffs:diurnal variations and pitch-angle distributions. J. Geophys. Res. 73, 87-95, 1968

Perona, G. E.: Theory on the Precipitation of Magnetospheric Electrons at the Time of a Sudden Commencement, J. Geophys. Res., 77, 101–111, 1972.

Pfotzer,G., Nuovo Cimento, Suppl. II, 8, 220, 1958

Piddington JH. Cosmic electrodynamics. Wiley-Interscience. 1969,

Pierce, J.A., J.Geophys. Res., 61, 475, 1956.

References

Potemra TA. The empirical connection of riometer absorption to solar protons during PCA events. Radio Science, 7, 71-7, 1972.

Quenby, J.J. and J. Wenk, Phil. Mag., 7, 1457, 1962.

Ranta A., H. Ranta, Storm sudden commencements observed in ionospheric absorption. Planet. Space Sci., 38,.365-372, 1990.

Ranta, H. Ionospheric Absorption Data from Finland. Monthly Data reports from Geophysical Observatory, Sodankylä (1972-83).

Ranta, H., A.Ranta, P.N. Collis, and J.K. Hargreaves. Development of the Auroral Absorption Substorm: Studies of Pre-onset Phase and Sharp Onset Using an Extensive Riometer Network. Planet. Space Sci.., 1287-1313. 1981

Ranta, H., Ranta, A., Yousef, S.M., Burns, J., Stauning, P., D-region observations of polar cap absorption events during the EISCAT operation in 1981-1989, J. Atmos. Terr. Phys., 55, 1993.

Ranta, H., H. Yamagishi and P. Stauning, Twilight anomaly, midday recovery and cutoff latitudes during the intense polar cap absorption event of March 1991, Ann. Geophys., 13, 262-276, 1995.

References

Reagan, J.B. and T.M. Watt, Simultaneous satellite and radar studies of the D region ionosphere during the intense solat particle events of august 1972, J. Geophys. Res., 81, 4579-4596, 1976.

Rees, M. H.: Auroral ionisation and excitation by incident energetic electrons, Planet. Space Sci., 11, 1209–1218, 1963.

Reid, G.C., Polar-Cap Absorption- Observation and Theory, Fundamentals of Cosmic Physics,1,167-202, 1974.

Reid, G.C. and C. Collins, J. Atmos. Terr. Phys., 14, 63, 1959.

Reid, G.C. and H.H. Sauer, The influence of the Geomagnetic Tail on Low-Energy Cosmic-Ray Cutoffs, j. Geophys. Res., 72, 197-208, 1967.

Richmond, A.D., Thermospheric dynamics and electrodynamics, in Solar Terrestrial Physics, Reidel, 523-607, 1983

Rietveld, M.T. and P.N. Collis, Mesospheric observations with the EISCAT UHF radar during polar cap absorption events: 2. Spectral measurements. Ann. Geophys., 11, 797-808, 1993.

Rishbeth, H. and Williams P. J. S.: The EISCAT ionospheric radar: the system and its early results, Q. J. R. Astr. Soc., 26, 478–512, 1985.

References

Roble R.G., B.A. Emery, On the global mean temperature of the thermosphere. Planet. Space Sci., 31,.597-614, 1983.

Roederer, J.G., Dynamics of Geomagnetically Trapped Radiation, Physics and Chemistry in Space,2, Springer-Verlag, 1970.

Rosen, L. H. and Winckler, J. R.: Evidence for the large scale azimuthal drift of electron precipitation during magnetospheric substorms, J. Geophys. Res., 75, 5576–5581, 1970.

Rosenberg T.J., Z. Wang, A.S. Rodger, J. R. Dudeney, K.B. Baker. Imaging riometer and HF radar measurements of drifting F region electron density structures in the polar cap. J. Geophys. Res., .98, 7757-7764, 1993.

Rostocker, G., B. Jackel, R.L. Arnoldy, The relayionship of periodic structure in auroral luminosity in the afternoon sector of ULF pulsations, Geophys. Res. Lett., 19, 613, 1992.

Rothwell, P., and J.J. Quenby, Nuovo Cimento, Suppl. II, 8, 249, 1958.

Russell, C.T. and McPherron, R.L ,Semiannual Variation of Geomagnetic Activity., J. Geophys. Res. , 78, 92, 1973.

References

Rycroft M.J., Enhanced energetic electron intensities at 100 km altitude and a whistler propagating through the plasmasphere, Planet. .Space Sci., 21, 239-251, 1973.

Sandstrom, A.E., Nuovo Cimento, Suppl. II, 8, 249, 1958.

Scholer M. Transport of energetic solar particles on closed magnetospheric field lines. Space Sci. Rev., 17, 3-44, 1975.

Schulz, M. and L.J. Lanzerotti, Particle Diffusion in the Radiation Belts, Physics and Chemistry in Space, 7, Springer-Verlag, 1974.

Shain, C.A., Galactic radiation at 18.3 Mc/s, Australian J. Sci. Res., A4, 258, 1951.

Shea, M.A., and Smart, D.F., Solar proton event patterns: The rising portion of five solar cycles, Adv. Space. Res., 29, 3325-3330, 2002.

Smart, D.F. and Shea, M.A., The Heliodistribution of solar flares associated with solar proton events, Adv. Space. Res., 17, 2113-2116, 1996.

Snyder, C.W., M. Neugebauer, U.R. Rae, J. Geophys. Res., 68, 6361, 1963.

Spencer, L.V., The theory of electron penetration, Phys. Rev., 98, 1597, 1955.

Stauning P., Absorption of cosmic noise in the E-region during electron heating events. A new class of riometer absorption events., Geophys. Res. Lett., 11, 1184-1187, 1984.

References

Stauning, P., High-latitude D- and E-region investigations using imaging riometer observations, J. Atmos. Terr. Phys., 58, 765-783, 1996.

Stauning, P., Ionospheric radio wave absorption processes in the dayside polar cap boundary regions, in: Polar cap boundary phenomena, (Eds) Moen, J., Egeland, A., and Lockwood, M., Kluwer Academic Publishers, pp. 233–254, 1998.

Stauning, P., Claur, C. R., Rosenberg, T. J., Friis-Christensen, E., and Sitar, R.: Observations of solar-wind-driven progression of interplanetary magnetic field By - related dayside ionospheric disturbances, J. Geophys. Res, 100, 7567–7585, 1995a.

Stauning P., J.K. Olesen, Observations of the unstable plasma in the disturbed polar E-region. Physica Scripta, 40, 325-332,1989.

Stauning, P., Yamagishi, H., Nishino, M., and Rosenberg, T. J.: Dynamics of Cusp-Latitude Absorption Events Observed by Imaging Riometers, J. Geomag. Geoelect., 47, 823–845, 1995b.

Stone, E.C., Local time dependence of non Stormer cutoff for 1.5 MeV protons in quiet magnetic field, J. Geophys. Res., 69, 3577-3582, 1964.

Storey, J.R., A.G. Fenton, and K.G. McCracken, Nature, 181, 1153, 1958

References

Störmer C., Phys. Rev, 45, 835, 1934.

Taylor, H.E., The latitude-local time dependence of low energy cosmic ray cut-offs in a realistic geomagnetic field, University of Iowa, Dept. of Phys. Astron., Rept. 67-8, May 1967.

Taylor, H.E. and E.W. Hones Jr., Adiabatic motion of auroral particles in a model of tge electric and magnetic fields surrounding the earth, J. Geophys. Res., 70, 3605-3628, 1995.

Tepley, C.A., J.D. Matthews and S. Ganguly, Incoherent scatter radar studies of mesospheric temperatures and collision frequencies at Arecibo. J. Geophys. Res. 86, 11330-11334, 1981.

Thomson J.J. Conduction of electricity through gasaea. Cambridge University Press. 1906.

Tsurutani, B.T., G.S. lakhina, Some basic concepts of wave-particle interactions in collisionless plasmas., Rev. Geophys., 35, 491, 1997.

Tsurutani, B.T., X.-Y. Zhou, J.K. Arballo, W.D. Gonzalez, G.S. Lakhina., V. Vasyliunas, J.S. Pickett, T. Araki, H. Yang, G. Rostocker, T.J.Hughes, R.P. Lepping, D. Berdichevsky, Auroral zone dayside precipitation during magnetic storm initial phases, J. Atmos. Sol. Terr. Phys., 63, 513-522, 2001.

References

Turunen, E., EISCAT incoherent scatter radar observations and model studies of day to twilight variations in the D-region during the PCA event of August 1989. J. Atmos. Terr. Phys. 55, 767-781, 1993

Turunen, E., Incoherent scatter radar contributions to high latitude D-region aeronomy, J. Atmos. Terr. Phys., 58, 707-725, 1996.

Uljev, V.A., Transport of energetic solar particles on closed magnetospheric field lines, Space Sci. Rev. 17, 3-44, 1978.

Uljev, V.A., A.V. Shirochkov, I.V. Moskin and J.K.Hargreaves, Midday Recovery of the polar cap absorption of 19-21 March 1990: a case study, J. Atmos. Terr. Phys, 57, 8, 905-915, 1995.

Vagina, L. I., Sergeev, V. A., Baker D. N., and Singer, H. J.: Use of mid-latitude magnetic data for modelling and diagnostics of magnetospheric substorms, Adv. Space Res., 18, 229–232, 1996.

Vasyliunas V.M. Large-scale morphology of the magnetosphere, in Solar-Terrestrial Physics. Reidel, .243-54, 1983.

References

Vondrak, R.R, G. Smith, V.E. Hatfield, R.T. Tsunoda, V.R. Frank and P.D. Perreault, Chantika model of the high-latitude ionosphere for application to HF propagation prediction. Rome Air Development Center Technical Report RADC-TR_78-7, 1978.

Von Mises, Richard. Mathematical Theory of Probability and Statistics, Chapters IX and IX, New York: Academic Press, 1964.

Waddington, C.J., Nuovo Cimento, 3, 930, 1956

Wang, Z., Rosenberg, T.J., Stauning, P., Basu, S., and Crowley, G., Calculations of riometer absorption associated with F region plasma structures based on Sondre Stomfjord incoherent scatter radar observations, Rad. Sci., 29, 209-215, 1994.

Wannberg, G, I. Wolf, L.-G. Vanhainen, K. Koskenniemi, J. Röttger, M. Postila, J. Markkanen, R. Jacobsen, A. Stenberg, R. Larsen, S. Eliassen, S. Heck, and A. Hunskonen, The EISCAT Svalbard Radar: A case study in modern incoherent scatter radar system design, Radio. Sci. 32, No. 6, 2283-2307, 1997.

Warwick, C.S. Propagation of solar particles and the interstellar magnetic field, in Cosmic Rays Solar Particles and Space Research (ed. B. Peters), Academic Press, 61-64,1963

Winkler, J.R. P.D. Bhavsar, A.J. Masley and T.C May, Phys. Rev. Letters, 6, 488, 1961.

References

Ziaddin, S., Simultaneous observations of pulsations in the geomagnetic field and in ionospheric absorption, Can. J. Phys., 38, 1714, 1960.